Ground-Based Near-Infrared Remote Sounding of Ice Giant Clouds and Methane

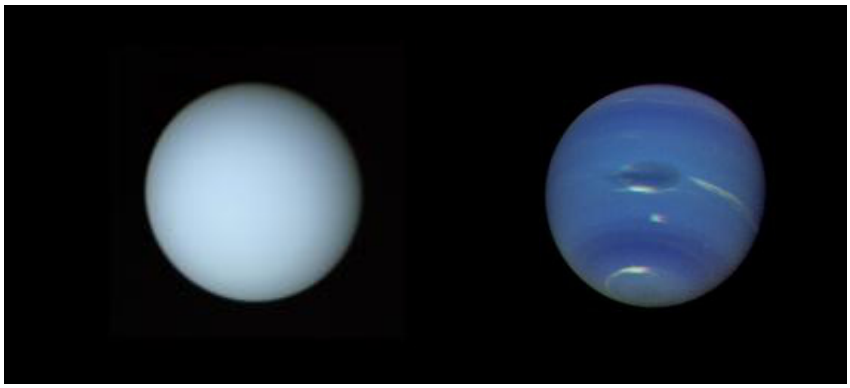

Dane Steven Tice

Submitted for the Degree of Doctor of Philosopy

October 2014

Lincoln College

Atmospheric, Oceanic and Planetary Physics

University of Oxford

Title page photos courtesy of NASA / JPL-Caltech / USGS.

Dedication

To Ariana

Without your unflagging support,
I would never have survived this undertaking,
nor come to Oxford in the first place.
Words cannot express my gratitude.

Acknowledgments

Many thanks to everybody who supported this research and helped guide and assist me as I navigated it. In particular:

Pat: for your constant support, encouragement, patience, and accessibility as I cut my teeth, and for carefully and constructively proofing 100s of these pages, some of them more than once. You made the whole process about as painless as it could have been, and your ideas and instruction were truly invaluable.

Mom, Dad, Joanna, Nana, Sam, Eric, Hal, Steve, Brian, Nate: whether you knew it or not, you often helped me along the way. Either as a sounding board when I was frustrated, as a cheerleader when I was dragging, or simply as a much-needed distraction from time-to-time. It was always comforting to know you were in my corner cheering for me, and just a phone call away.

Rhedyn: for giving me some perspective, and quickly reminding me, even at the end of the hardest days, that life is pretty darn good.

Leigh and Nick: for your suggestions and ideas, and being willing to put your work aside to give me a hand from time to time.

Ryan: for the workshop, several one-on-one meetings, and countless emails walking me through the Astrophysics SWIFT reduction package.

Jane and Anu: thanks for your 'air support' in my constant battle against LaTeX and my own formatting perfectionism.

Planetary Atmospheric Data Analysis Group: to anybody who served time listening to my weekly progress, and providing helpful suggestions and valuable criticism.

Tea and biscuits: enough said.

Contents

List of Figures

List of Tables

Abstract

The ice giants, Uranus and Neptune, are the two outermost planets in our solar system. With only one satellite flyby each in the late 1980's, the ice giants are arguably the least understood of the planets orbiting the Sun. A better understanding of these planets' atmospheres will not only help satisfy the natural scientific curiosity we have about these distant spheres of gas, but also might provide insight into the dynamics and meteorology of our own planet's atmosphere.

Two new ground-based, near-infrared datasets of the ice giants are studied. Both datasets provide data in a portion of the electromagnetic spectrum that provides good constraint on the size of small scattering particles in the atmospheres' clouds and haze layers. The broad extent of both telescopes' spectral coverage allows characterisation of these small particles for a wide range of wavelengths. Both datasets also provide coverage of the 825 nm collision-induced hydrogen-absorption feature, allowing us to disentangle the latitudinal variation of CH_4 abundance from the height and vertical extent of clouds in the upper troposphere.

A two-cloud model is successfully fitted to IRTF SpeX Uranus data, parameterising both clouds with base altitude, fractional scale height, and total opacity. An optically thick, vertically thin cloud with a base pressure of 1.6 bar, tallest in the midlatitudes, shows strong preference for scattering particles of 1.35 μm radii. Above this cloud lies an optically thin, vertically extended haze extending upward from 1.0 bar and consistent with particles of 0.10 μm radii. An equatorial enrichment of methane abundance and a lower cloud of constant vertical thickness was shown to exist using two independent methods of analysis.

Data from Palomar SWIFT of three different latitude regions (30° N, 0°, and 30° S latitude) of Neptune are analysed at multiple simultaneous zenith angles. Preliminary results show that a parameterised, two-cloud model similar to that applied to Uranus data provides good fits to data. The model has been enhanced for Neptune, now retrieving not only physical cloud parameters, but also the imaginary refractive index of particles from both clouds layers.

Results from both planets are compared and contrasted. The single scattering albedos derived for particles in the various cloud layers of both planets each show an abrupt, spectrally-narrow drop in reflectance near 1.0 μm, which provides a clue that will help identify the particles in tests against future, improved laboratory data. The location of cloud layers and methane on each planet suggests possible atmospheric circulation models.

Chapter 1

Introduction

Research is what I'm doing when I don't know what I'm doing.

— Wernher von Braun, *New York Times* Interview, 16 December 1957

From the plains of Africa, to the colonisation of nearly all of the flat and fertile land on Earth, mankind has always exhibited a curiosity of the unknown. Explorers set sail to cross vast oceans, set out to tame uncharted wilderness, and set their sights on conquering the highest mountains of the planet. Meanwhile, scientific minds wrestled to explain the new discoveries of these intrepid explorers.

Having explored and studied nearly every spot on Earth, one of the last great unknown expanses to be explored is the star systems and galaxies beyond Earth's blue atmosphere. It is to satisfy this innate curiosity to explore that we have pointed our telescopes at the planets of our solar system and other nearby systems. We seek to understand the Ice Giants because they are an unspoiled corollary to the atmosphere of our own planet. The techniques we develop to better explore these planets can aid us in exploring our own atmosphere. Insights about how atmospheric dynamics work in the simpler atmospheres of the Ice Giants can inform our understanding of

our own. And knowledge of the Ice Giants is starting to prove useful as we push farther into space and are discovering exoplanets in other star systems which resemble them.

This study of the Ice Giants is motivated in part to satisfy this basic human thirst for knowledge, and in part in the hope that what we learn in the outer reaches of our solar system can help us to forge farther into space, as well as help us to better understand our home planet.

1.1 An Overview of the Ice Giants

Lying farthest from the Sun, our solar system's 'ice giant' planets, Uranus and Neptune, have been the least understood of the planets ever since their discovery in the night sky. Because the ice giants lie much farther from Earth than the other planets, they appear much less bright than the five "classical planets" and were discovered much more recently (1781 and 1846, respectively). Table 1.1 summarises some of the basic information known about the ice giants themselves.

Due to the vast distance that separates them from the Earth, Uranus and Neptune also have a much smaller apparent size than the other planets and are more difficult to resolve with telescopes. While each of the classical planets has hosted at least one orbiter as well as flyby satellites, the ice giants have only been visited by a satellite for a close look once, when in the late 1980s *Voyager 2* flew past for a short series of observations. The limited quantity and resolution of data available contribute to make the ice giants arguably the most poorly understood in our solar system.

Irwin (2009) provides a summary of the basic properties of the ice giants. In this summary, we learn that like the gas giants, Jupiter and Saturn, Uranus and Neptune are composed primarily of hydrogen (H_2) and helium (He), with molecular abundance roughly equal to that found in the Sun. The gas and ice giants' similarities,

Table 1.1: Observed properties of the ice giants compared with Earth (adapted from Irwin (2009)).

Property	Earth	Uranus	Neptune
Solar Distance (AU)	1.0	19.2	30.1
Sidereal Orbital Period (years)	1.0	84	165
Orbital Eccentricity	0.017	0.046	0.009
Equatorial Radius (km)	6,387.0	25,559	24,765
Eq. Radius Relative to Earth	1.0	4.0	3.9
Oblateness $(R_e - R_p)/R_e$	0.0034	0.023	0.017
Mass (10^{24} kg)	5.97	86.625	102.78
Mass Relative to Earth	1.0	14.5	17.1
Mean Density ($g \cdot cm^{-3}$)	5.515	1.27	1.76
Sidereal Day (h:m)	23:56	17:14	16:06
Eq. Surface Gravity at 1 bar ($m \cdot s^{-2}$)	9.81	8.7	11.0
Escape Velocity ($km \cdot s^{-2}$)	11.2	21.1	23.3
Obliquity (°)	23.5	98	29
Equilibrium Radiating Temperature (K)	255	58	47
Mean Temperature at 1 bar (K)	288	79	70
Emitted / Absorbed Flux Ratio	1.0	1.06	2.52

however, stop there. The ice giants' radii are more than a factor of two smaller than those of the gas giants, and their masses are less than one fifth that of Saturn and one eighteenth that of Jupiter. This makes Uranus nearly as dense as Jupiter, the largest and most compressed giant planet, and nearly double the density of Saturn. Neptune, which is nearly 40% more dense than Uranus, is by far the most dense of the four giant planets.

Irwin (2009) continues to explain that the high densities and much smaller radii of the ice giants are due to the much higher abundance of heavier elements than on the gas giants. While Jupiter and Saturn contain approximately 3 and 5 times the solar abundance of elements heavier than helium, Uranus and Neptune have closer to 20 and 30 times the solar abundance, respectively. While still the subject of debate, it is generally believed that this enrichment of heavy elements is actually an artefact of proportionately less hydrogen and helium being collected by the ice giants during planet accretion. The smaller size of the ice giants simply made it impossible for them to gravitationally attract as much hydrogen and helium as the much more massive Jupiter and Saturn, not to mention the Sun.

These heavier elements on the ice giants, Irwin (2009) explains, have combined to contribute, in decreasing order, significant water (H_2O), methane (CH_4), ammonia (NH_3), and hydrogen sulphide (H_2S) to the ice giants' composition, not to mention a wide range of trace hydrocarbons and other molecular species. It is primarily in the upper atmosphere where the array of photo-dissociated and subsequently recombined molecules is quite varied. It is the abundance of methane at high altitudes which absorbs much of the red sunlight hitting the planet, and giving them their characteristic blueish colours.

An important clue about the formation age of the ice giants comes from exploring the ratio of deuterium (^2H, or simply D) to protium (H) found in the ice giants' atmospheres. Protium, by far the most abundant isotope of the hydrogen atom, has

a nucleus composed of just one proton. Deuterium, which is much rarer than protium, is the only other stable hydrogen isotope. Deuterium, unlike protium, also has a neutron in its nucleus making the isotope twice as massive. It is the ratio of deuterium to protium that proves useful in determining planetary formation age, though the method of making this calculation is beyond the scope of this text. D/H ratios are simply brought up in this context to provide an additional characteristic which distinguishes the ice giants from the gas giants, the latter of which have D/H ratios several factors smaller. On Uranus the D/H ratio of methane has been estimated at $(\mathrm{D/H})_{CH_4} = (2.9^{+0.9}_{-0.5}) \times 10^{-4}$ with $(\mathrm{D/H})_{H_2} = (9^{+9}_{-4.5}) \times 10^{-5}$ (de Bergh et al., 1986; Irwin et al., 2012b) . On Neptune studies have found $(\mathrm{D/H})_{CH_4} = (3.0^{1.0}_{0.9}) \times 10^{-4}$ and $(\mathrm{D/H})_{H_2}$ ranging from $(1.2^{+1.2}_{-0.8}) \times 10^{-4}$ to $(6.5^{+2.5}_{-1.5}) \times 10^{-5}$ (de Bergh et al., 1990; Feuchtgruber et al., 1999; Fletcher et al., 2010; Irwin et al., 2013).

Wind speeds and patterns on both ice giants, also discussed at length in Irwin (2009), are a fascinating feature of the pair of planets, and again prove the ice giants to be distinct when compared to their gas giant cousins (see figure 1.1). Though the colourful structure of belts and zones is much more subtle and simple on the ice giants, the gas and ice giants alike have a system of strong, stable wind jets that circle the planets. At the equator, all four giant planets have latitudinally wide zonal jets. However, these jets are prograde on the gas giants and retrograde on the ice giants. In the northern and southern midlatitudes, gas giant equatorial jets give way to a series of numerous, narrow, jets of alternating direction and much slower wind speeds as latitude increases. In contrast, the equatorial jets of each ice giant give way to just one prograde jet in both midlatitudes, the speed of which actually exceeds the equatorial jet in the case of Uranus. Overall, the wind speeds at the centre of all three Uranian jets, lying around 100 m/s (equatorial retrograde) and 250 m/s (midlatitudinal prograde), are comparable if not faster than nearly all the winds on the gas giants. The central wind speeds on the Neptunian jets are even more extreme, lying around

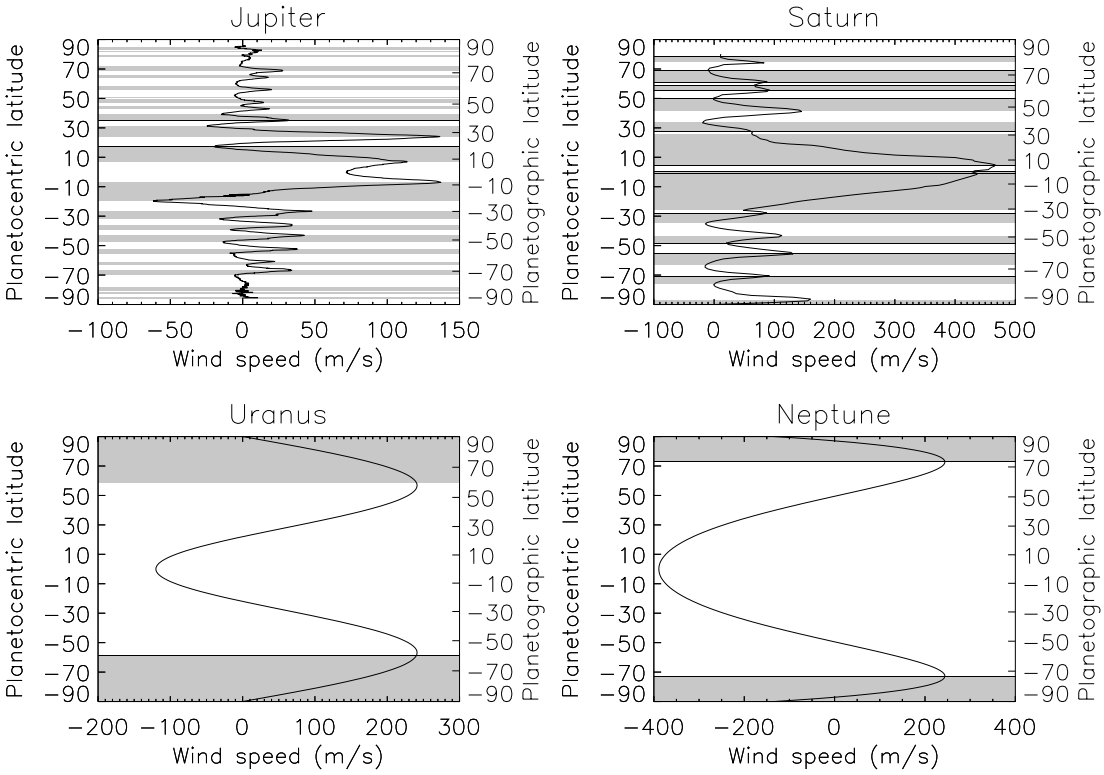

Figure 1.1: Wind speeds on the ice giants compared with those of the gas giants. Irwin (2009), used by permission.

250 m/s (midlatitudinal prograde) and 400 m/s (equatorial retrograde). In our solar system, the equatorial jet of Neptune is outpaced only by the Saturnian equatorial jet, which reaches well over 450 m/s.

One major puzzle that is noticed when studying the four giant planets is their widely varying radiative flux ratios. On planets that are all, essentially, composed of hydrogen and helium, it is surprising to find such variation in this basic attribute. Making some calculations from information found in Irwin (2009), it is apparent that the average ratio of emitted to absorbed flux among the giant planets is 1.76, indicating that on average, the circulation on the giant planets is driven through a combination of internal and solar forcing. Given this value, Jupiter and Saturn, individually, have unsurprising radiative flux ratios of 1.67 and 1.78, respectively. If the story

ended here, it would appear that for the giant planets of our solar system the radiative flux balance is a fairly universal characteristic, with very similar proportions of absorbed and emitted energy in each.

As it happens, however, the ice giants are the outliers in the spectrum of flux ratios. More than simply outliers, they in fact lie so far from the average that not only do they call into question the general trends already described, they each present a different and unique question to the dynamicists who study their internal natures. Irwin (2009) quotes a 1.06 flux ratio for Uranus. This planet therefore seems to have only a tiny internal heat source, indicating that the heat-driven dynamics of the planet can be almost entirely accounted for by the Sun, roughly 19 AU away, and merely a tiny disc in the dark sky. This low flux ratio, combined with the fact that Uranus' 98° axial tilt bathes the poles in alternate, 42-year periods of winter/night and summer/day, create a very unique set of atmospheric conditions that are highly seasonal. Those seen by *Voyager 2*, close to the last Uranian solstice, were, as already mentioned, very static and calm. Those dynamics seen closer to the latest equinox in 2007, as will be discussed a great deal in this thesis (see chapter 4), paint an entirely different picture of the Uranian atmospheric circulation. Finally, when looking to Neptune, the other end of the flux spectrum is encountered, with its massive 2.52 emitted/absorbed ratio. While this high ratio accounts for the incredibly active convective nature of the planet, the origins of the powerful internal heat source are not well understood.

The giant planets are slightly oblate, or squashed, due to their high rates of rotation and their gaseous composition. This creates a non-spherical gravitational field which, in turn, creates asymmetric forces upon their rings and moons, as well as any spacecraft passing within the sphere of their gravitational influence. Studying these variations, along with determining the polar moments of inertia of the planets, has allowed us to determine the approximate distribution of mass within the planets, and thus hypothesise their internal structures. While different variations of

the basic internal structures are still the subject of debate (see Atreya et al. (2006); Irwin (2009); Podolak and Helled (2012)), each possibility shares some principle features. The planets' mean densities suggest, as already noted, that the ice giants have a high abundance of atoms and molecules much heavier than helium. These heavy molecules, given the ice giants' internal temperatures on the order of 10^3 K, exist within the ice giants as a mixture of molecular ices. It is for these ices that the ice giants are given their collective name. Nearer the centre of the ice giants, where pressures increase to the order of 10^5 bar, these ices become a hot, homogeneous molecular fluid. Surrounding this molecular 'ice' fluid lies a less dense, and very cold hydrogen and helium shell. On Uranus, this outer covering of hydrogen and helium probably comprises the outer 5,000 km, or roughly 20% of the radius, while on Neptune, significantly more dense overall, it comprises the outer 3,500 km, or about 15% of the radius.

In the remainder of the Introduction, these outer H_2/He shells, which comprise the observable atmospheres of the ice giants, are explored in more detail. It is in this region of the planet that the research for this thesis focuses. In order to ensure that the reader is familiar with the general characteristics of the ice giant atmospheres, their atmospheric composition and general structure are first explored (section 1.2). Following this, a more in-depth review of the specifics of cloud and haze properties on each planet is included, divided by planet into sections 1.3 and 1.4. These two sections include an overview of results upon which this thesis is built, and a brief discussion of shortcomings of previous studies. The Introduction is then concluded with section 1.5, which presents the basic goals of the research contained here, and outlines the remaining format for the thesis.

1.2 Atmospheric Composition and Structure

The ice giant atmospheres are much colder than their gas giant cousins'. Despite the high overall concentration of methane and other hydrocarbons, the observable upper atmospheres of Uranus and Neptune appear to exist in "relative atmospheric purity" (Herbert and Sandel, 1999). This is due to cold tropopausal[1] temperatures which effectively produce a 'cold trap' above which many condensates form. This leaves a pure He/H_2 mix above several large, relatively stable and long-lasting cloud decks. Of the small amount of methane that does escape into the ice giant stratospheres through their respective cold traps, it is believed that a large portion photolytically dissociates into molecules and radicals which include H, CH, CH_2, and CH_3. These photolytic products then recombine, along with several other trace atmospheric elements and some elements which may come from the rings or moons, to enrich the stratospheres with trace amounts of many complex molecules (Irwin, 2009).

A relatively small amount of research has investigated these molecules on Uranus, but there are still several species that have been identified. Thermal emission between 4.6 and 5.0 μm has been detected on Uranus that is consistent with fluorescing carbon monoxide (CO) of a volume mixing ratio (VMR[2]) no greater than 2×10^{-8} between a presumed H_2S cloud at ~ 3.1 bar and the tropopause, and equal to 3×10^{-8} above the tropopause (Encrenaz, 2004; Encrenaz et al., 2004). There is evidence that Uranus' lack of strong vertical mixing might mean that CO is not always present, or at least quite depleted, in the troposphere, as its emission lines in the millimetre

[1] In planetary atmospheres, the bottom region of the atmosphere, where convection dominates heat transfer, and temperature cools with increasing altitude, is called the 'troposphere'. Above this region, where temperature begins to increase with increasing altitude, and radiative transfer begins to dominate the transport of heat, is the more stably stratified 'stratosphere' (Andrews, 2000; Houghton, 2002). The boundary between these layers is referred to as the 'tropopause', and lies at an approximate pressure of ~ 0.1 bar on both Uranus and Neptune, where the temperature is in the low 50s K.

[2] Here and elsewhere in this report, the VMR is used in discussion of the abundance of constituent gases. VMR, also known as mole fraction, is defined as $\text{VMR} = \frac{n_i}{n_{tot}} = \frac{p_i}{p_{tot}}$ for a number of constituent particles, n_i, relative to the bulk atmospheric number of particles, n_{tot} (Andrews, 2000).

range were not detected in some studies (Marten et al., 1993; Rosenqvist et al., 1992). Hydrogen cyanide (HCN), like CO, has been searched for but not found to date on Uranus (Encrenaz, 2004; Marten et al., 1993).

Water ice (H_2O), on the other hand, has been detected in the Uranian stratosphere with VMRs of between $(5-12)\times10^{-9}$ (Encrenaz, 2004; Feuchtgruber et al., 1997). Acetylene (C_2H_2) emissions have been detected on Uranus consistent with abundances of 10^{-8} (UV, Yelle et al. (1989)) and 4×10^{-7} (thermal infrared, Encrenaz et al. (1998)). An upper limit is set, using thermal infrared observations, of 2×10^{-8} (Orton et al., 1987b) for the abundance of ethane (C_2H_6).

On Neptune, where more research has been undertaken, a much larger number of trace molecular constituents have been identified. Like on Uranus, Neptunian CO has been detected, and has been seen and discussed over and over again (Bishop et al., 1995; Encrenaz, 2004; Feuchtgruber et al., 1997; Lodders and Fegley, Jr., 1994). Early estimates of CO abundances in the stratosphere of $(6.5\pm3.5)\times10^{-7}$ were based on millimetre data of Rosenqvist et al. (1992). Guilloteau et al. (1993) and Marten et al. (1993) saw emissions consistent with a VMR_{CO} of $(0.6-1.5)\times10^{-6}$ and $(1.2\pm0.4)\times10^{-6}$, respectively, with ground-based millimetre data. The latter author revisited submillimetre CO analysis and suggested uniform distribution in the upper stratosphere of $(1.0\pm0.2)\times10^{-6}$ (Marten et al., 2005). Naylor et al. (1994), using millimetre data, constrained tropospheric CO to abundances of $(0.7-1.3)\times10^{-6}$. Courtin et al. (1996) saw absorption bands in the reflected UV, placing the VMR at 2.7×10^{-7}. Submillimetre results from Encrenaz et al. (1996) constrained the VMR to less than 1×10^{-6} and preferred a value of 6×10^{-7}. Hesman et al. (2007) millimetre analysis found CO to be variable in altitude, placing its VMR at $(2.2^{+0.6}_{-0.4})\times10^{-6}$ in the upper stratosphere and $(0.6\pm0.4)\times10^{-6}$ in the lower stratosphere and troposphere, while Irwin et al. (2013) constrained this lower abundance to $\ll 1\times10^{-6}$. Lellouch et al. (2010), with far-infrared data, prescribed a stratospheric VMR of 1×10^{-6}. It should

be noted that the wide variation in these predicted concentrations is due to analysis of data that was collected over a span of more than two decades, as well as the focus of each study on different regions of the Neptunian stratosphere, where active dynamics lead to conditions which vary rapidly with time, geographic location, and altitude. It is believed that these abundances, particularly those in the upper stratosphere, require both internal and external sources of carbon, and new evidence suggests that perhaps external sources are more important (Fletcher et al., 2010; Hesman et al., 2007; Lellouch et al., 2010; Irwin et al., 2013).

Carbon dioxide (CO_2) has also been detected on Neptune, with stratospheric VMRs of 5×10^{-10} suggested (Feuchtgruber et al., 1997; Encrenaz, 2004). Thermochemical models have suggested similar Neptunian CO_2 abundances to that of CO (Lodders and Fegley, Jr., 1994). Hydrogen cyanide (HCN) has been detected on Neptune, with values of $(3.0 \pm 1.5) \times 10^{-10}$ (Encrenaz, 2004; Rosenqvist et al., 1992), $(3.2 \pm 1.5) \times 10^{-10}$ (Lellouch et al., 1994), and $(1.0 \pm 0.3) \times 10^{-9}$ (Marten et al., 1993, 2005) suggested, all from millimetre observations at different parts of the stratosphere.

Water (H_2O) in the Neptunian stratosphere has been detected in the thermal infrared at abundances of between $(1.5 - 3.5) \times 10^{-9}$ (Encrenaz, 2004; Feuchtgruber et al., 1997), in the far-infrared at a VMR of $(8.5 \pm 0.2) \times 10^{-10}$ (Lellouch et al., 2010), and modelled at up to 440 times the solar abundance (Lodders and Fegley, Jr., 1994).

Voyager 2 infrared observations detected thermal emissions that indicated that $\mathrm{VMR}_{C_2H_2} = 6 \times 10^{-8}$ in the Neptunian stratosphere (Bézard and Romani, 1991). In the upper stratosphere at 0.1 mbar, the VMR for C_2H_2 has been suggested to be 1.1×10^{-7} (Encrenaz, 2004), while thermal emissions indicate a VMR of $(3.3^{+1.2}_{-0.9}) \times 10^{-8}$ at 0.5 mbar (Greathouse et al., 2011).

C_2H_6 in the Neptunian stratosphere seems to be highly variable, having been detected in the thermal infrared at abundances of 6×10^{-6} (Orton et al., 1987b), 1.5×10^{-6} (Bézard and Romani, 1991), 1.3×10^{-6} (Encrenaz, 2004), 1.5×10^{-6} (Hammel et al.,

2006), $(8.5\pm2.1)\times10^{-7}$ (Fletcher et al., 2010), $(9.3^{+3.5}_{-2.6})\times10^{-7}$ (Greathouse et al., 2011), and $(0.5-1.2)\times10^{-6}$ (Fletcher et al., 2014). Significant VMRs of C_2H_6 were tracked for 19 years in Hammel et al. (2006, 2007) and used as a proxy for temperature variations in the stratosphere.

A few other molecules have received mention in the literature. Ethylene (C_2H_4) has been detected in the Neptunian stratosphere (Bézard et al., 1999; Encrenaz, 2004), with an abundance at 2.8 μbar, from a thermal infrared emission, of $(5.0^{+1.8}_{-2.1})\times10^{-7}$ (Fletcher et al., 2010). Methyl radicals (CH_3) have been detected with thermal infrared data and given a column abundance above 0.2 mbar of $(1.6^{+1.2}_{-0.9})\times10^{13}$ molecules $\cdot$ cm^{-2} (Bézard et al., 1999; Encrenaz, 2004). Meadows et al. (2008), using thermal infrared observations, detected diacetylene ($VMR_{C_4H_2}=(3\pm1)\times10^{-12}$) and methylacetylene ($VMR_{CH_3C_2H}=(1.2\pm0.1)\times10^{-10}$), citing their VMRs at 0.1 mbar. Molecular nitrogen (N_2) is assigned a maximum abundance of 7×10^{-3} according to far-infrared observations (Burgdorf et al., 2003). Ammonia (NH_3), which is thought to exist in the deep atmosphere of Neptune(Lindal, 1992), has been assigned an upper limit for VMR of 3×10^{-9} by UV observations (Courtin et al., 1996). The same observations indicate that cyanoacetylene (HC_3N) exists with no more than a 5×10^{-8} abundance (Courtin et al., 1996). Phosphine (PH_3) emissions have been searched for in millimetre data, but with no results, supporting the hypothesis that there is no PH_3 supersaturation in Neptune.

As already mentioned, one of the principle characteristics of the ice giants is their thick cloud structures, generated when gaseous molecules condense in the cold atmospheric temperatures. Though specific, observation-based details about composition and altitude are still the subject of much debate, there exist simple models, known as Equilibrium Cloud Condensation Models (ECCMs), which predict the height and composition of these stable cloud decks (Irwin, 2009). The models assume that warm gas parcels from the interior rise but do not mix with the surround-

ing air.[3] At an altitude where the VMR for a particular constituent molecule is equal to the saturation VMR of that molecule in the surrounding, cooler air, the molecule condenses out of the parcel to form a cloud. The parcel continues to rise through increasingly cool surrounding air, and the VMR of the gas in question continues to decrease, following the decreasing saturation VMR. See figures 1.2 and 1.3 for Uranian and Neptunian baseline atmospheric profiles, which are used to calculate the location of the ECCM-predicted cloud layers. Moving upwards from the tropopause, the surrounding air temperatures begins to increase, rather than decrease, as does the saturation VMR. But since the gas was, for the most part, condensed out of the air parcel at lower altitudes, the constituent gas' VMR above the tropopause remains constant. For the ice giants, these constant stratospheric VMRs are generally quite low, allowing us to consider the tropopause to act as the 'cold trap' already mentioned.

Irwin (2009) describes the ECCM predictions for Uranus (see figure 1.4), which begin in the deep atmosphere with a large water cloud that exists between 100 and 1000 bar, depending on the exact H_2O abundance in the deep atmosphere. Above this, at approximately 40 bar, an ammonium hydrosulphide (NH_4SH) cloud is expected to form. This will be followed by a cloud of either ammonia (NH_3) or hydrogen sulphide (H_2S) somewhere between 2 and 8 bar, depending on which of those species has a higher deep abundance.[4] Finally, at about 1.5 bar, a methane (CH_4) ice cloud is predicted.[5]

[3] This assumption of no vertical or horizontal mixing is the ECCM's greatest inaccuracy. Although the models predict the base altitude of the cloud deck fairly accurately, predictions of the optical or vertical thickness of the clouds, as well as the abundance profile above the cloud's base altitude, are much poorer. These features are dependent on the rate of uplift, which governs the amount of mixing possible with the surrounding air, and the rate of formation and size of the aerosol particles. Particle size, in turn, dictates how these particles move in the atmosphere, and how quickly they are able to descend to warmer temperatures to re-evaporate.

[4] Since the two species in question react together to form NH_4SH, the lesser of the two will be consumed in the production of the deeper NH_4SH cloud.

[5] Signorell and Jetzki (2007) predict that any methane clouds on the ice giants will, based on the pressures and temperatures which characterise the planets, contain crystalline ices.

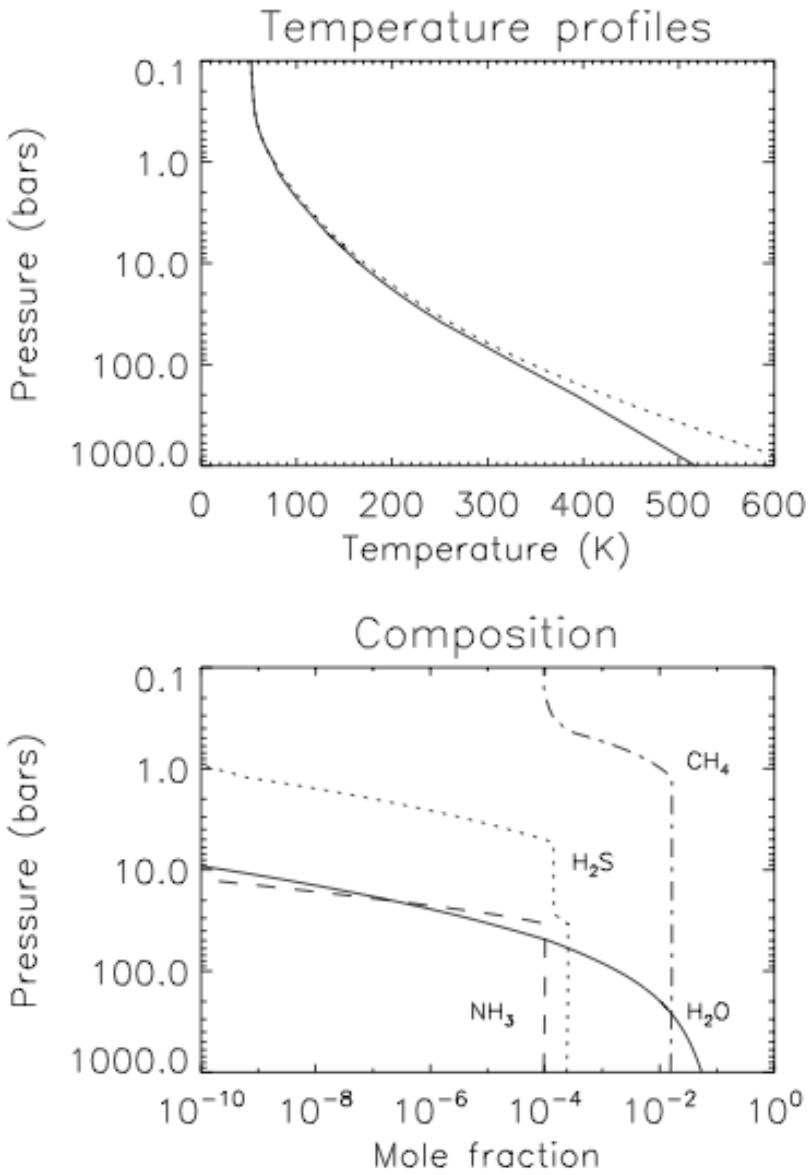

Figure 1.2: Uranian tropospheric temperature profile (upper panel) and principle constituent VMR profiles (lower panel). These profiles are used to calculate the Uranian ECCM-predicted condensation cloud decks shown in figure 1.4. Adapted from Irwin (2009) and used by permission.

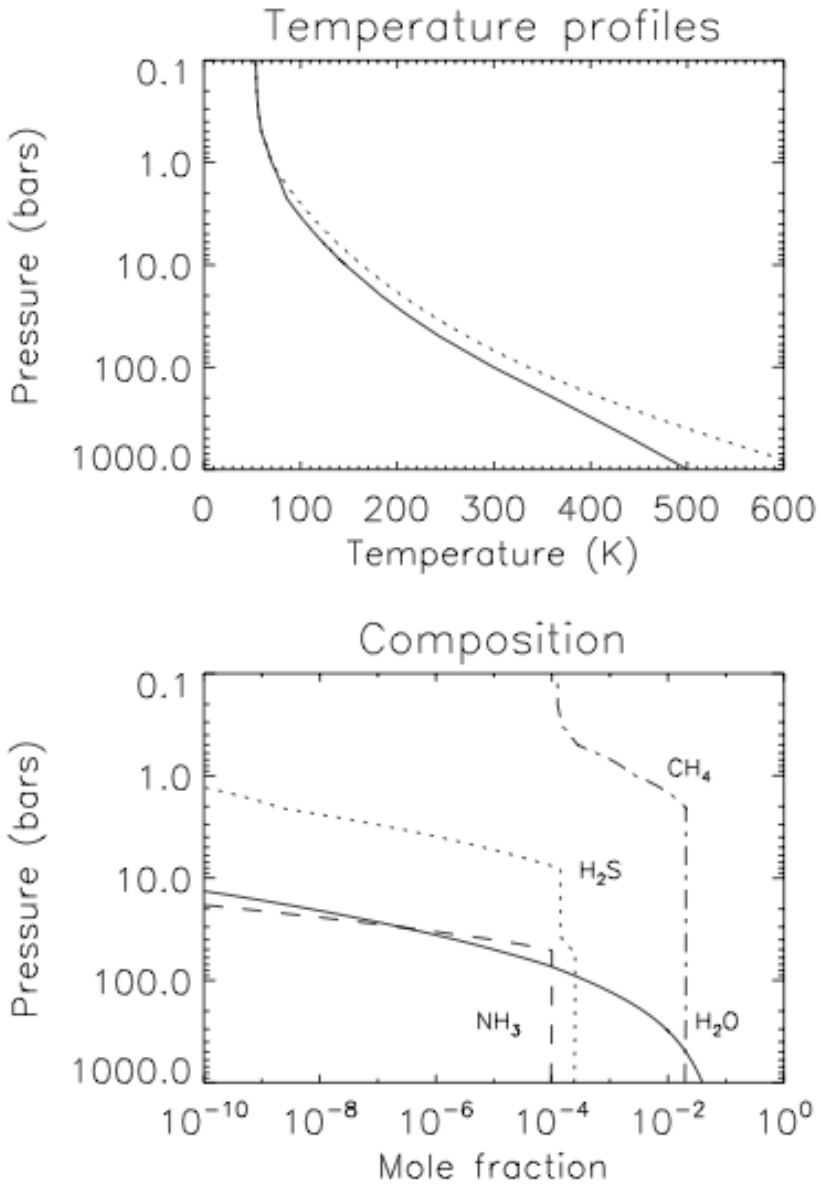

Figure 1.3: Neptunian tropospheric temperature profile (upper panel) and principle constituent VMR profiles (lower panel). These profiles are used to calculate the Neptunian ECCM-predicted condensation cloud decks shown in figure 1.5. Adapted from Irwin (2009) and used by permission.

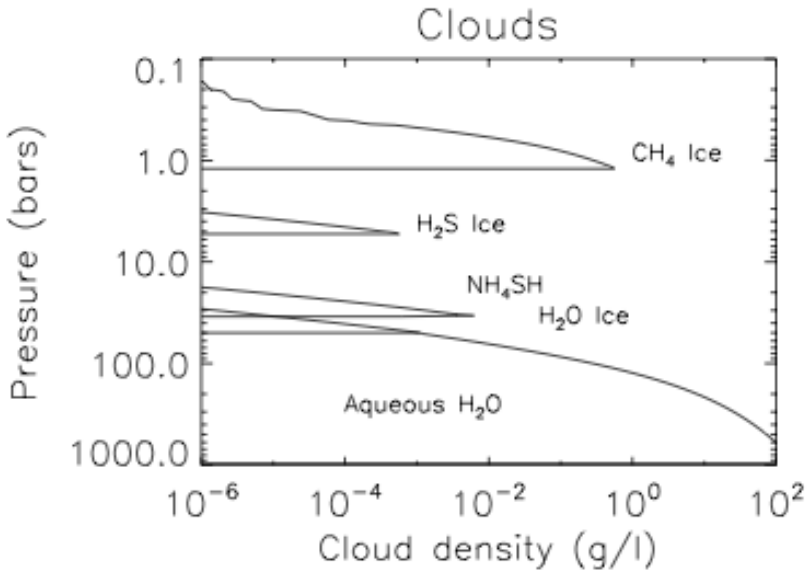

Figure 1.4: Plot of ECCM-predicted Uranian condensation cloud decks in the troposphere. Adapted from Irwin (2009) and used by permission.

Above the tropopausal cold trap, Irwin (2009) continues, the abundance of most condensable material in the Uranian atmosphere is well below the saturated VMR and so does not form large or long-lasting cloud layers. Nevertheless, there is sufficient stratospheric methane that photolyses, and is then able to combine with other trace elements, as already discussed, to form complex hydrocarbons and other molecules. As these products diffuse downwards through the atmosphere, photochemical and eddy mixing models predict that they condense to form haze layers of C_4H_2 ice ($p > 0.1$ mbar), C_2H_2 ice ($p > 2.5$ mbar), and C_2H_6 ice ($p > 15$ mbar). These hazes effectively combine to produce an optically thin stratospheric layer which lies mostly between the tropopause and the 1 mbar level, though below approximately 30 mbar the various ice particles have likely coalesced to sufficient size to gravitationally drop out of the stratosphere.

The Neptune ECCM (see figure 1.5), also described thoroughly in Irwin (2009), predicts identical cloud composition in the troposphere as was seen on Uranus, but

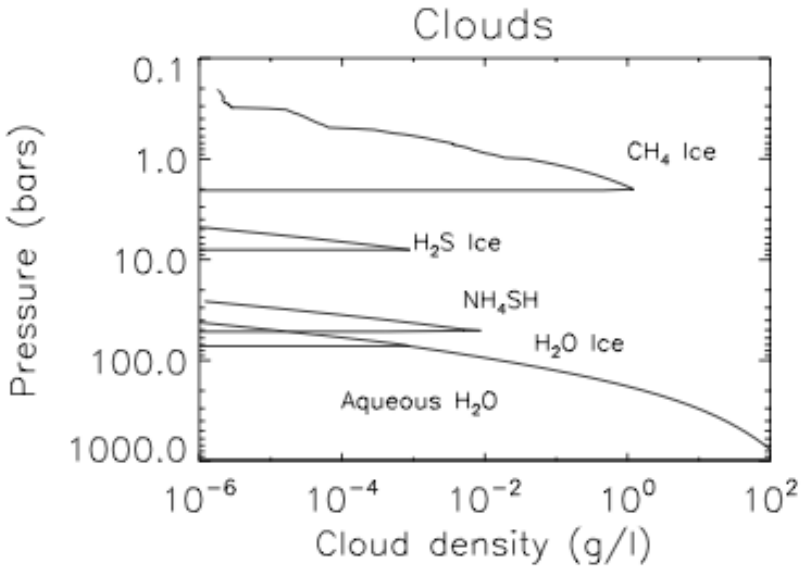

Figure 1.5: Plot of ECCM-predicted Neptunian condensation cloud decks in the troposphere. Adapted from Irwin (2009) and used by permission.

at altitudes of 50 bar (H_2O), 37 – 50 bar (NH_4SH), 7 – 8 bar (H_2S/NH_3) and 1.5 – 2 bar (CH_4). And again, as with Uranus, a number of different stratospheric haze layers are predicted, each composed of molecular products of methane photodissociation. Neptune's more active transport dynamics cause more haze-producing methane to reach the stratosphere, which consequently form more optically thick hazes (figure 1.7). Higher stratospheric methane abundance produces hazes more spatially varied and dynamic than their Uranian counterparts. It is proposed that rapid growth of tropospheric CH_4 particles causes them to rain out quickly, which keeps the main methane cloud deck thin (Irwin, 2009). As a result, stratospheric hazes have comparable optical thickness to that of the tropospheric CH_4 cloud layer. Principal predicted components of this stratospheric haze are C_4H_2, ($p > 2$ mbar), C_2H_2 ($p > 6$ mbar), and C_2H_6, ($p > 10$ mbar). It is possible that a second, stratospheric CH_4 layer exists at a stratospheric condensation level (Baines et al., 1995a,b; Irwin, 2009).

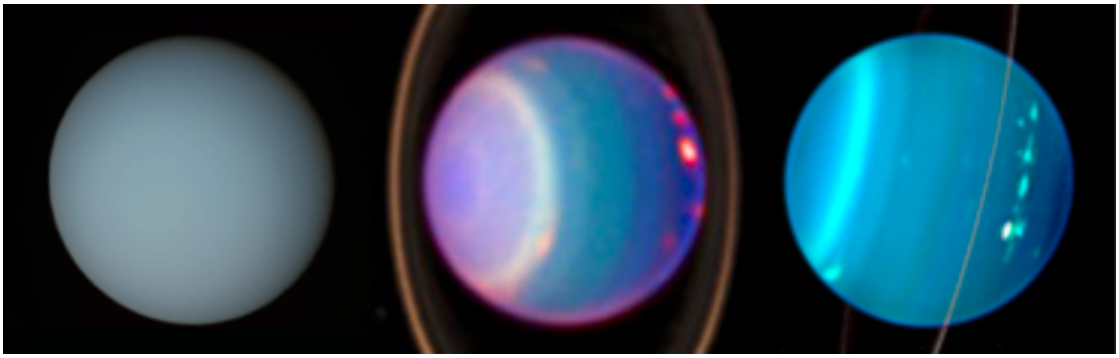

Figure 1.6: Uranus as seen in 1986 (*Voyager 2*), 1998 (HST), and 2004 (Keck). Evolution to a more dynamic upper atmosphere can be seen as the planet approaches the 2007 equinox. *Voyager* and HST images courtesy NASA / JPL-Caltech / USGS. Keck image credit: Lawrence Sromovsky, University of Wisconsin-Madison / W. M. Keck Observatory.

As Uranus approached equinox in 2007, a different picture of the planet unfolded than was provided by *Voyager 2* data (see figure 1.6). Uranus, in the 10 years surrounding the equinox, has been anything but the static and homogeneous blue sphere it seemed to be in 1986. The cloud model developed by Sromovsky and Fry (2008) contains a deep (6 – 8 bar) cloud layer which, in 2006, exhibited a reflectivity increase from 2% at 33° N to 3 – 4% in the southern hemisphere. As for the shallow (2 – 3 bar) cloud, the reflectivity displayed an increase from 0.5% at 33° N to ∼ 1% at a 43° S bright band feature. This feature is close to the similar feature noted in 2002 by Karkoschka and Tomasko (2009) and showed in the upper cloud a localised ∼ 25% reflectivity increase, and higher altitude with 10% less cloud-top pressure. In addition to the marked changes in the upper cloud at this band feature, the lower cloud moved approximately 1.4 bar deeper.

The single cloud predicted by Irwin et al. (2010, 2011a, 2012a,b) showed, just as in the Sromovsky and Fry (2008) upper cloud of the same altitude, a decrease in cloud base pressure polewards of about 40° N, S. This pressure decrease, combined with

a similar, though slower, polewards decrease in fractional scale height[6] of the cloud produceed a local maximum in cloud-top height at both 45° N, S. Two possible explanations are suggested for this trend in the cloud. First, and perhaps more likely, is that an equatorial methane enrichment which would require the latitudinal trends in the clouds. This possibility will be discussed and studied in detail in section 4.3. Alternately, it was also discussed that the trend could be consistent with two separate cloud decks, including both an upper deck in midlatitudes consisting of presumably CH_4, and a lower deck more visible at the equatorial region consisting of H_2S or NH_3. While two distinct decks would be consistent with the ECCM predictions for Uranus, it was not clear why the clouds would not cover the entire latitudinal extent of the planet (Irwin et al., 2010, 2011a; Sromovsky and Fry, 2007).

As the planet moved closer and closer to the 2007 equinox, it became a progressively more active and evolving disc in the night sky. Between the *Voyager 2* flyby in 1986 and 2001, when the Hubble Space Telescope (HST) made an observation of the planet, the disc-average brightness had decreased by 35% (Karkoschka, 2001). Throughout these 16 years, however, a host of more localised changes were contributed to this overall darkening trend. HST images that show development of a bright ring at 70° S over the 10 years beginning in 1994 (Rages et al., 2004). The south pole itself reached a temporal brightness peak in 1994, and darkened during the following decade, while a polar collar at 45° S brightened in the 2 – 4 bar pressure region relative to the south pole. At least ten high-contrast, discrete clouds became apparent on the planet by 1997, with many more appearing in 2001 data (Karkoschka, 1998, 2001). After 40 years of perpetual daylight in the southern hemisphere, 2004 data of Uranus was modelled successfully with a deep cloud at approximately 4.55 bar that

[6] An atmospheric scale height is defined as the altitude over which the pressure of an atmosphere decreases by a factor of e, and can be represented by $H = \frac{RT}{Mg}$ where R is the universal gas constant, T is the temperature, M is the mean molecular mass, and g is the gravitational acceleration of the planet in question (Houghton, 2002). The "fractional scale height" refers to the ratio of the scale heights of the constituent cloud and the atmosphere, i.e. $H_{constituent}/H_{atmosphere}$.

dissipated completely north of 50° N. This marked hemispheric asymmetry was predicted to reverse after the equinox in 2007, with the cloud layer covering the northern pole and disappearing in the south (Sromovsky and Fry, 2007).

During the years surrounding the 2007 equinox, a large number of major changes occurred on Uranus with a similar timescale as those seen prior to 1982, four years before the southern summer solstice (Karkoschka, 2001). During the equinoctial changes, the southern polar collar (45° S) seemed to disappear, while a new collar at 45° N seemed to simultaneously appear (Hammel et al., 2005; Irwin et al., 2010, 2011a; Sromovsky et al., 2009). By 2005, ground-based images recorded discrete features brighter in the infrared than any seen before on Uranus, and subsequent studying of images revealed these specific features originated in late 2004 (Sromovsky et al., 2007). Throughout 2006 and 2007, Norwood and Chanover (2009) observed the upper, 2-bar cloud layer in the northern hemisphere brighten, while similar clouds in the southern hemisphere dimmed, just as predicted by Hammel et al. (2006). In 2006 to 2008, Irwin et al. (2010, 2011a) observed the same brightness trends in the upper cloud deck. Karkoschka and Tomasko (2009) found that a model utilising a single, extended haze above these cloud decks reproduced their data better than several, separate condensation layers that would be predicted by the photochemical and eddy mixing models mentioned above. The same paper explained the dark albedo of the planet's near-IR methane windows through methane absorption and conservatively scattering aerosols in the stratosphere.

This flurry of activity seen in Uranus in the early years of this century was matched by activity seen in 1989 when *Voyager 2* flew past Neptune (see figures 1.7 and 1.8). Consequently, telescopes have been pointed again and again over the past 28 years to see what new mysteries the eighth planet of our solar system would reveal. Two of the most fascinating features of the upper atmosphere that were revealed in the *Voyager* flyby came in the form of huge storm systems, seen in figure 1.7, unimag-

inatively named the Great Dark Spot (GDS) and the Second Dark Spot (DS2).

It was noticed that both of these storms oscillated slowly, in both latitude and longitude, with respect to constantly rotating reference frames defined to equal the mean drift rate of the storms (Sromovsky, 1991). Proving to be long-lived features of the planets southern hemisphere, they nevertheless evolved slowly in time. Between January and August of 1989, the GDS increased in latitudinal extent from 8° of the planets surface to 17° latitude, while its centre simultaneously moved northward from 26° S to 17° S. A pattern was noticed in the similar slow changes displayed by DS2. A 36 day period defined the storm's movements against the rotational reference frame, a time during which DS2 oscillated 2.4° in latitude and 47.5° in longitude with respect to its average longitudinal drift. Following the same 36 day period the storm's bright core expanded to reach its greatest width at the northernmost point of its drift, before drifting southward and slowly contracting again. Also evident on the Neptunian disc were several highly variable South Polar Features (SPFs) that displayed the same mean longitudinal drift rate as DS2. Ruling out any connection of the SPFs with the DS2 in the deep interior of the planet left the study with no viable hypothesis to explain the coupling of the two features (Sromovsky et al., 1993).

Two years after *Voyager 2* flew past Neptune, the HST was employed to check in on the dynamic blue planet. The GDS had likely dissipated upon reaching the equator in 1990, providing a great change in the planet's southern hemisphere, but despite this, three bright features tracked in the southern hemisphere and two in the northern hemisphere revealed that the wind speeds at the planet's surface had remained constant in the years since their first measurement (Sromovsky et al., 1995). In 1999, several discrete features as well as bright southern bands were studied by Max et al. (2003), with the brightest clouds determined to have tops just below the tropopause. Later, in 2000 and 2002, no less than 18 bright discrete features were counted on Neptune. Divided into three categories, some were classified as derived from subsidence

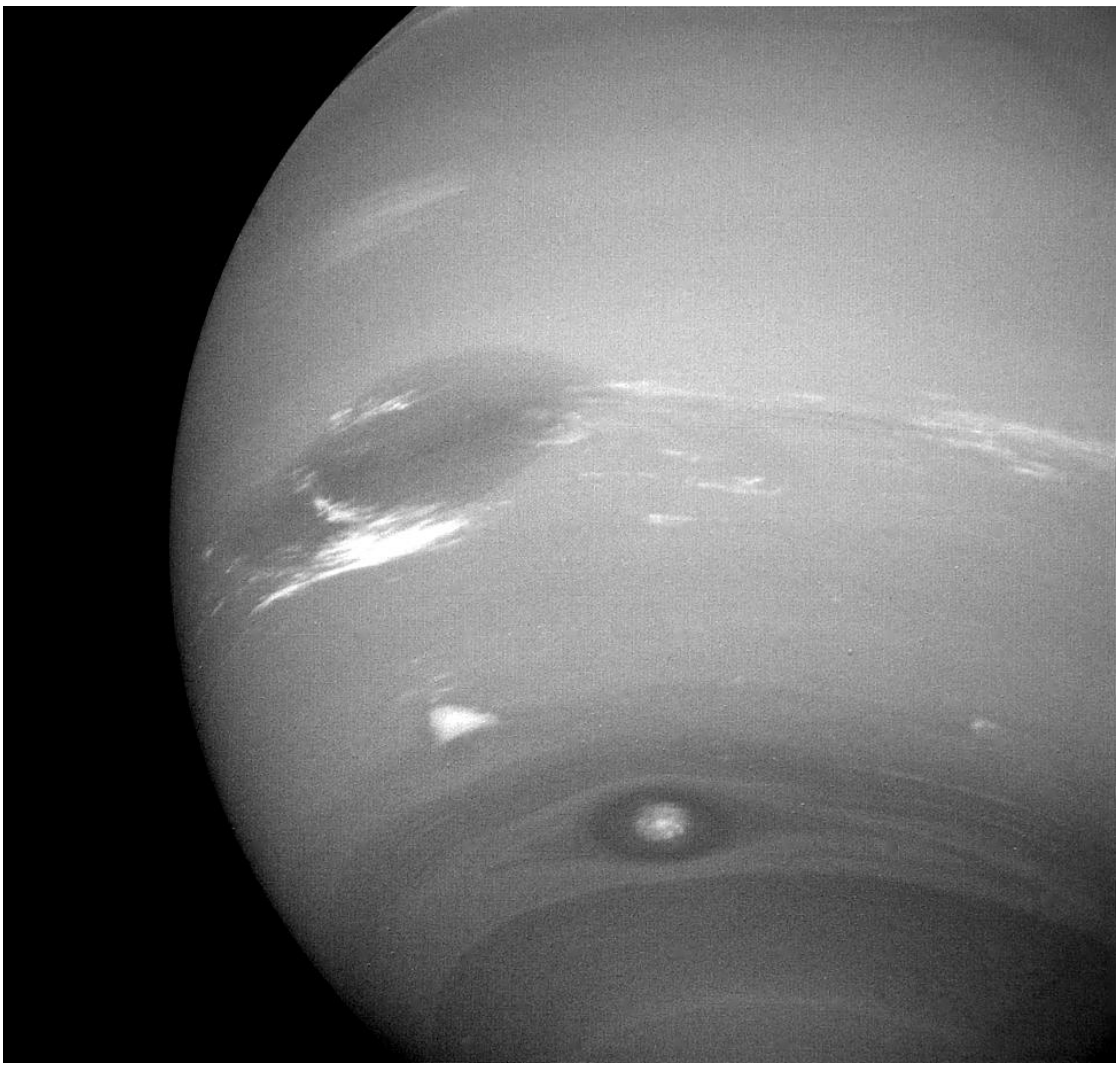

Figure 1.7: *Voyager 2* image showing several visible features of Neptune, providing evidence of the active transport features of the planet. In addition to the many bright, discrete clouds that are visible, the Great Dark Spot (large, dark spot at centre left of planet) and Second Dark Spot (smaller dark spot at bottom middle of planet) can be seen. Image courtesy of NASA / JPL-Caltech / USGS.

of stratospheric haze and located between 30° N and 45° S and at stratospheric pressures between 23 and 64 mbar. The other two sets were thought to be derived from upwelling, with some clustered between 30° S and 50° S and 100 – 140 mbar, while the final set resided close to 70° S and lay between 170 and 270 mbar (Gibbard et al., 2003).

In 1996 HST and NASA's Infrared Telescope Facility (IRTF) were used to together to track another 18 features on the planet, again confirming the strong winds first measured by *Voyager 2*. New dark spots were also observed, with the first lying at 15° N and later being named the Northern Great Dark Spot 15 (NGDS15). At 32° N a second large, dark storm was observed which later became known as the Northern Great Dark Spot 32 (NGDS32), seemed to carry some bright cloud features along with it (Sromovsky et al., 2001a). When these storms were revisited two years later by the HST, neither was observed, though a large bright feature believed to have been the NGDS32's companion was seen. In place of the NGDSs, the data revealed an increased number of discrete features in the southern midlatitudes than were seen two years earlier, and also indicated that the disc-averaged albedo of the planet had undergone a modest increase in magnitude. Monitoring of these southern midlatitudinal features revealed that they were rapidly evolving, generally displaying significant changes if not total formation or dissipation on times scales between one and two Neptunian days (16 – 32 hours) (Sromovsky et al., 2001b). Further study of the missing NGDSs between 1991 and 2000 with various ground-based and HST images led to the conclusion that NGDS32 probably existed between October of 1994 through to at least 1996, while the NGDS15 existed by March of 1996 and was visible for at least 16 months. In contrast to the *Voyager*-era GDS and DS2, these NGDSs seemed to have been stable in their latitudinal and longitudinal drifts, not displaying the oscillatory nature of the earlier storms (Sromovsky et al., 2002).

In the first decade of this century, Neptune continued to be a constantly changing

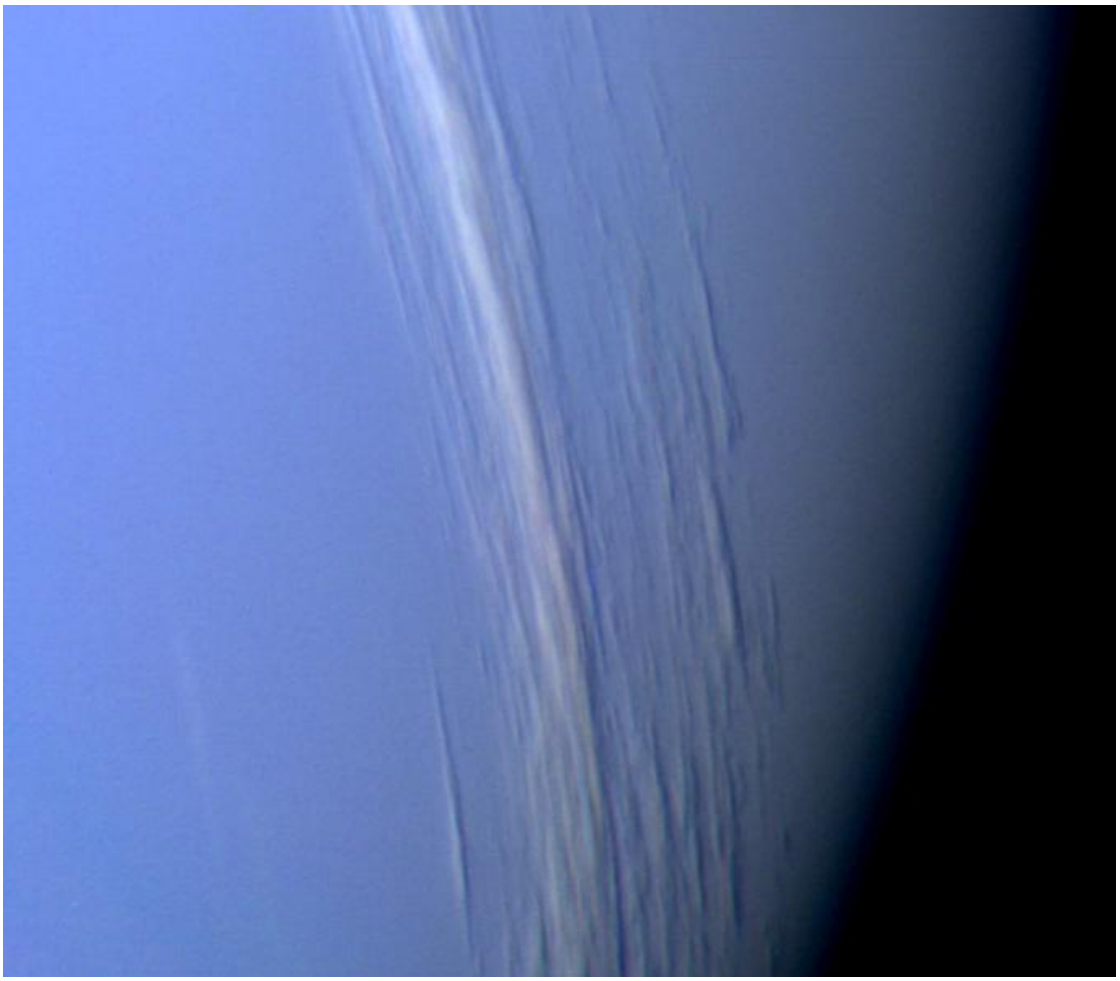

Figure 1.8: *Voyager 2* image showing complex vertical structure of Neptunian clouds. Image courtesy of NASA / JPL-Caltech / USGS.

object of study. Between 1996 and 2002 the net result of increases in brightness in the bright midlatitudinal bands of the planet led to a 40% increase in brightness in the 850 – 1000 nm band while more modest brightness increases of less then 10% were simultaneously observed at 467 and 673 nm (Sromovsky et al., 2003). Despite these relatively simple overall changes, many regions of the planet were displaying their own unique behaviours (Karkoschka, 2011). Between 1994 and 2008, two unusually dark bands at 70° S and 10° N, which were attributed to either decreased haze opacity of increased methane abundance in the stratosphere, were identified in the red/near-IR spectral range and remained constant in brightness despite the global changes going on. A dark band in the blue band (410 – 630nm) extending from 60° S – 30° S had a brightness which decayed exponentially with a time constant of 5 ± 1 year, a behaviour attributed to a settling of dark aerosols to higher atmospheric pressure levels. Simultaneously, all other latitudes brightened with the same time constant, though to a much lesser degree. One exception to this brightening trend occurred between 1994 and 1996, when a short darkening anomaly between 15° N and 30° N coincided with two short-lived dark spots which appeared in the same region.

2003 infrared and radio data of de Pater et al. (2014) revealed the southern mid-latitudes to be the coolest on the planet (mid-IR), while northern midlatitudes were the warmest. The south pole was quite bright in the IR, a characteristic attributed through use of the radio data to subsidence in the area leading to compression and adiabatic heating. The SPFs, still visible, were described as convective storms (de Pater et al., 2014). Ground-based data in 2003 and 2004 showed many discrete clouds which evolved over the course of hours, days, and weeks, though a few seemed to persist for a decade or more. In addition to these features, an asymmetry was observed in north-south circulation patterns (Sromovsky and Fry, 2005). Hammel and Lockwood (2007) confimed that the south pole was still the brightest region of the planet in the mid-IR. Looking again to the south pole in 2007, Luszcz-Cook et al.

(2010) observed a cloud split into 2 segments and rejoin again two days later, citing strong convection as the cause of such drastic and rapid evolution. These south polar clouds were modelled with a single cloud layer at $p > 0.4$ bar. Several bright, discrete clouds at the south pole were observed in 2009 by Irwin et al. (2011b), and were used to infer a rotation rate for the cloud belt at southern polar latitudes.

On the dynamically active Neptune the discrete clouds and large storm features described above are not the only participatants in the planet's active meteorology. Evidence suggests that long-lived stratospheric and tropospheric hazes are among the myriad properties that display large-scale, spatial variability. Few specific examples of this have been noted, however. One example comes from work by Bézard and Romani (1991), who note spatial variability in the emission of C_2H_2 in their 1989 *Voyager 2* data . The lowest emission is around 50 – 60° S, with the peaks in the emission at the equator and 80° S. The interpreted cause for this result is deep acetylene circulation in which cool acetylene convects upward at midlatitudes, eventually to return to the deep atmosphere at the equator and southern pole.

An final interesting point regarding temporal variation on Neptune is the possibility, described in Irwin (2009), that Neptunian haze formation might occur in an episodic manner. Ions or solid particles are necessary to act as nuclei in order for haze particles to condense. Evidence indicates that these particles are most likely derived from the ionisation of upper atmosphere molecules by cosmic rays, or alternatively, by meteors which descend into the Neptunian atmosphere. Given either formation hypothesis, the particles are relatively limited in the upper stratosphere. It is proposed that this lack of condensation nuclei might drive periods of hydrocarbon supersaturation followed by rapid haze formation.

1.3 Uranus

As already mentioned, the *Voyager 2* flyby of Uranus in 1986 led to analysis which described Uranus as a relatively uninteresting planet from a dynamical point of view. Analysis of ground-based telescope data in the years that followed initially supported this view until discrete clouds were first seen in the 1990s, growing in number as Uranus approached its 2007 equinox (see figure 1.6). At this time, a flood of observations occurred, with analysis giving particular focus to the changes in the atmosphere that had been driven by the seasonally-variable solar forcing in the upper atmosphere. Despite this, there remain a number of issues for which agreement upon well-constrained answers has not been reached.

The spectrum of reflected red and near-infrared sunlight in Uranus' upper atmosphere is produced by methane absorption and a series of cloud and haze layers. Numerous studies have examined Uranus data in different portions of the visible and near-infrared spectrum, including Baines and Bergstralh (1986) (0.35 – 1.05 μm), Pollack et al. (1987) (0.43 – 0.60 μm), Rages et al. (1991) (0.35 – 0.62 μm), Karkoschka and Tomasko (2009) and Sromovsky et al. (2011) (0.3 – 1.0 μm), and Irwin et al. (2007, 2009, 2010, 2011a, 2012a) (1.17 – 1.65 μm UKIRT/UIST and 1.48 – 1.80 μm Gemini-North). It is widely accepted that the deepest of these detectable clouds is an optically thick cloud, most likely composed of condensed ammonia (NH_3) or hydrogen sulphide (H_2S), though Very Large Array (VLA) radio data suggests a low equatorial NH_3 abundance which would shift the likely composition of this cloud strongly towards H_2S (Orton et al., 2007a). Many characteristics of this cloud are actively disputed, including its vertical extent and its depth, which is strongly dependent on the assumed mixing ratio of its constituents, with estimates ranging anywhere from 1.5 bar to 9.0 bar, with deeper clouds generally associated with lower mixing ratios (Irwin et al. (2007, 2009, 2010, 2011a, 2012a); Sromovsky and Fry (2007)). Some studies have assumed particles in this thick cloud that are consistent with the molecular

species predicted by models (Baines and Bergstralh, 1986; Rages et al., 1991), while others have attempted to constrain the particle properties given model fits to observed spectra (Irwin et al., 2007, 2009, 2010, 2011a, 2012a; Karkoschka and Tomasko, 2009; Sromovsky et al., 2011).

Some studies also reported a vertically thin methane condensation cloud in the upper troposphere. In this methane cloud, Rages et al. (1991) proposed particles of 1.0-μm radii at 1.2 – 1.3 bar and Sromovsky et al. (2011) suggested 1.2-μm radii at $\sim$ 1.25 bar. Other studies found the best agreement to observations without specifically modelling a methane condensation cloud as distinct from the deeper, thicker cloud already discussed (Irwin et al., 2007, 2009, 2010, 2011a, 2012a). Finally, above these clouds, some models include an optically thin haze. In this haze, Pollack et al. (1987), using photochemical models, preferred particle radii of 0.13 ± 0.02 μm, while Sromovsky et al. (2011) found best agreement with data when using 0.1-μm particles. In the latter model, the haze was broken down into a slightly thinner haze from just above 1.0 bar to 0.1 bar, and a second, slightly thicker haze above the tropopause. Irwin et al. (2007, 2009, 2010, 2011a, 2012a) found their best model fits while employing a single particle type of $\sim$ 1.0-μm radii to model both the tropospheric clouds and upper hazes, but their data were largely in narrow wavelength ranges longward of 1.0 μm, making detection of smaller particles in either cloud layer difficult.

It should be noted that while general agreement has been reached for cloud opacities and pressures, the same cannot be said with respect to proposed scattering properties for the particles in each cloud. Also worth noting is that the accuracy of the scattering properties in all these studies is limited by the relatively narrow spectral windows (or in the case of the *Voyager 2* data, the inability of seeing narrow spectral features in the broadband reflectance images). Some of the studies look at the spectrum exclusively shortward of 1.0 μm (Baines and Bergstralh, 1986; Karkoschka and Tomasko, 2009; Pollack et al., 1987; Rages et al., 1991; Sromovsky et al., 2011), while

others analyse data that lies exclusively longward of this mark (Irwin et al., 2007, 2009, 2010, 2011a, 2012a).

A final shortcoming in most *Voyager*-era studies is that atmospheric methane profiles on Uranus were assumed to be invariant with latitude. At the time ground-based observations were generally poorly resolved spatially, often averaging over the visible disc of Uranus. Additionally, ground-based observations could only see the planet from the south pole to about 60° S, since it was in the middle of a southern summer. The assumption that methane was latitudinally invariant was thus necessary given the limited data, poor spatial resolution of most observations, and lack of ground-based coverage of Uranus' equator and northern hemisphere. Moreover, the spectral dominance of methane in the near-infrared makes it inherently difficult to distinguish between spectral features derived from methane and those derived from cloud opacities. Latitudinally constant values for methane were therefore assumed, despite the known likelihood of their inaccuracy. In general, studies cite latitudinally-constant deep methane abundances which vary widely between about 1.6 and 4.6% (Baines and Bergstralh, 1986; Irwin et al., 2010, 2011a, 2012a; Sromovsky et al., 2011).

Karkoschka and Tomasko (2009) first highlighted the necessity of latitudinally variable profiles for accurate modelling of the Uranian atmosphere while analysing 2002 HST observations. They used a reflectivity analysis at $\sim$ 825 nm to address this problem, citing methane mixing ratios of 1.4 and 3.2% for high and low southern latitudes respectively, as evidence of at least a 50% enrichment at the equator. Irwin et al. (2010, 2011a, 2012a) examined the issue further, and initially found that spectra in the H-Band were equally well constructed using a methane enrichment at the equator or a reduction of tropospheric cloud-top pressure in the midlatitudes. This significant lack of agreement upon methane profiles is compounded further by limitations intrinsic in the data of each of the above studies. Karkoschka and Tomasko (2009) and Sromovsky et al. (2011) were forced, given Uranus' season during their ob-

servations, to view the planet from just 75° S to 30° N, limiting their ability to study methane in the northern hemisphere. Irwin et al. (2010, 2011a, 2012a) were limited primarily by the lack of data shortward of 1.0 μm. This gave rise to their initial conclusion that given the spectral range of their Gemini data, no preference could be given to either of their two proposed solutions. This disagreement has been resolved somewhat after the reanalysis of the telescope observations with improved methane line absorption data, and the subsequent publishing of Irwin et al. (2012b)

1.4 Neptune

The upper atmosphere of Neptune, like Uranus, is characterised by one or more optically thick cloud layers that form the effective bottom of the observable atmosphere, above which lie a number of haze layers extending high into the stratosphere. Also like Uranus, the visible-red and near-infrared spectrum of the planet is produced by sunlight entering the atmosphere, interacting with the absorptive methane and scattering clouds and hazes, and finally returning to the spectrometers. Slightly more discerning geographic choices must be made for analysis of Neptunian spectra, however, because the cloud and hazes are generally much more optically thick, and evolve much more quickly than on Uranus, meaning that very different atmospheric columns are often found in close geographic proximity to one another.

Starting at the bottom, the relatively stable, optically thick cloud is generally thought to be hydrogen sulphide (H_2S). Though this bottom cloud is thought to cover the entire planet and form a more or less unvarying and long-lived 'background' upon which the active tropospheric convective and subsidence meteorology occurs, there is also evidence to suggest that even these deep clouds evolve seasonally and over distance scales ranging from 10s to 1000s of kilometres (Baines et al., 1995a; Irwin et al., 2011b; Sromovsky and Fry, 2007). This rapid and extreme variability makes

comparing one study to another quite difficult, but a summary of the characteristics the clouds most often display will be attempted.

When modelled, particles of the visible H_2S cloud in the troposphere are generally found to lie well above the 7 – 8 bar levels predicted by the ECCM, presumably uplifted by active vertical circulation in the troposphere. *Voyager 2* data placed the H_2S cloud at approximately 3.8 bars (Baines et al., 1995a,b; Sromovsky et al., 2001a), while more recent studies seem to favour a pressure level of 2 – 3 bars (Irwin et al., 2010, 2011b, 2013). In the former case, cited haze opacities were $\tau_{0.62\,\mu m} = 0.85$ and $\tau_{0.89\,\mu m} = 0.58$, and in the latter $\tau_{1.6\,\mu m} \simeq 1.1$ for the bright belt at 30° S and $\tau_{1.6\,\mu m} \simeq 0.7$ for the dark region near the equator. Karkoschka (2011); Karkoschka and Tomasko (2011) successfully employed two distinct haze models for these presumed H_2S clouds in the southern midlatitudes, though in neither case was a specific molecular species suggested. In the first, an optically thick, bright haze extending from 1.4 – 3 bar and an optically thick, dark haze below 3 bar were used. In the second, they employed an optically thin haze with a cloud-top at 1.4 bar which extended to levels below 10 bar. In both cases, haze opacities varied with latitude, but fell in the range $0.10/\text{bar} \lesssim \tau \lesssim 0.16/\text{bar}$. Given that these hazes were significantly more vertically extended than the more compact cloud layers of the earlier models discussed, it is not surprising that the peak opacity was much lower.

While all recent studies (Irwin et al., 2010, 2011b, 2013; Karkoschka, 2001; Karkoschka and Tomasko, 2011) use 1.0-μm-radius particles for the proposed H_2S cloud, there are a range of values for scattering properties of the particles. *Voyager 2* analysis suggest that the cloud had high single-scattering albedos[7] of $\bar{\omega}_{0.63\,\mu m} =$

[7]The 'single-scattering albedo', a dimensionless quantity represented in this thesis with $\bar{\omega}_0$, and having a possible range of 0 – 1, is a wavelength-dependent representation of the efficiency of an aerosol particle in scattering light. With $\bar{\omega}_0 = 1$, the particle is a perfect scatterer, meaning that all light incident on the particle is scattered (in some direction). With $\bar{\omega}_0 = 0.5$, half of the light incident on the particle is scattered, and the other half of it is absorbed, either by the particle itself or the gas between the particles, and so on.

0.915 ± 0.006, $\bar{\omega}_{0.75\ \mu m} = 0.775 \pm 0.012$, and $\bar{\omega}_{0.83\ \mu m} = 0.803 \pm 0.010$ (Baines and Hammel, 1994). At longer wavelengths of the near-infrared, Irwin et al. (2010, 2011b, 2013) modelled the phase function of the cloud particles with a fairly strongly forward-scattering, single Henyey-Greenstein function[8] with asymmetry parameter $g = 0.7$. Given this assumption, the study found best agreement with observations for wavelength-dependent albedos varying between 0.6 and 0.8 at 1.5 – 1.62 μm and even higher albedos for wavelengths below 1.2 μm. In contrast to Irwin's scattering approximation, *Voyager 2* analysis was not able to constrain forward-scattering, but did find that shallow back-scattering was necessary at 0.75 μm, assigning a Henyey-Greenstein back-scattering asymmetry parameter of $-0.22 \leq g_2 \leq -0.07$. When moving focus to the equatorial region, where the H_2S cloud appears much darker, a similar wavelength region was assigned much lower single-scattering albedos. Testing cases both including and omitting a methane cloud at 1.3 bar, Sromovsky et al. (2001a) cited upper limits of $\bar{\omega}_{1.27\ \mu m} \lesssim 0.2$ and $\bar{\omega}_{1.6\ \mu m} \lesssim 0.1$ for the H_2S cloud.

Only early *Voyager 2* data analysis suggests a separate, tropospheric methane condensation cloud, so it is possible that this ECCM-predicted cloud is prevented from forming due to energetic vertical mixing of the atmosphere, or that if it does exist, its thickness, both optically and vertically, are sufficiently small to have only an insignificant impact on observational data. There is also evidence that this cloud, which would lie in the upper troposphere, varies as dramatically as stratospheric hazes, evolving over timescales as fast as minutes (Baines et al., 1995a). When this cloud was evident, it was reported to be vertically thin and lie in the 0.9 – 1.5 bar pressure range (Baines et al., 1995a; Burgdorf et al., 2003; Pryor et al., 1992). Pryor et al. (1992) reported the methane condensation layer to have optical depth $\tau_{0.75\ \mu m} = 1.0$, and the constituent particles to be characterised by a double Henyey-Greenstein phase

[8] See chapter 3 for a more complete mathematical description of Henyey-Greenstein phase function approximations. Here, it is sufficient for the reader to know that asymmetry parameters (g) vary from -1 (strongly back-scattering) to 1 (strongly forward-scattering).

function approximation with $f = 0.42$, $g_1 = 0.9$, and $g_2 = -0.11$ (strongly forward-scattering, weakly back-scattering) and a single-scattering albedo of $\bar{\omega}_{0.75\,\mu m} = 0.838$. Baines et al. (1995a) reported its opacity to be $\tau_{0.6\,\mu m} = 0.085$, and adopted the Pryor et al. (1992) values for Henyey-Greenstein parameters and albedo. Burgdorf et al. (2003) reported improved model fits when adding a cloud with Mie-satisfying, methane ice particles of 1.5 – 4.0 μm radii, and extending from the condensation level to > 5% of an atmospheric scale height.

Several studies omit the methane condensation layer, and simply account for tropospheric methane absorption by setting the tropospheric mixing ratio. As with Uranus, however, the observed spectrum can often be reproduced with either changes in the methane abundance or changes to the cloud-top pressure, and so consequently there is no consensus as to what the tropospheric methane mixing ratio should be. Values as low as $VMR_{CH_4} \simeq 0.02$ and as high as $VMR_{CH_4} \simeq 0.04$ are easy to find in the literature (Baines et al., 1995b; Irwin et al., 2010, 2011b; Lindal, 1992), though the two most recent publications, from separate research groups, have favoured the higher of the two values (Irwin et al., 2013; Karkoschka and Tomasko, 2011).

While tropospheric methane may indeed be well-mixed, there is increasing evidence that stratospheric methane is not well mixed, but rather highly variable in both altitude and latitude (Irwin et al., 2011b, 2013), possibly by factors as large as 4 (Karkoschka, 2011). It should be noted that it has also been suggested that even latitudinal methane variability may extend downwards into the upper troposphere, with abundance differences of up to a factor of 3 possible as deep as 1.8 bar (Karkoschka and Tomasko, 2011). A thorough review of the literature on methane does seem to confirm the hypothesis of high stratospheric methane variability, with published values covering more than two orders of magnitude in different altitudes and years. Orton et al. (1987b) found abundances < 0.02 , while Lellouch et al. (2010) suggested

$VMR_{CH_4} = (1.5 \pm 0.2) \times 10^{-3}$ for the mid-stratosphere, with levels decreasing with decreasing altitude. In a series of studies, Irwin et al. (2010, 2011b, 2013) tested a range of abundances between $4.7 \times 10^{-5} \leq VMR_{CH_4} \leq 1.5 \times 10^{-3}$, which when combined with varying stratospheric cloud pressures, all yielded good fits to the H-band[9] spectra. Baines and Hammel (1994) published a value of 3.5×10^{-4}, while Fletcher et al. (2010) determined VMRs of $(9 \pm 3) \times 10^{-4}$ at 50 mbar and $(9 \pm 3) \times 10^{-5}$ at 1 μbar.

When looking finally at other stratospheric hazes on Neptune, there are a variety of examples. Particle radii range in size by an entire order of magnitude from 0.1 – 1.0 μm. The reality for Neptunian stratospheric hazes is probably that a large range of particle sizes exist, with smaller particles influencing shorter wavelength spectra and larger particles contributing more to longer wavelength spectra. This hypothesis seems reasonable given that Baines and Hammel (1994); Gibbard et al. (2002); Karkoschka and Tomasko (2011); Pryor et al. (1992), which used observations with wavelengths $\lambda \leq 1$ μm, used stratospheric aerosols of $r \leq 0.2$ μm, while Irwin et al. (2010, 2011b, 2013) observing at $\lambda \geq 1.0$ μm, used $r = 1.0$ μm. The existence of these latter, larger haze particles year after year is yet another testament to the active convective nature of the Neptunian upper atmosphere, because particles of this size would quickly fall out of the stratosphere, and would need constant replenishing from below to be seen consistently over the time span these studies represent.

Various hazes were described at most levels of the stratosphere, starting at the tropopause and extending all the way up to levels in the 10s of μbars. Optical depths for these aerosol layers ranged from 0.04 – 1.1, which is probably a real feature of the hazes given different wavelengths associated with the published opacities, as well as the known variability of haze layers at different locations on the planet (Baines and Hammel, 1994; Irwin et al., 2010, 2011b, 2013; Karkoschka, 2011; Karkoschka and Tomasko, 2011; Pryor et al., 1992). In general, the haze opacities seemed to be greater

[9]The H-band is the methane window located between approximately 1.4 and 1.8 μm. See table 2.1 for all methane window names in the near-infrared.

at shorter wavelengths. Some studies quoted refractive indices, but again with a wide variety depending on the wavelength of the data and the region of the stratosphere being observed. Real parts were all in the 1.3 – 1.5 range, while imaginary parts[10] of the refractive indices ranged from 1×10^{-4} – 1×10^{-1} (Baines and Hammel, 1994; Karkoschka, 2011; Karkoschka and Tomasko, 2011; Pryor et al., 1992). Irwin et al. (2010, 2011b, 2013) represented scattering instead with a single-scattering albedo that ranged from 0.4 in dim regions to 1.0 in bright regions.

The areas of general agreement within the Neptunian atmospheric research, as well as the shortcomings of this research, mirror those concerning Uranian research to date. On Neptune, it is widely agreed that the atmosphere contains a deep, relatively stable H_2S cloud at the bottom of the observable atmosphere, above which a series of rapidly-evolving and latitudinally-dependent aerosol layers exist. However, is there a discrete, well-defined methane condensation layer, or is this ECCM-predicted layer dispersed due to Neptune's active vertical transport mechanisms? For that matter, is the ECCM-predicted H_2S layer a well-defined layer, as was modelled in Baines and Hammel (1994); Burgdorf et al. (2003); Irwin et al. (2010, 2011b, 2013); Pryor et al. (1992), or is it dispersed into a extended haze as modelled in Karkoschka (2011); Karkoschka and Tomasko (2011)?

When looking at properties of the Neptunian aerosols more closely, there is a great deal of work that still needs to be done. Because, just as with Uranus, all the previous studies have been limited to data exclusively shortward of 1.0 μm (Baines and Hammel, 1994; Karkoschka, 2011; Karkoschka and Tomasko, 2011; Lindal, 1992; Pryor et al., 1992), or exclusively to data longward of 1.0 μm (Burgdorf et al., 2003; Gibbard et al., 2002; Irwin et al., 2010, 2011b, 2013; Lellouch et al., 1994; Max et al., 2003; Orton et al., 1987b,a). Additionally, *Voyager 2* images are inherently limiting

[10]The index of refraction, $\tilde{n} = n + i\kappa$, is an important descriptor of light's interaction with aerosol particles. The imaginary part, κ, represents the amount of absorption of light in the aerosol. If an aerosol is a perfect scatterer and absorbs no light, $\kappa = 0.0$. The less familiar imaginary part, like the real part, is wavelength-dependent, temperature-dependent, and dimensionless.

due to their broadband nature (Lindal, 1992), the distribution of particle sizes has been difficult to determine. Small particles, in general, satisfy the short wavelength studies, while larger ones satisfy the long wavelength studies. Analysis of a dataset with wide spectral range, with the aim of determining a more complete picture of relative abundances of varying particle sizes would be helpful.

Again as was found with Uranus, only recently did studies begin to consider the possibilities of varying methane profiles with latitude (Irwin et al., 2010, 2011b, 2013; Karkoschka, 2011; Karkoschka and Tomasko, 2011). In these studies, it was clearly demonstrated that methane profiles are very likely to vary across the planet's latitudinal extent, and that observations could be reproduced with models of widely varying methane profiles by adjusting the stratospheric haze profiles. But none of these studies was able to offer a definitive preference for what the methane profiles were at any given latitudinal region of the planet.

Finally, with a planet that evolves as quickly and as continually as Neptune seems to do, it is important to revisit the planet from time to time if for no other reason than to see what new discrete features have appeared, and to see if any evolution has occurred in the more stable layers that exist (like the putative H_2S cloud, for example). In the past 10 years, high-spatial-resolution studies capable of resolving and studying latitudinal bands and discrete clouds on the planet have been performed in 2007 (Irwin et al., 2010), 2009 (Irwin et al., 2011b, 2013), 2010 (Irwin et al., 2013), as well as a study of temporal variations between 1994 and 2010 (Karkoschka, 2011). Clearly, it is high time that Neptune was observed again to see what secrets the last several years hold.

1.5 Thesis Topics and Format

In this thesis, ice giant observations from two new datasets are analysed. Both planets were observed in 2009 with the NASA Infrared Telescope Facility's near-infrared spectrometer, SpeX, which provided latitudinally-resolved spectra from 0.8 to 1.8 μm. Neptune was observed again in 2012 with the SWIFT spectrograph, covering a range of 0.6 to 1.0 μm, at the Palomar Observatory's Hale Telescope.

The SpeX observations of Uranus will be used to address many of the unresolved and disputed properties of the Uranian upper atmosphere. Recall that the numerous studies of optical properties in the scattering clouds and hazes mentioned in section 1.3 were all limited to narrow spectral ranges either above or below 1.0 μm. The wide spectral range of SpeX will allow us to formulate a set of optical properties of these clouds that cover a much wider spectral range than has been previously made. The coverage shortward of 1.0 μm is particularly well-suited to examining small particle sizes in these hazes and clouds.

The Uranus data is also very well suited to providing further, valuable information about the proposed latitudinal variability of methane abundance. The data was recorded in 2009, just two years after the Uranian equinox, providing wider latitudinal coverage, particularly of the northern hemisphere, than the Karkoschka and Tomasko (2009) and Sromovsky et al. (2011) studies. Because the data extends to the 825 nm spectral region, the only region shortward of 2.0 μm where methane is not the dominant absorber, they will be able to complement the Irwin et al. (2009, 2011a, 2012a,b) studies and provide a preference for one of their two assumptions of the methane abundance. Finally, the 2009 data provides an additional datapoint in the temporal evolution of the Uranian equinox so that possible temporal changes in the methane variability issue can also be explored.

As for Neptune, poor-quality SpeX data does exist which might be useful in determining background models for clouds and hazes in the dark, equatorial band of the

planet, as well as in the bright band in the southern midlatitudes. While the quality of the spatial resolution is quite low due to bad seeing conditions on the night of the sole Neptune observation (see chapter 2 for further details), SpeX does nevertheless offer the wide spectral range to simultaneously fit data above and below 1.0 µm. For this reason, taking a look at this data is worthwhile for the chance to retrieve physical and optical properties of the clouds and hazes that cover a wider range than previous studies.

The Neptune SWIFT data, while covering a spectral region only shortward of 1.0 µm, still holds a great deal of potential. The spectral extent of the spectrometer includes five methane absorption bands and five methane windows, allowing us to probe optical and physical aerosol properties in the upper tropopause as well as throughout the stratosphere. Unlike SpeX, this data has a high spatial resolution and has imaged the entire planet repeatedly over the four nights of observations. This allows discrete cloud features on the planet to be resolved and studied, and can observe regions of interest in a wide range of zenith angles. In addition, it will allow, like the SpeX data, a rare opportunity to utilise the 825 nm region and make an attempt to see if the question of methane profiles versus haze opacity can be answered.

Before exploring the questions just outlined, further background information is required concerning the data and the analysis techniques employed. Chapter 2 provides a thorough presentation of the data analysed in this thesis and the reduction required to transform the raw data into a useable format. Chapter 3: Retrieval Theory and NEMESIS then provides an overview of the various techniques used to study this data. Results of this study are presented next, with the information being divided into a chapter for Uranus, 4, and a chapter for Neptune, 5. This thesis closes with chapter 6: Conclusions and Future Work, which summarises the major results of this thesis and outlines future work that could be pursued.

Chapter 2

Telescopes, Spectrometers, and Data Reduction

Where there is an observatory and a telescope, we expect that any eyes will see new worlds at once.

— Henry David Thoreau,
A Week on the Concord and Merrimack Rivers

Before embarking upon the analysis of data, the telescope observations needed to be collected and reduced into a useable form. This chapter first describes the various telescopes and spectrometers that were used to collect the raw data (section 2.1), catalogues those data (section 2.2), and details the relevant processes used to reduce them (section 2.3). Each of those sections is further subdivided into a section for each telescope.

2.1 Telescopes and Spectrometers

This section introduces the three telescopes used, either directly for analysis, or just for relative calibration purposes. A brief description of the facilities' capabilities and

characteristics are provided, as well as a presentation of the observational dates and techniques employed. Sections 2.1.1: Infrared Telescope Facility and 2.1.3: Palomar Observatory describe the two telescopes from which data for this thesis was recorded. The short section Gemini-North (2.1.2) describes relevant details of that telescope, where data was acquired that was used for relative calibrations of the new data from the IRTF and Palomar Observatory.[1]

2.1.1 Infrared Telescope Facility

The first set of observations for this study were acquired on the 18th, 25th and 28th of August, 2009 using NASA's InfraRed Telescope Facility. Both ice giants were imaged with SpeX, a medium resolution spectrograph with a spectral range of 0.8 μm – 5.4 μm that was purpose-built by the Institute for Astronomy, U.S.A. (Rayner et al., 2003). The spectrometer was operated in the short-wavelength, cross-dispersed mode (SXD), which covers the spectral range of 0.8 μm – 2.4 μm. The 0.5 × 15.0 arcsecond slit was oriented along the central meridian of the planets' discs (see figure 2.1). The raw data were split by wavelength into six "orders" and imaged onto a 1024 × 1024 pixel array as shown in figure 2.2 (upper). Given the array size, slit length, and observational technique, each pixel in the array represents scattered sunlight from a rectangular box along the central meridian of the planet with an 'x' extent of 0.5" and a 'y' extent of 0.15". The effective viewing ranges and spectral resolutions of each of the six orders (which are numbered 3 through 8) are summarised in table 2.1.

Table 2.2 lists all recorded observations for this study, as well as indicating the time, duration, and airmass[2]. Observed spatial resolution at 1.6 μm (see 2.2.1 for

[1] Because Gemini-North observations were not directly analysed in the course of this thesis, section 2.1.2 contains only a brief summary of relevant information. Further details on the Gemini-North observations, if required, can be found in Irwin et al. (2011b,a, 2012b,a, 2013)

[2] Airmass, as defined for ground-based, astronomical observations, is the path length through the Earth's atmosphere through which the viewing object's light must pass to reach the telescope. It is important to note the airmass of an observation, because the higher the airmass, the more atmospheric

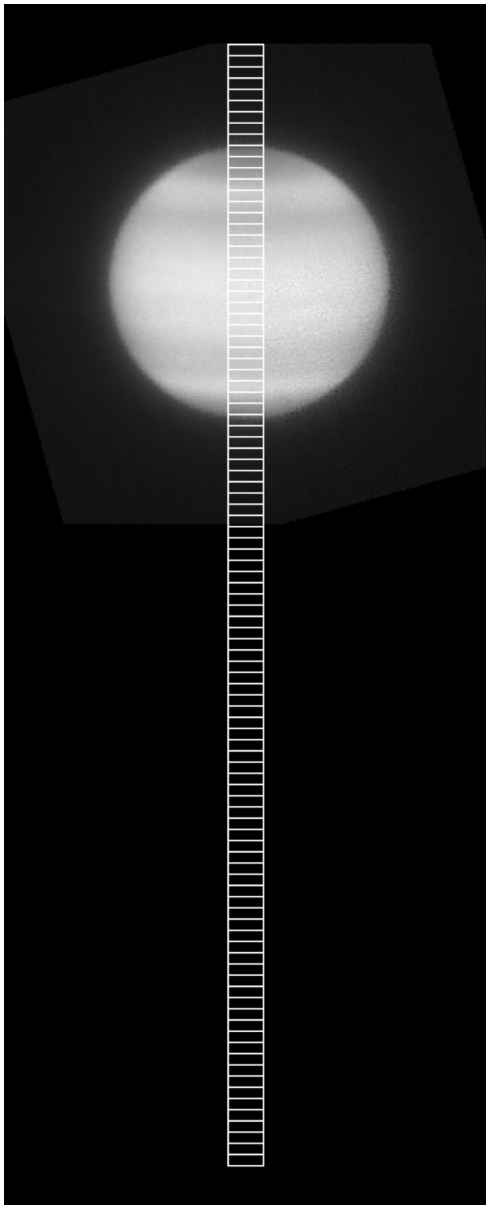

Figure 2.1: Diagram of the SpeX slit position across Uranus' disc (same positioning was used for Neptune). Each small white box represents the portion of the 0.5 × 15.0 arcsecond slit that is mapped onto a single 0.5 × 0.15 arcsecond pixel of the raw data array. The diagram shows relative size of Uranus' disc to the total, 100-pixel slit length. The Uranus image in the diagram is from September 2009, observed with Gemini-N/NIRI.

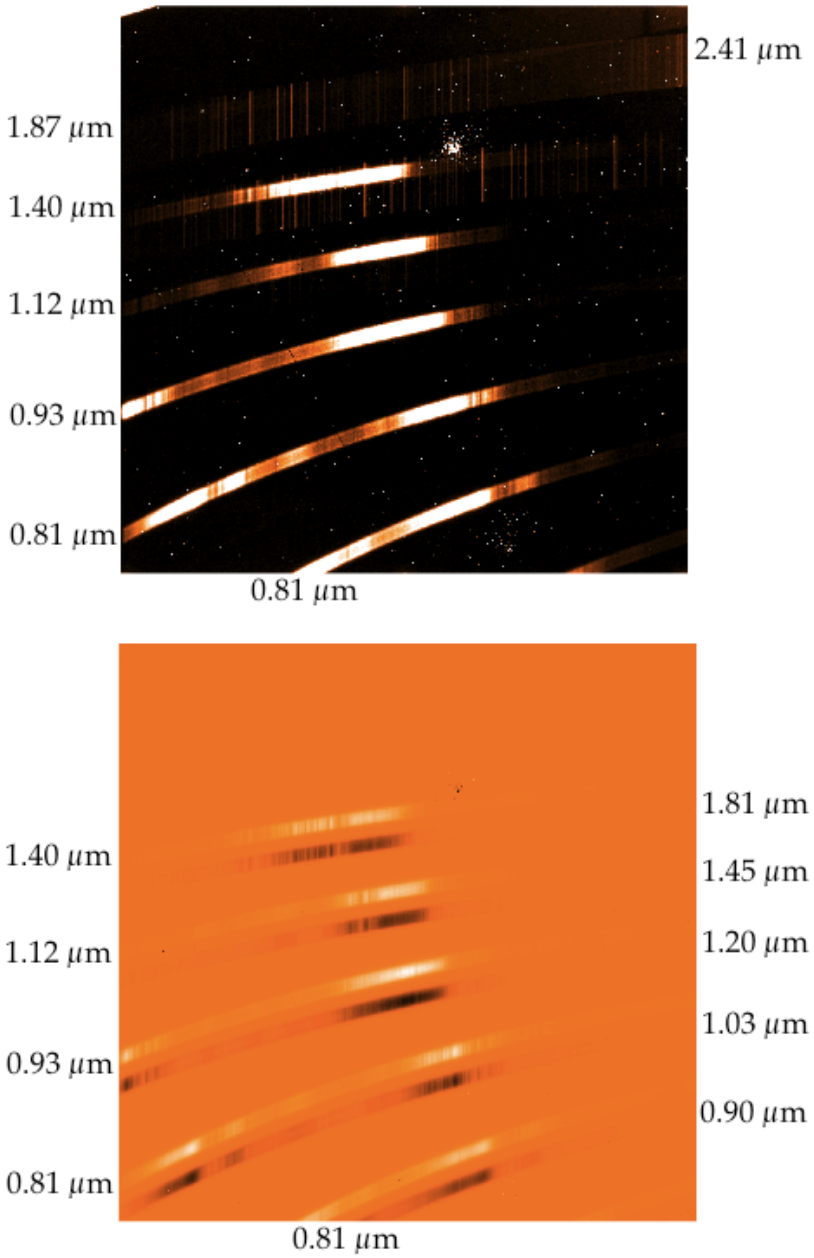

Figure 2.2: A sample of six wavelength 'orders' of raw SpeX data as imaged onto the 1024 × 1024 pixel array (upper) and a sample of a partially reduced 'AB' pair of raw SpeX data (lower).

Table 2.1: Wavelength specifications , window names, and spectral resolutions for SpeX SXD mode. Spectral resolutions calculated within each order from $R = \lambda/\Delta\lambda$.

Order	Window Name	Wavelengths (μm)	Spectral Resolution
8	I	0.81 – 0.90	$R \leq 1200$
7	z	0.81 – 1.03	$R \leq 1050$
6	J1	0.94 – 1.20	$R \leq 1050$
5	J2	1.13 – 1.45	$R \leq 1050$
4	H	1.41 – 1.81	$R \leq 1050$
3	K	1.88 – 2.42	$R \leq 1050$

further discussion of spatial resolution as a wavelength-dependent quantity) is also listed for the stellar standard observations given the seeing[3] at the time of the observation. The spatial resolution was calculated for each stellar standard observation by multiplying the spatial pixel width, 0.15", by the full-width-half-maximum number of pixels on the array of the point-source stars.

2.1.2 Gemini-North

In September 2009, observations of both Uranus and Neptune were recorded using the ALTAIR adaptive optics system, allowing spatial resolutions of 0.1", on the Gemini-North 8.1-m telescope at Mauna Kea, Hawaii. While both the Near InfraRed Imaging and Mapping Spectrometer (NIRI) and the Near Infrared Integral Field Spectrometer (NIFS) were employed, all calibration work here came from the latter. The NIFS instrument acquired spectral-mapping images of both Uranus and Neptune

absorption and refraction negatively impacts the quality of the observation (see footnote on "seeing".

[3]Observational "seeing" is the angular resolution achievable by an Earth-based telescope given the movement of the Earth's atmosphere through the telescope viewing path. As air molecules pass in front of the telescope, the index of refraction of the telescope's view of the sky changes. This change causes images to become blurred, generally beyond the angular resolution of the telescope itself. Telescopes are often placed at high altitudes in order to minimise the path length of the light through the atmosphere, though even atop Mauna Kea, at 4,200 metres, the airmass is only reduced by about one third compared to sea level. More importantly, Mauna Kea is situated at nearly 20° N latitude, where the descending Hadley cell creates a stable air column and, in turn, better seeing conditions.

Table 2.2: IRTF SpeX observations including date, time, duration, airmass, and seeing. Spatial resolution is calculated by measuring the full-width-half-maximum, in pixels, of the point-source standard stars, and then multiplying by the 0.15" spatial width of each pixel. See table 2.5 and section 2.2.1 for spatial resolutions of planet observations.

Date	*Target*	*Start Time (UTC)*	*Duration (seconds)*	*Number of 'AB' Pairs*	*Approximate Airmass*	*Spatial Resolution at 1.6 μm (arcseconds)*
18Aug09	HD1160 (A0 Standard)	14:36	30	2	1.6	0.5 ± 0.1
	Uranus	14:50	60	1	1.4	*
	Uranus	14:52	120	6	1.4 – 1.5	*
	SAO146912 (G2 Standard)	15:24	60	2	1.6	0.5 ± 0.1
25Aug09	HD1160 (A0 Standard)	14:53	30	2	1.3	0.5 ± 0.1
	Uranus	15:04	120	7	1.7 – 1.9	*
	SAO146912 (G2 Standard)	15:37	60	1	2.0	1.1 ± 0.1
28Aug09	HD1160 (A0 Standard)	10:50	30	3	1.1	0.6 ± 0.1
	Uranus	11:05	120	9	1.1	*
	SAO146912 (G2 Standard)	11:58	60	1	1.1	0.6 ± 0.1
	Neptune	12:33	120	6	1.7	*
	SAO146912 (G2 Standard)	13:18	60	1	1.2	0.6 ± 0.1
	Uranus	13:53	120	7	1.3 – 1.4	*
	HD1160 (A0 Standard)	15:00	30	2	1.4	0.8 ± 0.1
	Uranus	15:13	120	2	1.9	*
	SAO146912 (G2 Standard)	-	120	2	2.0	1.3 ± 0.1

over a 3" × 3" box. The observations employed an H-grating which sampled wavelengths between 1.476 and 1.803 μm at a spectral resolution of $R = 5290$. As explained in section 2.3, the relative calibrations for both IRTF (2009) and Palomar (2012) observations were dependant on the absolutely calibrated NIFS images, though the precise method of obtaining these calibrations differed slightly.

2.1.3 Palomar Observatory

The most recent observations analysed in this thesis were recorded at the Palomar Observatory in California. Near-infrared spectra of Neptune were acquired over four nights between the 29th of June and the 2nd of July of 2012. The images were recorded using the 5.08 metre Hale Telescope, the latest Palomar Adaptive Optics System, P3K, and the integral field spectrograph, SWIFT. Five-minute exposures simultaneously covered the range of 0.650 – 1.000 μm with a spectral resolution linearly rising from of $R = 3250$ at 0.650 μm to $R = 4400$ at 1.0 μm. Seeing varied with airmass, but was generally better than 0.3".

The SWIFT spectrograph has a 44 × 89 spatial pixel, or 'spaxel', viewing field. For the data analysed here, the spectrometer operated in the medium resolution, 0.080" mode, so that each of these spaxels imaged an 0.080" × 0.080" square of sky. This allowed us to image the entire Neptunian disc simultaneously in the 3.5" × 7.1" viewing field.

SWIFT has 2 image slicers, known as the 'master' and 'slave'. In SWIFT these slicers take the form of a stack of mirrors. The 'master' and 'slave' each take one half (lengthwise) of this rectangular field and slice it into one long slit which is then fed into a traditional long-slit spectrograph (Tecza et al., 2006). The result is broken back into 22 'slitlets', each of which is expanded, when output as raw data, into 0.650 – 1.0 μm spectrum. A diagram of this entire process is shown in figure 2.3. The resulting output can be seen in figure 2.4, which shows an example of a raw, uncali-

brated SWIFT 'master' image of Neptune.

Table 2.3 summarises the observations taken, including their time, date, and airmass. All planet observations were integrated for 5 minutes; the A1V star, HR7950, used for telluric correction was integrated for 2 seconds. A handful of observations were thrown out, and are not included in the table. These included another observation of HR7950 which was very noisy, and a few Neptune observations in which the planet was imaged too close to the edge of the detector, causing portions of the planet to be cut off from view.

2.2 Observation Quality

This section discusses the relative strengths and weaknesses of the data recorded and studied for this thesis, as well as explaining which portions of the data were chosen for analysis, and why. Information is included for the IRTF data (section 2.2.1: SpeX) as well as the data from the Palomar Observatory (section 2.2.2: SWIFT).

2.2.1 SpeX

There exists in the SpeX data a significant spread of airmasses during the three nights' observations, as was apparent from table 2.4. There is a rough correspondence between airmass and spatial resolution, and hence a rough correspondence between airmass and a particular observation's scientific value. In the case of Neptune, there are only six observation pairs from which to choose. In the case of Uranus, however, there exists a wider selection of observations. The most useful frames to analyse will be those characterised by relatively low airmasses and thus the best angular resolution. Unfortunately, determining an accurate value for angular resolution for a planetary observation is more difficult than for standard stars due to the extended nature of the source. This is because the source is more than one pixel wide, and the edge of

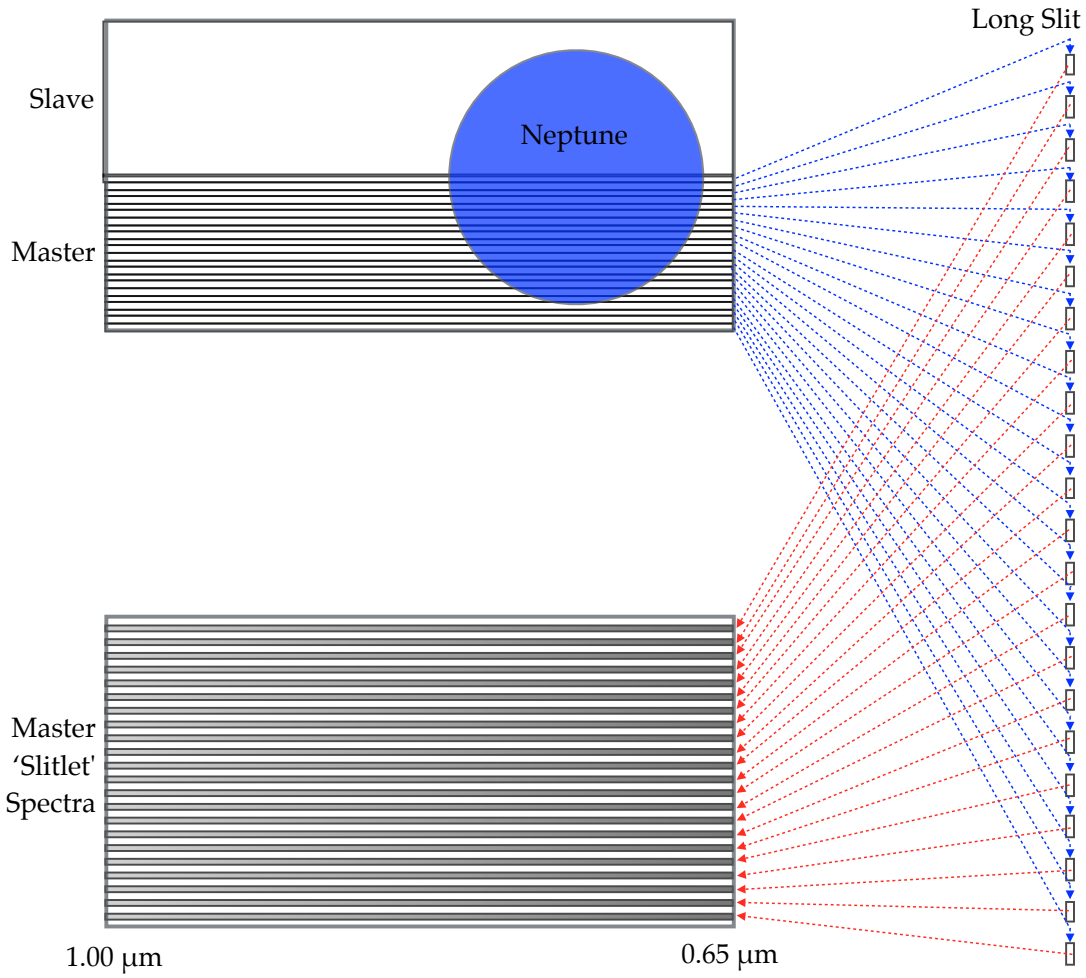

Figure 2.3: The top image in this diagram shows the position and approximate size of Neptune in the SWIFT image window. As can be seen, the image window is divided into two portions, named the 'master' and the 'slave'. In this diagram, the master is shown divided into 22 sections, each $7.12'' \times 0.08''$ in size and known as slits, which the SWIFT slicer separates and splices together lengthwise, as indicated by the blue arrows. The resulting $156.64'' \times 0.08''$ 'long slit' is fed into the long-slit spectrograph. The slit is then split back into 22 'slitlets'. Each 'slitlet' is expanded into the 0.650 – 1.0 μm spectrum, and are recombined as shown by the red arrows. The resulting array contains 22 'slitlet' horizontal rows, each of which contains spectral information in the horizontal direction and spatial information in the vertical direction. For an example of an actual data array output, see figure 2.4. The same process shown here occurs, in parallel, for the slave slicer and spectrograph.

Table 2.3: Palomar SWIFT observations that were selected for use. All selected frames were observed with Palomar SWIFT at 0.080" resolution. All Neptune observations were integrated for 5 minutes. HR7950 was the A1V-type star used as a stellar standard for the removal of telluric absorptions features, and was observed with 2-second integrations. Spatial resolution was calculated by multiplying the excess number of horizontal spaxels, compared with the actual width of the body, by the spaxel width of 0.080". Note that the observations occurred in California between the nights of 29Jun12 and 02Jul12. Since all the observations were recorded after midnight UTC, they appear 1 day later in the table.

Target	Frame #s	Date	Start Time (UTC)	Approximate Airmass	Spatial Resolution (arcseconds)
Neptune	193 – 194	30Jun12	10:08	1.514	0.16 ± 0.04
	195 – 196		10:26	1.467	0.16 ± 0.04
HR7950	207	30Jun12	12:15	1.679	0.24 ± 0.04
Neptune	060 – 061	01Jul12	10:39	1.434	$0.08^{+0.04}_{-0.00}$
	063 – 062		10:55	1.414	0.16 ± 0.04
	064 – 065		11:10	1.402	0.16 ± 0.04
	067 – 066		11:25	1.397	0.16 ± 0.04
	183 – 184	02Jul12	09:31	1.470	0.16 ± 0.04
	189 – 190		10:17	1.470	0.16 ± 0.04
	192 – 191		10:33	1.438	0.16 ± 0.04
	193 – 194		10:49	1.417	0.16 ± 0.04
	201 – 202		11:25	1.397	0.16 ± 0.04
	204 – 203		11:40	1.401	$0.08^{+0.04}_{-0.00}$
	205 – 206		11:56	1.413	$0.08^{+0.04}_{-0.00}$
	208 – 207		12:12	1.433	0.16 ± 0.04
	181 – 182	03Jul12	10:24	1.447	0.16 ± 0.04
	184 – 183		10:39	1.423	$0.08^{+0.04}_{-0.00}$
	185 – 186		10:54	1.408	0.16 ± 0.04
	188 – 187		11:09	1.399	0.16 ± 0.04
	189 – 190		11:23	1.397	0.16 ± 0.04

Figure 2.4: A sample of a raw, uncalibrated Palomar SWIFT image of Neptune. This is the 'master' image, produced by breaking the lower half of the original field of view into one long slit, and then breaking this slit into the 22 slitlets which appear here as horizontal lines. Each of these lines contains spectral information in the horizontal direction and 7.12" of spatial information (at 0.08" resolution) in the vertical direction.

the disc is difficult to define. The problem of identifying the disc's edge arises because the atmosphere gradually thins, as opposed to having a definite termination point, and also because at some wavelengths the disc edge is subject to limb-brightening, while at others is subject to limb-darkening. As a result, it is not possible to simply count the pixels in the full-width-half-maximum as was done with point source stellar standards. Through a careful qualitative review of the various frames, differences in image resolution were noted. Frames were then classified based on a qualitative ranking system. Through this means, ten Uranus frames from among the fourteen observed on the 18th of August were chosen to use for all the Uranus analysis described in this paper. For the Neptune analysis, eight of the twelve available frames were chosen. When analysis commenced, the selected pairs for each planet were co-added to produce one spectrum for analysis with a higher signal-to-noise than the spectra taken individually. Table 2.4 summarises the observations selected for aver-

Table 2.4: IRTF SpeX observations that were selected for use. All selected frames were observed with IRTF SpeX in short-wavelength, cross-dispersed mode (SXD). HD1160 was the A0-type star used as a stellar standard for the removal of telluric absorptions features.

Target	Frame #s	Date	Start Time (UTC)	Duration (sec)	Approximate Airmass
HD1160	148 – 149	18Aug09	14:36	30	1.156
	150 – 151		14:37	30	1.159
Uranus	152 – 153	18Aug09	14:50	60	1.370
	154 – 155		14:52	120	1.382
	156 – 157		14:57	120	1.409
	162 – 163		15:12	120	1.490
	164 – 165		15:16	120	1.521
Neptune	075 – 076	28Aug09	12:33	120	1.703
	077 – 078		12:38	120	1.743
	079 – 080		12:42	120	1.784
	085 – 086		12:57	120	1.928

aging and analysis, as well as the standard A0 star used for their telluric corrections.

Finally, when characterising the angular resolution of ground-based telescope data, it is important not only to consider the effects of earth's atmosphere on angular resolution, but the wavelength-dependant quality of this effect. Due to random and rapidly varying changes in refractive indices within the inhomogeneous air column through which incoming radiation must pass, the incoming wavefront is distorted. As stated earlier, this limits the practical resolution which the telescope can achieve. This effect is more pronounced at lower wavelengths that approach the visible, a property first predicted theoretically by Fried (1966), later confirmed in numerous experimental studies including Boyd (1978); Selby et al. (1979), and summarised nicely in Wynne (1999). The full scope of these theoretical calculations is unnecessary to consider in this thesis, though the interested reader could consult the sources

cited above. For the purposes of this work, it is only necessary to know the end result of a lengthy analysis of the modulation-transfer function (MTF), and the wave structure function upon which it depends.[4] This result allows Fried (1966) to show that the first Fourier term defining the spatial frequency of the telescope's focal plane is proportional to $\lambda^{1/5}$. This prediction relies on three assumptions, namely that the integration times are sufficiently long, that the wavelength-dependent change of the refractive index of air is small (such as in the visible and near-infrared), and that the MTF is fixed (such as when looking at data from a single telescope). From this result, it follows that a good, first-order characterisation of the degradation of angular resolution with decreasing wavelength is

$$s = s_{\text{ref}} \left(\frac{\lambda}{\lambda_{\text{ref}}} \right)^{-1/5}. \tag{2.1}$$

In this equation, s is the calculated angular resolution at wavelength λ based upon a known reference solution, s_{ref}, at wavelength λ_{ref}. When doing analysis of methane using the 825 nm region in particular (see section 4.3.2), it is important to know the angular resolution in the I-band[5], where the data is the least resolved. Given the difficulty already described of directly measuring this resolution for an extended source, and because equation 2.1 is meant only as a first-order estimation, three methods are employed and compared, with results as shown in table 2.5.

H-band and I-band "Method 1" resolutions are calculated by finding the stellar standard observation that lies closest in airmass and time to the planet observations in question. The observed width of the point-source is then counted in the H-band

[4] The MTF is a measure of how well the contrast in a source is transferred through an optical system to a resulting image. The wave structure function is a relation that expresses the phase and amplitude structure of a light source.

[5] The terms 'I-band', 'z-band', 'J1-band', 'J2-band', 'H-band', and 'K-band' represent viewing windows between regions of strong water vapour absorption in the atmosphere. The conventional names of these windows will sometimes be used in this thesis, and for reference have been included in table 2.1.

Table 2.5: Angular resolutions of Uranus and Neptune observations with IRTF. "Method 1" values are determined from the width of the stellar standard closest in airmass and time to chosen planet observations. "Method 2" values are counted from raw planet frames, rather than comparable stellar standard frames. I-band "method 3" values calculated from H-band values using equation 2.1.

Target	***H-Band (arcseconds)***		***I-Band (arcseconds)***		
	Method 1	*Method 2*	*Method 1*	*Method 2*	*Method 3*
Uranus	0.5 ± 0.1	0.5 ± 0.1	0.8 ± 0.1	0.6 ± 0.1	0.6 ± 0.1
Neptune	0.6 ± 0.1	0.5 ± 0.1	0.8 ± 0.1	0.8 ± 0.1	0.7 ± 0.1

and in the I-band. Pixels are then converted to arcseconds using the 0.15" / pixel latitudinal resolution of the array. Though it is quite accurate to count pixels across a bright, theoretically point-source object, there is one major uncertainties in this method. This uncertainty arises from the fact that no data is available for stellar standard observations identical in airmass and time to the planet observations for which spatial resolutions are desired.

H-band and I-band "Method 2" refers to the procedure of counting the pixel width in the full-width-half-maximum across the planet's central meridian, rather than a comparable stellar standard. From this value, obtained from counting pixels in the appropriate spectral band, the theoretical polar width of the planet (assuming no distortion due to atmospheric turbulence or absorption) is subtracted, with this result being taken as the effective pixel resolution for the image. Converting pixels, as before, to arcseconds provides a value for the angular resolution. The largest factors of error in this method arise, as already mentioned, from the difficulty in accurately defining the edges of the planet as the atmosphere gradually thins. In the I-band, limb brightening effects on the reflectance values at the disc's edge were determined to be less than 5% of the overall magnitude (see section 4.3.2 and figure 4.11 for a thorough discussion of limb effects in the I-band), and therefore much smaller than the uncertainties already mentioned.

"Method 3" refers to the procedure of using equation 2.1 to calculate the I-band resolution. H-band "Method 1" values are assumed as reference values. The inherent errors in this method arise from: (1) the fact that the H-band reference for the equation comes not from the planet observation itself, but from a star observation which doesn't have precisely the same airmass, and presumably has a slightly different angular resolution than the planet observations and (2) the fact that equation 2.1 is only a rough guide to degradation of angular resolution with wavelength.

As shown in table 2.5, all methods produce results that are consistent within error. Looking at I-band results only (section 4.3), achievable resolutions will be reduced by less than 15% compared with the H-Band, and this reduction should not significantly impact the usefulness of the data.

Given the variable seeing during the observation session, the spatial resolution of the Uranus data range from an approximate spatial resolution of 0.5" in the H-band to 0.7" in the I-band. Each spatial pixel in the H-band is therefore capable of latitudinally resolving roughly 16° (7000 km) of Uranus at the sub-observer point (8° N). For Neptune, the poorer seeing leads to a slightly poorer spatial resolution. This, combined with the increased distance to the planet, allow us to latitudinally resolve the centre of disc (29° S) to approximately 27° (13,000 km) in the H-Band.

2.2.2 SWIFT

The Palomar SWIFT data, like the SpeX data, was observed at a range of airmasses, though the overall range was not as dramatic. Additionally, the SWIFT data was observed using the P3K adaptive optics system, designed to minimise or even remove any distortion of the image due to poor atmospheric seeing. To verify the angular resolution of the data, the same method of counting pixels that was described in section 2.2.1 was employed. In short, Neptune's equatorial width during the observations should have been 29 spaxels. The angular resolution cited is the number of spaxels

beyond 29 multiplied by the spaxel angular width of 0.080".

As you can see in table 2.3, the angular resolutions are much better than those achieved with IRTF, which lacked adaptive optics. In addition, it should be noted that since the spectral range is smaller, equation 2.1 suggests that any degradation of spatial resolution with decreasing wavelength should be within the error of the measured value. This was verified by counting pixels at a range of wavelengths. No degradation was ever noticed.

Given the seeing during the observations, the spatial resolution of Neptune is no worse than 0.16", roughly equal to 3400 km, which at the sub-observer point (28° S) is roughly equal to 8° latitude and 9° longitude.

2.3 Data Reduction

In this, the final section of this chapter, the data reduction process is discussed. This process was required to prepare the raw data for analysis. Again, a section is included for the spectrometers used at both telescope facilities: 2.3.1: SpeX Data Reduction and 2.3.2: SWIFT Data Reduction.

2.3.1 SpeX Data Reduction

After selection of specific observation frames from which to base the analysis for both Uranus and Neptune, a great deal of further calibration and processing is required to reduce the data for input into the retrieval process. Many of the procedures are handled within an IDL software package, SpeXtool, which is designed to aid in processing SpeX data (Cushing et al., 2004; Vacca et al., 2003). This software works quite well for point-source data, such as stellar standard observations, used for telluric corrections. For extended-source data, like the Uranus and Neptune data, SpeXtool lacks the ability to reduce more than the centre-of-disc spectra, so additional IDL routines

were written and employed to fill in gaps in SpeXtool's capabilities. Each of the steps required to convert raw SpeX data into a fully calibrated, retrieval-ready format is described in this section. The overall process, for clarity, is summarised graphically in figure 2.5.

The initial stages of data reduction for all SpeX data were handled by SpeXtool. The raw images are combined with flatfield frames in order to adjust the images according to the specific sensitivity of each pixel in the frame. This "flatfielding" ensures that the zero level is uniform throughout the array and no systematic errors are introduced due to variations in pixel sensitivity. SpeXtool also performs basic calibrations of both wavelength and flux.

The next reduction step was to subtract a negative image ('B') from a positive one ('A') to produce spectral image frames. The reason for this 'A − B' subtraction is to remove any background radiation from the observational frames. Minor sources of background radiation in the near-infrared are "dark current", meaning residuals detected by the array, or any emissions from the telescope itself. Most important in the near-infrared, however, is fluorescence of OH, or "airglow", which produces the vertical lines seen in the first panel of figure 2.2. To allow for 'A − B' subtraction, all observations, both of stellar standards and of the ice giants are recorded in pairs, as the telescope 'nods' up and down. Since both Uranus and Neptune are small enough to fit in the SpeX slit twice, the nods are performed so that the target lies in the upper 50 pixels of the slit for the first ('A') frame, and the lower 50 pixels of the slit in the second frame ('B'). Both the 'A' and 'B' images are integrated for the same length of time so that they each contain the same amount of background radiation. Subtraction thus removes any residual background radiation from the frame, and leaves a single frame with one positive and one negative image. An example of the results of this process on one of the Uranus observations is shown in figure 2.2 (lower). For further details on the SpeXtool processes of flatfielding, wavelength and flux calibration, and

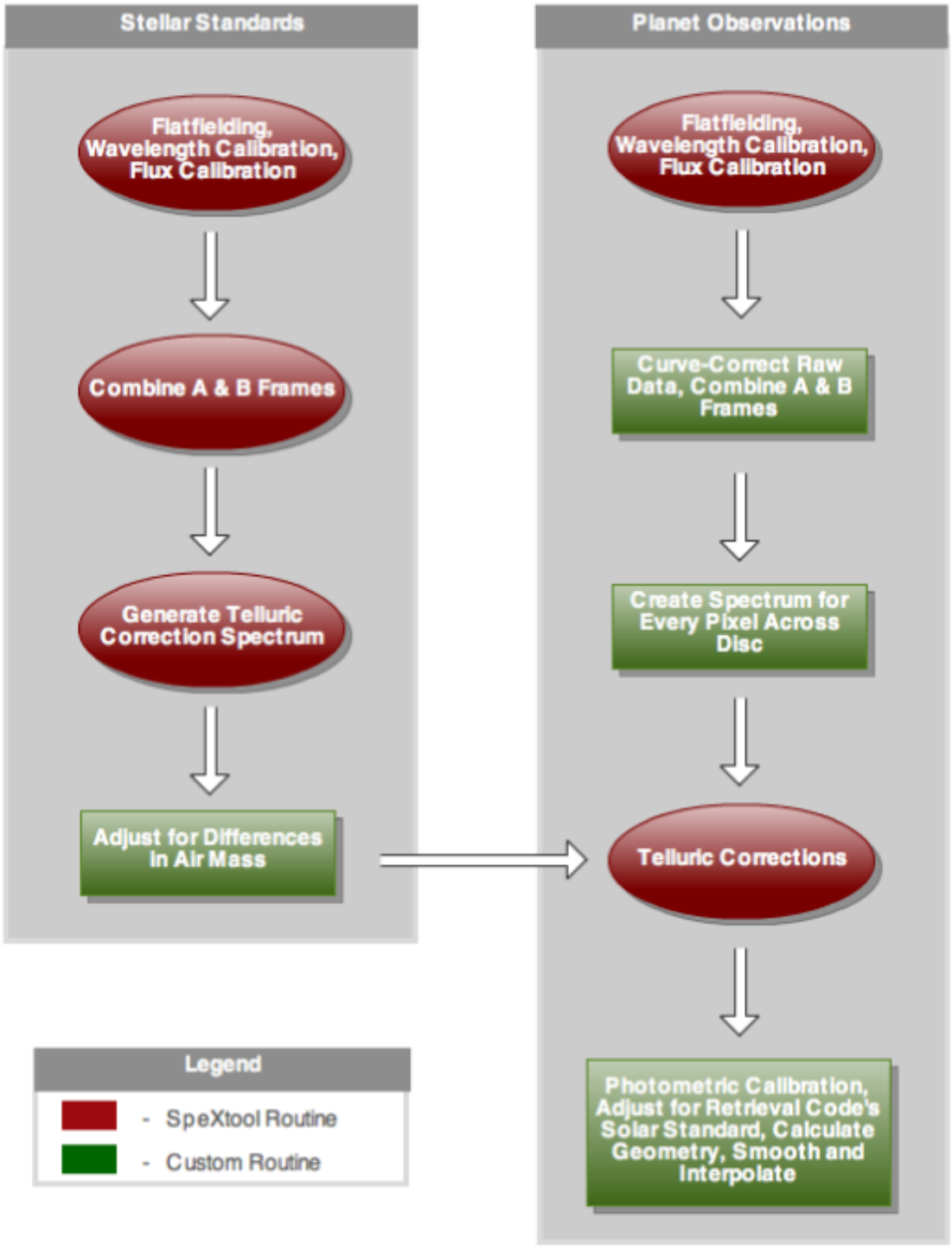

Figure 2.5: Overall calibration process for reducing IRTF SpeX Uranus and Neptune data. This includes, as noted in the chart, stellar standard and planet reductions, outlining all steps done in SpeXtool and all steps for which additional processing routines were written.

co-adding, see Cushing et al. (2004)

Since SpeXtool is well-suited to operate on point-source observations, further calibration was possible within SpeXtool for the stellar standard images, which are used later for removal of telluric features in the data. SpeXtool takes the 'A − B' frames and locates the central, brightest pixel in both the positive and negative images. SpeXtool then produces for this central pixel a spectral output for the observed star in each SXD-mode order. The upper frame of figure 2.6 shows the raw data for a standard star observation that is input into SpeXtool, while the lower frame shows the spectrum produced by SpeXtool.

As mentioned earlier, SpeXtool does not handle extended sources as thoroughly as point-sources. To successfully prepare the planet observations for retrieval, new routines were designed to handle the extended source data. First, SpeXtool routines were used to co-add all the AB pairs selected for each planet, and to produce a single frame of the averaged A and B observations, as shown in the lower panel of figure 2.2. From this point, SpeXtool can only select the bright mid-point of the data at each wavelength, and produce one output spectrum as it did for the stellar standards.This centre-of-disc observation output would ignore all data for other latitudes on the planet. In order to keep all latitudinal data, an IDL code was developed to correct for the curves in the data frame and extract data spectra for each pixel on the target disc (the central meridian of the planet). The curve-corrected data frame is shown in figure 2.7.

At this point, the next reduction step for the planet images was to calculate observational noise levels. This was accomplished by using 18 off-planet pixels located between the 'A' and 'B' images. At each spectral location, the observational noise (for both the 'A' and the 'B' image) was assumed to be the standard deviation of these 18 pixels from a straight line fit to the dark background between the planets. Then, the spectral data within these two images was extracted and added together (positive im-

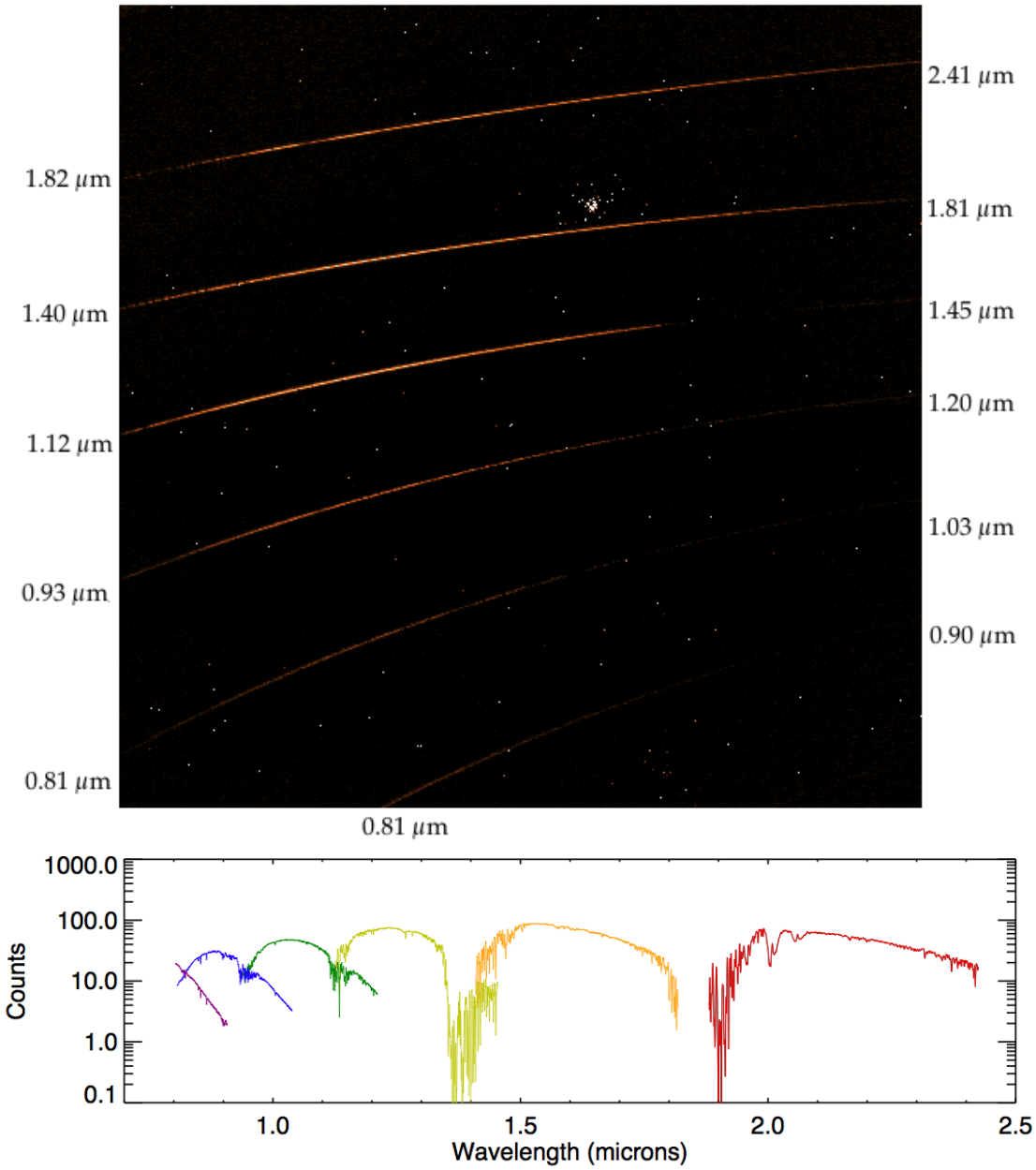

Figure 2.6: Sample of IRTF standard star observation. Upper frame shows raw 'A' image; lower frame shows spectrum extracted by SpeXtool, with each order represented by a different colour.

Figure 2.7: Sample of IRTF Uranus observation output from an IDL-based curve-correction code. The input to this curve-correction code that produces this frame is shown in figure 2.2 (bottom).

age minus negative image) to produce a final, single spectral signal. The associated uncertainty with this final 'A − B' image was calculated by multiplying the uncertainty mentioned above by $\sqrt{2}$ since two images were combined to create the final spectrum.

When observing from Earth-based instruments, one of the most important considerations is that radiation from the target is passing through Earth's atmosphere before reaching the spectrometer. This means that any spectral results are influenced by the absorbers, like water, in Earth's atmosphere. To correctly retrieve and interpret Earth-based data, one must develop a method of cancelling out the telluric features from the spectrum. SpeXtool includes a routine that is well-suited to convert stellar spectra into telluric correction spectra that can be applied to remove telluric features from the ice giant observations. To do this, SpeXtool creates a model spectrum of an observed A0 type star near the target, HD1160 in this case. This model spectrum can be divided by a real A0 star observation, which produces a telluric correction

spectrum. This correction spectrum, when multiplied by the target observations, removes any telluric absoprtion features. This correction spectrum also normalises the spectrum to negate the intensity variations produced by variations in instrumental throughput. An example correction spectrum is shown in figure 2.8. To construct the model spectrum used to generate this telluric correction, SpeXtool starts with a high-resolution spectrum of Vega, an A0 type star, and then completes the following procedure:

1. Normalise A0 stellar standard observation near a chosen spectral absorption feature
2. Determine radial velocity shift of the standard star by cross-correlation of the absorption feature in the observed spectra and the Vega model
3. Shift, scale, and redden Vega spectrum to match radial velocity, brightness, and redness of observed star
4. Construct convolution kernel from a small region near a dominant absorption feature found in both spectra
5. Convolve kernel with model
6. Scale equivalent widths of various hydrogen lines in model to match observation
7. Shift model in each order appropriately to make up for remaining shift in wavelength calibration

Much of the above process is automated, though there is still a fair amount of user input required. One important decision of the user is to chose an appropriate absorption feature to use in steps 1, 2, and 4. The Paschen-delta (Pa-δ) hydrogen absorption line is chosen because it is strong in all A0 type stars, and is located in

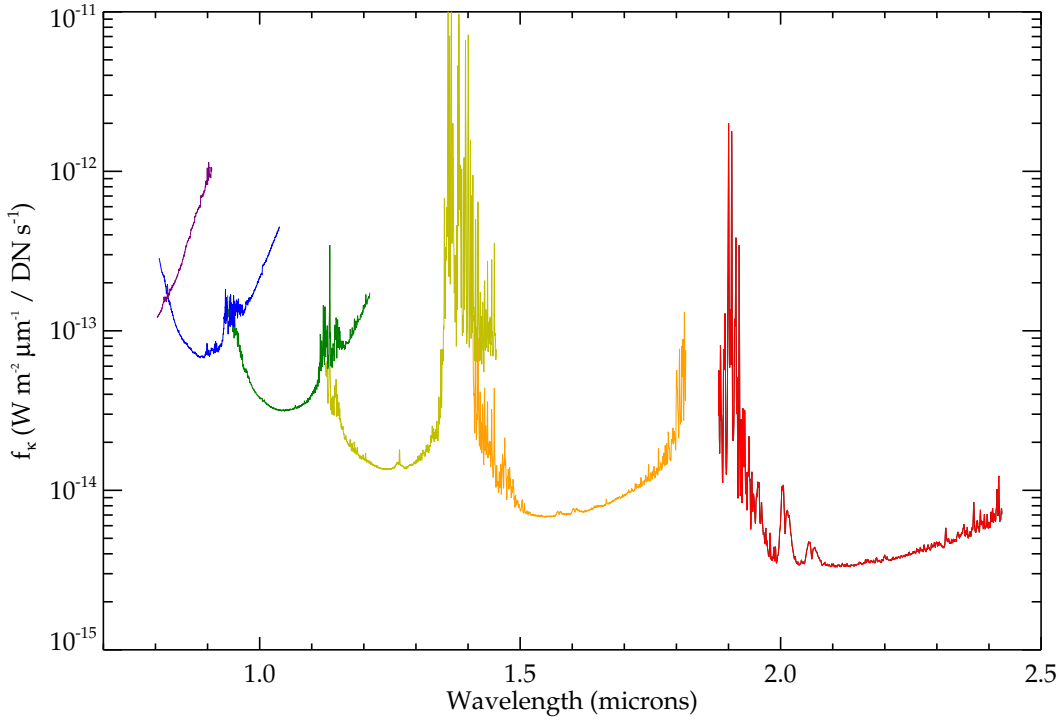

Figure 2.8: Sample of IRTF telluric correction spectrum as generated by SpeXtool. Correction for each SXD order shown in different colours.

the middle of the J1 spectral window, making it relatively unaffected by telluric absorption. For the normalisation in step 1, required to account for the instrument's throughput effects on the spectrum, the user inputs various regions of the spectrum with high signal-to-noise and few absorption and emission features. For these user-specified regions, SpeXtool generates various polynomial fits, the best of which must be selected by the user. In step 4, the half-maximum points of the absorption feature are identified so that SpeXtool could determine the size of the convolution kernel. This kernel is then used to broaden lines and smooth features of the model to match those seen in the observation. In step 5, each hydrogen line is examined in turn by the user, and various scaling factors can be tested until each of the model's hydrogen features match the line shape from the observation. It is possible to remove these telluric lines, without accidentally impacting any possible contributions from the reflected sunlight spectra of the planet, because of the Doppler shifting of the object's spectrum, which moves its lines slightly, allowing them to be distinguished from telluric ones. This step is important, as it removes the final key spectral difference between Vega and other A0 stars. For more discussion of the process of generating the telluric correction, see Vacca et al. (2003).

SpeXtool did not allow standardisation of step 7 over each latitude (all of which had to be handled separately). A series of trials with a random sampling of the data showed that the largest wavelength corrections required were on the order of 5×10^{-4} μm, while most were substantially smaller than that. Currently, since the data is eventually convolved and smoothed to a resolution of 2×10^{-3} μm, it was decided to omit step 7 as it would not effect the final spectra used for retrieval.

Before applying these telluric correction spectra to the data, a few slight adjustments were still necessary. Since the standard star observations and the planet observations were sometimes separated by more than an hour, there was generally a slight difference in airmass between the two observations. To account for this, slight

corrections needed to be made to the telluric correction spectra. An IDL code was written which computed a normalisation curve for each order's telluric correction spectrum. Dividing these normalisation curves by the telluric correction spectra produced plots of effective atmospheric absorption. From this, constructing an atmospheric transmission plot is straightforward ($T = 1 - A$ for absorption A). The transmission plot is multiplied by $e^{\Delta a}$ where Δa is the difference in airmass between the star and planet observations. This transmission spectrum is now accurate for the airmass of the planet observation rather than that of the star. By reversing the transformations (normalisation and absorption to transmission) a new, airmass-adjusted telluric correction spectrum is produced.

At this point, the telluric corrections for each order are multiplied by the data. All the latitudes and all the orders are combined, yielding one telluricly-corrected datacube for all latitudes and across the entire IRTF spectral range. A final IDL code finishes the data reduction. First the code applies photometric calibrations so the intensity of the data is transformed from counts to radiance per steradian. Since the version of the NEMESIS retrieval code (see chapter 3) used for IRTF analysis utilised a very coarse solar spectrum and the data is far more spectrally resolved, adjustments needed to be made to ensure that features were not apparent in the data that would be lost to the retrieval code. To overcome this potential issue, the data was multiplied by the ratio of the coarse solar spectrum from NEMESIS to a highly accurate solar spectrum convolved to the data's resolution. Finally, geometry data is compiled to assign latitudinal information to each pixel in the data.

By comparing the reduced spectra with other similar studies, it was determined that the absolute radiometric calibration using the A0 star was unsuccessful. This was most likely due to blurring of the standard star beyond the edges of the viewing slit, making the total radiance of each wavelength extremely difficult to accurately estimate.

Instead, Uranus and Neptune SpeX data were scaled so that the magnitude of the reflectance peak in the H-band matched Uranus spectra observed one month later under photometric conditions by Irwin et al. (2011a) with the Gemini-North Near infrared Imager and Spectrometer (NIFS). The first step was to further reduce the absolutely-calibrated NIFS data to compensate for the differences in both spatial and spectral resolutions between the two telescopes. First, NIFS images of Uranus were convolved with a Gaussian point-spread function which 'blurred' the image and imitated the spatial resolution of the SpeX (see figure 2.9 for a visual comparison of the two images). Reflectance values from this convolved image were then sampled over a series of 21 0.5" $\times$ 0.15" boxes running along the central meridian of the planet, simulating the pixel size of each point of spectral data from SpeX. Finally, the magnitude of the H-band reflectance peak (here defining this as the average of 40 spectral brightness values between 1.571 μm and 1.610 μm) was calculated for each of these 21 points. These H-band brightness values were then matched with comparable H-band brightness values of the reduced but uncalibrated SpeX data and used to radiometrically calibrate the SpeX data. All latitudes were scaled according to a factor determined based on the central pixel, imaging the sub-Earth point on each planet, in order to avoid any complications due to limb effects. Figure 2.10 shows a sample of how the resulting, calibrated brightness values of a SpeX image of Uranus agree well with the modified Gemini Uranus data at all latitudes. Any discrepancies were well within the error associated with the IRTF spatial resolution. It should also be noted that this same process was effective for Neptune, despite this planet's numerous discrete cloud features because these features were not resolvable with IRTF (nor with the 'blurred' Gemini-North images).

Photometrically-corrected intensities were then smoothed across a triangular instrument function and resampled at the same resolution as the κ-distributions employed (see sections 4.1 and 4.3.3 for details). Finally, a region of the data surrounding

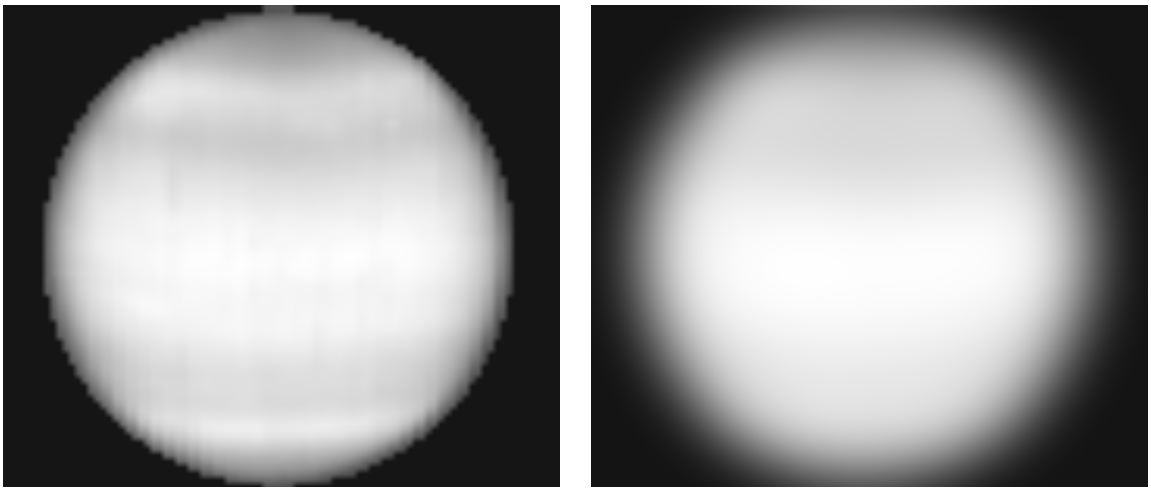

Figure 2.9: September 2009 Gemini NIFS image of Uranus averaged from 1.571 μm to 1.610 μm. Left frame is original image; right frame is image convolved to IRTF spectrometer's resolution.

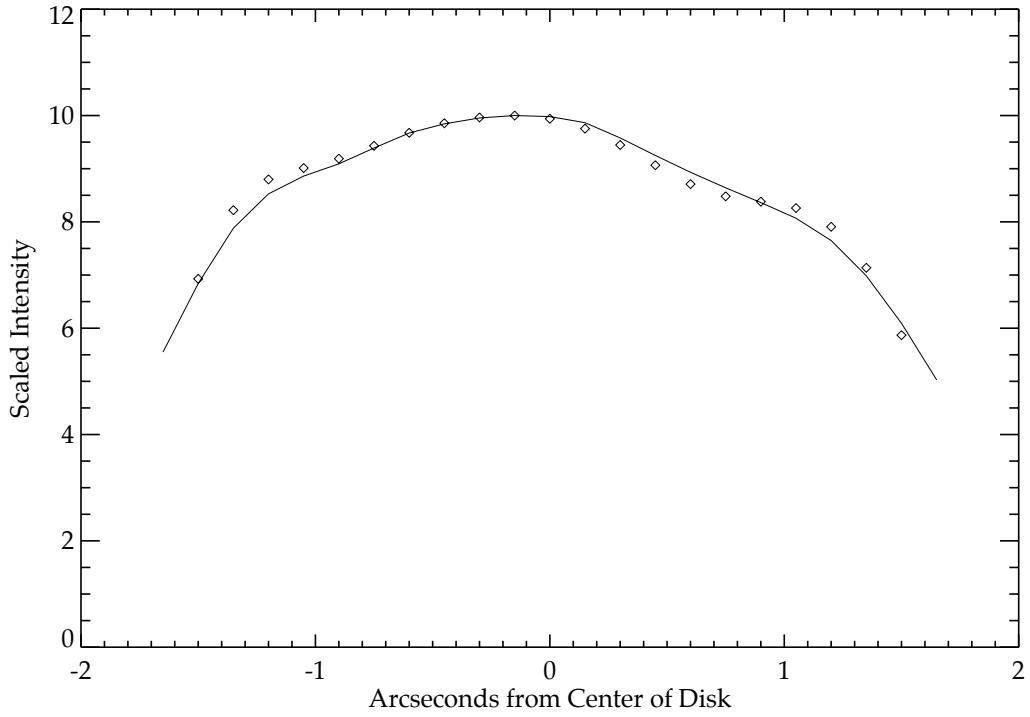

Figure 2.10: September 2009 Gemini variations of radiance along Uranus' central meridian (diamonds) compared with August 2009 IRTF results (solid line). Both curves show averaged data over the H-band peak between 1.571 μm and 1.610 μm.

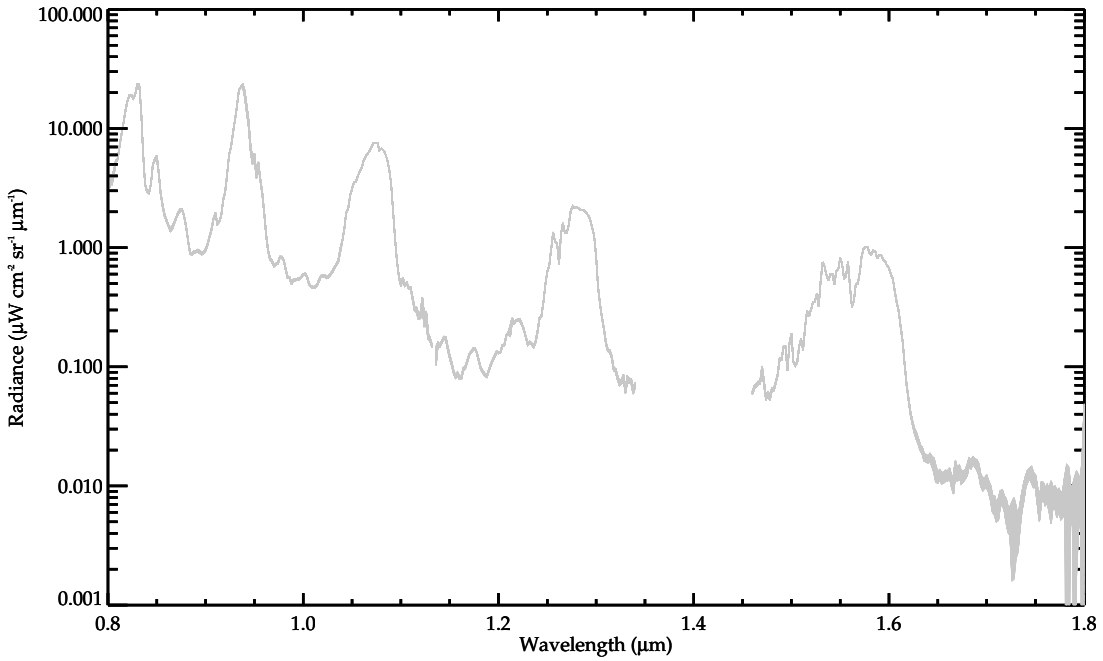

Figure 2.11: Sample of a fully processed, equatorial SpeX data spectrum after all data reduction procedures are completed. Gray vertical extent represents the observational error. The blank regions (at 1.134 μm and surrounding 1.4 μm) are areas of poor signal-to-noise that were ignored in analysis. Areas of dramatically increased uncertainty (such as $\lambda \gtrsim 1.72$ μm) occur at edges of some of the spectroscopic orders where the instrument response is relatively poor.

1.4 μm was removed prior to analysis due to poor signal-to-noise, an issue occurring due to extremely high telluric absorption in the region. A sample of a processed equatorial data spectrum is shown in figure 2.11.

2.3.2 SWIFT Data Reduction

For each 5-minute SWIFT observation of Neptune, two consecutive exposures were performed just like with the IRTF observations. The telescope was nodded back and forth such that the Neptunian disc was imaged alternately in the left and right halves of the long, 44 × 89 'spaxel' viewing field (see figure 2.12). This allowed, as with the 'A'

and 'B' IRTF images, subtraction of two consecutive exposures to eliminate residual background radiation.

After collection of the observations, the first stages of data reduction were handled using the IRAF-based Swiftred package developed by R. Houghton et al. (in preparation). As with the SpeXtool package used for initial reduction of IRTF data, Swiftred contained the standard point-source reduction steps, but lacked some additional reduction capability that was required for a spectral analysis of an extended source. After utilising Swiftred's capability for 'master'/'slave' recombination, bias subtraction, flat-fielding, illumination correction, image reconstruction, cosmic ray removal, and wavelength calibration within Swiftred, additional IDL procedures were developed to complete the reduction process. The 'AB' pair of Neptune images in figure 2.12 is an example of the final result after processing in the Swiftred package.

The newly-developed IDL code continued the reduction process in several important ways. It was discovered that a linear, wavelength-dependent offset was present between the 'master' and 'slave' portions of the Swiftred-reduced images, producing images in which the upper and lower halves of the Neptunian disc were not aligned. An example can be seen in figure 2.12. It was also discovered that the centroid of the Neptunian disc, once the offset had been corrected, drifted across the detector array in a wavelength-dependant linear fashion. The IDL code contained subroutines to correct both of these issues. The code also combined the 'A' and 'B' frames, and used the dark region between the left-hand (negative) and right-hand (positive) images to assign uncertainty values to each wavelength, using the same process outlined in section 2.3.1. The IDL code also rotated the Neptunian image so that the planet's north pole was oriented upwards, and assigned geometry information to each spaxel. The code removed telluric features and accounted for wavelength-dependent instrument sensitivity by dividing the Neptune spectra by the spectrum of HR7950 (see table 2.3). The visual results of this extra calibration

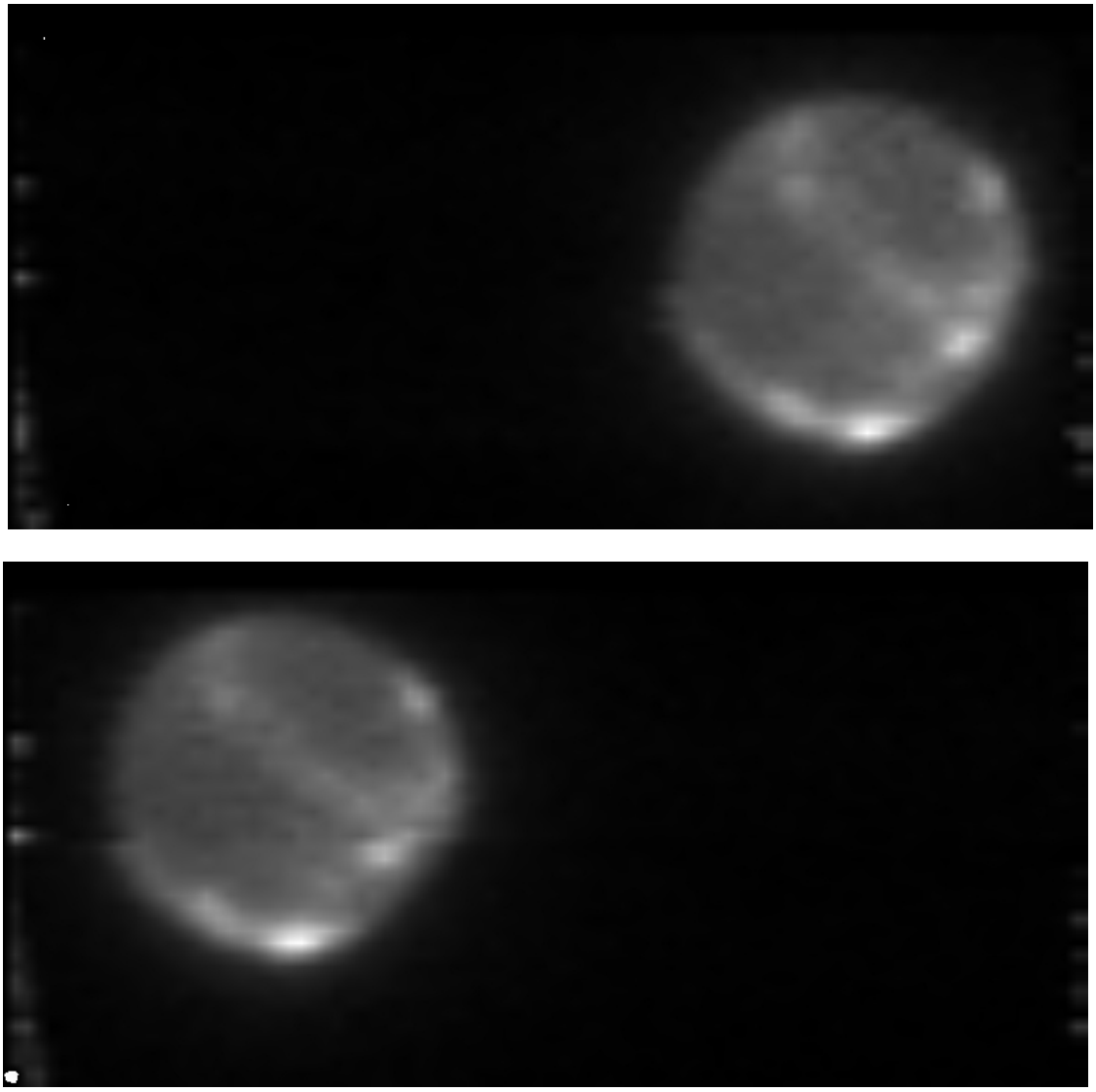

Figure 2.12: A sample of an 'AB' pair of Neptune observations after processing in the Swiftred package, but prior to additional IDL-processing developed for this thesis. The results of the telescope 'nod' can be seen with the 'A' image (top panel) appearing in the right half of the frame, and the 'B' image (bottom panel) on the left. The offset between 'master' and 'slave' portions of the image can be seen in both panels.

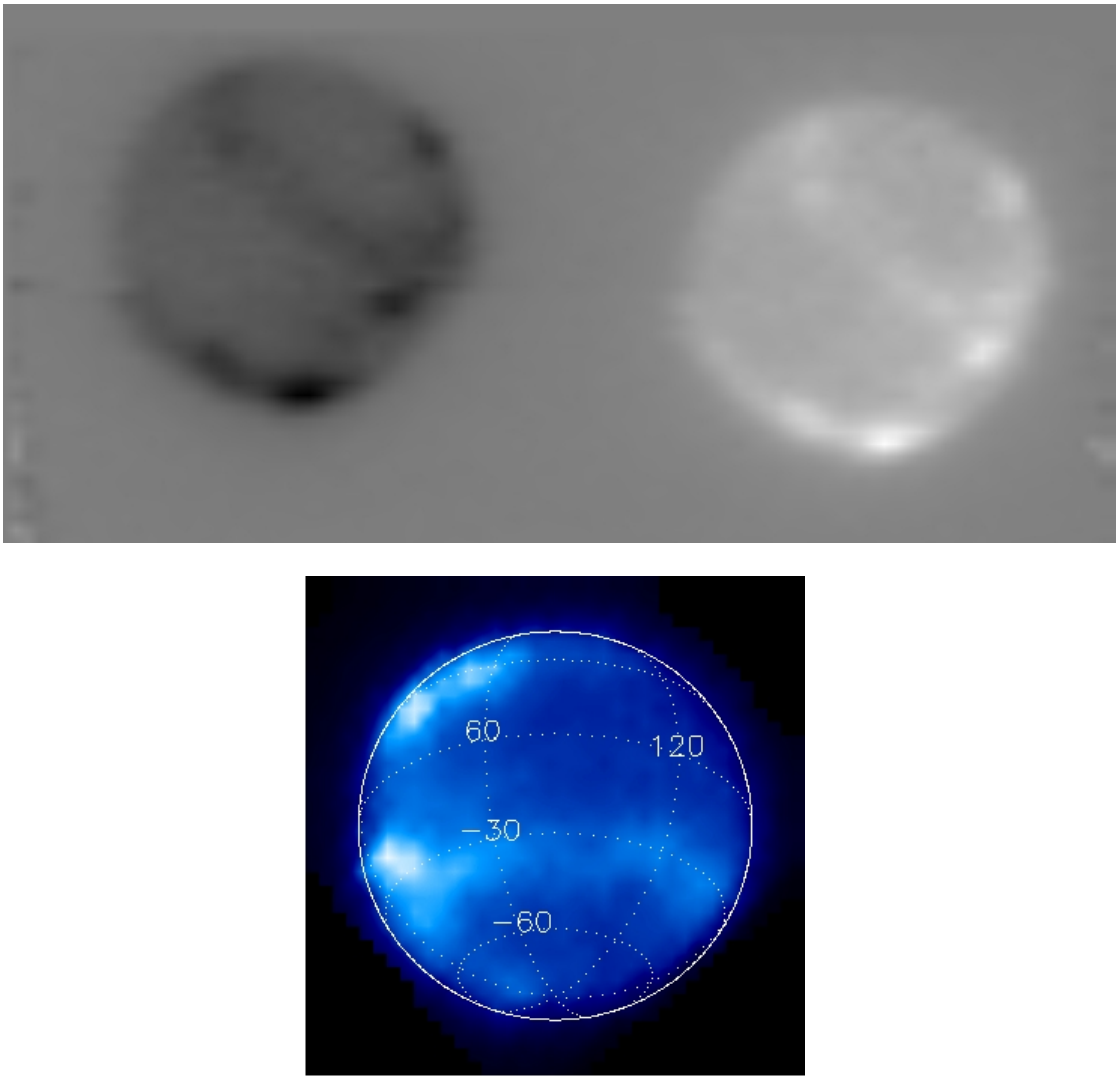

Figure 2.13: A sample of an 'A – B' image of Neptune observations immediately before and after processing in the newly-developed IDL code.

routine can be seen in figure 2.13, which is a fully calibrated, '$A - B$' version of the images in figure 2.12.

In the case of the SWIFT images, radiometric calibration was achieved slightly differently than the method described in the previous subsection for SpeX data, due to three issues which complicated the process. Firstly, Neptune is a much more dynamically active planet, with numerous short-lived convective clouds appearing, moving,

evolving, and disappearing across the entire visible atmosphere. This meant a calibration based only on a 0.5" wide meridional slice might be suspect if cloud features were visible in one image and not another. (This first concern was not an issue with the poor spatial resolution of the IRTF spectrometer, since no discrete clouds were resolvable in the raw data, but needed to be considered for both SWIFT and NIFS images, in which the telescope's adaptive optics systems allowed for resolution of single discrete cloud features). Secondly, the wavelength range of SWIFT spectrometer did not directly overlap that of the absolutely-calibrated Gemini data, so another source for calibration was needed. And finally, Gemini-North images of Neptune were acquired in September 2009 while SWIFT data was taken several years afterwards in June and July 2012 (see section 2.1).

Photometric calibration was completed by a two-step process which accounted for the issues cited in the previous paragraph. First, an IRTF observation of Neptune (August 2009, see section 2.1.1) was relatively calibrated to an absolutely calibrated Gemini-NIFS observation of Neptune (September 2009, see section 2.1.2)) using the overlapping spectral region from 1.55 – 1.60 μm. To minimise the effects of differences in discrete cloud features between the two observations, spectra from both Gemini and IRTF, both averaged over a large swath of the planet, were utilised. In the case of Gemini, this average spectrum was obtained from the spectrum for the central region of Neptune (figure 2.14), which represented a 0.44" × 1.72" region of the planet, mimicking the field of view of the CRyogenic high-resolution IR Echelle Spectrograph (CRIRES) instrument on the Very Large Telescope (VLT). In the case of the IRTF spectrum, nine central meridional pixels, for a field of view of 0.5" × 1.35", were averaged. This field of view closely approximates the size of the VLT field of view, while simultaneously ensuring that no limb effects affect the IRTF spectrum. Finally, to complete the first stage of the calibration, the Gemini observation was convolved over a gaussian instrument function that produced a spectrum with a poorer spectral

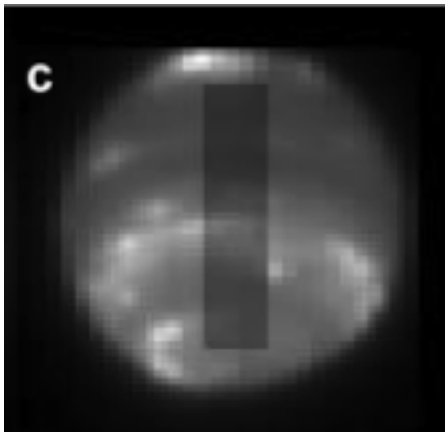

Figure 2.14: Gemini-North image of Neptune showing the field-of-view of the VLT. Reproduced by permission from figure 1c of Irwin et al. (2013).

resolution equalling that of the IRTF observations.

For the second step in the relative calibration, this newly-calibrated IRTF spectrum was used to calibrate the SWIFT spectra (June & July 2012, see section 2.1.3) using the overlapping region from 0.80 – 1.03 μm. As before, large, central fields of view of the approximate area of the VLT-CRIRES field of view were averaged to account for differences in discrete clouds. In the case of the SWIFT data, this was accomplished by averaging a region 6 pixels wide by 21 pixels high. And as before, the SWIFT spectrum was convolved to mimic the poorer-spatial resolution of the IRTF spectrum. This two-step process was performed individually for each SWIFT observation. The resulting relative calibration factors, k, were very consistent, with $\overline{k} = 3.7 \times 10^{-14}$ and $\sigma_k = 1.9 \times 10^{-15}$. For a graphical example of the calibration process, see figure 2.15.

That concludes this chapter of the thesis. The telescopes and spectrometers employed for data acquisition have been described, the quality of the data captured has been discussed, and a thorough explanation of how the data was reduced and calibrated, to prepare for its analysis, has been given. Before beginning to look at results of this analysis, chapter 3 will provide the reader with a discussion of the principle analysis techniques employed in this thesis.

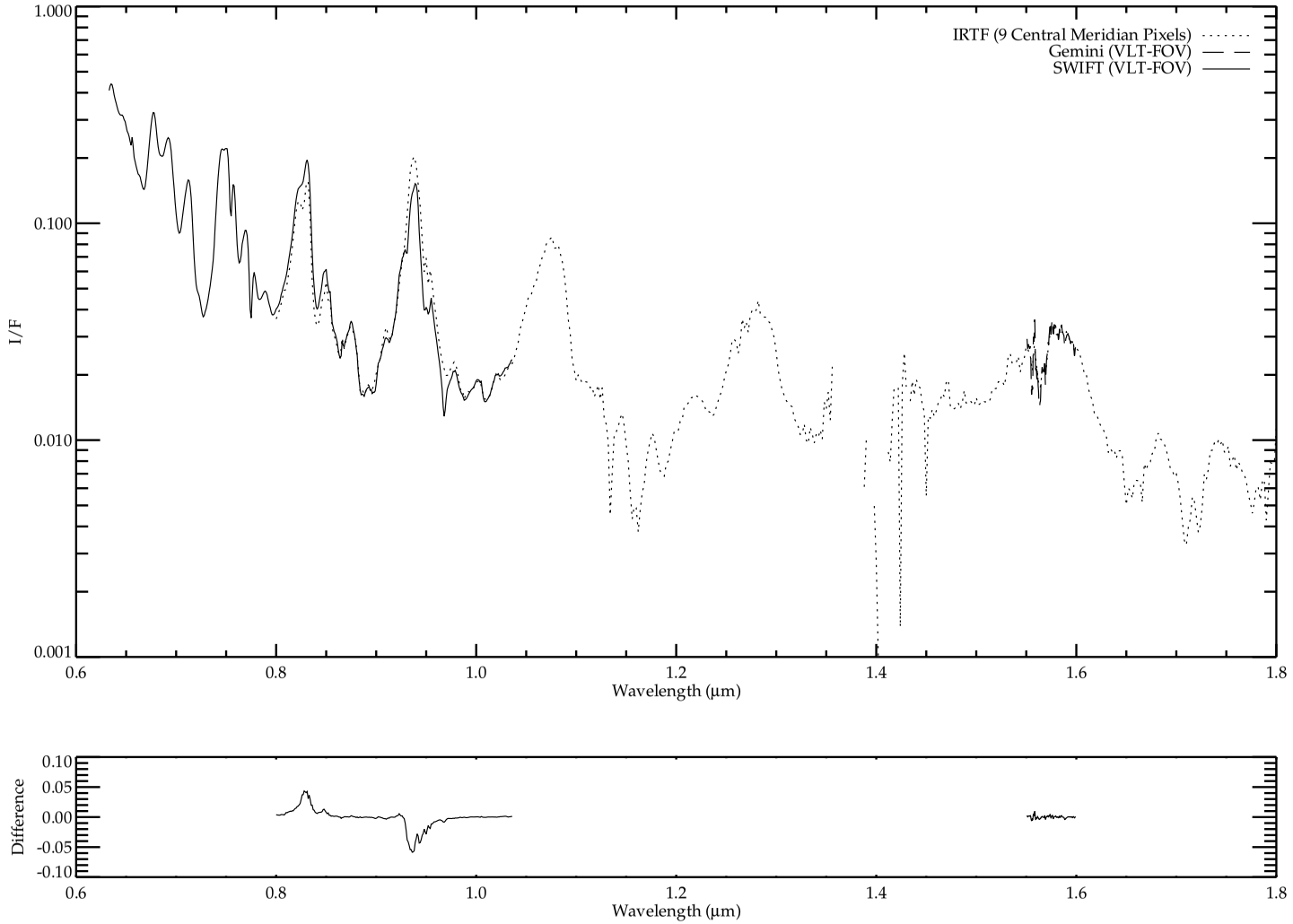

Figure 2.15: Example of the relative calibration of a SWIFT Neptune spectra (solid line) based on IRTF (dotted line) and Gemini (dashed line). Upper frame shows reflectivity (I/F) as a function of wavelength for all three instruments, while the lower panel shows the difference spectrum in the spectral regions of overlap, which were used for calibration. All spectra shown are convolved across a gaussian instrument function to the spectral resolution of the IRTF SpeX instrument. All spectra shown are averaged across large regions of the planet, as shown in the plot legend.

Chapter 3

Retrieval Theory and NEMESIS

Do not worry about your difficulties in Mathematics. I can assure you mine are still greater.

— Albert Einstein

Most of the analysis and results to be discussed in this paper rely on the Non-linear optimal Estimator for MultivariatE spectral analySIS (NEMESIS), a general-purpose retrieval code for planetary modelling (Irwin et al., 2008). To perform a NEMESIS retrieval, a set of atmospheric *a priori* parameters are used to create an initial "guess" model for the atmosphere. This model is then iteratively adjusted based on an optimal estimation technique (Rodgers, 2000) to determine the forward model which best fits the observational data spectrum. This optimal estimation technique enables physically plausible solutions to be found despite the under-constrained data, which is typical of planetary applications.

This first subsection below provides a very brief summary of the physics involved in near-infrared NEMESIS retrievals (section 3.1). The latter subsection explains the correlated-κ approximation which is employed by the retrieval code to increase the efficiency of the gas species' absorption calculations (section 3.2). For a more complete discussion of radiative transfer and retrieval and Mie theories, see Andrews

(2000); Goody and Yung (1989); Hansen and Travis (1974); Houghton (2002); Irwin (2009); Rodgers (2000). For a more complete description of the NEMESIS retrieval code, see Irwin et al. (2008).

3.1 Review of Radiative Transfer, Retrieval Theory, and Mie Theory

In the near-infrared and "visible-red", the spectral region of this study's data, the observed spectrum is governed by sunlight scattered back from various levels of the ice giant atmospheres. To produce an accurate "forward model" of reflected sunlight, model parameters must include vertical profiles of temperature, pressure, and all primary absorbing gases in the atmosphere (hydrogen, helium, and methane in the case of the ice giants). The model must also characterise any cloud particles (scatterers).

Scattering particles have inherent, wavelength-dependent single-scattering albedos and extinction efficiency spectra, as well as a wavelength-dependent "phase function" describing the relative probabilities of different scattering directions. Producing forward models also requires a set of phase functions for the wavelengths involved. Phase functions are modelled using Mie theory, which describes plane wave scattering off of spherical particles.[1] However, since in the research described here the exact composition of the scattering clouds is not known, the phase functions are approximated using a "combined Henyey-Greenstein" approximation of the full Mie

[1] For liquid particles, this assumption of sphericity is accurate. As already noted, however, in the ice giants many of the scattering particles are likely crystalline ices with complex structures. The spherical approximation can still be employed here because, to first order, a set of randomly oriented crystals are indistinguishable from spheres of the same mean radius.

theory solutions. The combined Henyey-Greenstein equation takes the form

$$p(\theta)=\frac{1}{4\pi}\left[f\frac{1-g_1^2}{\left(1+g_1^2-2g_1 cos\theta\right)^{3/2}}+(1-f)\frac{1-g_2^2}{\left(1+g_2^2-2g_2 cos\theta\right)^{3/2}}\right] \tag{3.1}$$

for a scattering angle, θ. The first parameter, f, is some fraction between 0 and 1 that represents the relative weights of the two scattering peaks, represented by the two terms of the equation. The parameters g_1 and g_2 are asymmetry factors for each scattering peak. By convention, and in this thesis, the first term in the equation represents the forward scattering peak ($0 \leq g_1 \leq 1$) while the second term represents back-scattering ($-1 \leq g_2 \leq 0$), though mathematically this could easily be reversed. The approximation in equation 3.1 produces, based on just three variables, a good representation of both forward and back-scattering phase function peaks, and provides us with a convenient and succinct method of describing the phase functions.

To produce a model spectrum for the NEMESIS optimal estimation scheme, values must be provided for each variable in the following radiative transfer equation for scattering of sunlight:

$$\begin{aligned}\cos\theta\frac{dI_{\bar{\nu}}\left(\tau_{\bar{\nu}},\theta,\phi\right)}{d\tau_{\bar{\nu}}} =& I_{\bar{\nu}}\left(\tau_{\bar{\nu}},\theta,\phi\right)\\ &-\frac{\bar{\omega}_0(\tau_{\bar{\nu}})}{4\pi}\int_0^{2\pi}\int_0^{\pi}p\left(\theta,\phi;\theta',\phi'\right)I_{\bar{\nu}}\left(\tau_{\bar{\nu}},\theta',\phi'\right)cos\theta' d\theta' d\phi'\end{aligned} \tag{3.2}$$

where $I_{\bar{\nu}}$ is the intensity of radiation, $\tau_{\bar{\nu}}$ is the optical thickness, $\bar{\omega}_0$ is the single-scattering albedo for aerosols and gas[2], and $p\left(\theta,\phi;\theta',\phi'\right)$ is the phase function for light incident at zenith angle, θ', and azimuth angle, ϕ', and subsequently scattered

[2] $\bar{\omega}_0=\sigma_{sca}/\sigma_{ext}$ here is a combined single-scattering albedo for both aerosols and gas. The combined scattering cross-section, σ_{sca}, is due to aerosol scattering and gaseous Rayleigh scattering. The extinction cross-section, $\sigma_{ext}=\sigma_{sca}+\sigma_{abs}$, requires a σ_{abs} that accounts for both aerosol and gaseous absorption, and the same combined σ_{sca}

in the direction described by θ and ϕ. Figure 3.1 defines these four angles for light incident at the origin of a 3-dimensional coordinate axis.

3.2 Correlated-κ Approximation

To calculate the solution to the radiative transfer equation (equation 3.2) requires information about the positions and strengths for each absorption line for each gas in the model atmosphere. Direct "line-by-line" calculations for the entire atmosphere require thousands of calculations for each iteration of the optimal estimation scheme, since for each gas in each layer at each temperature, the line strength and width must be computed. Since scattering calculations are already very time-intensive, avoiding line-by-line calculation times is a necessity. To accomplish this, without significantly reducing accuracy, a correlated-κ approximation is used, as described by Lacis and Oinas (1991). Without the correlated-κ approximation, calculation of the transmission of an atmospheric path in each layer of the model requires a sum over all absorption lines of all constituent gases over a sufficiently small dv to resolve the individual line shapes in the equation

$$\bar{\tau}(m) = \frac{1}{\Delta v} \int_{v_0}^{v_0+\Delta v} \exp\left(-m \sum_j \kappa_j(v)\right) \mathrm{d}v \tag{3.3}$$

for a frequency interval v_0 to $v_0+\Delta v$. Here m represents the total path amount in the layer (molecules·cm^{-2}) and $\kappa_j(v)$ is an absorption spectrum of the jth line expressed in cm^2·molecule^{-1}. The correlated-κ approximation can be employed to rewrite this transmission with much more efficiency, because the order in which the lines occur bears no impact on the result. To do this, only the fraction of the frequency domain, $f(\kappa)d\kappa$, which is occupied by all absorption coefficients between κ and $\kappa + d\kappa$ is

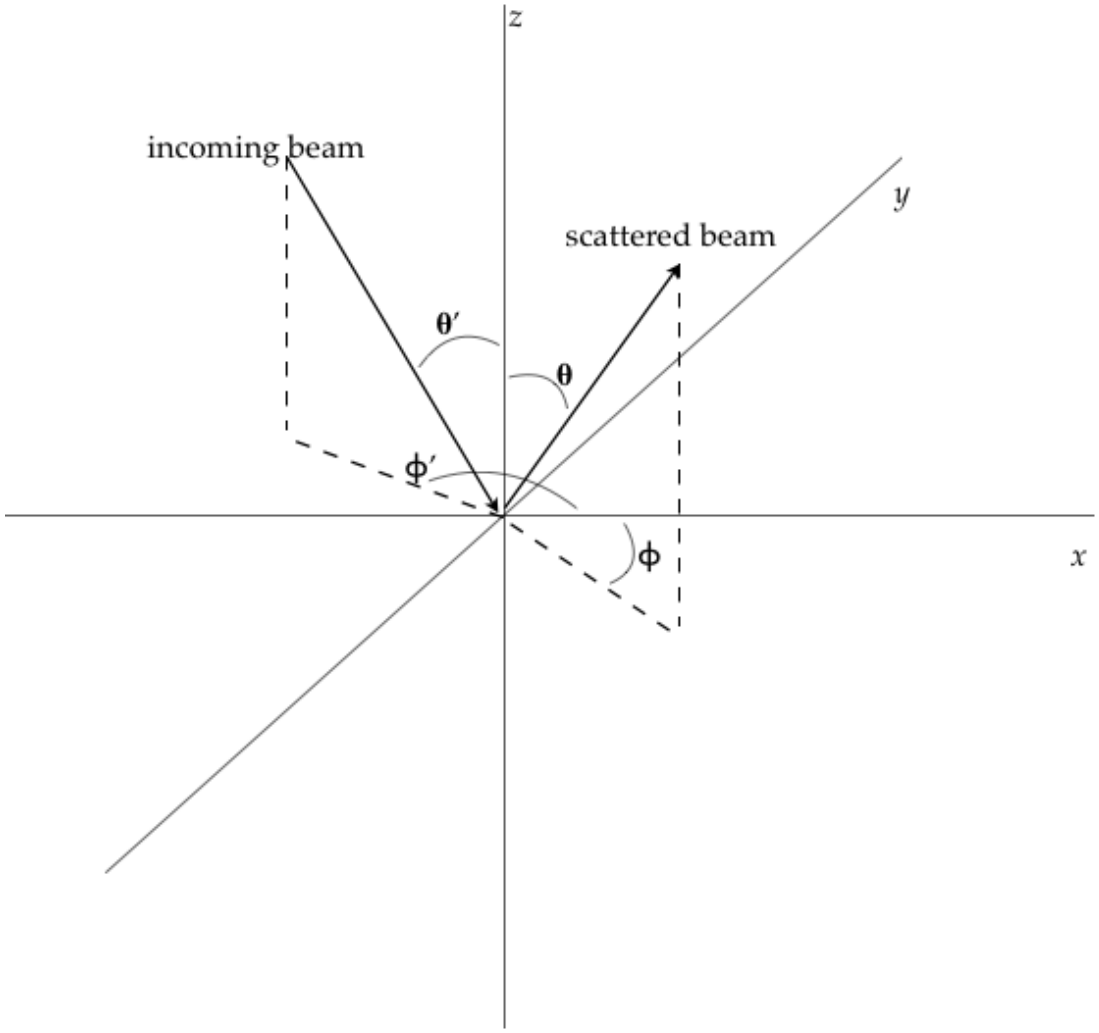

Figure 3.1: Angle definitions for incident and scattered light. The origin of the axis is the point at which light is scattering, and the axis system is defined so the z axis is normal to the surface of the planet at the origin and pointing away from the planet. Incident zenith angle, θ', and azimuth angle, ϕ', are defined for the incoming beam of light as shown in the diagram. θ and ϕ are defined in corresponding fashion for the scattered beam emitted from the atmosphere.

considered. Then, the transmission function is rewritten:

$$\bar{\tau}(m) = \int_0^\infty f(\kappa) e^{(-m\cdot\kappa)} d\kappa.$$

Recall that the order of occurrence of these absorption coefficients, κ, is arbitrary. This allows us to define a frequency distribution, $g(k)$ that is smooth, increasing, and single-valued:

$$g(k) = \int_0^k f(\kappa) d\kappa.$$

This function will have an inverse, $\kappa(g)$, referred to as the κ-distribution. Like $g(k)$, the κ-distribution is smooth and single-valued, therefore allowing us to rewrite the transmission function as

$$\bar{\tau}(m) = \int_0^1 e^{\left(-m\cdot\kappa(g)\right)} dg$$

or more appropriately for a numerical computation, in terms of the discrete summation

$$\bar{\tau}(m) = \sum_{i=1}^{N} e^{(-m\cdot\kappa_i)} \Delta g_i \tag{3.4}$$

where Δg_i is the weight of the ith quadrature in the summation. Because the integral in equation 3.4 is smooth, a much larger step size can be used, without much loss of accuracy, than for the rapidly varying integral in equation 3.3. NEMESIS uses a Gaussian quadrature scheme to choose between 10 and 20 quadrature points, and find a balance between sampling accuracy and computational efficiency.

κ-distribution tables are calculated, prior to model runs, for all the temperatures and pressures found on the planet. These homogeneous κ-distribution tables can be

applied to each model layer, each of which is considered to be homogeneous. The name "correlated−κ" arises from the fact that transmissions are generally well correlated in adjacent layers. This correlation allows us to add together the transmissions in each layer through use of the formula

$$\bar{\tau}_{tot} = \sum_{i=1}^{N} \exp\left(-\sum_{j=1}^{M} m_j \kappa_{ij} \right) \Delta g_i$$

where m_j is the path amount in the jth layer, and κ_{ij} is a κ-distribution in the ith quadrature point and the jth model layer. Given enough *homogeneous* model layers, a suitable result is obtained for the mean properties of the entire *inhomogeneous* atmosphere. Irwin et al. (2008) has found that comparison of correlated-κ results with more accurate line-by-line results agree within 5%. This is acceptable given that uncertainties in gas absorption data and spectral measurements are often of a similar magnitude. Computational time is drastically reduced, as each gas requires between 10 and 20 distribution calculations, not thousands as in the line-by-line method.

Chapter 4

Uranus from IRTF SpeX Observations

Remember that all models are wrong; the practical question is how wrong do they have to be to not be useful.

— George E. P. Box,
Empirical Model-Building and Response Surfaces

This chapter explores the analysis of Uranus that was completed with data from SpeX at the IRTF (see chapter 2). The results of this analysis were subsequently published in Icarus (Tice et al., 2013). Section 4.1 explores the various model atmospheres tested, describing their relative strengths and weaknesses. Section 4.2 describes the specific details of the model that was selected to use for analysis, including the retrieved physical parameters for the two clouds in the model and the optical properties associated with the constituent scattering particles. Finally, section 4.3 provides a discussion of latitudinal methane variability on Uranus, including results from two independent methods of study that were employed, both aimed at disentangling latitudinal variations in methane from cloud variations in the upper troposphere.

4.1 Building and Testing Model Atmospheres

This section is divided into two subsections. The first, subsection 4.1.1, outlines some general assumptions and model parameters, while subsection 4.1.2 goes into the specifics of the various models that were tested, providing a justification of the two-cloud parameterised model as the final choice for use in analysis.

4.1.1 Preliminaries

Before choosing a model to describe the Uranian atmosphere, a few issues needed consideration so that the NEMESIS retrievals would yield meaningful results. The first of these considerations was noted in section 2.2.1. Each pixel of IRTF data covered a relatively large latitudinal range of the planet, and thus a range of viewing and lighting geometries were represented in each single data pixel. In order to account for this, the method detailed in Irwin et al. (2009) was followed, in which all model calculations were made and averaged out at two zenith angles for any given pixel, in order to balance computational time with geometric accuracy. To accomplish this, the weighted distribution of five zenith angles in each pixel, as predefined in the five-angle quadrature scheme, were first obtained. Though any zenith angle could be used through interpolation between quadrature points, points were always chosen to match those in the quadrature scheme, in order to reduce interpolation error and computational expense. The weights of the two most significant quadrature angles were chosen for analysis, with their weights scaled to represent the total fraction of the disk of Uranus within the given pixel. For all pixels away from the limb and with no contribution from off-planet space, the total of the two weights was 1.0. Prior to publication of Irwin et al. (2009), the author compared results of this type to a few random cases in which all five zenith angles were used. No significant loss of accuracy was found to exist when using only two of the five angles (P. G. J. Irwin, personal

communication, 5 January 2015).

As mentioned in section 3.2, band coefficients for methane, the primary absorber in the Uranian atmosphere, were needed to calculate correlated-κ tables. Band models were based on those used in Irwin et al. (2006), as revised for consistency with other data in Karkoschka and Tomasko (2010) following the method of Irwin et al. (1996). κ-distributions used throughout sections 4.1.2 and 4.2 were sampled every 0.002 μm, and SpeX data was smoothed with a triangular instrument function and resampled to this same value (see section 2.1.1). The choice of sampling at 0.002 μm was made so that all regions of the spectrum would be considered equally given an even spacing of points across the entire spectrum. In this way, reasonable computational times were achieved for the time-consuming scattering calculations, while simultaneously ensuring that model fits would agree equally well with the entire, wide range of the IR spectrum over which our data lie. This resampling prevented the raw sampling rate of the data, which increases with decreasing wavelengths, to place more weight on lower wavelength regions of the spectrum, at the possible expense of the fit at longer wavelengths.

The only other absorbers in Uranus' atmosphere in the near-IR are collision-induced H_2-H_2 and H_2-He, which were modelled using the coefficients of Borysow (1991, 1992); Borysow et al. (2000); Zheng and Borysow (1995). An equilibrium ratio of ortho/para H_2 at all pressures and latitudes was assumed (Conrath et al., 1998; Fouchet et al., 2003). For all retrievals in this section, the latitudinally-invariant methane profile was fixed to a deep abundance of 1.6%, gradually reducing above this deep abundance following a 30% relative humidity curve, as in Irwin et al. (2009, 2010). See section 4.3 for further discussion of methane abundance in the Uranian atmosphere.

In addition to observational errors mentioned in section 2.1.1, additional "forward-modelling errors" were considered during the retrieval process to account

for systematic inaccuracies in our model. In general, when retrieving a model atmosphere, model characteristics are imposed such that the atmosphere suggested has a high degree of "physical plausibility". To do this, it is required that retrieved clouds, temperatures, and gas profiles smoothly vary, or that these quantities are parameterised to achieve the same affect. Of course in reality, the clouds would never follow a truly perfect, parameterised profile, and thus a systematic error is introduced. To produce a spectrum of forward-modelling errors, an equatorial cloud profile is retrieved in which the model is constructed to fit the data as well as possible, without any of the constraints of "smooth variation" mentioned above. For example, if the best-fit is achieved with a cloud that repeatedly jumps back and forth between greatly different opacities in each layer of the model, or a temperature profile that has large jumps between layers,the result would normally be disregarded, labelling it not physically plausible. Instead, the difference between the spectrum calculated with this ill-conditioned profile and the measured spectrum at the equator is smoothed, and this smoothed difference is considered to be the "forward-modelling error". This additional error value serves to include in the retrieval process a consideration for uncertainties introduced through cloud parameterisation. This method of assigning errors is a rough one at best, but it does serve as a reasonable proxy for those errors, since they are impossible to empirically determine. The relative magnitude of the forward modelling and observational error varied widely across the spectrum, because the observational error was relatively constant across the spectrum, while the parameterisation forward modelling error was greatest when the reflectance values were greatest, a natural result of the method for determining this error, as just described. On average, however, the forward modelling error was about an order of magnitude greater than the observational error, reflecting the high signal-to-noise of the observations.

The final consideration was how to assign optical properties to the cloud particles

in this and subsequent models, since the exact molecular composition of the clouds is unknown. Due to the unknown nature of the cloud particles, several assumptions were made which effectively parameterised the model particles in the simplest way possible, thus allowing analysis to infer spectral properties of the particles directly from the observational data, and ensuring that no unnecessary complexity was included in the model. To calculate a realistic curve of wavelength-dependent scattering cross-sections for the cloud particles, the same method employed in Irwin et al. (2009, 2010) was used. Namely, the cross-sections was calculated by first assuming that the particles were spherical and satisfied Mie theory given an assumed refractive index of $n = 1.4 + 0i$. This refractive index was arbitrarily assumed, but lies in the general region of very cold methane ($n \approx 1.3$, Brunetto et al. 2008; Satorre et al. 2008) and ammonia ($n \approx 1.4$, Martonchik et al. 1984) ices. The sphericity assumption is a good first-order approximation for randomly oriented ice particles, which the particles in both clouds are likely to be (Signorell and Jetzki, 2007). Once wavelength-dependent cross-sections were determined for these Mie-satisfying-particles, which were assumed to have a modified-gamma size distribution (arbitrary variances were assumed to be $\beta_{TC} = 0.05$ and $\beta_{UH} = 0.10$), sphericity stipulation was relaxed by using a wavelength-independent Henyey-Greenstein phase function to model the phase function, thereby allowing for the possibility of particle populations that might not be spherical. For a full discussion of the specific Henyey-Greenstein parameters and single-scattering albedos selected, see section 4.2.

4.1.2 Two-Cloud Parameterised Model

After the data reduction was complete (chapter 2), the data were analysed as described in chapter 3. In short, a model would be created that was capable of reproducing the reflected sunlight spectrum of the Uranus data, and use the NEMESIS retrieval tool to optimally estimate the values for the variables in this model. Having

dealt with viewing and lighting geometries, selection of absorber and temperature data, uncertainty values, and cloud scattering properties, it was required to choose a method of modelling the clouds and hazes in the atmosphere that would best suit the data.

A large number of published models existed, though all of them, as discussed more fully in the Introduction, covered different latitude regions, different observational dates, and most importantly different spectral ranges than data from this study. Despite the many differences, it must be determined if any of these previously published models would fit the new data. Ultimately, it was determined that the needs of the new data would best be met by using a new model containing two parameterised cloud layers. It was also determined that none of the previous models would prove useful for application here. This section details the tests that were performed with the previously published models, why they were ruled out, and how the choice of the "parameterised two-cloud" model was arrived at.

Table 4.1 summarises the various models tested from previously published works, as well as the models developed here and ultimately chose to employ. First, attempts to fit a single, continuous cloud model based on results from Irwin et al. (2009, 2010) are discussed. Irwin's hydrogen, helium, methane, and temperature profiles were employed. Irwin's method of modelling the scattering phase function of the cloud particles with a single Henyey-Greenstein approximation and incorporating a wavelength dependent single-scattering albedo was also utilised (see section 4.2 for further details). In agreement with Irwin's conclusions, good agreement was found for spectral fits between 1.0 and 1.8 μm. NEMESIS retrievals of continuous, vertical cloud profiles based on this model suggested a vertical cloud structure characterised by an optically thick, vertically thin cloud deck between 2 and 3 bar, with poorly-constrained evidence of an additional extended haze layer at pressures less than 1.0 bar.

Table 4.1: Description of free and fixed parameters in each retrieval type discussed. 'Free' indicates a free retrieved parameter, while 'SF' means a scaling factor is retrieved to adjust the *a priori* value. If a value is listed in the table, this fixed value is used at all wavelengths, while a '-' indicates a value that does not exist in the given model. In the first three models shown, hydrogen, helium, and temperature profiles are fixed to values used by Irwin et al. (2009, 2010). For the latter two (Sromovsky-based) models, the reanalysed profiles from Sromovsky et al. (2011) were used instead. In every case, ortho/para H_2 ratios are assumed to be at equilibrium at all pressures and latitudes, and all particles scatter according to a Henyey-Greenstein phase function with a fixed $g = 0.7$ asymmetry parameter and wavelength-dependent single-scattering albedos and scattering cross-sections. All free parameters are simultaneously retrieved, and a χ^2/n_y value is calculated to reflect goodness-of-model-fit.

Model	CH_4 Deep Abund.	CH_4 Rel. Hum.	Total Opacity				Fractional Scale Height				Base Pressure (mbar)		
			CH_4 Cond. Cld.	Trop. Cld.	Upp. Haze	Haze 2	CH_4 Cond. Cld.	Trop. Cld.	Upp. Haze	Haze 2	Trop. Cld.	Upp. Haze	Haze 2
Preferred (Parameterised) Two-Cloud Model	1.6%	30%	-	Free	Free	-	-	Free	Free	-	Free	1000	-
Preferred Methane / Two-Cloud Model	SF	SF	-	Free	Free	-	-	Free	Free	-	Free	1000	-
Irwin et al. (2009, 2010) Continuous Single-Cloud Model	1.6%	30%	(single, 39-layer continuous-cloud profile is retrieved)										
Sromovsky et al. (2011) Three-Cloud Model	Free	30%	Free	Free	Free	-	0.05	0.05	1.0	-	Free	900	-
Sromovsky et al. (2011) Four-Cloud Model	Free	30%	Free	Free	Free	Free	0.05	0.05	0.5	0.5	Free	900	100

This model, however, produced poor fits shortward of 1.0 μm, particularly in the methane absorption bands at approximately 0.9 and 1.0 μm. It is in this region where the cloud retrieval is most sensitive to hazes due to relatively weak methane absorption when compared with collision-induced hydrogen absorption (see section 4.3 for a full discussion). Further adjustment of *a priori* values and scattering particle properties resulted in inconsistent results, which in general exhibited under-constraint of the cloud retrieval, model fits characterised by χ^2/n_y values of no better than ~ 25 ($\chi^2/n_y \lesssim 1$ is expected for satisfactory fits), or both (see figure 4.1, dash-dotted line).

In an attempt to improve the fit shortward of 1.0 μm, a second, continuous cloud layer was added to the Irwin model to provide the necessary reflectance in the 0.9 and 1.0 μm methane absorption bands, where reflectance originated in regions of the atmosphere higher in altitude than the deep cloud layer. Forward models indicated that this discrepancy could be corrected by adding an optically thin haze ($\tau \leq 0.03$) containing smaller particles and characterised by a larger vertical extent (on the order of one atmospheric scale height) than retrieved in previous models.The original cloud layer was constrained to lie at pressures greater than 1.0 bar, while the new haze particles were constrained above 1.0 bar. This second cloud layer, while it did at times seem to improve the fit, only exacerbated the problem of under-constraint, and rendered the results inconsistent and inconclusive. In short, efforts with an Irwin-like continuous cloud model gave us two insights: at least two distinct clouds would probably be required in the final successful model, and that the available data was not sufficiently spectrally resolved to constrain two, continuous clouds.

To address the under-constraint of the continuous cloud retrievals, this continuous cloud model was exchanged with a parameterised representation.These two parameterised clouds will subsequently be referred to as the tropospheric cloud (TC) and upper haze (UH). As shown in Table 4.1, for both of these cloud layers, three parameters are retrieved: total opacity, cloud base pressure, and fractional scale height

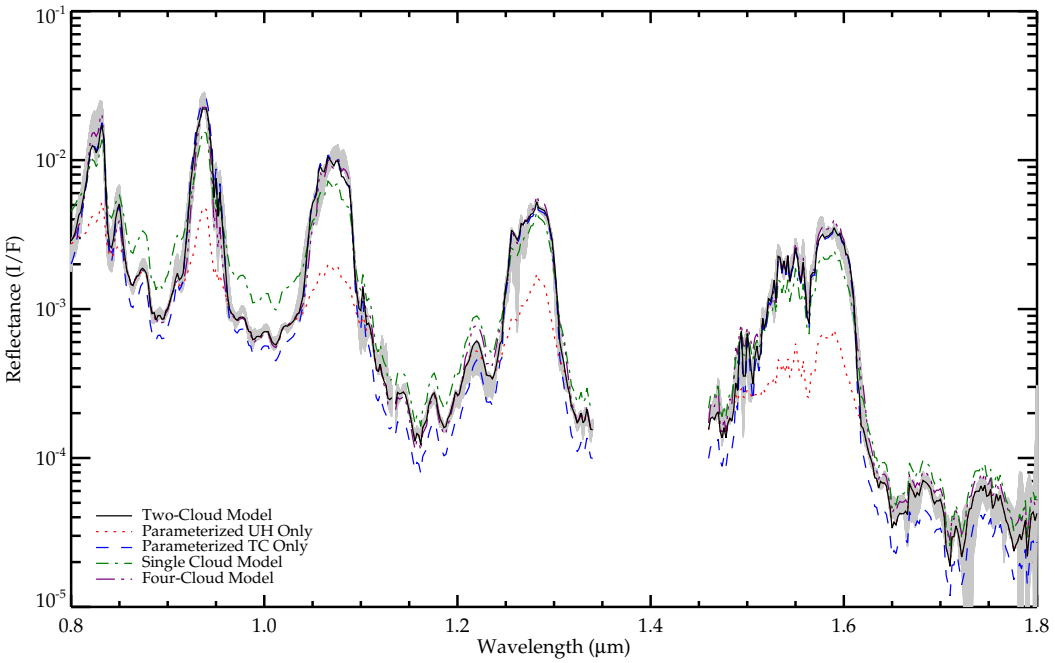

Figure 4.1: Sample retrievals of 1) the two-cloud parameterised model (solid line), 2) the Irwin et al. (2009, 2010) single-cloud model (dash-dotted), and 3) the Sromovsky et al. (2011) four-cloud model (dash-triple-dotted) for comparative purposes. Gray region indicates observational data and error, as in figure 2.11, plus the added "forward-modelling error" for systematic uncertainties in the absorption line data. See table 4.1 for a summary of each of these retrievals. Model (1) produces the best overall fit to data ($\chi^2/n_y = 1.0$). The retrieved cloud profile in model (2) is quite poorly-constrained, and the accuracy of the model fit decreases with decreasing wavelength ($\chi^2/n_y = 28$). Model (3) produces a fit ($\chi^2/n_y = 2.3$) nearly equalling the quality of model (1), but struggled to provide equally good fits on both sides of 1.0 μm. Model (3) also provides poorer constraint of retrieved parameters than model (1) does. In addition to the retrievals shown, the figure also shows two forward models based on cloud retrieval (1), but where only the upper haze layer is included (dotted) and only the tropospheric cloud layer is included (dashed) in the model. Note that the upper haze (UH) alone successfully models the spectrum in regions of high methane absorption, while the tropospheric cloud (TC) alone successfully produces the spectrum at methane windows; neither cloud can alone produce the required spectrum at all wavelengths. All retrievals and models are for centre-of-disc observations at $\sim 8°$ N latitude, the latitude with the lowest airmass, and thus the clearest view into the deep atmosphere.

(FSH). For ease of comparison with other publications, the total opacity at 1.6 μm is presented throughout this chapter, rather than particle density, which is the retrieved quantity. Total opacity is a wavelength-dependent quantity derived from multiplying the wavelength-dependent extinction cross-section by the retrieved particle density. The FSH is defined as the relative rate of decreasing particle density as compared with the scale height of the atmosphere, i.e. a cloud of FSH = 1.0 decreases from its maximum, or base level, opacity, τ_{max}, to τ_{max}/e in one atmospheric scale height. Accordingly, a cloud of FSH < 1.0 decreases to τ_{max}/e in a shorter vertical extent than one atmospheric scale height, while a cloud of FSH > 1.0 requires more than one full atmospheric scale height to thin to τ_{max}/e. Because the TC deck was shown to be vertically thin in continuous cloud retrievals, as well as the results in Irwin et al. (2010, 2011a, 2012a), parameterised characterisation of the cloud is quite accurate when FSHs are very low. Because the upper hazes are likely the product of photolysis of trace gases in the upper atmosphere, which subsequently 'drizzle' down through the stratosphere, the parameterised model is presumably accurate to first order because it will be thickest at the base and then gradually thin with decreasing pressure. Using this parameterised model rather than continuous cloud profiles greatly reduces the number of model variables, reducing under-constraint of the model.

Implementation of this two-cloud model represented a significant improvement to the results. Retrieving six free parameters, rather than 78, provided much better constraint of the results. The addition of a second cloud layer, with different scattering properties than those of the first cloud, also provided a much better fit to observed spectra. Figure 4.1 provides a visual justification of adding this second cloud layer. The dotted and dashed lines in the figure show two forward model spectra based on the retrieval parameterisations for two clouds. The dotted spectrum shows a forward model for a case where only the UH layer existed, and it can be seen that it fits the data well only in regions of strong methane absorption. The dashed spec-

trum shows a forward model containing the TC but no UH. This model fits the data well only in regions of weak methane absorption. These two spectra make it apparent that neither cloud was able to independently reproduce accurate radiances for all regions of the spectrum. The solid line in the figure contains an equatorial example of the preferred, parameterised two-cloud retrieval upon which the forward models are based, and is characterised by a χ^2/n_y value of 1.0.

As a final verification of the validity of the two-cloud model, transmission plots generated for a haze-filled atmosphere (UH without TC) indicate ample light transmission to well below the proposed TC deck in the upper troposphere (figure 4.2). The transmission plot indicates that two-cloud parameterised retrievals should be sensitive to all three cloud parameters in the UH (since nearly all near-infrared sunlight passes through this layer completely), as well as, at the very least, being capable of setting a lower limit for TC opacity, and an accurate retrieval of cloud-top pressure (since this cloud is sufficiently thick to block nearly all near-infrared sunlight when added to the model).

Despite now having a model that seemed to fit the data well, it was also needed to test parameterised cloud models that utilised the recent reanalysis of Hubble Space Telescope Imaging Spectrograph (STIS) data of to see if they offered any significant improvement to the fit (Karkoschka and Tomasko, 2009; Sromovsky et al., 2011). This reanalysis produced revised temperature, hydrogen, helium, and methane profiles, and notably added the predicted methane condensation cloud to the atmosphere. Optical properties were modelled quite differently as well. The notable differences, when compared with the models already discussed, are that cloud particles are characterised by empirically-determined double Henyey-Greenstein phase functions that vary with wavelength, refractive indices with a wavelength-dependent imaginary component, and single-scattering albedos that are relatively constant

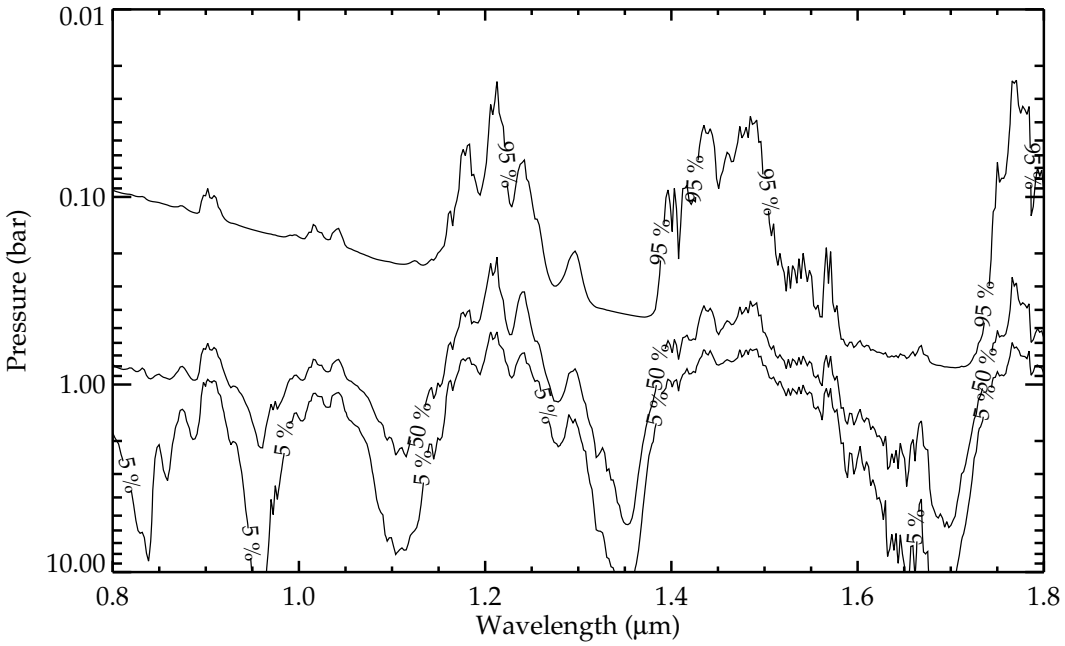

Figure 4.2: Light transmission as a function of wavelength through a simplified Uranian model atmosphere containing H_2, He, CH_4 and an optically thin, parameterised upper haze layer (but no TC). The haze was modelled with a base pressure of 1.0 bar and a total opacity of 0.03. Transmission levels of 95%, 50%, and 5% are shown. Since most light, in the absence of the optically thick TC, can penetrate well below the 1-bar level, the two-cloud parameterised model is sensitive to all parameters in the UH as well as cloud-top height and a lower limit for opacity in the TC.

when extrapolated into the 0.8 – 1.8 μm range[1]. This model, like those previously discussed, used particle cross-sections that varied with wavelength and assumed the real part of the refractive index to be 1.4. In the first variation of these Karkoschka/Sromovsky tests, a three-cloud model was used that included the TC at 2 – 3 bars, a methane condensation cloud at the ∼ 1-bar condensation level, and an UH extending upward from 900 mbar, each with unique scattering properties found in the Karkoschka/Sromovsky model. In the second variation, a four-cloud model was used that was identical to the three-cloud version except that the UH was broken into a stratospheric haze from 10 – 100 mbar and a tropospheric haze from 100 – 900 mbar, again with unique scattering properties for each cloud layer based on the original models. In both cases, models fit the observed spectrum about as well as the two-cloud parameterised model ($\chi^2/n_y \approx 2.4$, see dash-triple-dotted line, figure 4.1). The addition of several more degrees of freedom, however, introduced several new correlations between various parameters in the model. These correlations ultimately prevented these retrievals from providing as much parameter constraint as the parameterised two-cloud model provided. Because of these new correlations, the added complexity of the model itself, and the lack of any improvement of the fit to data, it was decided not to incorporate the Sromovsky models into this analysis.

An additional consideration that caused us to favour the parameterised two-cloud model over either of the Sromovsky-like models was that it was found to be difficult to simultaneously provide good fits to the spectrum above and below 1.0 μm while also choosing parameters that smoothly join the model used in Karkoschka and Tomasko (2009) and Sromovsky et al. (2011), which ends just below 1.0 μm. On the contrary, when using the new two-cloud parameterised model it was found that it was possible to provide a good fit across the entire spectral range, while simulta-

[1]It should be noted that the constancy of the single-scattering albedo, $\bar{\omega}$, is most likely an artefact of the mathematical expression employed by Karkoschka and Sromovsky. They do not claim that their expression for $\bar{\omega}$ applies in the 0.8 – 1.8 μm range under examination here, which would be surprising given the wavelength-dependent imaginary part of the refractive index in their optical model.

neously using optical properties and characterisations that joined smoothly those values found in Irwin et al. (2007, 2009, 2010, 2011a, 2012a) at areas of spectrally-overlapping data.

In reality, of course any model selected will provide an imperfect representation of the cloud layers, which are both presumably inhomogeneous mixtures of a dominant species heavily 'polluted' by photochemically-produced hydrocarbons drizzling down from the upper atmosphere. Given this imperfect nature of all the models tested,it was decided that the simplest model that fits the data should be employed, rather than imposing more complex solutions than are constrained by the data. The parameterised two-cloud model, which was ultimately chosen, met this "simplest solution" criteria, as well as providing the best χ^2/n_y values, minimised correlations between model parameters. It also allowed us to achieve well-constrained retrievals of cloud parameters which joined smoothly with those in previous studies at other spectral regions.

4.2 Final Retrieved Cloud Model

This section is also divided into two subsections, the first of which details the optical properties that were fixed in the model, and the justifications for those choices (subsection 4.2.1). Subsection 4.2.2 then discusses the physical properties that were retrieved for the cloud layers in the model.

4.2.1 Optical Properties

Once a parameterised, two-cloud model was chosen, retrievals were performed with various optical properties imposed to see which combinations of parameters would best fit the observational data. Ultimately, it was found that in both clouds, an approximation of the phase function using a single Henyey-Greenstein phase function

with an asymmetry parameter of $g = 0.7$ at all wavelengths fit the data well, just as found in Irwin et al. (2010, 2011a); Sromovsky and Fry (2007). The single Henyey-Greenstein function was chosen in favour of the double Henyey-Greenstein, or some other wavelength-dependent phase function, because of the lack of knowledge about the physical makeup of the clouds in both layers. It was found, as previously reported in Irwin et al. (2010, 2011a), that only Henyey-Greenstein phase functions that corresponded to highly forward-scattering particles ($g > 0$) allowed sufficient light through the haze to reach the main cloud deck, and that a haze composed of isotropic scatterers could not accurately reproduce the observed spectrum. As shown by Irwin et al. (2010), either the asymmetry parameter or the single-scattering albedo can be modified to produce the needed changes with wavelength, but here, as in that study, it was decided to leave the asymmetry parameter fixed and only vary the albedo.

With the asymmetry parameter fixed, the model spectra were strongly dependent upon the single-scattering albedos of the two types of cloud particles. Through a series of parameterised, two-cloud retrievals that employed different fixed albedo values, it became very clear that a strong wavelength dependance was needed in the particle model. The TC single-scattering albedo dramatically affected the height of the five reflectance peaks, and there was no wavelength-independent albedo value that produced accurate peak brightnesses everywhere. Similarly, no invariant UH albedo, which produced small changes to all wavelengths in the spectrum, was found that allowed a cloud retrieval to provide optimum fit across the entire spectrum. Because of this, wavelength dependent single-scattering albedos were adopted for both clouds, as shown in figure 4.3. For the UH particles, albedos were found of $\bar{\omega} = 1.0$, with the exception of a sharp drop between 0.8 and 1.1 μm that reaches a minimum of $\bar{\omega} = 0.6$ at 1.0 μm. In the TC deck a single-scattering albedo was found of $\bar{\omega} = 0.7$ that gradually increased below 1.4 μm until reaching $\bar{\omega} = 1.0$ at 1.0 μm. Figure 4.4 compares the model fit achieved with the preferred single-scattering albedos with

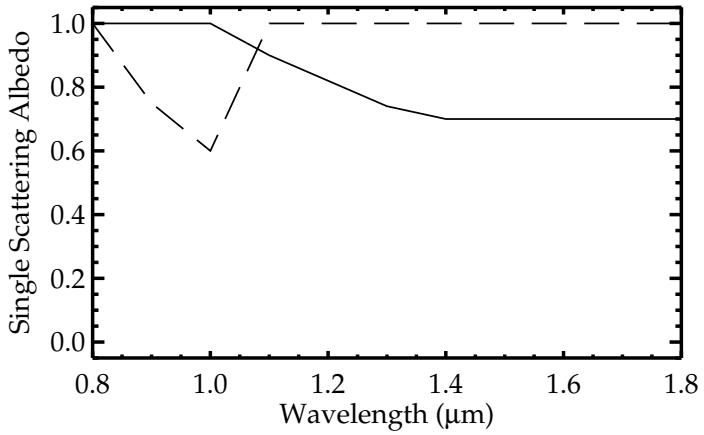

Figure 4.3: Single-scattering albedo as a function of wavelength for cloud particles in the TC (solid line) and UH (dotted line). The TC albedo must increase at shorter wavelengths to provide sufficient light penetration to deep clouds; the UH albedo must drop abruptly to reduce reflectance to within uncertainty of measurement at 1.0 μm methane absorption band (see figure 4.4).

two other cases: 1) where the UH particles albedo drop at 1.0 μm is omitted, and 2) where the TC particles albedo increase shortward of 1.4 μm is omitted.

The trend of increasing $\bar{\omega}$ as wavelength decreases for the TC deck was noted in Irwin et al. (2010), though the increase in that study did not begin until shortward of 1.2 μm, and their data extended only as low as 1.0 μm. The value of $\bar{\omega} = 0.7$ is slightly below the preferred values of $\bar{\omega} = 0.75$ found in Irwin et al. (2010, 2011a); Sromovsky and Fry (2007), a change that is counter-balanced by slight differences in cloud opacity in their models.

Recall (section 4.1.1) that the scattering particles in both cloud decks were modelled with an assumed refractive index of $n = 1.4+0i$, phase functions represented by single Henyey-Greenstein approximations, wavelength-dependent single-scattering albedos, and wavelength-dependent scattering cross-sections assuming a modified-gamma distribution of particle sizes. Given these assumptions, several parameterised, two-cloud retrievals were tested, representing a range of possible fixed par-

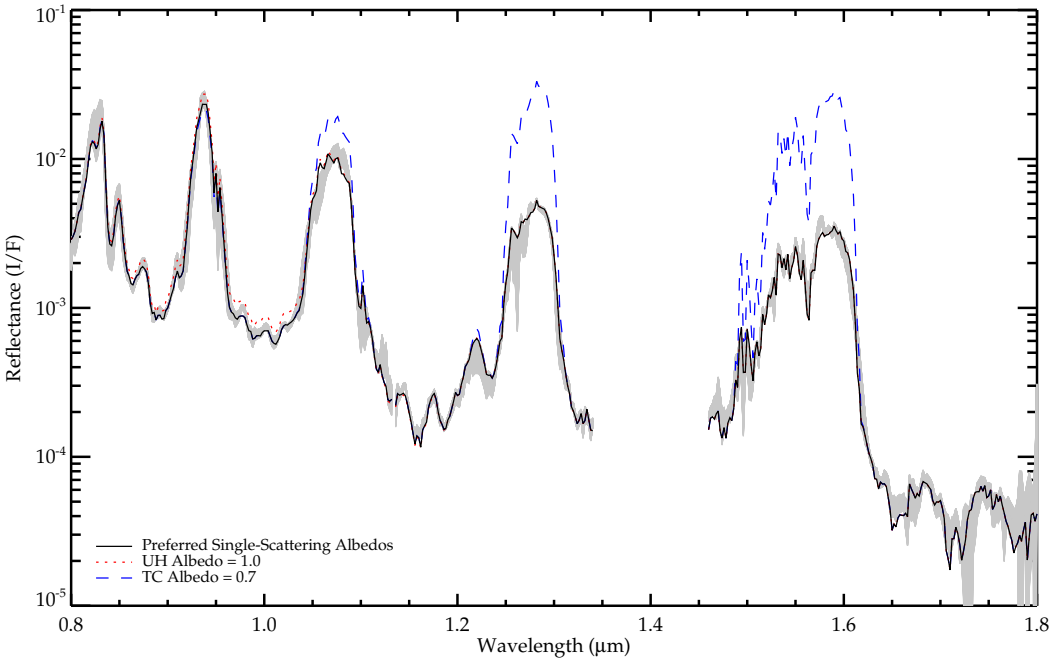

Figure 4.4: Model fit achieved at $\sim$ 8° N latitude) with the preferred single-scattering albedos compared with forward models of two other cases: 1) where the UH particles albedo drop at 1.0 μm is omitted, and 2) where the TC particles albedo increase shortward of 1.4 μm is omitted. The preferred model is shown in solid black; case (1) shown in dotted red; case (2) shown in dashed blue. The gray region indicates observational spectrum and both random and systematic errors. As the figure indicates, the TC albedo increase at short wavelengths is necessary to simultaneously fit all reflectance peaks. Without the TC increase at short wavelengths, the retrieval prefers a TC that is more optically thick, which produces reflectance peaks longward of 1.0 μm that are far too bright, as is seen clearly in the figure. A drop in the UH albedo serves as a proxy for some form of additional stratospheric absorption, and brings reflectance in the 1.0-μm methane window within the uncertainty range.

ticle sizes. In each test case, the retrieval algorithm chose different parameters for cloud opacity, base pressure, and fractional scale height in order to provide the best fit to the spectrum for the fixed particle size under consideration (and the associated scattering cross-sections). By locating the minimum χ^2/n_y value, which indicates the best-fitting model for this series of retrievals, a preference for particle size in both the TC and UH was determined, as shown in figure 4.5. The uncertainties associated with the locations of the χ^2/n_y minima, and hence the uncertainties of the preferred particle sizes, are taken by following the χ^2/n_y curve from the minima to a location where $\Delta(\chi^2/n_y) = 1/n_y$, representing an uncertainty region of 1σ.

For the TC, a particle radius of 1.35 μm was strongly preferred. This mean radius is slightly higher than 1 μm, the value suggested by Rages et al. (1991) for two latitudes in the southern hemisphere and Irwin et al. (2010, 2011a, 2012a) for the mid-latitudes and equatorial regions, but well below the Rages' upper limit of $r \ll 10$ μm. UH particles in this model were assumed to have mean radii of 0.10 μm. Figure 4.5 (lower) demonstrates the rationale for this choice, indicating that the ability of the retrieval algorithm to fit the observations was optimised for UH particle radii of 0.10 μm, though this value was not nearly as tightly constrained as the TC radii. This proposed radius is in agreement with Sromovsky et al. (2011), who cited a haze particle radius of 0.1 μm, and with the analysis of Pollack et al. (1987), who preferred a value of 0.13 ± 0.02 μm at 20°. The hazes in the former paper were thicker in the stratosphere, while in the latter paper they existed entirely in the stratosphere, near the upper edge of the proposed UH, which is vertically thicker and extends down to 1.0 bar. It is unclear whether the "UV-absorbing aerosols" mentioned in these papers could be the same particles detected here, albeit with a very different vertical distribution, or whether the two proposed particles represent distinct atmospheric species.

A series of parameterised two-cloud retrievals performed with various fixed-base

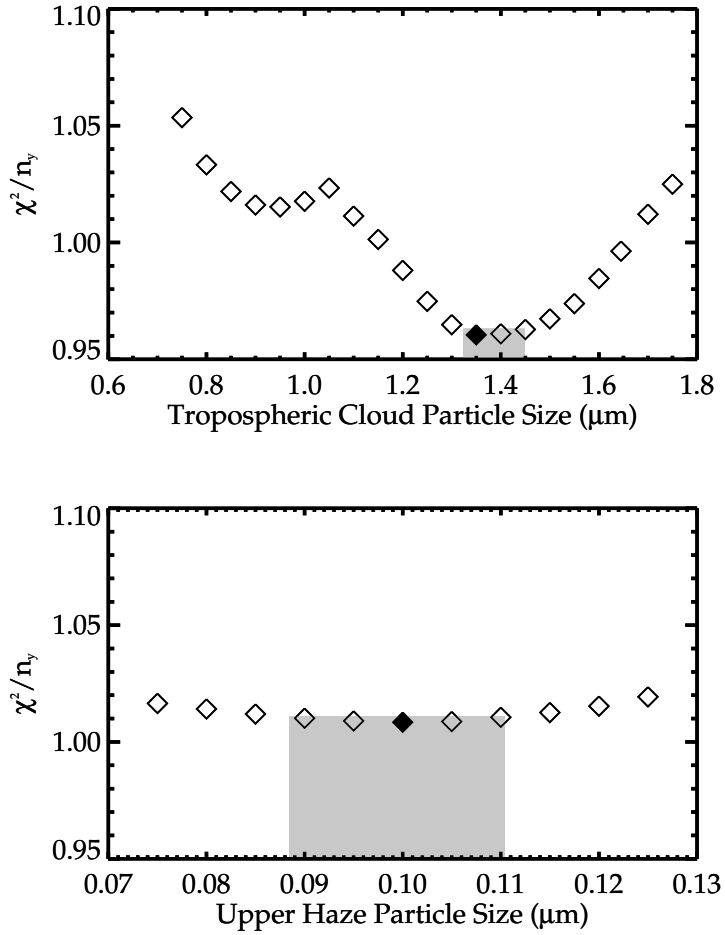

Figure 4.5: χ^2/n_y values for retrievals of two parameterised clouds for different assumed particle radii in the TC (upper) and UH (lower) layers. In both cases, the particle cross-sections have been calculated assuming the fixed mean radii shown in the figure and modified-gamma distributions of $\beta_{TC} = 0.05$ (upper panel) and $\beta_{UH} = 0.10$ (lower panel). In each retrieval shown, the five free parameters in the cloud model were allowed to vary without constraint to achieve the best possible fit (see table 4.1). The retrievals are based on centre-of-disc observations ($\sim 8^\circ$ N latitude). The figure demonstrates that this model strongly favours TC particles of $r = 1.35$ μm (upper) and a weaker preference for UH particles $r = 0.10$ μm (lower). The darkened plot symbol in each panel represents the preferred value (lowest χ^2/n_y), while gray regions of plot represent an uncertainty region of 1σ surrounding the optimal value.

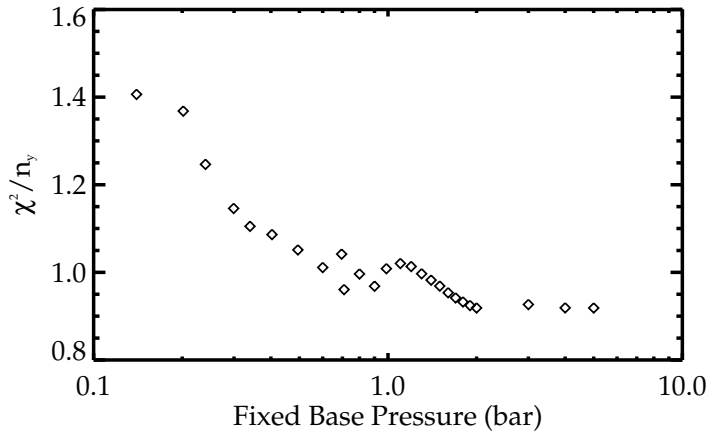

Figure 4.6: χ^2/n_y values for retrievals of two parameterised clouds in which the base pressure of the upper haze is constrained at various values between 0.1 and 5.0 bar. In each retrieval shown, the five free parameters in the cloud model were allowed to vary without constraint to achieve the best possible fit (see table 4.1). The retrievals are based on centre-of-disc observations at $\sim 8^\circ$ N latitude. The χ^2/n_y values of the fits dramatically improve as the haze base is lowered from the tropopause towards the top of the TC deck, where the values then remain relatively constant, with the spectrum being dominated by the much thicker TC rather than any remaining opacity of the UH. This figure clearly demonstrates that scattering effects from the haze extend well below the tropopause, and informed the decision to base analysis on an UH layer with a fixed-base pressure near the top of any TC opacity around 1.0 bar.

pressures for the UH informed the decision to fix the base pressure at 1.0 bar for all analysis here. The χ^2/n_y parameters of these retrievals are shown in figure 4.6. The general trend in the figure is that the quality of the model fit increases dramatically as the base of the haze moves deeper to higher pressures in the atmosphere, until it reaches the top of the TC, where the much thicker particle distribution in that cloud dominates the spectra. After reaching the TC, relatively little change occurs in the quality of the model fit, so it was decided to set the UH base pressure to 1.0 bar, which would fall just above the TC top for all subsequent cloud retrievals.

4.2.2 Physical Properties

Given the cloud particle assumptions detailed in section 4.2.1, the retrieved cloud parameters produce cloud profiles (figures 4.7 and 4.8) that are consistent with the cloud profiles retrieved by Irwin et al. (2010, 2011a, 2012a) using H-Band data from UKIRT and Gemini-N. The retrieved cloud parameters represent accurate model fits across the entire 0.8 – 1.8 μm data range, as indicated by the low χ^2/n_y values (figure 4.7, first panel). As in the Irwin papers, these retrievals show a TC top pressure that decreases when moving from the equator to the midlatitudes.

An example model fit, at ∼ 8° N latitude, is shown in figure 4.1 (solid line). All model spectra, like the example provided, fit the data well and were produced using the retrieved parameters of the two-cloud model previously described.

For all the final cloud retrievals detailed in figures 4.7 and 4.8, the UH base pressure at all latitudes was fixed at 1.0 bar, as discussed in section 4.2.1. The other five cloud parameters (total opacity in both clouds, FSH in both clouds, and TC base pressure) in the model were allowed to vary without constraint. Results were consistent, within error, for a range of *a priori* parameter values, demonstrating that the retrieved cloud parameters were not dependent upon specific *a priori* values.

Due to the optically thick nature of the TC, there was, as expected, a strong correlation between base altitude and fractional scale height in the TC. Due to this strong correlation in the TC parameters, comparable χ^2/n_y values could also be achieved with a wide range of fractional scale height and base altitude pairs, so long as a similar TC-top height was designated.

4.3 Latitudinal Methane Variability

Most areas of the near-infrared spectrum of ice giants are completely dominated by methane absorptions, leading to one of the most fundamental weaknesses in the un-

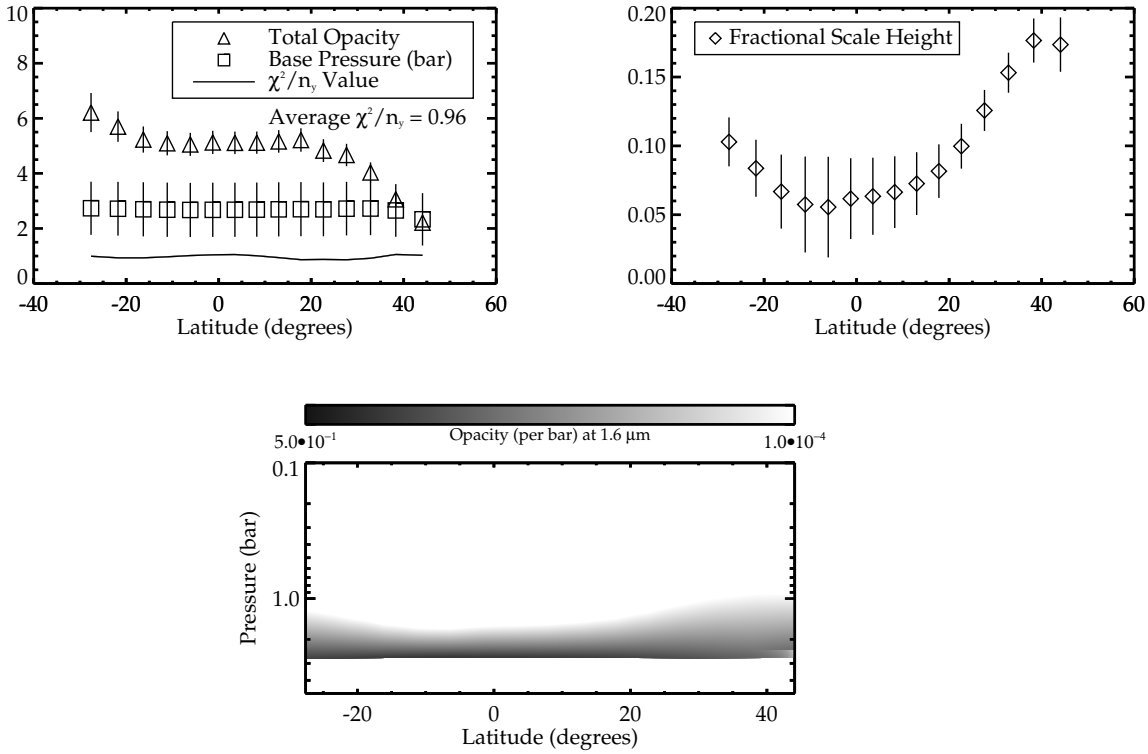

Figure 4.7: Parameterised two-cloud retrieval results for TC deck as a function of latitude. The upper panels show retrieved parameters and χ^2/n_y value; the lower panel shows latitudinal vertical cloud structure (in units of optical depth per bar at 1.6 μm) constructed from the retrieved parameters. The retrievals show that the fractional scale height (FSH) of the TC increased strongly when moving from the equator towards the midlatitudes, while the base pressure remained constant within error, indicating a cloud-top height that moved to lower pressure levels in the midlatitudes.

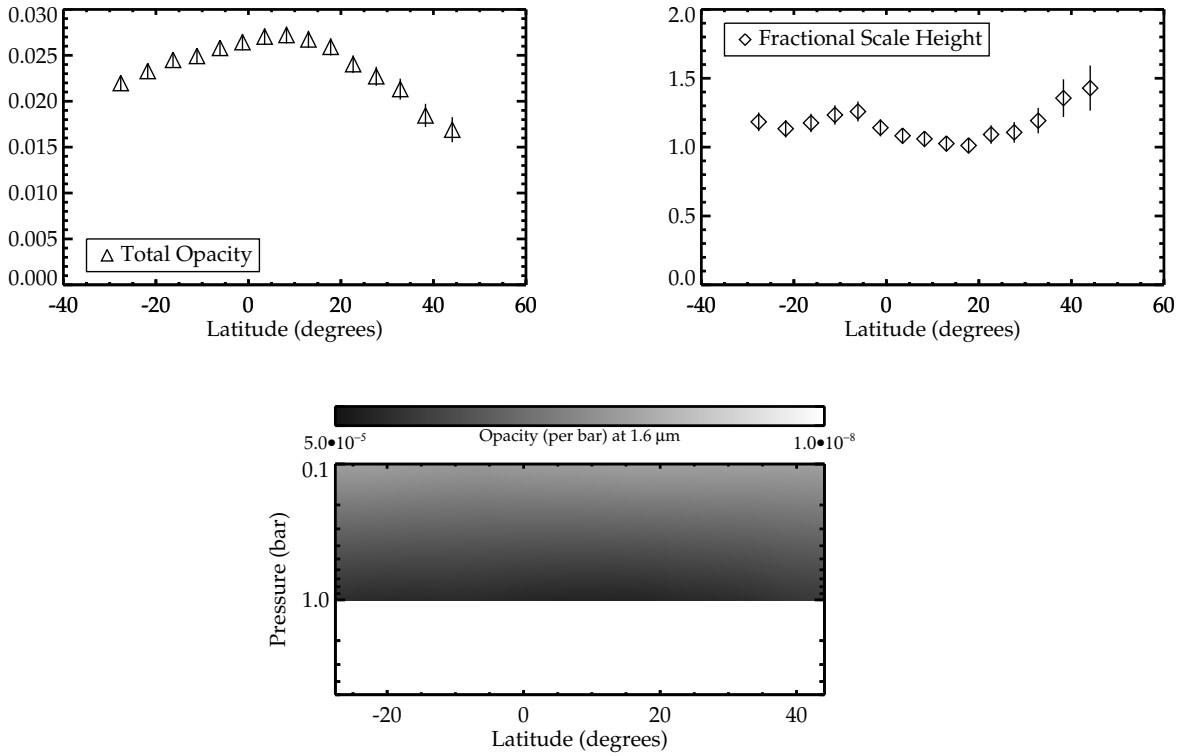

Figure 4.8: Parameterised two-cloud retrieval results for UH layer as a function of latitude. The upper panels show retrieved parameters; the lower panel shows latitudinal vertical cloud structure (in units of optical depth per bar at 1.6 μm) constructed from the retrieved parameters. The χ^2/n_y values at each latitude are found in the first panel of figure 4.7. The retrieval shows that the UH extends to roughly the same pressure at all latitudes, with a slight opacity maxima near 10° N.

derstanding of these planets. Pairing the spectral dominance of methane absorptions with temperatures cool enough to condense methane into solids, it is very difficult to determine if near-infrared spectral features are derived from changes in aerosol profiles and properties, or changes in methane abundance. As discussed in 1.1: An Overview of the Ice Giants, most previous studies of the ice giants were unable to study the likely possibility of latitudinal methane variability, instead fixing methane abundances in favour of analysis of the clouds in the upper atmosphere.

This section first verifies that the SpeX data is sensitive to methane abundances (section 4.3.1), and then explores the issue through two independent techniques. The first technique , an analysis of the reflectance of the upper atmosphere due to both collision-induced hydrogen absorption and methane absorption, comprises section 4.3.2. This section begins with a thorough description of the procedure used, because this subsection does not rely on the NEMESIS retrieval code as do all the other analysis sections of the thesis. The second technique employed in the methane study again employs NEMESIS retrievals, and chapter, 4.3.3 focuses on these results.

4.3.1 Sensitivity of Model and Data

To confirm that this model and data were sensitive to varying methane levels in the atmosphere, the procedure detailed in Irwin et al. (2012a) was followed, in which six fixed-methane profiles were shown, at three latitudes, to have a dramatic effect on retrieved cloud-top height. The six different methane profiles which were used in the Irwin study, and again here, represent deep methane mole fractions of 1.6 and 4.0%, each with three different relative humidity scenarios above the clouds. The first variation is a 30% relative humidity at all levels, the second is 30% relative humidity above the methane condensation level, and the third represents a 100% relative humidity everywhere. (The profile with a deep 1.6% mole fraction and 30% relative humidity at all levels corresponds to the fixed methane abundance used in sections 4.1 and 4.2).

Using these six profiles and comparable latitude regions as Irwin et al. (2012a), it was found that the cloud retrieval also produced TC altitudes that varied by more than 1.0 bar depending on the methane profile. Changes of this magnitude are more than sufficient to account for the changes in TC pressure retrieved for a fixed-methane case, such as that presented in section 4.1. This, in turn, suggests the need for a more refined treatment of methane profile in the model so that it can be attempted to disentangle the spectral effects of aerosol and methane variations.

In the I-Band (0.8 – 0.9 μm), SpeX has a finer grid spacing of spectral points since the spectral resolution of the instrument remains relatively constant as the wavelength decreases ($R = \lambda/\Delta\lambda = 1200$, see section 2.1.1). In order to improve the sensitivity of both the reflectance and retrieval analyses in this section, the raw data was resmoothed and resampled to a finer grid, as described in section 2.1.1. The data, as well as a new κ-table, were now sampled at a spacing of 0.2 nm. This provided a tenfold increase in the sampling rate of the I-Band when compared with the analysis of the full spectral range in sections 4.1 and 4.2. This improved resolution allowed us to make use of the full resolution of the I-Band data in order to best distinguish between spectral changes due to cloud opacity and those due to methane profile variations.

4.3.2 Reflectance Analysis at 825 nm

As demonstrated in Baines and Bergstralh (1986) and Karkoschka and Tomasko (2009), the methane-dominated spectrum of ice giants in the near-infrared has a unique H_2-H_2 absorption feature at 825 nm. Model absorption values were again obtained for this feature from Borysow (1991); Borysow et al. (2000); Zheng and Borysow (1995). In this region, this absorption of collision-induced hydrogen quadrupoles contributes as strongly to the spectrum as methane, providing an opportunity to distinguish between spectral features derived from methane absorption and spectral changes due to vertical shifts in the height of the cloud deck. The hydrogen absorp-

tion feature can be seen clearly in figure 4.9, which shows transmission from space to the 2 bar level (just above the proposed TC deck) through two model atmospheres in which the only absorbers are methane (solid line) and hydrogen (dotted line).

For the reflectance analysis, 81 spectral points between 818 and 834 nm were confirmed to have approximately the same reflectance, despite having methane and collision-induced H_2 absorption coefficients that varied greatly. The 81 spectral locations were divided into four categories based on which absorptions (H_2 or CH_4) were dominant in the particular spectral location. To make this determination, ratios were calculated between hydrogen and methane absorptions. Based on the value of these ratios, each spectral location was placed into one of four categories. The four shades of grey in the background of figure 4.9, and the corresponding bins shown in figure 4.10, indicate which spectral locations were chosen for which categories. The same terminology was adopted as that chosen by Karkoschka and Tomasko (2009), categorising the points into groups where "only methane" absorptions were important, where "methane and hydrogen" absorptions were equally important, and where absorptions were contributed by "mostly methane" or "mostly hydrogen". These category names, inherited directly from the earlier work, are not terribly accurate qualitative descriptions of relative absorber strength, but do make comparisons with the earlier paper more straightforward. Since the average reflectance of each of these four groups is similar, comparison of the groups allows one to distinguish between latitudinal reflectance trends due to methane variability and those trends due to changes in cloud opacity. If a latitudinal trend is observed in both methane-dominated and hydrogen-dominated curves, it can be attributed to cloud opacity; but if a trend is observed in methane-dominated curves alone, and is not evident in hydrogen-dominated curves, the trend can be attributed to a change in latitudinal methane profile.

To guarantee that results were valid in the entire Uranian upper atmosphere, the

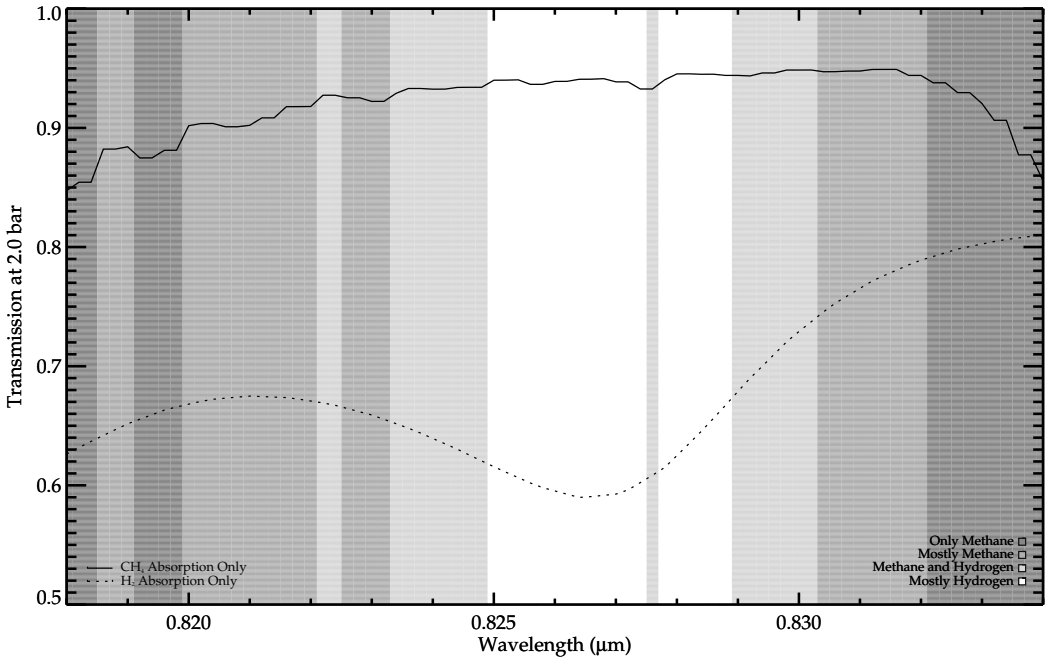

Figure 4.9: Example of the reflectance study technique. For this reflectance study, each of the 81 spectral data points between 0.818 μm and 0.834 μm are of approximately uniform intensity , and are grouped into one of four categories based on the relative strengths of methane and hydrogen absorptions (see figure 4.10 for more information). This plot shows transmission from space to the 2 bar level through a Uranus-like atmosphere in which the only absorbers are methane or hydrogen, as indicated in the left legend. The collision-induced hydrogen quadrupole absorption feature can be seen, centred near 827 nm. The four shades of grey in the background of the figure indicate the points chosen for each category, corresponding to the bins shown in figure 4.10, and listed in the lower right legend. Given the relative strength of the hydrogen absorption in this methane window, difference in the shape of reflectance curves of different relative absorber strengths allow any spectral variations due to cloud opacity to be distinguished from those due to methane absorption.

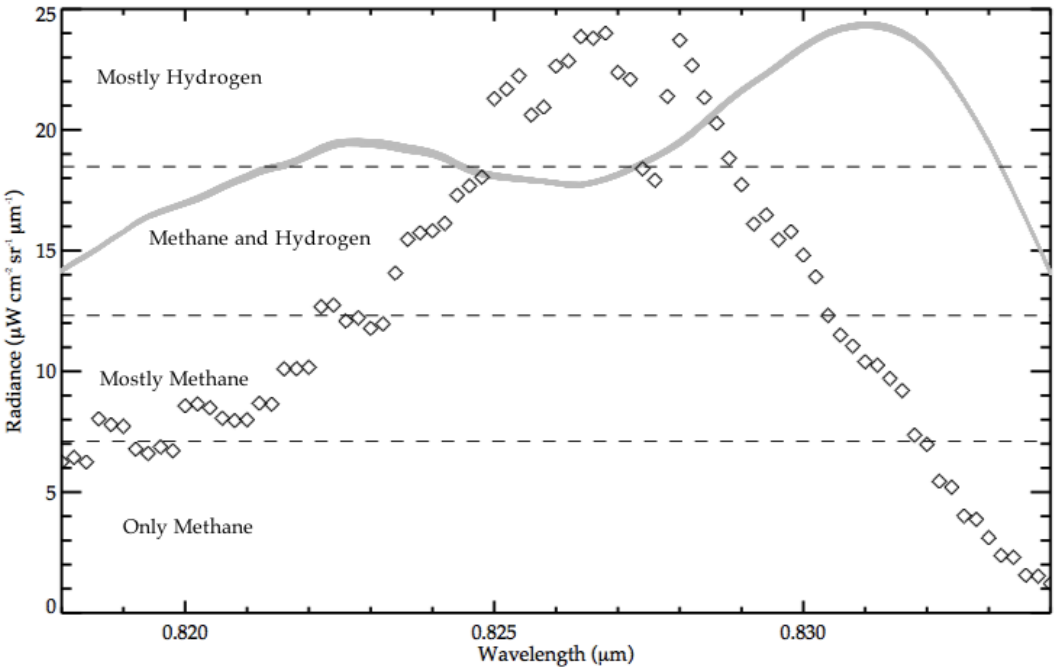

Figure 4.10: Example of the reflectance study technique. For this reflectance study, each of the 81 spectral data points between 0.818 μm and 0.834 μm are of approximately uniform intensity, and are grouped into one of four categories based on the relative strengths of methane and hydrogen absorptions. This plot shows an equatorial observed spectrum for Uranus, to demonstrate the similarity in radiance of each of the values (grey line, the thickness of which indicates uncertainty). Diamonds in this panel show the arbitrarily scaled ratios of hydrogen to methane absorption levels (see figure 4.9 for more information on the absorption levels). The dotted lines show the bins that are used to put the spectral locations into four categories, with each bin labelled on the plot.

reflectance analysis just described was undertaken for several temperature and pressure combinations between 90 and 130 K and 2.0 and 4.0 bar. As absolute levels of absorption changed with temperature and pressure (the latter change due to changes in abundance with altitude), the ratios between H_2 and CH_4 absorption remained relatively consistent. Each temperature/pressure combination tested was consistent, of course, with the upper troposphere of Uranus.

The reflectance study here differed from the aforementioned Karkoschka and Tomasko (2009) study because here Uranus is viewed in 2009 (two years after equinox) whereas the earlier study examined Uranus in 2002 (five years prior to equinox), though at a higher spatial resolution. The seven-year period between the two studies is widely known to be a dynamic time in the Uranian upper atmosphere. Comparison of this study with the Karkoschka and Tomasko (2009) paper allowed an investigation of any temporal evolution in the latitudinal methane profiles. Perhaps even more importantly, this study, which occurred closer to the equinox, allowed us to examine latitudinal methane trends from 50° S to 65° N, a region of a larger latitudinal extent, including 35° of additional northern hemisphere coverage, compared with the previous study.

Plots were produced of observed reflectance for these four absorber groups shown in figures 4.9 and 4.10. In this reflectance plot (figure 4.11, left panel), the "mostly hydrogen" reflectance curve was normalised to the horizontal to reflect the assumption of well-mixed latitudinal hydrogen abundances. This normalisation was necessary in order to remove the effects of partial measurement of space near the edges of the disc, which cause the apparent reflectance to artificially diminish when moving to higher latitudes. With the "mostly hydrogen" curve appearing horizontally, it also enabled easier comparison to the curves with greater methane contributions, to which the same normalisation factors were of course applied. In order to ensure that any trends evident in the plot were not also present in an atmosphere

with well-mixed methane, a reflectance plot was produced (figure 4.11, right panel), for a model Uranus atmosphere equal to the retrieved result in section 4.2.2 at all latitudes. This panel, with reflectance again separated into four relative absorption-strength categories and normalised for well-mixed hydrogen, shows the amount of limb-brightening that would be observable in the spectral locations dominated by methane absorption. The limb-brightening effect in the right panel is caused by increased scattering in the upper atmosphere as viewing angle increases. For ease of comparison, each curve in the model Uranus panel has been scaled so that the reflectance minimum in each of the four curves lies at the same level as the minimum of the observational panel.

Both panels of figure would be expected to be identical if methane were latitudinally well-mixed. In this scenario, only the limb-brightening trends from the right panel would be seen mirrored in the left panel, with no additional trends specific to methane-dominated absorption curves. In other words, identical plots would validate a null hypothesis that methane, like hydrogen, is well-mixed with latitude, and that any variations in reflectivity were derived either from latitudinal changes in cloud opacities or changes in the zenith angle at which the atmosphere is viewed. But as figure 4.11 clearly shows, the curvatures of the latitudinal reflectances are increased in the left-hand panel. This indicates that some of the latitudinal absorption trends are attributable to methane alone. As methane becomes increasingly important from one reflectance curve to the next, a trend is seen of increasing absorption towards the equator, relative to the midlatitudes. This trend must be accounted for by methane absorption and not cloud opacity, because the trend doesn't exist in the "mostly hydrogen" curve. The trend, therefore, must must be attributed to an enriched amount of methane at the equator.

For each temperature/pressure combination tested, methane enrichment percentages compared to equatorial values were calculated at each latitude using the

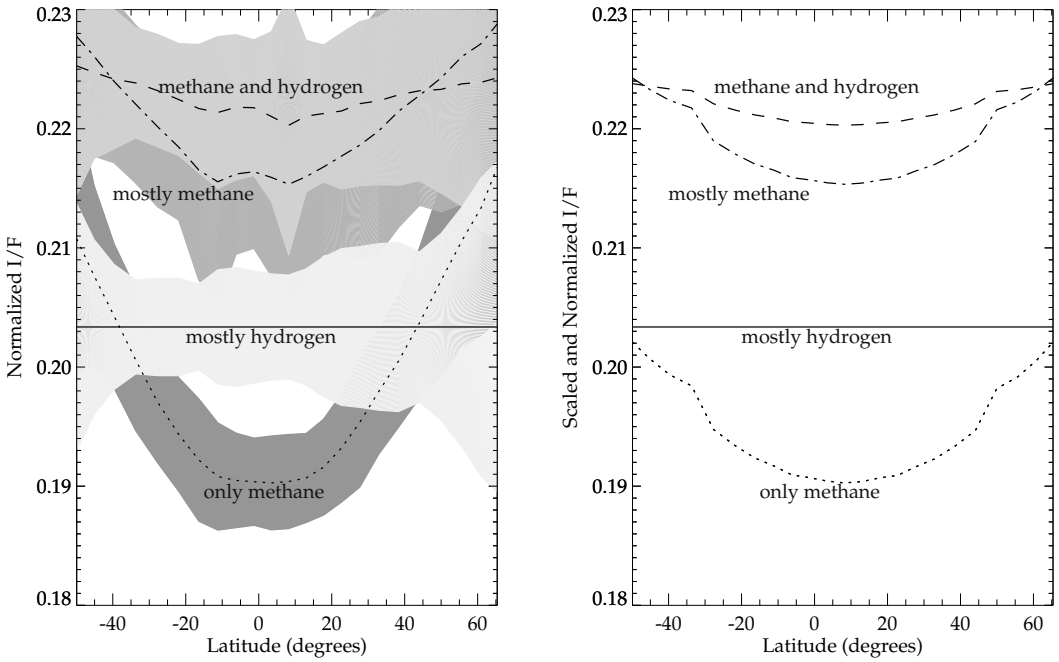

Figure 4.11: The two panels show the average reflectivity with latitude for spectral locations between 818 and 834 nm that are dominated by "only methane", "mostly methane", "methane and hydrogen", and "mostly hydrogen" absorptions. Both panels represent methane and hydrogen absorption coefficients at approximately 2 bar and 90 K, though other Uranian-like combinations of pressure and temperature were also tested with similar results. The panel on the right is a synthesised result for the model Uranus atmosphere derived in section 4.2, with a latitudinally unvarying vertical methane profile, effectively showing the limb-brightening that would be seen in such an atmosphere. The panel on the left shows the true observational data, with grey regions indicating error. Varying shades of grey are simply for clarity. To ease interpretation of both plots, the curves have all been normalised so that the "mostly hydrogen" curve is horizontal, indicating the assumption of latitudinally well-mixed hydrogen. In the right panel, the curves are also scaled so that each curves' reflectance minimum is aligned with the corresponding minimum on the left. When moving from the "mostly hydrogen" curve to those curves in which methane absorption plays an increasingly dominant role, a clear trend of increased reflectance in the midlatitudes is observed, though to a greater degree in the left panel. Since the reflectance trends are greater than the synthetic limb-brightening curves, there must be an additional factor at work. The required explanation is that in the true Uranian atmosphere on the left, an enriched amount of methane at the equator absorbs additional light, resulting in the more pronounced limb-brightening in the midlatitudes.

following equation

$$\text{Enrichment Percentage at } l = \left(\frac{R_{max} - R_l}{R_{max}} - \frac{B_{max} - B_l}{B_{max}} \right) \times 100$$

where R is the "only methane" reflectance from the left panel, B is the "only methane" reflectance from the right panel. Subscripts represent the location of the reflectance, with l representing a given, single latitude and max representing the location where the maximum reflectance value is found. R_{max} and B_{max} are the highest levels of reflectance observed, and are accordingly treated as reflectance at locations on the planet with the base, non-enriched level of methane. Thus the left-hand term of the subtraction represents the total reflectance enrichment, while the right-hand term represents the limb-brightening contribution to reflectance enrichment. Results were similar for each temperature/pressure combination. Results were combined with a weighted average based on uncertainty to provide a maximum methane enrichment of $10 \pm 1\%$ centred at 1° S but extending fully between 16° S and 12° N.

This value for equatorial methane enrichment is much less than that determined by Karkoschka and Tomasko (2009), who found 50% enrichment. In order to explain the seeming contradiction, the different spectral and spatial resolutions of the two studies were considered, as well as the difference and dates of the observations. The spectral resolution of the spectrometers was ruled out as a possible explanation for the different enrichment values. This study employed 81 spectral points, compared to Karkoschka and Tomasko (2009)'s 10 samples, but when the IRTF data were convolved and smoothed to the approximate spectral resolution of the earlier study, an identical result was found for equatorial methane enrichment. As for spatial resolution, the Karkoschka and Tomasko (2009) data was acquired with approximately five times the resolution of the data. As a result, the data would "blur" reflectance maxima and minima to some extent, decreasing the difference between them and

yielding an accordingly smaller apparent methane enrichment. The relative minima of methane abundance in Karkoschka and Tomasko (2009) was at $\sim 40^{\circ}$ S, within the viewing region of this data. If the southern minima remained unmoved between the two studies, this region is sufficiently close to the planet's 2009 limb that the IRTF data's poor spatial resolution would have impacted the perceived minima, "blurring" it to a smaller amount.

As a final test to ensure that the data here did not directly contradict the possibility of Karkoschka and Tomasko (2009)'s 50% enrichment ratio, a series of cloud retrievals were performed in which fixed methane abundance were fixed to the enriched values presented in the earlier study. With these methane values, enriched by 50% at the equator, reasonable model fits were still retrieved ($0.92 \leq \chi^2/n_y \leq 1.23$), and cloud-top height became invariant, as was found to be the case with enriched methane in Irwin et al. (2010, 2011a, 2012a,b). It was concluded, based on these reasonable fits when using a 50% enrichment value, in combination with the likelihood of a "blurred" and therefore reduced reflectance peak in this study, that the result should only be trusted to provide a lower boundary of 9% for equatorial methane enrichment, resolving the seeming disparity in the two results.

Perhaps the most important point to remember when comparing the results of this study and Karkoschka and Tomasko (2009) is the significant time difference between the two datasets. This seven-year difference is known to be a dynamic period of change in the Uranian upper atmosphere. Part of the disparity in enrichment values, then, is likely to be a reflection of a real seasonal change between the 2002 observations in Karkoschka and Tomasko (2009) and the 2009 data used here. Other atmospheric changes of comparable magnitude have been documented in the years surrounding the equinox (Irwin et al., 2009, 2010, 2011a, 2012a; Sromovsky and Fry, 2005, 2007, 2008; Sromovsky et al., 2007, 2009, 2011), so it is not unreasonable to suppose that the change in equatorial methane enrichment could be real. Unfor-

tunately, because of the marked differences in both spatial and spectral resolution between the two datasets, and the conclusion that this dataset provides only a lower boundary for methane enrichment levels, a definitive argument in favour of a real temporal change on Uranus is impossible to make.

Another major difference between the two studies was that, due to the limitations of the visible disc in 2002 versus 2009, Karkoschka and Tomasko (2009)'s data covered a latitudinal range of approximately 80° S – 30° N latitude. The data for this study, measured closer to the equinox, covered a range of approximately 50° S – 65° N latitude, and thus shows a more complete picture of equatorial methane enrichment with respect to both northern and southern midlatitudes.

One final difference between the two reflectance studies is worth noting. The Karkoschka and Tomasko (2009) study places the latitudinal position of the methane enrichment maximum near 15° S latitude while the analysis here suggests a broader maximum centred at 1° S. As noted in section 2.1.1, the spatial resolution across the equatorial regions of the planet is roughly 16° latitude, so this discrepancy could be explained by that error. Even though the two values lie within the latitudinal uncertainty, it is unlikely that the poor spatial resolution of this data would cause such a large change in the location of the maximum, nor serve to broaden it so noticeably. It seems much more likely that any inaccuracy introduced by the lower spatial resolution would have a symmetric effect on the location of the central methane enrichment peak, and produce no net effect upon latitudinal position or extent. It is suggested, therefore, that the methane enrichment maximum has likely elongated northward during the equinoctial period, though further monitoring as the planet moves into northern spring will be vital to confirm whether this trend is real.

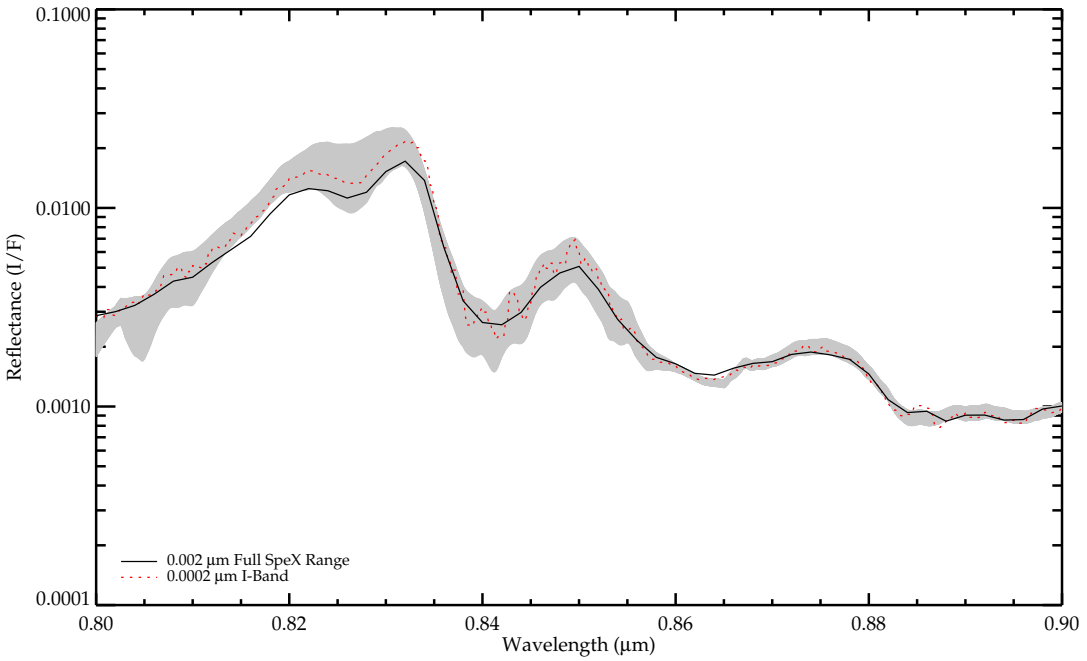

Figure 4.12: Comparison between centre-of-disc Uranus fit to data from section 4.2 (solid black line) and new, control fit based on 0.0002 resolution I-Band data (dotted red line). Both models are for data at the Uranian centre-of-disc ($\sim 8^\circ$ S) and are retrieved with same fixed, free, and *a priori* values. Good agreement with the observational spectrum and with each other is shown.

4.3.3 Methane Retrievals in the I-Band

Retrievals of cloud parameters and methane abundance were performed using only the resampled (0.2 nm spacing) data from the SpeX I-Band, between 0.8 and 0.9 μm. A control I-Band retrieval was conducted in which methane remained fixed, and the two parameterised cloud layers were retrieved as before. Figure 4.12 shows this retrieval, and demonstrates that the model derived from the I-Band alone agreed, within error, to that derived from the full 0.8 – 1.8-μm region (discussed in section 4.1).

Retrievals were then conducted that allowed free variation of the same five cloud parameters (FSH in both clouds, total opacity in both clouds, and base pressure in

the TC). In addition, to these variables, a scaling factor was retrieved that multiplicatively adjusted the entire methane profile from the *a priori* value. The *a priori* values were the same as the fixed profile used in section 4.2, specifically a 1.6% deep methane abundance with a 30% relative humidity elsewhere. This constrained method of varying the methane profile ensured that a realistic result was produced, though at the cost of restricting the range of possible methane profiles the optimal estimation process would consider.

In this narrower spectral window, the two distinct cloud models were revisited that were first tested in fitting the observations across the whole $0.8-1.8$ μm range (see section 4.1.2). In contrast with the earlier tests, the sub-micron fit quality achieved with the more complex cloud model (Karkoschka and Tomasko, 2009; Sromovsky et al., 2011) was comparable to that achieved using the two-cloud parameterised model. In addition to comparable fit quality, the retrieved cloud properties and methane abundances always displayed the same latitudinal trends in both models, and specific parameter values agreed within error. Since neither optical cloud model seemed to suggest a clear advantage, it was again decided to perform analysis here with the simpler Irwin-like optical model. This choice provided more consistency with the earlier work presented, allowing for more meaningful comparisons to be made. This also allowed us to reaffirm the previously stated preference for the model that provided a good fit to data with the most simple set of model assumptions and values.

The results of these dual methane and cloud retrievals are shown in figure 4.13. Allowing methane to scale freely produced results that fit the data significantly better than those in the earlier, fixed-methane analysis (section 4.2). Approximate methane enrichment values at each latitude were this time calculated with

$$\text{Enrichment Percentage at } l = \left(\frac{S_l - S_{min}}{S_{min}}\right) \times 100$$

where S represents the retrieved scaling factor, l represents the latitude in question, and min refers to the minimum scaling factor retrieved (which was located at the unenriched midlatitudes). The result is a broad methane enrichment peak centred at 6° S latitude of 36±26%, when compared with the relative methane minimum value at 44° N. This value is consistent, within error, with the suggested lower boundary value of 10%, with Karkoschka and Tomasko (2009)'s 50% enrichment value. It should be noted, however, that the poorly-constrained result is also in fact within 1.5σ of no enrichment at all.

This result, while not particularly robust, does nevertheless show a broad enrichment curve very similar to that discovered during the reflectivity analysis. Simultaneous retrieval of these six parameters stretches the limits of the data due to strong correlations between methane abundance and several parameters in the clouds, most importantly optical depth of the UH and cloud-top height of the TC. This result does show, however, that the retrieval method is a valuable technique for methane abundance studies, and would prove particularly useful if data were more spectrally and spatially resolved, or if there were fewer free parameters in the two aerosol layers. Presumably the most important of those three issues is the spatial resolution. SpeX I-Band seeing was calculated to be 0.7" (see section 2.2.1 and table 2.5), whereas the more robust Karkoschka and Tomasko (2009) result was determined with Hubble data of a 0.1" spatial resolution. As discussed in the previous section (4.3.2), the spatial resolution of the data likely produces a lower-than-actual equatorial enrichment value, leading us to again consider the result as a lower boundary for enrichment. The centre of the enrichment lies at 6° S latitude, again supporting the conclusion that the enrichment peak has been migrating and extending northward since the 2002 data analysis, which placed the peak at 15° S. Spatial resolution most likely has no effect on the location of the enrichment peak.

The figure also shows that the cloud-top pressure of the TC is more uniform in

this methane and cloud retrieval. This change is consistent with the link, discussed both in the opening of section 4.3 and in Irwin et al. (2012a), between the TC base and methane column abundance. Using the above parameters in the model, fits across all latitudes are excellent, with an average χ^2/n_y value of 0.35. An example fit for the equatorial region is shown in figure 4.14.

As a final point of interest, figure 4.15 shows this same equatorial, centre-of-disc fit against observations, but plotted over the entire SpeX spectral range. Since the retrieval did not take into account data from wavelengths longward of 1.0 μm, we would not expect the fit to be accurate in long wavelengths. Still, the plot has a goodness-of-fit $\chi^2/n_y = 9.46$, and demonstrates that the variable methane profile should be applicable to the entire spectral range of SpeX.

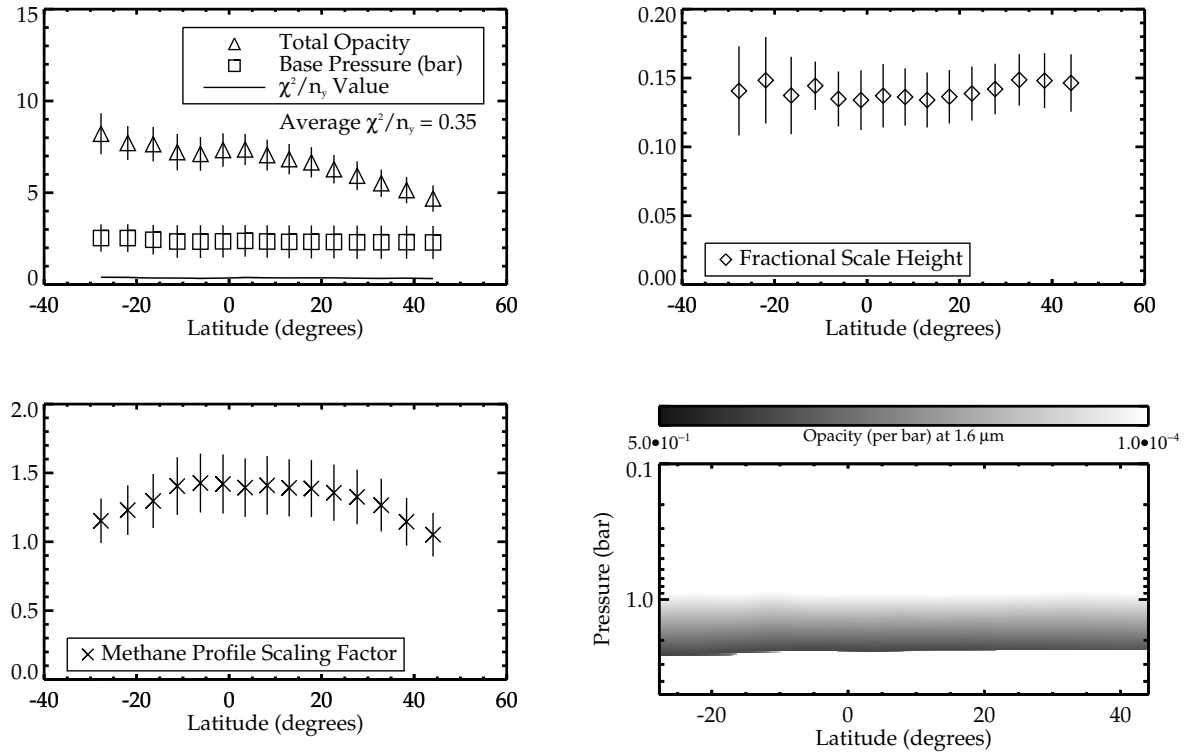

Figure 4.13: I-Band retrieval results for methane and the TC deck as a function of latitude. The methane plot (lower left panel) shows the retrieved multiplicative factor applied to *a priori* methane abundance profile, which has a 1.6% deep mole fraction and is limited at all levels to 30% relative humidity. The two upper panels show retrieved parameters of the TC as well as the χ^2/n_y value at each latitude. The lower right panel shows the latitudinal vertical TC structure (in units of optical depth per bar at 1.6 μm) constructed from the retrieved cloud parameters. The cloud parameters show that this combination of the three retrieved cloud parameters produces a cloud-top that is much more uniform in pressure than that of the earlier fixed-methane retrievals. Instead, the latitudinal changes in the spectrum are modelled most accurately in this retrieval by enriching the methane abundance at the equator relative to the midlatitudes.

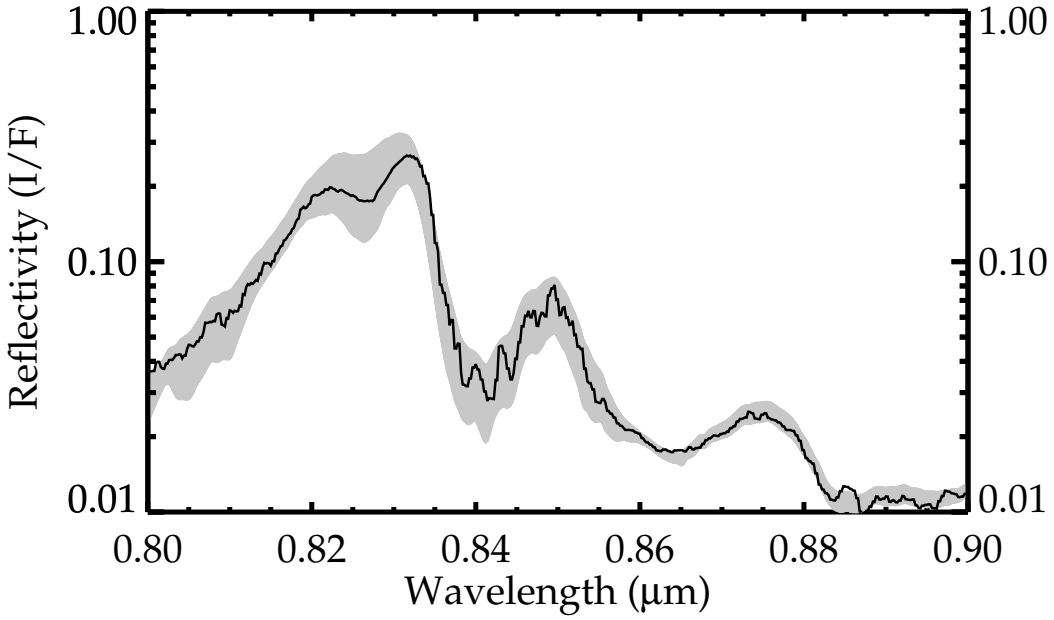

Figure 4.14: Example of a model fit (solid line) to observations (gray region) for an I-Band-only retrieval using high-resolution κ-tables. In this example, at $\sim 8°$ N latitude, six parameters are retrieved: base cloud pressure (TC only), cloud FSH (TC and UH), cloud total opacity (TC and UH), and methane scaling factor. The methane scaling factor produced a multiplicative adjustment to the *a priori* methane profile (1.6% deep abundance and 30% relative humidity). For this retrieval, $\mathrm{chi}^2/\mathrm{n_y} = 0.37$. This value is comparable to goodness-of-fit values at all latitudes, which combine for an average $\mathrm{chi}^2/\mathrm{n_y} = 0.35$.

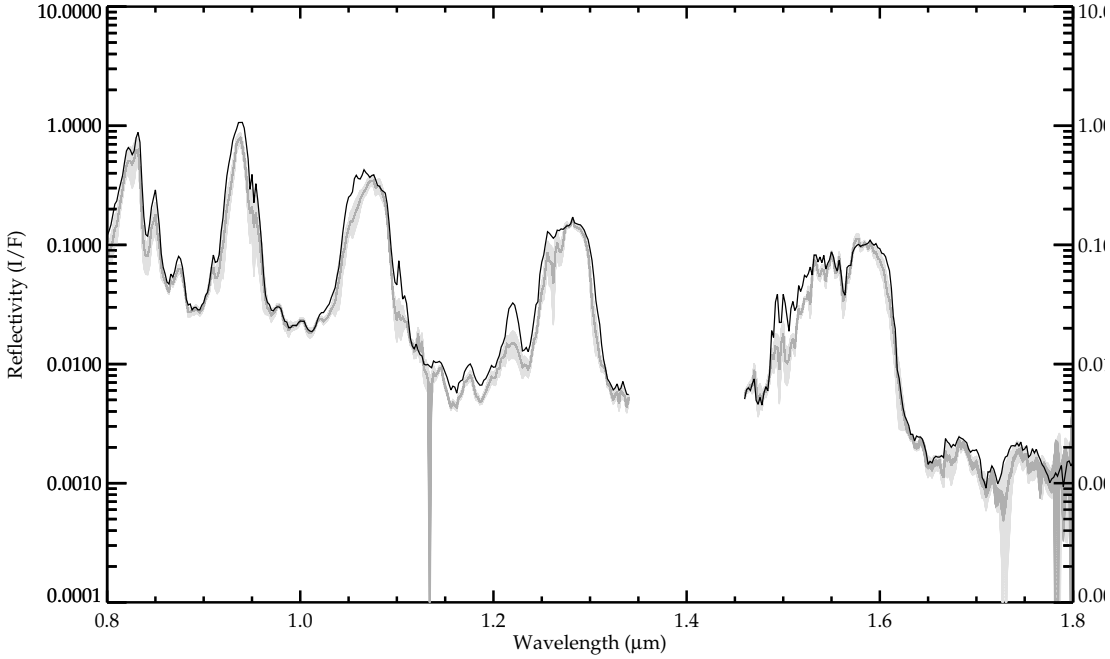

Figure 4.15: Example of a model fit (solid line) to observations (gray region) for an I-Band-only retrieval using high-resolution κ-tables, but compared with the spectrum across the entire 0.8 – 1.8 μm spectral window. In this example, at ∼ 8° N latitude, six parameters are retrieved: base cloud pressure (TC only), cloud FSH (TC and UH), cloud total opacity (TC and UH), and methane scaling factor. The methane scaling factor produced a multiplicative adjustment to the *a priori* methane profile (1.6% deep abundance and 30% relative humidity). For this forward model, $\mathrm{chi}^2/\mathrm{n_y} = 9.46$. The high $\chi^2/\mathrm{n_y}$ is not surprising given the retrieval for which this model fit is based did not take any data longward of 1.0 μm into account. Still, the model fits the data sufficiently well to demonstrate that the variable methane profile would be applicable to the entire SpeX spectrum.

Chapter 5

Neptune from Palomar SWIFT Observations

> *The sciences do not try to explain, they hardly even try to interpret, they mainly make models. By a model is meant a mathematical construct which, with the addition of certain verbal interpretations describes observed phenomena. The justification of such a mathematical construct is solely and precisely that it is expected to work.*
>
> — John von Neumann, "Method in the physical sciences" in *Neumann Compendium*

This chapter describes work done to date on analysing observations of Neptune taken at the Palomar observatory using the SWIFT spectrometer in 2012 (see chapter 2). The first section, 5.1, describes a new retrieval algorithm implemented in the NEMESIS retrieval tool. This new capability is applied to the SWIFT data, and section 5.2 describes some basic attempts at model reproductions of the observational spectra as well as outlining some challenges that were specific either to the new SWIFT data, which has never before been used for planetary science, or to the new retrieval

technique. The final section, 5.3, presents the analysis results achieved to date.

5.1 Refractive Index Retrieval

Perhaps the biggest weakness of the work published in Tice et al. (2013), and subsequently explained in chapter 4, is that large spectral ranges were analysed with two assumptions of altitudinal and spectral invariance. First, all refractive indices were assumed to be conservative (no imaginary part), and secondly, all Henyey-Greenstein parameters were assumed to be constant. As already discussed in section 4.1.1, the former assumption meant that particles in both cloud decks were assumed to have extinction cross-sections consistent with Mie scatterers, and then subsequently single-scattering albedos were independently adjusted with wavelength in violation of the former assumption of conservative aerosol particles. The latter assumption meant that phase functions for large, lower cloud particles of radii on the order of 1 μm were assumed to match phase functions for particles an order of magnitude smaller in the upper hazes. Despite these false assumptions, excellent reproduction of observational data was possible because the upper haze was so thin that its impact on the overall spectrum was, though non-negligible, quite small.

On Neptune, however, where stratospheric hazes are known to be much more optically thick than on its planetary neighbour, it seemed likely that these assumptions would have more damaging impacts on attempts to model the atmosphere. Subsequent to the publication of Tice et al. (2013), a new capability was implemented in the NEMESIS retrieval code, with the goal of producing a reanalysis of the earlier work that would not rely on these assumptions (Irwin et al., 2015). Namely, a method of retrieving indices of refraction was constructed. This new technique is described here.

From a standpoint of basic atmospheric physics, the inaccuracies in previous

modelling (chapter 4) arose from permitting the independent adjustment of extinction cross-sections, phase functions, and single-scattering albedos of the scattering aerosols. In reality, these three quantities are all interconnected and dependent on one another, and tied with a fourth quantity, namely the imaginary part of the refractive index, which as mentioned briefly in the Introduction, is used to describe the amount of absorption of light when passing through a substance. Also worthy of consideration in this new scheme is the real part of the refractive index. There is not an abundance of laboratory data (nor any *in situ* data) for ice giant hydrocarbon refractive indices, but what little there is indicates that viable options lie within a fairly narrow range in the near-infrared. Ammonia ice, for example, has $n_{0.6677\ \mu m} = 1.423$, while methane ice is $n_{1.0\ \mu m} = 1.313$ (Martonchik et al., 1984; Martonchik and Orton., 1994; Satorre et al., 2008). Icy films composed of differing ratios of CH_4 and N_2 have refractive indices of $n \simeq 1.2 - 1.3$, and pure N_2 ice and CO_2 ice both have indices of $n \simeq 1.3$ (Brunetto et al., 2008; Satorre et al., 2008).

In the new retrieval algorithm, the retrieved parameters are the imaginary parts of the index of refraction at a range of preselected output wavelengths, along with the particle size distribution mean radius and variance assuming a standard-gamma size distribution. The new scheme requires *a priori* values and errors for these retrieval values, as well as a fixed real refractive index at a specified reference value, and a correlation length for the imaginary refractive index spectrum. Values for extinction cross-section and single-scattering albedo are no longer fixed as part of the retrieval, but are computed in a self-consistent manner during the forward-modelling procedures within the retrieval code. Henyey-Greenstein phase parameters are done away with entirely, as it was determined that Mie-calculated phase functions at a 2° resolution for each output wavelength, can be computed and used with little or no loss in computational efficiency with current computing technology unlike the case with older computers. In practice, however, Henyey-Greenstein parameters are eas-

ily computed after a solution is converged upon, and will continue to be used as a simple means of representing and approximating the general shape of the scattering phase function.

As far as the specific procedure used in the new retrieval scheme, the optimal estimation technique (see chapter 3 and Rodgers (2000)) is used as before, but now attempts to converge upon a solution for the imaginary refractive index of the aerosol particles at each specified output wavelength. During this process, the correlation length is used to enforce retrieved values that are smoothly varying with wavelength. After each retrieval iteration, NEMESIS then uses a Kramers-Kronig analysis (Sheik-Bahae, 2005), along with the reference value for the real refractive index, to compute self-consistent values for the real refractive indices at each output wavelength. This spectrum of real and imaginary indices of refraction, in tandem with retrieved mean radius and variance values for the standard-gamma size distribution, allow Mie theory (Hansen and Travis, 1974) to be applied to compute self-consistent values for the extinction cross-sections, single-scattering albedos, and phase functions at each output wavelength. It is these values, all self-consistent with the originally retrieved imaginary refraction indices, that are used to compute a model spectrum for comparison with the data.

5.2 Preliminary Work

This section, which describes initial considerations and challenges encountered when working with the new retrieval scheme and the SWIFT data, is divided into several subsections. Subsection 5.2.1 describes the basic assumptions used to construct the Neptune model, sources from which correlated-κ tables were computed, and a discussion of fixed values chosen within the retrieval scheme. In this section there is also a discussion of certain correlations between retrieval parameters that were dis-

covered in early tests, and how these correlations were dealt with. Subsection 5.2.2 provides some of the results of initial retrievals that probed one latitude at a range of zenith angles. It was during these retrievals that it was discovered that additional geometric error needed to be considered when dealing with SWIFT data. This section provides a full discussion of the sources of these additional uncertainties, and outlines the procedure chosen to account for them during the retrieval process.

5.2.1 Retrieval Physics

As with the Uranus analysis of chapter 4, a few characteristics of the dataset needed consideration before analysis could begin. Unlike with the SpeX data, an abundance of high-quality images were available from which to choose spectra to analyse (see figures 5.1 through 5.3). The decision was made to take advantage of this, and the capability of NEMESIS to analyse observations from multiple zenith angles simultaneously, thereby giving NEMESIS different paths through the atmosphere which would help constrain the model for a given feature (be it a band of clouds at a certain latitude, or a discrete cloud feature). In the normal NEMESIS distribution package, the program is equipped to deal with up to 1024 spectral locations, which was vastly insufficient to hold native-resolution SWIFT data, let alone at multiple zenith angles. While this number could have simply been increased, full-scattering computations would be lengthy enough without giving the retrieval tool more than 1024 points to fit. Instead, SWIFT data were resampled for each feature examined, choosing the sampling rate such that the full spectral range in all the zenith angles chosen for analysis would remain under 1024 values. For example, if 5 zenith angles were chosen, the data would be resampled so that each zenith-specific spectrum contained 204 points. 5 zenith angles $\times$ 204 points $=$ 1020 total spectral locations, a number that would fit within the 1024 array allocated to it.

Recall that for each SpeX Uranus retrieval only one pixel (and one viewing geome-

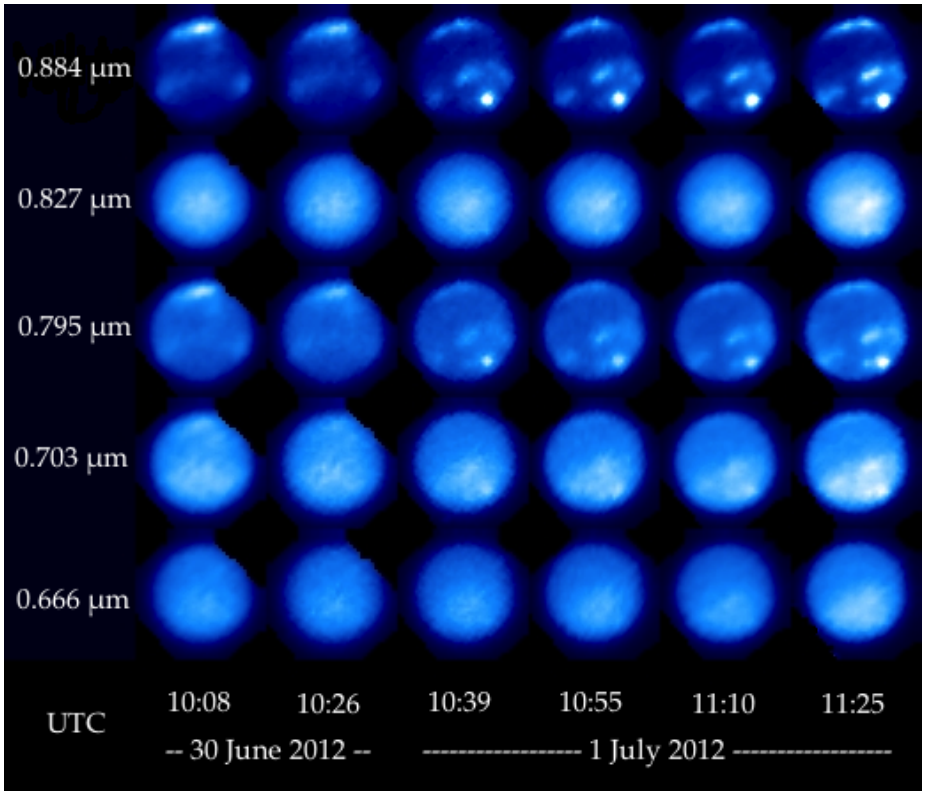

Figure 5.1: Collage of SWIFT Neptune observations observed on 30 June and 1 July, 2012 at five wavelengths, as indicated. Transmission curves of these wavelengths can be found in figure 5.4.

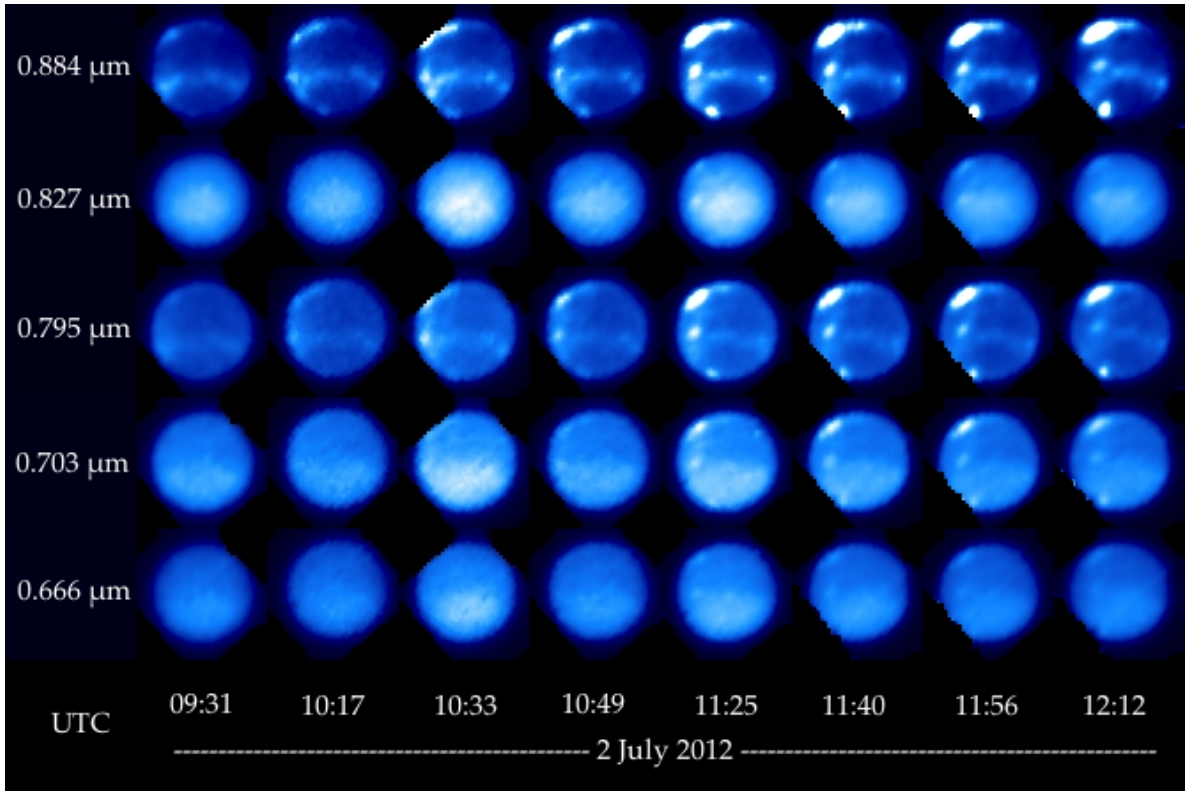

Figure 5.2: Collage of SWIFT Neptune observations observed on 2 July, 2012 at five wavelengths, as indicated. Transmission curves of these wavelengths can be found in figure 5.4.

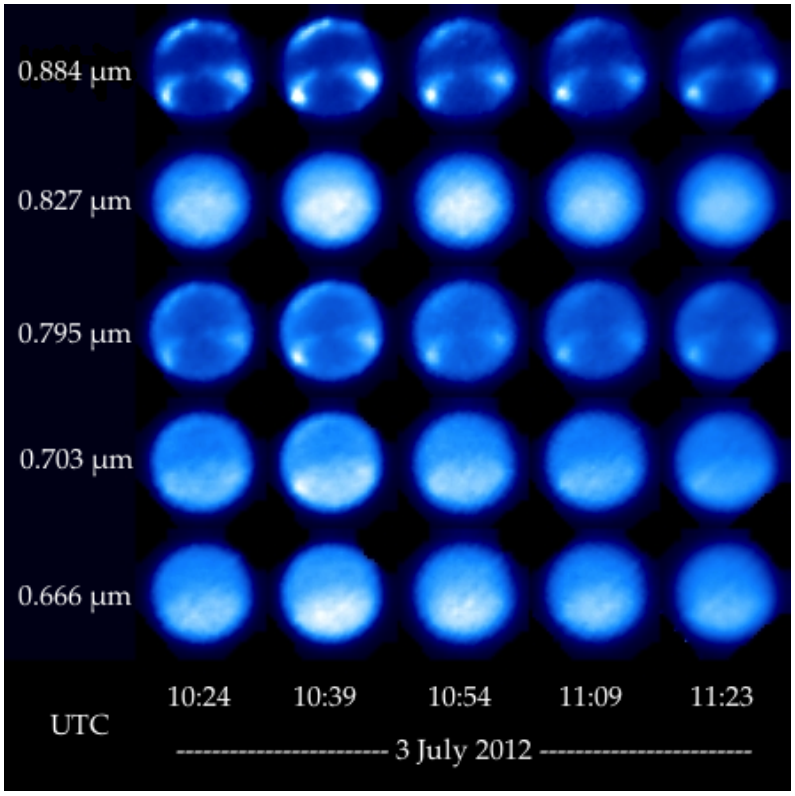

Figure 5.3: Collage of SWIFT Neptune observations observed on 3 July, 2012 at five wavelengths, as indicated. Transmission curves of these wavelengths can be found in figure 5.4.

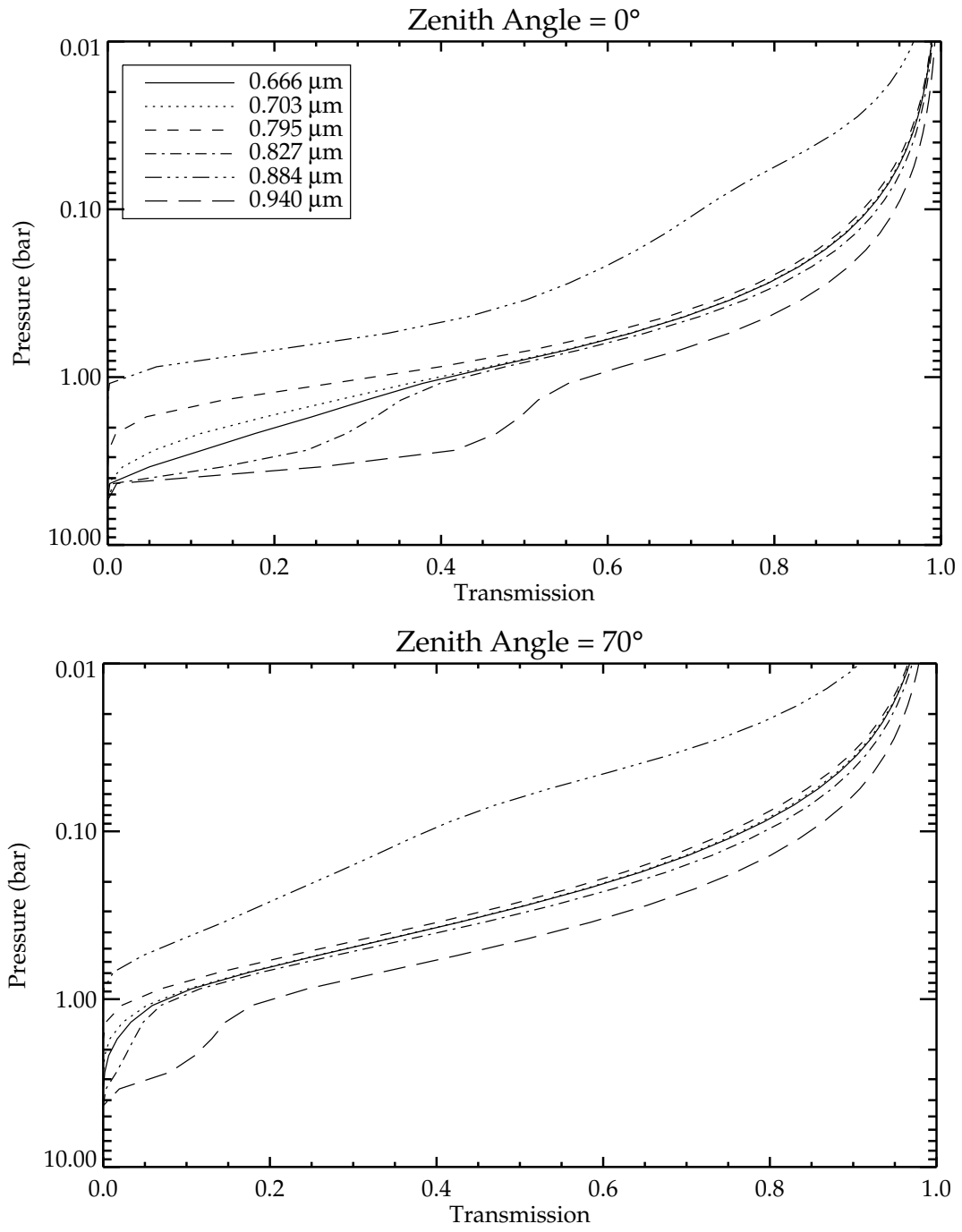

Figure 5.4: Both panels show transmission from space through a Neptune model atmosphere for six different wavelengths, as shown in the legend (upper panel). The upper panel shows light transmission for a 0° zenith angle, while the lower panel shows light transmission for a 70° zenith angle. It is clear that light transmission through this model atmosphere decreases much more quickly at high zenith angles, imposing a limit to high pressure information content when compared with nadir viewing.

try) were retrieved at a time. Nevertheless, a weighted distribution of the two closest viewing geometries was calculated for each retrieval to model the low spatial resolution of the IRTF data. The SWIFT data, unlike the SpeX data, utilised an adaptive optics system, and so the spatial resolution on the planet was significantly better (see section 2.2.2). It was then decided that since such a small range of the planet was being viewed with each pixel of the telescope, multiple zenith angles did not need to be considered for each pixel retrieved. Still, a different consideration needed to be made with regard to viewing geometries. Since features would be viewed from multiple zenith angles simultaneously, and the ability to use as many features as possible would be advantageous, it was decided that 5 zenith quadratures would require too much interpolation during the running of the scattering model and so the number of zenith angles listed in the quadrature file was increased from 5 to 9.

As with Uranus, the only absorbers that needed consideration in the model were methane and collision-induced absorption of H_2-H_2 and H_2-He. For methane, band models from Irwin et al. (1996), revised according to Irwin et al. (2006) with Karkoschka and Tomasko (2010) data were employed again. κ-tables were created with this data at numerous sampling sizes, because as mentioned above, observational spectra of many different sample rates were utilised depending on how many zenith angles were desired for simultaneous retrieval. Since the generation of κ-tables is a one-time operation, tables were produced for each sample rate selected so that a table existed for the exact spectral points used in any given retrieval run. In this way, no interpolation of the κ-tables was ever necessary during the retrievals themselves, making them more computationally efficient.

For the collision-induced absorptions, the ortho/para hydrogen ratio was again considered to be at equilibrium (Conrath et al., 1998; Fouchet et al., 2003) and absorptions were modelled based on coefficients found in Borysow (1991, 1992); Borysow et al. (2000); Zheng and Borysow (1995). The atmospheric reference pro-

files used here for temperature and abundance of H_2, He, and CH_4 were taken from Fletcher et al. (2014) and based on a number of recent studies. (Baines and Hammel, 1994; Conrath et al., 1993; Fletcher et al., 2010; Feuchtgruber et al., 2013; Greathouse et al., 2011; Karkoschka and Tomasko, 2011; Lellouch et al., 2010; Lindal, 1992; Moses et al., 2005; Orton et al., 1987b, 1990).

Lastly, a description of the model is in order. As with Uranus, the atmosphere was modelled with two clouds, each fully described by three parameters: base altitude, fractional scale height, and total opacity. In the deeper of the two clouds (from hereon called the TC, or tropospheric cloud), base altitude and opacity were retrieved from *a priori* values of 1 bar and $\tau = 1.0$, respectively. The fractional scale height of the TC was constrained to 0.1 because only the cloud-top was accessible by the data, and therefore the fractional scale height and the base altitude had a strong correlation if both retrieved.

The higher of the two clouds (hereafter called the UH or upper haze) was parameterised in the same way as the TC. Because the fractional scale height and base altitude of this cloud were highly correlated, tests were run in the following two ways:

Altitude Tests were performed in which the cloud base altitude was fixed at a range of plausible values between 0.01 and 1.0 bar. Fractional scale height and total opacity were free, retrieved parameters with *a priori* values of 0.1 and 1.0, respectively.

Fractional Scale Height Tests were performed in which the fractional scale height was fixed at a range of plausible values between 0.046 and 4.6. Cloud base altitude and total opacity were free, retrieved parameters with *a priori* values of 0.08 bar and 1.0, respectively.

In addition to retrieving these physical parameters for the TC and the UH, the new retrieval scheme was used to characterise separate aerosol particles in each haze. *A*

priori values for the standard-gamma size distribution were mean radii of 1.0 in the TC and 0.1 in the UH, both with a variance of 5%. In both clouds, the real refractive index at 1.0 μm was equal to 1.4, which as already mentioned is close to the known possible values for hydrocarbon ices on the ice giants (Brunetto et al., 2008; Martonchik et al., 1984; Martonchik and Orton., 1994; Satorre et al., 2008). In both clouds the imaginary part of the refractive index was started at 1.0×10^{-3}, in other words highly conservative. As already mentioned, the other optical properties of the clouds were computed from the values mentioned above in a self-consistent manner.

To produce "forward modelling error", or proxies for systematic errors in the absorption band data, the same procedure was followed as was performed with SpeX Uranus data. For details, see the fourth paragraph of section 4.1.1.

5.2.2 Geometric Errors

As results of early retrievals were analysed, it was discovered that the spectra for lowest 5 or 6 zenith angles were being reproduced well, while the same models were struggling to reproduce the data for the highest 3 or 4 viewing geometries. The synthetic spectra were consistently too bright for the observations at high zenith angles. In considering the possible source of this discrepancy at high zenith angles, three probable sources were identified.

First, because some of the high zenith angle pixels are on the extreme limb of the planet, and the observation seeing was only better than 0.3" (nearly 4 pixel-widths), off-planet dark space is likely 'bleeding in' to data pixels that lie within 3 or 4 pixels from the 1 bar limb. This causes a spurious reduction of the apparent brightness of the entire spectrum at that pixel. This would result in model spectra that were too bright to accurately reproduce the observational data. To truly account for this source of error, and size and shape of the point-spread function would need to be considered, and used to calculate a percentage, for each pixel analysed, that reflected

what portion of that pixel fell off the limb of the planet. This percentage could then be used to adjust the reflectance to match the reflectance from a true 'point source' on the planet. Because near-limb pixels were not analysed whenever possible (zenith angles were generally restricted to those $\theta \leq 65°$, see section 5.3), this complicated error analysis was not completed.

Second, at higher zenith angles, the plane parallel approximation which is employed by the scattering calculations gets less and less accurate (see figure 5.5). Consider that when incoming solar radiation scatters through the atmosphere on a nadir path, straight down through the atmosphere towards the centre of disc, each layer boundary in the model is very nearly flat and parallel to the next. As the light passes each layer boundary of the model atmosphere, it does so at about the same angle. But as the zenith angle increases, the slant at which the incoming solar radiation hits the atmosphere is larger and larger. The radiation travels on a longer path through each layer, and consequently reaches the next layer boundary at a very different geographic location than the previous. This large change in location from one layer transition to the next creates a large change in the angle at which light moves across the boundary. This means that the angle of entry to each successive layer is changing, and so using a constant zenith angle in calculations (plane parallel) is less and less accurate as zenith angles increase. To analyse this source of geometric error, comparisons would need to be made between NEMESIS (plane parallel) and a fully spherical radiative transfer code (such as one employing the Monte Carlo method). Running this comparison would have been extremely time intensive, and again since high zenith angle analysis was generally not performed (see section 5.3), this error analysis was omitted here.

Third, as zenith angle increases, the magnitude of the change in zenith angle from one pixel to an adjacent pixel is larger than at nadir. Consider that if geometric assignment is one pixel off at nadir, this might be a change of 1 or 2 degrees to the

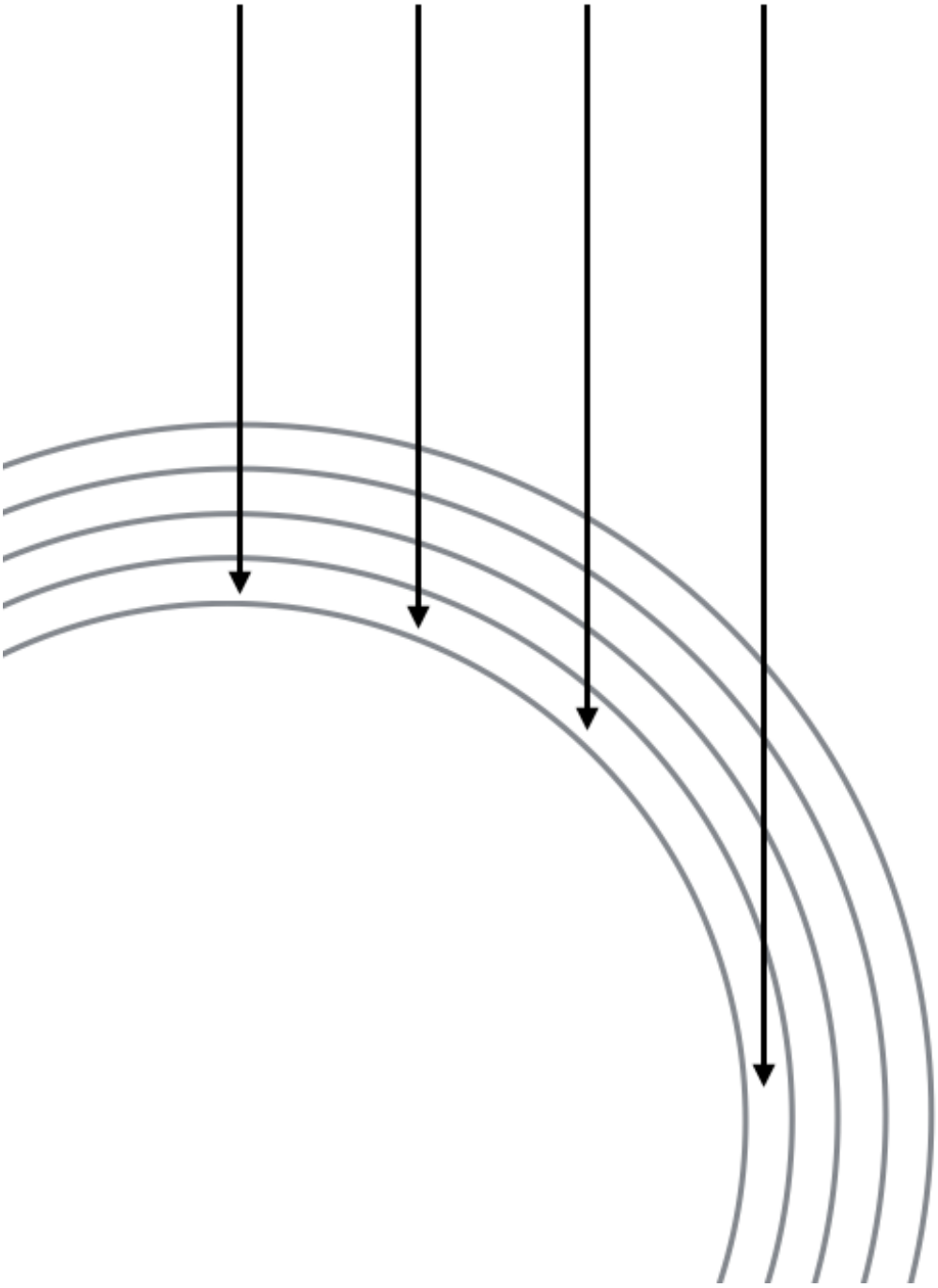

Figure 5.5: Diagram showing incoming solar radiation passing through layers of a model atmosphere. On the left, solar light is on a nadir path, and crosses each layer boundary at the same angle. As zenith angle increases, towards the right of the diagram, the incoming beam crosses each layer at a different angle. Using a plane-parallel approximation for scattering of light, where each layer is crossed at the same angle, thus loses accuracy as zenith angle increases.

zenith angle, and a small change to the resulting spectrum. A one pixel error at the limb of the planet, however, corresponds to a zenith angle difference of more than 10 degrees. That large a difference in zenith angle means the change to the spectrum will be larger as well.

Based on this third source of geometric error, it was determined that an additional uncertainty needed to be added to the observational data to account for geometric errors introduced as the zenith angle increased. In order to compute this value, a line of adjacent pixels was chosen that followed the bright band at 30° S latitude where a good-fitting, near-nadir model had been retrieved. Pixels from close to the nadir of the planet to the limb (see figure 5.6) were used to produce a series of zenith angles at which to produce forward-model synthetic spectra. For each wavelength in the spectral range, the difference between adjacent pixels' synthetic model spectra was calculated, effectively giving us a proxy to the error that would be caused by a single pixel difference in geometry. Note that the pixels from the centre of the planet towards the left limb, which might have produced *retrieval* results that were systematically inaccurate in the opposite direction than retrieval results from those points chosen (figure 5.6). Despite this, these pixels on the left half of the planet did not need to be considered because they had identical zenith angles to those on the right, and so would produce identical *forward model* results, and thus identical difference values for our error proxy. Also recall that the spatial resolution should never have produced an error of more than 1 pixel in either direction (see table 2.3). Therefore, smoothing this difference curve slightly, as shown by the example in figure 5.7, provided a reasonable estimate of how much additional error to add to observational uncertainty based on zenith angle.

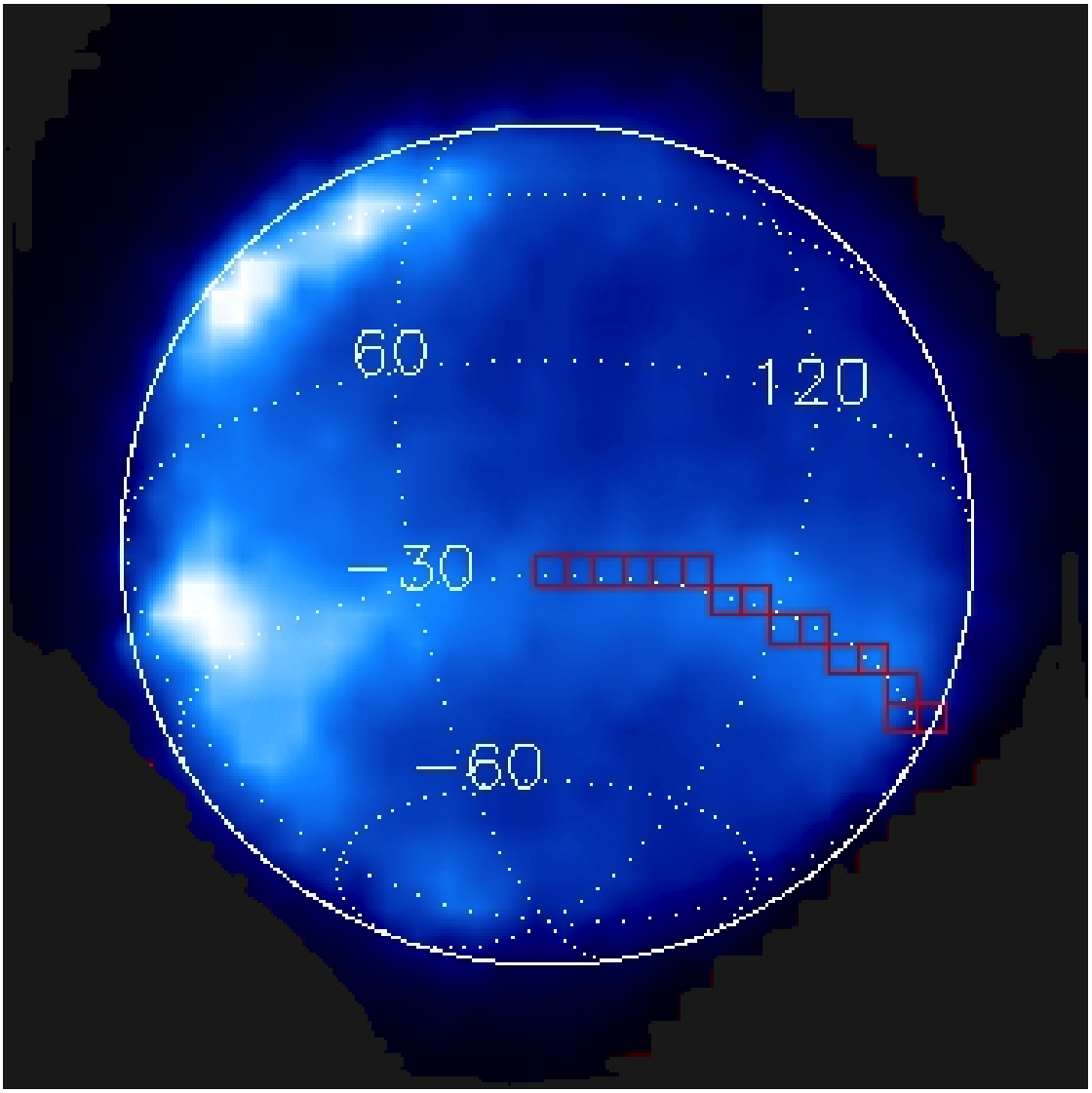

Figure 5.6: SWIFT image of Neptune captured at 10:49 UTC on 2 July 2012 that shows pixels used to generate synthetic spectra for use in calculating geometric error. From centre of image, pixels selected were all adjacent, and had zenith angles of 4°, 6°, 9°, 13°, 17°, 21°, 26°, 30°, 36°, 41°, 48°, 54°, 64°, 68°, and 81°. If comparisons had been made between these synthetic spectra and observational data, a swath from one limb to the other would have needed to be used, rather than just from the centre of the planet. Because the error estimation was based solely on synthetic forward model spectra, this was unnecessary, as the points shown here provided a complete error estimation for all zenith angles between 0° and 90°.

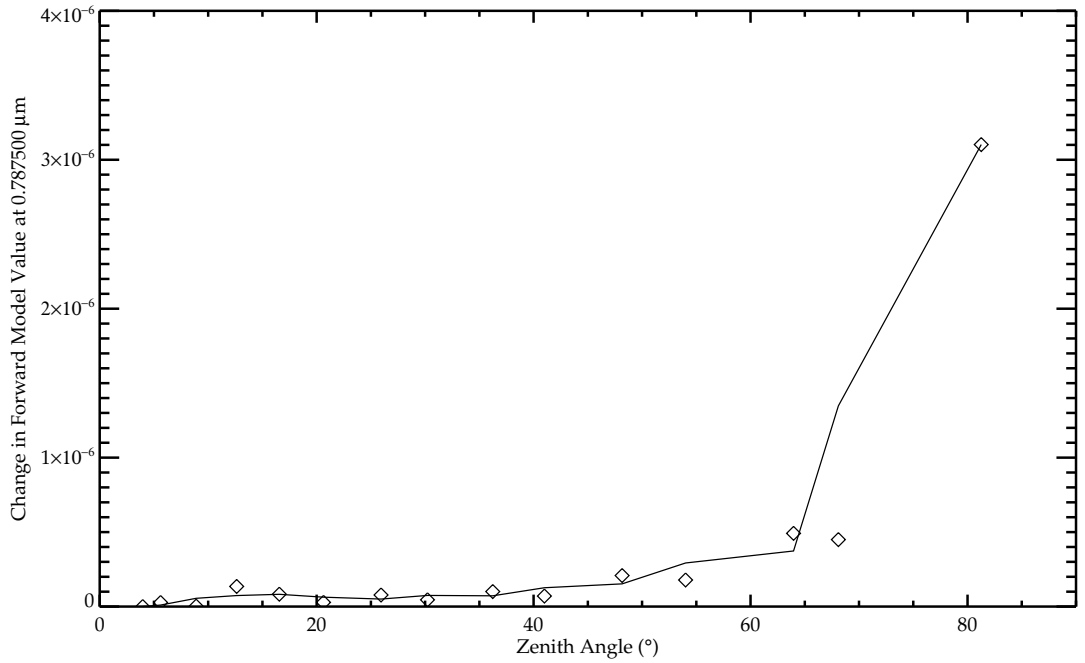

Figure 5.7: This sample shows the method of determining how much additional 'geometric error' to add to observational uncertainty in SWIFT data based on zenith angle. In this plot, the diamonds are the differences between adjacent pixels' forward-model spectra at 0.7875 µm. The solid line traces these points with very slight smoothing. For an observation at a certain zenith angle, this curve is used to determine how much additional error to add to the random uncertainty of the observation. The process is repeated at every wavelength and for observations of any zenith angle needed. As can be clearly seen, trustworthiness of observations past 65° zenith angles becomes drastically reduced.

5.3 Early Results

During the tests described in section 5.2.2, it was discovered that to run retrievals with nine zenith angles, even when resampling the data so that the spectra of all nine zenith angles could be stored in a standard 1024 number array within NEMESIS, was computationally very expensive. After each iteration of the optimal estimation retrieval scheme, computing the forward model, which required a scattering calculation at each point in the spectrum for each zenith angle was highly time consuming, particularly at the higher zenith angles. This decrease is speed is because at high zenith angles, many additional Fourier components are required in the azimuth decomposition. Given the deadline for completion of this thesis, it became impractical to proceed with this method of analysis because each retrieval would take approximately 1 week of computational time.

Analysis which included any zenith angle higher than approximately 65° was abandoned, because the higher zenith angles were associated with the largest observational uncertainty, as discussed in section 5.2.2, and were also the most computationally expensive. Analysis of the bright belt of latitude around 30° N required us to make an exception to this rule, because only one zenith angle below 65° was available given the distance from the sub-Earth point to the centre of this latitude region on the disc. Unfortunately, this improvement in computational time still did not yield sufficiently rapid retrievals, with each retrieval still taking about half a week.

To make one additional improvement in computational time, which ultimately allowed retrievals to finish on the order of several hours rather than several days, only approximately 10 points of the spectrum were retrieved, judiciously choosing points that covered nearly the entire wavelength range and placed approximately equal emphasis on relative maxima (where methane windows allowed light transmission and reflection off of the deep, opaque cloud layer) and relative minima (where light reached only shallowly into the atmosphere to be reflected by the stratospheric

hazes before it was absorbed by methane). Once these retrievals were complete, it was possible to compute, in less than an hour, the forward model for the entire spectrum, in order to see how the retrieved model fit all the spectral points in the observational data.

This section presents the results of this modified analysis technique. As mentioned earlier in section 5.2.1, values for TC fractional scale height were still fixed, as well as either the fractional scale height or the base altitude of the UH. Accordingly, a range of retrievals were performed in hopes of using goodness-of-fit values to determine a preference for fractional scale height and base altitude of the UH. Finally, a small number of 'control' retrievals were conducted where all zenith angles were used as a means of testing how costly the reduction in zenith angles was to the results. The results of all of this are presented in this section, with results divided into subsections for each latitude band analysed: 5.3.1: Bright Band at 30° S, 5.3.3: Dark Equatorial Band, and 5.3.4: Bright Band at 30° N. A brief review of a control test at 30° S, along with its implications is also included in section 5.3.2, between the Bright Band at 30° S and Dark Equatorial Band subsections.

5.3.1 Bright Band at 30° S

In the southern midlatitudes of Neptune, there exists a stable, long-lived band of bright clouds that has been visible since the *Voyager* era. At the time of the 2012 SWIFT observations of the planet, this latitude band of clouds passed very close to the centre-of-disc, providing us with the widest range of zenith angles of any noticeable features on the planet (see figure 5.8). Early attempts were made to retrieve a fit using spectra of sample rate $\Delta\lambda = 0.0033$ μm at eight zenith angles ranging from $4.0° \leq \theta \leq 81.3°$. The eight selected zeniths corresponded to those that were located closest to the nine zenith angles defined in the new NEMESIS quadrature scheme. To improve the computational speed of these attempts, as noted above, it was elected

to use spectra containing 13 points that defined each local minima and maxima of the spectrum, and to retrieve free cloud parameters at four simultaneous zenith angles. The 4° angle was chosen in order to make sure reflectance peaks that probed the deep cloud would be constrained, and the other three, higher-zenith angles were chosen to attempt to best constrain the upper hazes.

Though more tests are needed to fine-tune the results, the latest retrievals do display some general trends. The retrievals seem to be favouring TCs with particle radii 1.0 μm $\lesssim r \lesssim$ 1.1 μm and base altitudes of 4.0 bar $\lesssim p \lesssim$ 4.5 bar. Favoured UHs seem to have particles of 0.25 μm $\lesssim r \lesssim$ 0.30 μm, though further tests are required to determine exactly which fractional scale height, opacity, and base altitude combinations produce the best fits. It is likely that to answer this question properly, additional zenith angles will be required, which of course will increase the analysis time severely.

Table 5.1 and figures 5.9 – 5.14 show example results of one of the best-fitting retrievals of the bright cloud at 30° S, which achieved a $\chi^2/\mathrm{n_y} = 3.46$. These results were achieved by fixing the UH fractional scale height to 1.0. Table 5.1 summarises for the example retrieval the *a priori* and retrieved values of the three cloud parameters and the particle size distribution for both clouds in the model. The table also includes an 'Improvement Factor', listed as a percentage, which quantifies how much additional constraint was achieved for each model parameter when compared with the *a priori* constraint. For base altitude, in which the *a priori* error, σ, is the standard deviation of the value x, this improvement factor is equal to $\left(1 - \frac{\sigma_{\mathrm{ret}}}{\sigma_{\mathrm{apr}}}\right) \times 100$ where 'ret' denotes the retrieved value and 'apr' denotes the *a priori* value. In the case of the other four quantities in the table, the errors are actually given as fractional errors, ς, where $\ln \varsigma$ is the standard deviation of the value $\ln x$. For these values, the improvement factor listed is $\left(1 - \frac{\varsigma_{\mathrm{ret}}/x_{\mathrm{ret}}}{\varsigma_{\mathrm{apr}}/x_{\mathrm{apr}}}\right) \times 100$.

Figure 5.9 shows a graphical representation of the results from the table. As can

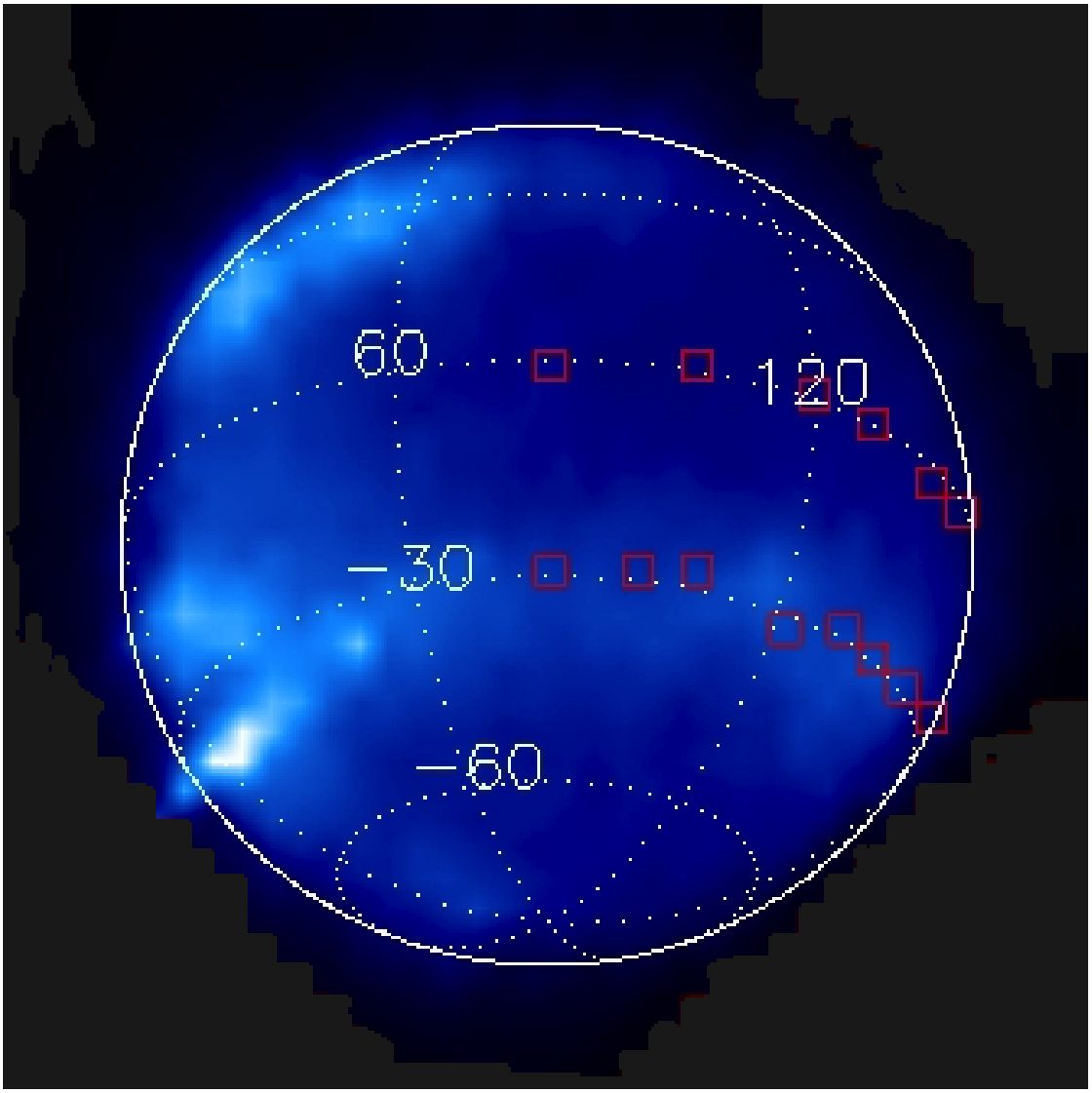

Figure 5.8: Image of Neptune recorded on 02 Jul 2012 at 10:17 UTC. Red boxes indicate which eight pixels were selected for different viewing angles of the bright band at 30° S and which six were selected for the dark band at 0° latitude.

Table 5.1: Retrieval results for the physical parameters of the Neptunian clouds at 30° S. 'τ' denotes total opacity of cloud, 'Base' denotes base altitude of cloud, 'FSH' denotes fractional scale height, 'a' is the mean radius of the standard gamma particle size distribution, and 'b' is the associated variance. The errors associated with these values are fractional in every case except base altitude, in which a traditional standard deviation is listed. The improvement factor for values with fractional errors, presented as a percentage, is equal to $\left(1-\frac{\varsigma_{\rm ret}/x_{\rm ret}}{\varsigma_{\rm apr}/x_{\rm apr}}\right)\times 100$ where 'ret' denotes retrieved values, 'apr' denotes *a priori* values, and $\ln\varsigma$ is the standard deviation of the value $\ln x$. The improvement factor for base altitude is simply $\left(1-\frac{\sigma_{\rm ret}}{\sigma_{\rm apr}}\right)\times 100$ where σ is the standard deviation.

Cloud Deck	Parameter	*A priori* Value	Error	Retrieved Value	Error	Improvement Factor (%)
TC	τ	1.0	0.5	2.3	0.3	70
	Base	-18 ± 10 km		-43 ± 8 km		20
	FSH			0.1	[fixed]	
	a	1.0μm	0.2μm	1.09 μm	0.05 μm	80
	b	0.050	0.005	0.049	0.005	0
UH	τ	0.1	0.05	0.18	0.04	60
	Base	44 ± 10 km		-2 ± 3 km		70
	FSH			1.0	[fixed]	
	a	0.1 μm	0.02 μm	0.26 μm	0.03 μm	40
	b	0.050	0.005	0.043	0.004	7

be seen in the figure, the TC has a cloud-top[1] pressure of $p=3.4$ bar and a total opacity of approximately $\tau=2.3$ (13% uncertainty) at 1.0 μm. The UH has a base altitude of $p=1.0$ bar ($h=-2$ km) and a total opacity of $\tau=0.18$ (22% uncertainty) at 1.0 μm. Figure 5.10 shows retrieved refractive indices of the TC, and figure 5.11 shows the retrieved particles sizes as well as self-consistently modelled single-scattering albedos, extinction cross-sections, and Henyey-Greenstein parameters for these particles. The results for the UH are shown in figures 5.12 and 5.13. Finally, the fit is shown at the four selected zenith angles in figure 5.14.

[1]For all discussion of SWIFT Neptune results, the cloud-top of the TC will be defined as the location in the cloud above which the total optical depth at 1.0 μm is 1.0.

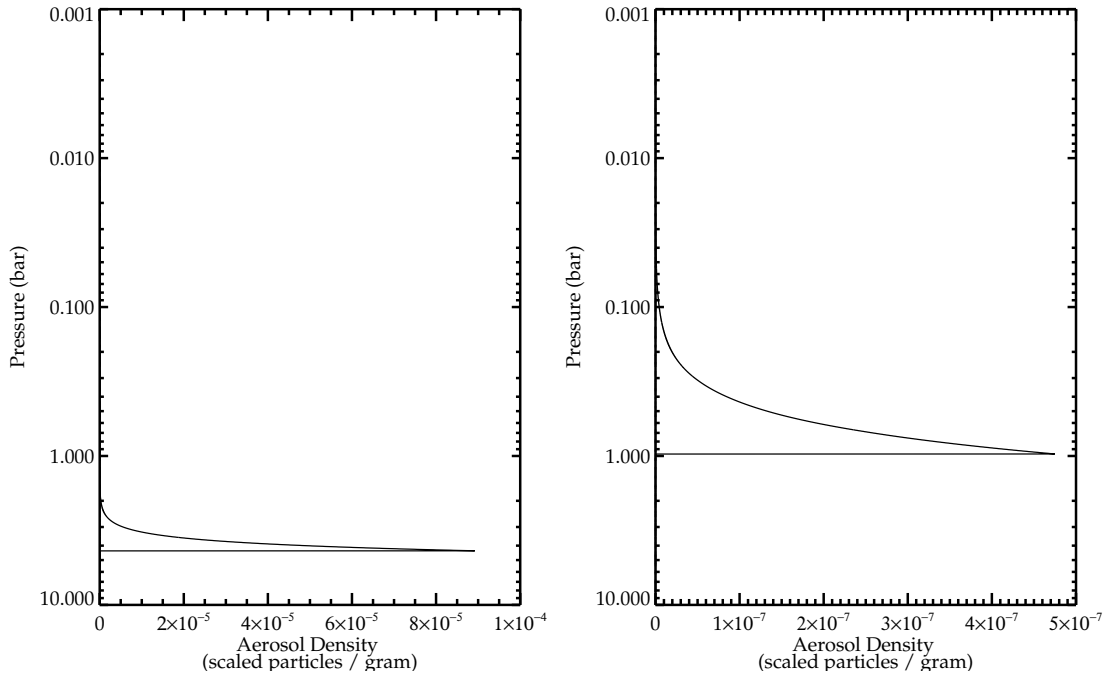

Figure 5.9: Retrieval results for the physical parameters of the Neptunian clouds at 30° S. The left panel shows the TC, which has a total opacity of $\tau = 2.3$ (13% uncertainty) at 1.0 μm, and the right panel the UH, which has a total opacity of $\tau = 0.18$ (22% uncertainty) at 1.0 μm.

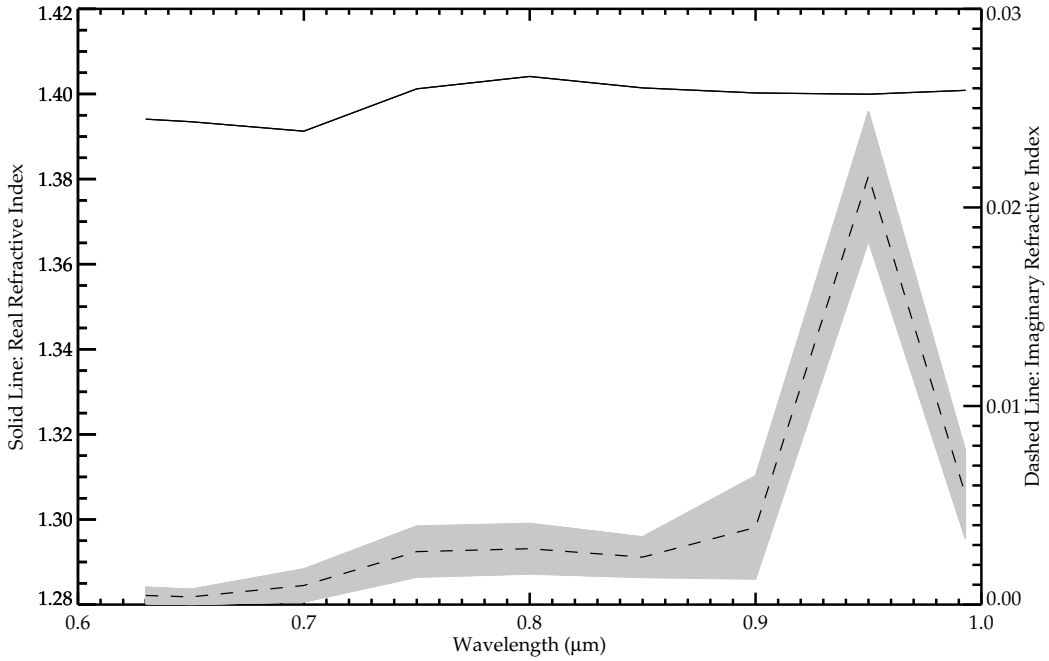

Figure 5.10: Retrieval results for the refractive index of the TC at the Neptunian bright band at 30° S. The dashed line (right axis) shows the retrieved imaginary part of the refractive index of aerosol particles in the TC, with error shown in grey. The solid line (left axis) shows the real part of the refractive index, calculated from the imaginary part with a Kramers-Kronig analysis using a reference value for the real refractive index at 1.0 μm of $n = 1.4$.

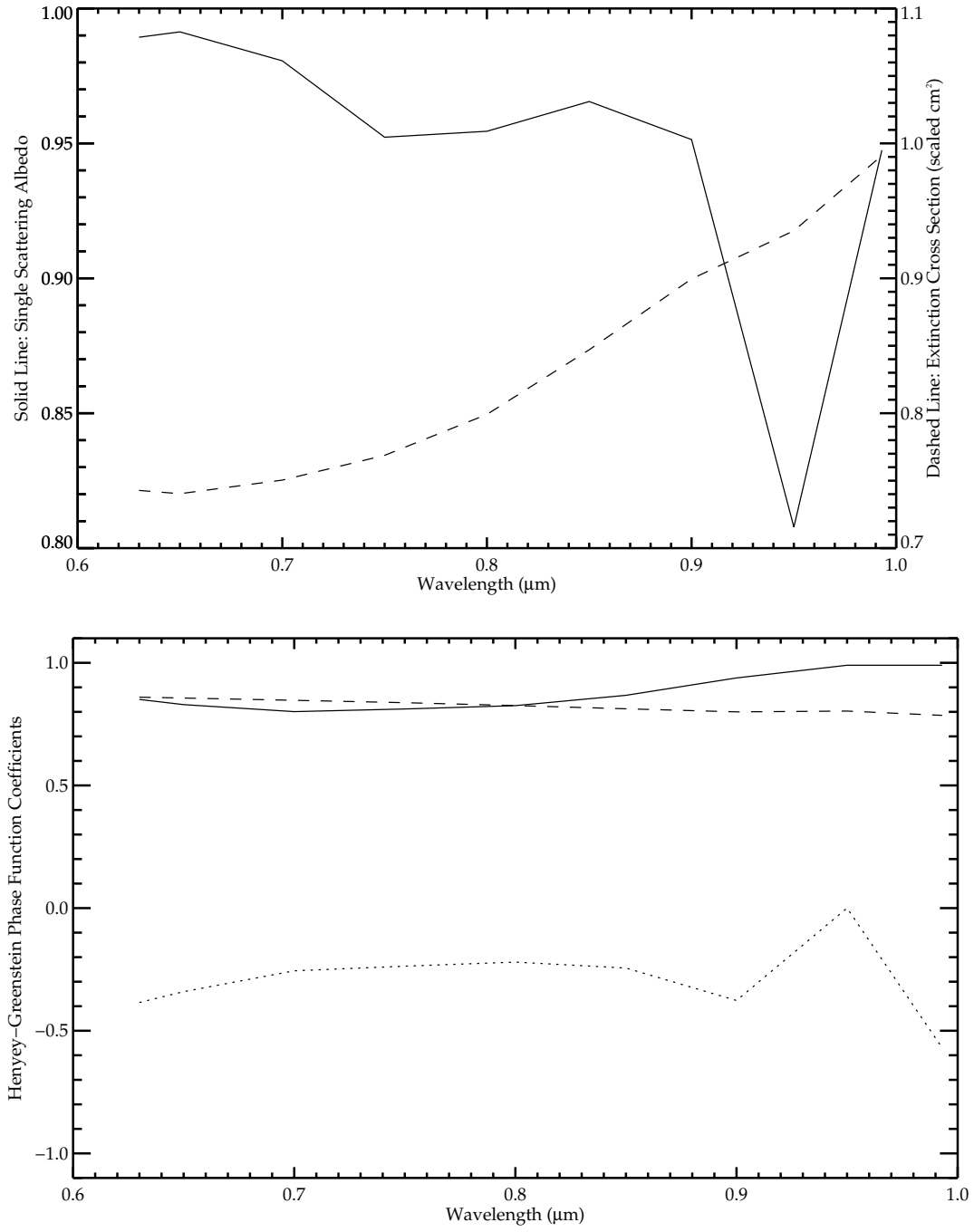

Figure 5.11: Self-consistently modelled aerosol cloud particle parameters for the TC in the Neptunian bright band at 30° S. Starting with the refractive indices shown in figure 5.10 and the retrieved particle size distribution, shown in table 5.1, the self-consistent single-scattering albedo and extinction cross-sections for particles in the TC are calculated. The results for single-scattering albedo (solid line, left axis) and extinction cross-section (dashed line, right axis) are shown in the upper panel. Note that the extinction cross-section has been normalised so that it equals 1.0 cm^2 at 1.0 μm. The lower panel shows the self-consistent Henyey-Greenstein parameters of the derived phase function. The solid line represents f, while g_1 and g_2 are the dashed line and dotted line, respectively.

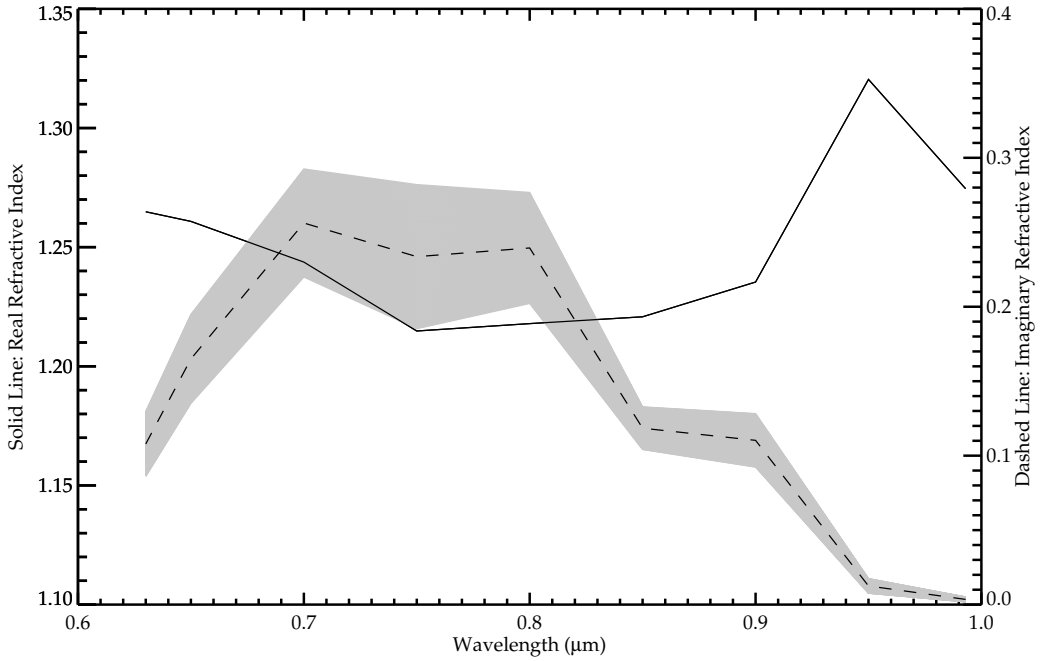

Figure 5.12: Retrieval results for the refractive index of the UH at the Neptunian bright band at 30° S. The dashed line (right axis) shows the retrieved imaginary part of the refractive index of aerosol particles in the UH, with error shown in grey. The solid line (left axis) shows the real part of the refractive index, calculated from the imaginary part with a Kramers-Kronig analysis using a reference value for the real refractive index at 1.0 μm of $n = 1.4$. .

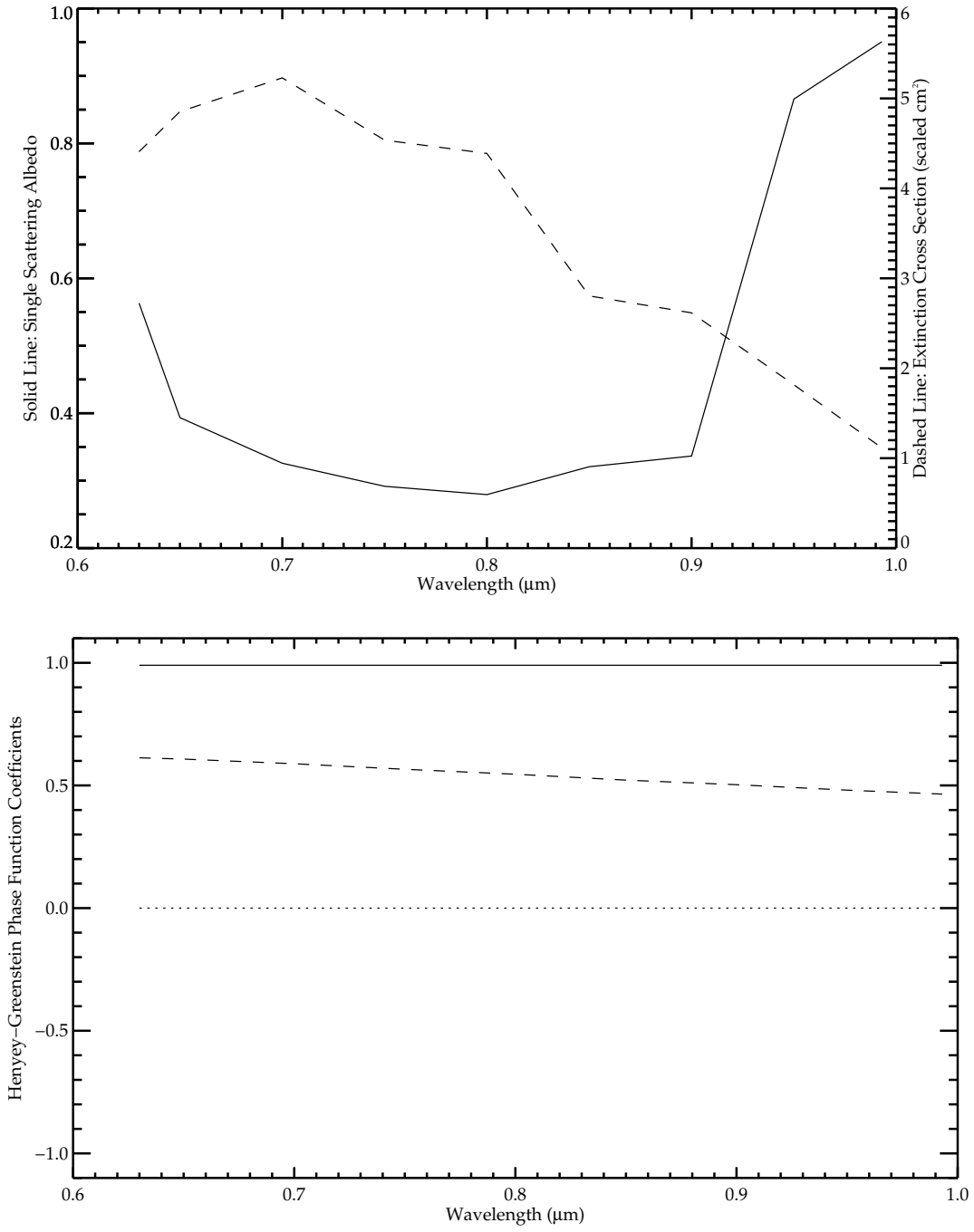

Figure 5.13: Self-consistently modelled aerosol cloud particle parameters for the UH in the Neptunian bright band at 30° S. Starting with the refractive indices shown in figure 5.12 and the retrieved particle size distribution, shown in table 5.1, the self-consistent single-scattering albedo and extinction cross-sections for particles in the UH are calculated. The results for single-scattering albedo (solid line, left axis) and extinction cross-section (dashed line, right axis) are shown in the upper panel. Note that the extinction cross-section has been normalised so that it equals 1.0 cm^2 at 1.0 μm. The lower panel shows the self-consistent Henyey-Greenstein parameters of the derived phase function. The solid line represents f, while g_1 and g_2 are the dashed line and dotted line, respectively. Notice that $g_2 \simeq 0$, which indicates that while the forward scattering peak (g_1) was constrained by the retrieval, the backscattering peak was not, and remained at the *a priori* value of 0.

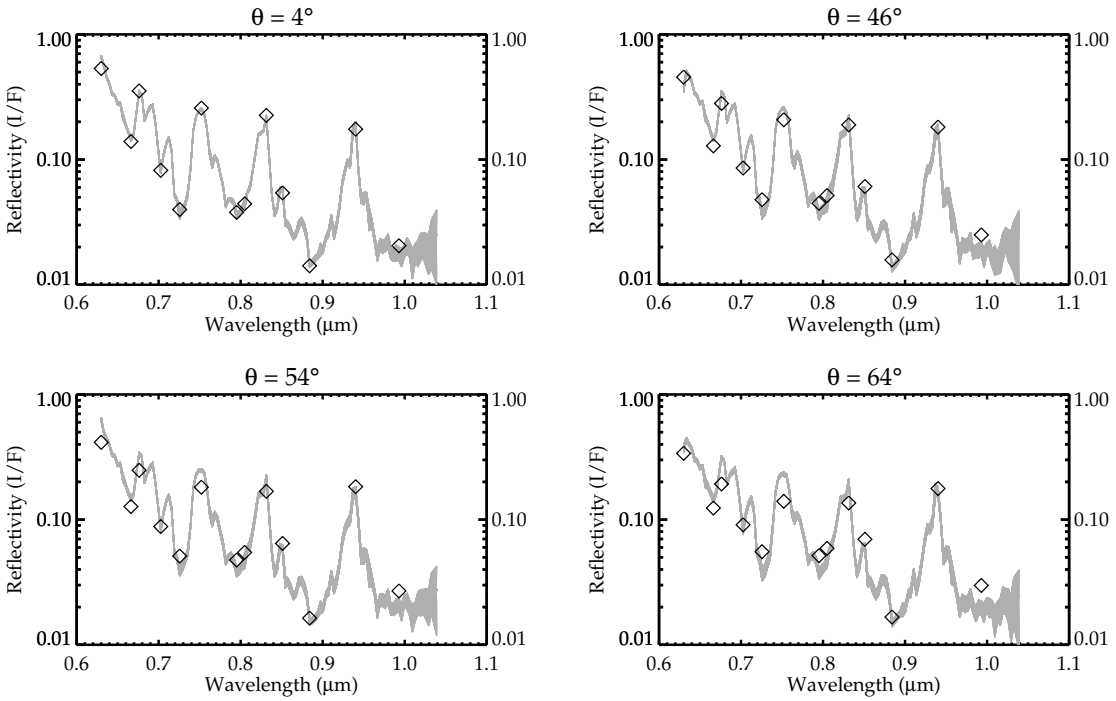

Figure 5.14: The model fit to data at 30° S is shown at the four zenith angles retrieved, as indicated above each panel. Diamonds on the plots are the spectral points that were retrieved, while the grey spectrum is the observational data and total uncertainty (random noise, geometric error, and forward-modelling error). Goodness-of-fit for the model is $\chi^2/n_y = 3.46$.

5.3.2 Control Test at 30° S

A control test was performed in an attempt to determine how large an impact the reduction of spectral points and zenith angles had on retrieval results. In the control run, all eight zenith angles were retrieved simultaneously using spectra composed of 124 wavelengths. The control was performed for a retrieval in which the UH base altitude was fixed at 1.0 bar, and the UH fractional scale height was retrieved. The results of this retrieval were quite good, achieving a goodness-of-fit parameter of $\chi^2/n_y = 2.96$. It is interesting to note that this control test retrieved a value of 1.23 ± 0.05 for the UH fractional scale height, which is at least in the same order of magnitude as the 'preferred' value that was noticed in the quicker runs. However, since this retrieval was not fixed at the preferred fractional scale height of 1.0, the full results of the retrieval will not be presented. Only the spectral fits will be shown at each zenith angle, which can be seen in figure 5.15.

In order to answer the question of how costly the reduction of zenith angles and spectral points is, the results were used of the corresponding four-zenith, 13-point retrieval in which UH base altitude was fixed at 1.0 bar. Using the model retrieved in this run, model spectra of 124 wavelengths were constructed for 8 zenith angles, plotting these model spectra against the observational data in exactly the same fashion as the control retrieval had done. These plots are shown in figure 5.16. The goodness-of-fit parameter for these forward models was $\chi^2/n_y = 14.5$. The χ^2/n_y improvement by more than one order of magnitude, and a comparison of the visual fit between figure 5.15 and figure 5.16 make it clear that the impact of reducing the spectral points and zenith angles is severe. While we have been able to retrieve models with good fits to observational data, it is abundantly clear that if time permitted, returning to retrievals of all possible zenith angles and spectral points would be preferable, and would produce significantly improved results.

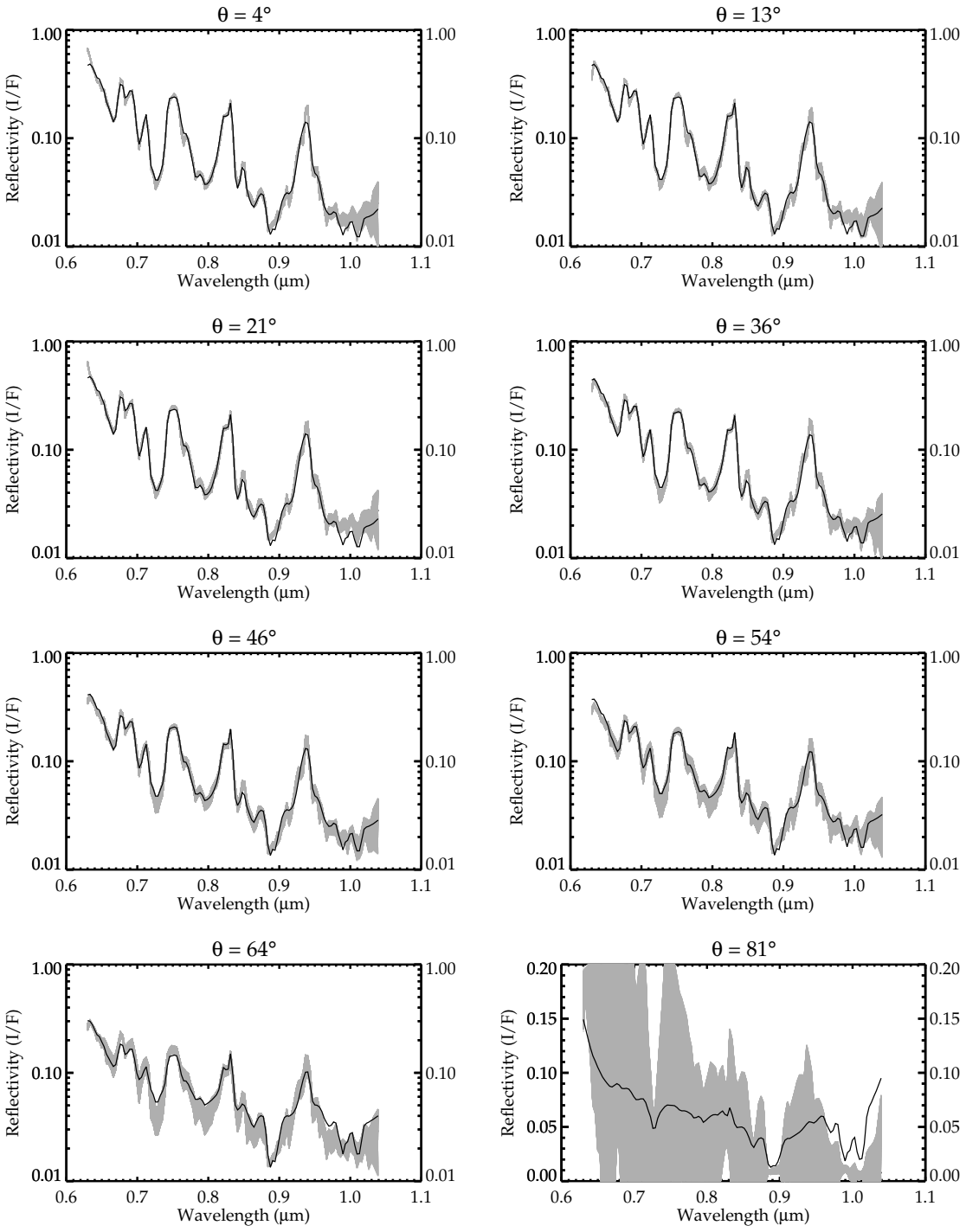

Figure 5.15: The model fit to data at 30° S is shown at the eight zenith angles retrieved, as indicated above each panel, with a more thoroughly sampled spectrum. The solid line on the plots is the model spectrum composed of 124 spectral locations, while the grey spectrum is the observational data and total uncertainty (random noise, geometric error, and forward-modelling error). Note that the final zenith angle has been plotted in a linear scale due to the size of its total uncertainty, which would not fit cleanly on a logarithmic scale like the other plots. Goodness-of-fit for this model is $\chi^2/n_y = 2.96$.

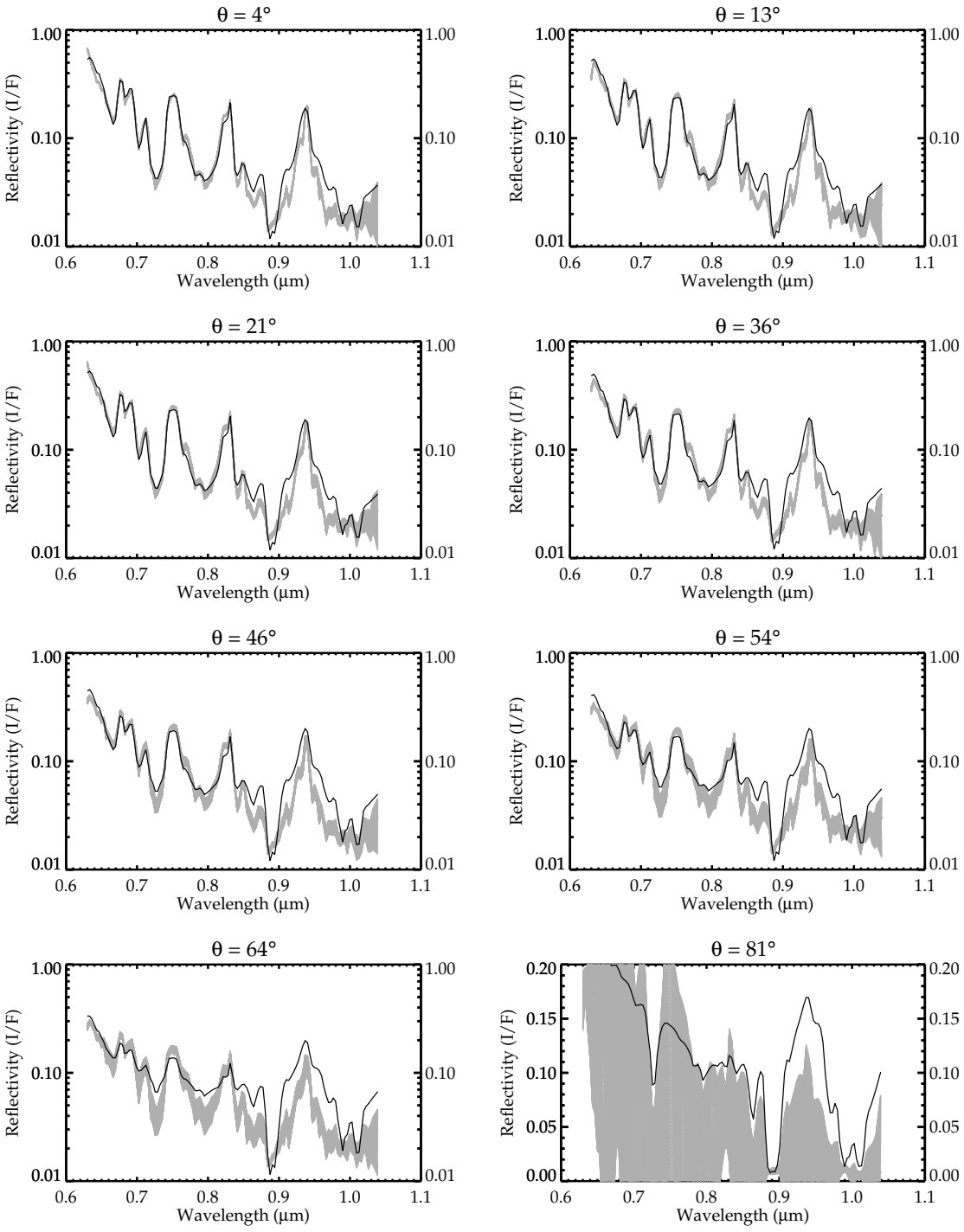

Figure 5.16: The model fit to data at 30° S is shown at the eight zenith angles used in the control, as indicated above each panel, with a more thoroughly sampled spectrum. The solid line on the plots shows the model used in these plots, which came not from the eight-zenith, 124-spectral point control but from the corresponding four-zenith, 13-spectral point retrieval with the same *a priori* and fixed values. The grey spectrum is the observational data and total uncertainty (random noise, geometric error, and forward-modelling error) at all zenith angles and 124 spectral locations. Note that the final zenith angle has been plotted in a linear scale due to the size of its total uncertainty, which would not fit cleanly on a logarithmic scale like the other plots. Goodness-of-fit for this model is $\chi^2/n_y = 14.5$, compared with $\chi^2/n_y = 2.96$ when retrieving at all eight zenith angles and 124 spectral locations (see figure 5.15).

5.3.3 Dark Equatorial Band

Behind the discrete features that constantly dance across the Neptunian surface, another long-lived feature appears at the equator. Compared with the band just examined at 30° S, the equator plays host to a belt that is much darker. Though not quite as close to the centre-of-disc in the 2012 observations, SWIFT still has access to a good spread of zenith angles from $24° \leq \theta \leq 75°$. Just as described in the section 5.3.1, initial attempts were made with all zenith angles near the defined zenith quadrature values and as many spectral locations as would fit within the standard 1024 array. This equated, in this case, to six zenith angles and a sampling size of $\Delta\lambda = 0.0025$ μm. The pixel locations of the selected zenith angles are shown in figure 5.8. Without sufficient time to run these week-long retrievals, 13 spectral locations and four zenith angles were selected, just as before, to use for retrievals.

The results at the equatorial band are a bit contradictory. About a third of the tests, which we will call group 'α', converged to a comparable χ^2/n_y value to the example shown for 30° S, specifically in the range of $1.5 \lesssim \chi^2/n_y \lesssim 2.5$. The preferred UH in group α retrievals was markedly different than those at 30° S. This set of UH results, when compared with those at 30° S, converged on a particle size of about $r \simeq 0.02$ μm, a full order of magnitude smaller than 30° S. Also markedly different in the group α UH were imaginary indices nearly three orders of magnitude smaller, and a derived phase function with a backscattering peak of equal strength to the forward peak (recall no backscattering convergence occurred at 30° S). The UH in group α was at a higher location in the atmosphere (base at 0.1 bar instead of 1.0 bar), had a particle density one order of magnitude less, but had comparable fractional scale height. In the group α TC, the imaginary refractive index of the particles in these retrievals was also about an order of magnitude smaller the same parameter at 30° S, though the shape of the spectrum of imaginary indices was similar, i.e. with flat with a sharp upward feature at about 0.95 μm.

The other two thirds of the results converged upon a different type of solution, and generally had $7 \lesssim \chi^2/n_y \lesssim 10$. UH results in this group, which we will call group 'β' had imaginary refractive indices, particles sizes ($r \simeq 0.25$ μm), and phase functions nearly identical to those retrieved at 30° S, though the haze was generally much thinner both vertically (fractional scale height of 0.1) and optically (approximately half the particle density). In group β, it was the TC which was most different from 30° S. The group β TC particle imaginary refractive index had a similar magnitude to that at 30° S, but the only feature, a sharp increase in magnitude, was found at 0.75 μm rather than 0.95 μm like at 30° S.

There are aspects of both group α and group β that seem reasonable. For example, the UH in both these groups will impact the spectrum much less than the haze at 30° S, which is what would be expected given the darker nature of the 0° band. Also reasonable was that both groups showed comparable improvement factors for the model variables, though it should be noted that the thinner haze made both groups unable to improve values for the UH fractional scale height or base altitude, whichever was free. Perhaps the most alarming aspect of both 0° retrieval groups is that the TC imaginary refractive index is also markedly different than that found at 30° S, which would not be expected. Even if the TC had changed opacity, height, or scale height, it presumably would contain the same type of particles, something which seems to be unlikely when comparing the refractive indices. Just as at 30° S, it seems that to argue definitively in favour of one group over the other would require retrievals performed with more zenith angles or increased spectral sampling rates.

To present a sample of results at this latitude, we elected to display a group α result for two reasons. First, this retrieval group had models which better reproduced the observational spectrum. Second, the one 'control' test performed, with full spectral sampling and eight zenith angles, fell into this group. The specific example chosen had a free UH base altitude and a fixed base fractional scale height of 1.0. This

Table 5.2: Retrieval results for the physical parameters of the Neptunian clouds at 0° S. 'τ' denotes total opacity of cloud, 'Base' denotes base altitude of cloud, 'FSH' denotes fractional scale height, 'a' is the mean radius of the standard gamma particle size distribution, and 'b' is the associated variance. The errors associated with these values are fractional in every case except base altitude, in which a traditional standard deviation is listed. The improvement factor for values with fractional errors, presented as a percentage, is equal to $\left(1-\frac{\varsigma_{\mathrm{ret}}/x_{\mathrm{ret}}}{\varsigma_{\mathrm{apr}}/x_{\mathrm{apr}}}\right)\times 100$ where 'ret' denotes retrieved values, 'apr' denotes *a priori* values, and $\ln\varsigma$ is the standard deviation of the value $\ln x$. The improvement factor for base altitude is simply $\left(1-\frac{\sigma_{\mathrm{ret}}}{\sigma_{\mathrm{apr}}}\right)\times 100$ where σ is the standard deviation.

Cloud Deck	Parameter	*A priori* Value	Error	Retrieved Value	Error	Improvement Factor (%)
TC	τ	1.0	0.5	2.0	0.3	70
	Base	-18 ± 10 km		-40 ± 5 km		50
	FSH			0.1	[fixed]	
	a	1.0μm	0.2μm	1.08 μm	0.04 μm	80
	b	0.050	0.005	0.050	0.005	0
UH	τ	0.1	0.05	0.05	0.02	20
	Base	44 ± 10 km		48 ± 10 km		0
	FSH			1.0	[fixed]	
	a	0.1 μm	0.02 μm	0.022 μm	0.003 μm	30
	b	0.050	0.005	0.047	0.005	7

was the preferred fractional scale height among the group α results. Table 5.2 and figures 5.17 – 5.22 show example results for one of the best group α equatorial retrievals in the same format as those results shown in section 5.3.1 (30° S). These results are characterised by a goodness-of-fit of $\chi^2/\mathrm{n_y}=1.76$.

As shown in table 5.2 and figure 5.17, this retrieval produced a model TC with a cloud-top pressure of $p=3.4$ bar and a total opacity of approximately $\tau=2.0$ (30% uncertainty) at 1.0 μm. This is slightly less opaque than the cloud retrieved at 30° S, but the values do agree within their uncertainties. Both clouds are very similar in vertical thickness and altitude.

In the same table and figure, notice that the retrieved UH at the equator has a base

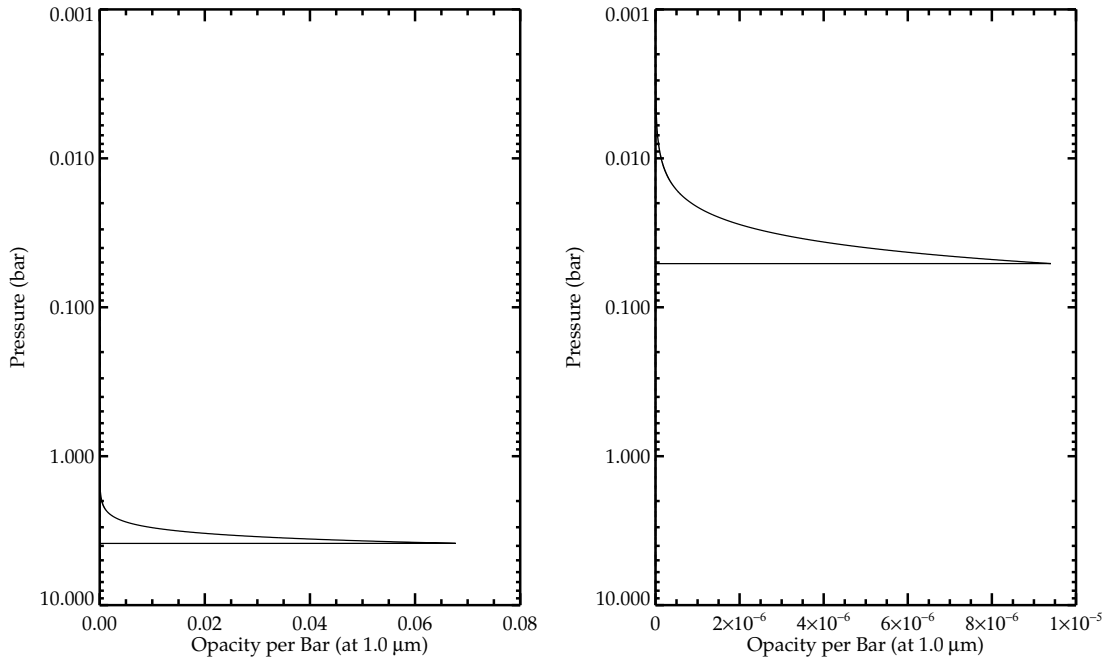

Figure 5.17: Retrieval results for the physical parameters of the Neptunian clouds at 0° latitude. The left panel shows the TC, which has a total opacity of $\tau = 2.0 \pm 0.3$ at 1.0 μm, and the right panel the UH, which has a total opacity of $\tau = 0.05 \pm 0.02$ at 1.0 μm.

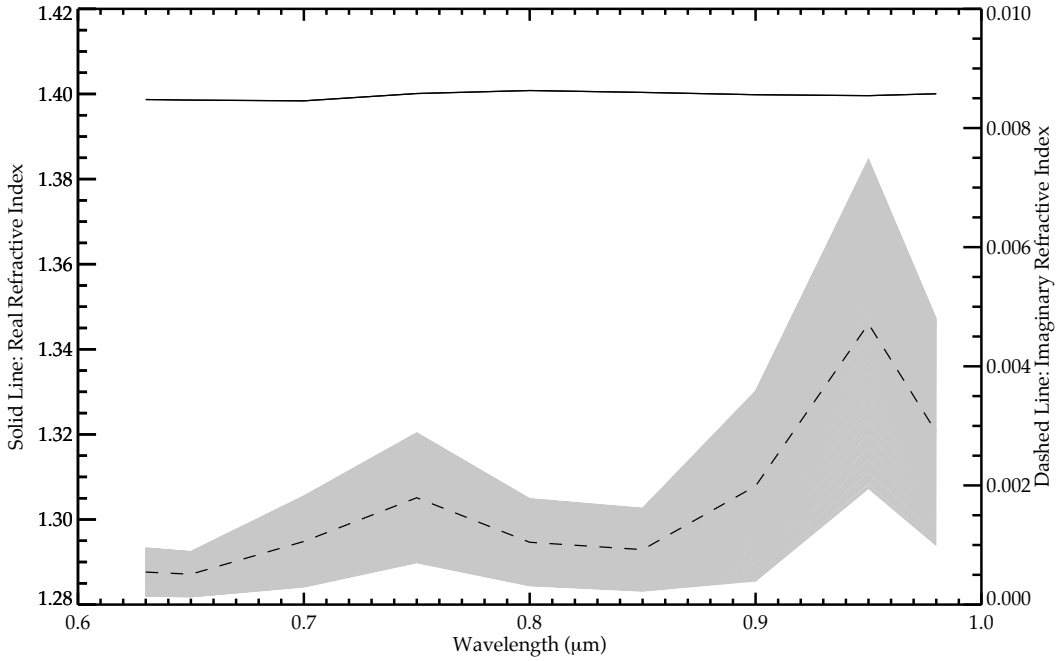

Figure 5.18: Retrieval results for the refractive index of the TC at the Neptunian dark band at 0° latitude. The dashed line (right axis) shows the retrieved imaginary part of the refractive index of aerosol particles in the TC, with error shown in grey. The solid line (left axis) shows the real part of the refractive index, calculated from the imaginary part with a Kramers-Kronig analysis using a reference value for the real refractive index at 1.0 μm of $n = 1.4$.

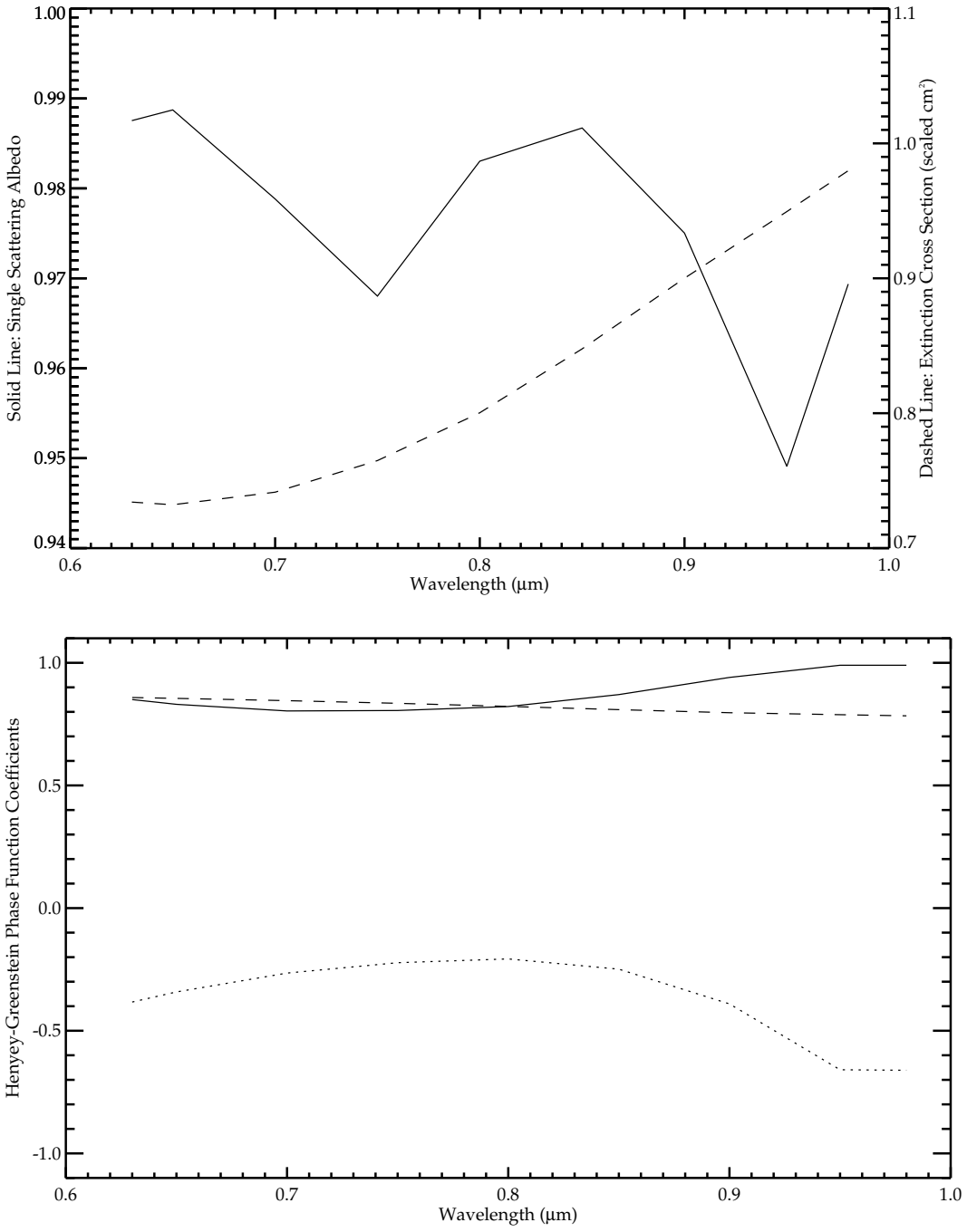

Figure 5.19: Self-consistently modelled aerosol cloud particle parameters for the TC in the Neptunian dark band at 0° . Starting with the refractive indices shown in figure 5.18 and the retrieved particle size distribution, shown in table 5.2, the self-consistent single-scattering albedo and extinction cross-sections for particles in the TC are calculated. The results for single-scattering albedo (solid line, left axis) and extinction cross-section (dashed line, right axis) are shown in the upper panel. Note that the extinction cross-section has been normalised so that it equals 1.0 cm^2 at 1.0 µm. The lower panel shows the self-consistent Henyey-Greenstein parameters of the derived phase function. The solid line represents f, while g_1 and g_2 are the dashed line and dotted line, respectively.

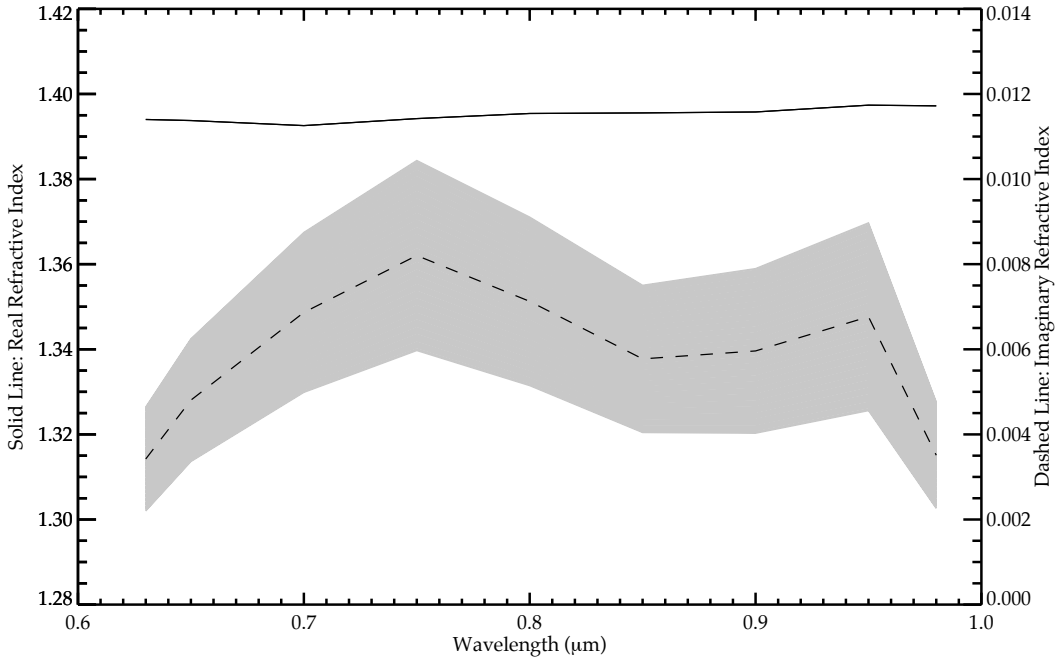

Figure 5.20: Retrieval results for the refractive index of the UH at the Neptunian dark band at 0° latitude. The dashed line (right axis) shows the retrieved imaginary part of the refractive index of aerosol particles in the UH, with error shown in grey. The solid line (left axis) shows the real part of the refractive index, calculated from the imaginary part with a Kramers-Kronig analysis using a reference value for the real refractive index at 1.0 μm of $n = 1.4$. .

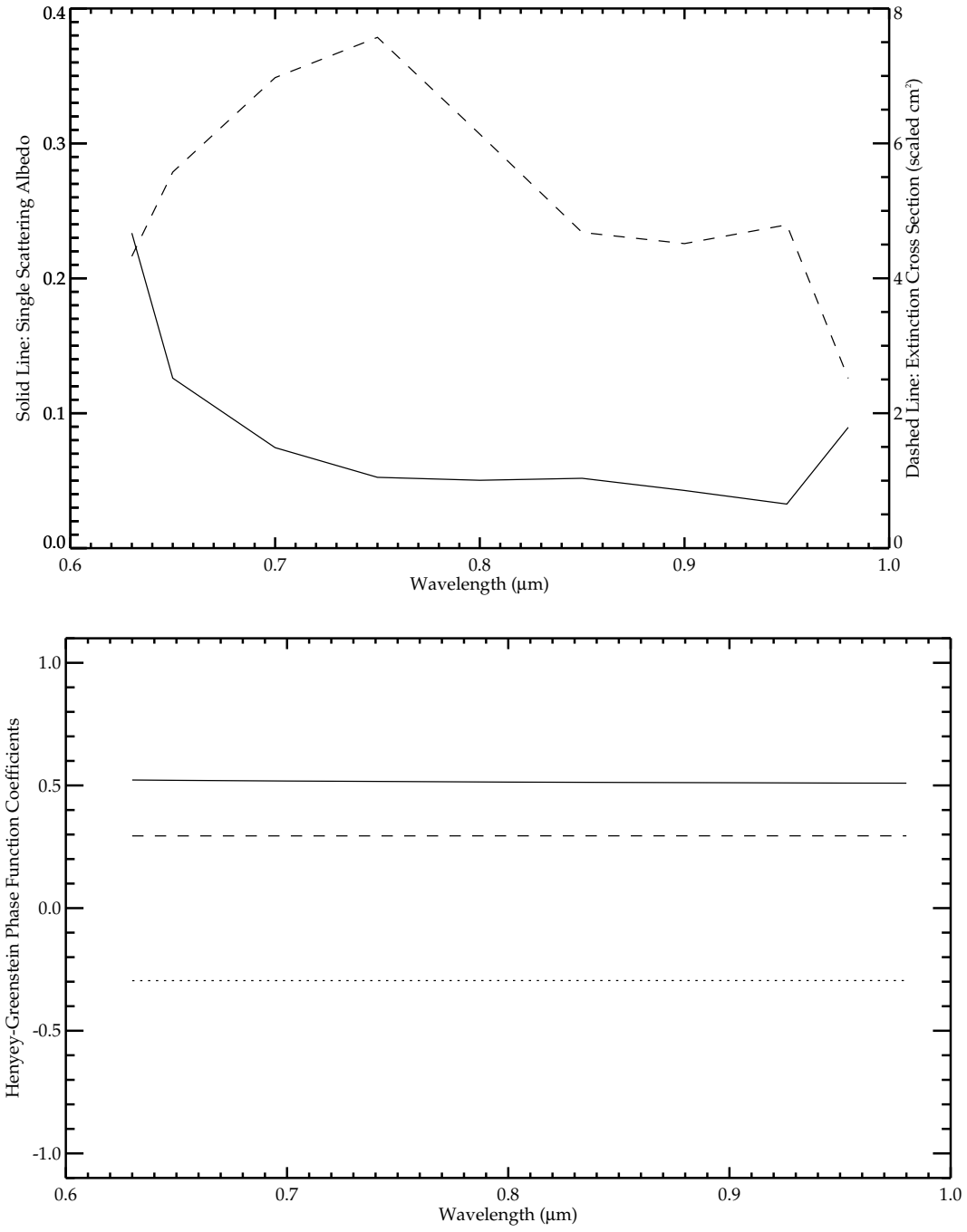

Figure 5.21: Self-consistently modelled aerosol cloud particle parameters for the UH in the Neptunian dark band at 0° latitude. Starting with the refractive indices shown in figure 5.20 and the retrieved particle size distribution, shown in table 5.2, the self-consistent single-scattering albedo and extinction cross-sections for particles in the UH are calculated. The results for single-scattering albedo (solid line, left axis) and extinction cross-section (dashed line, right axis) are shown in the upper panel. Note that the extinction cross-section has been normalised so that it equals 1.0 cm^2 at 1.0 μm. The lower panel shows the self-consistent Henyey-Greenstein parameters of the derived phase function. The solid line represents f, while g_1 and g_2 are the dashed line and dotted line, respectively.

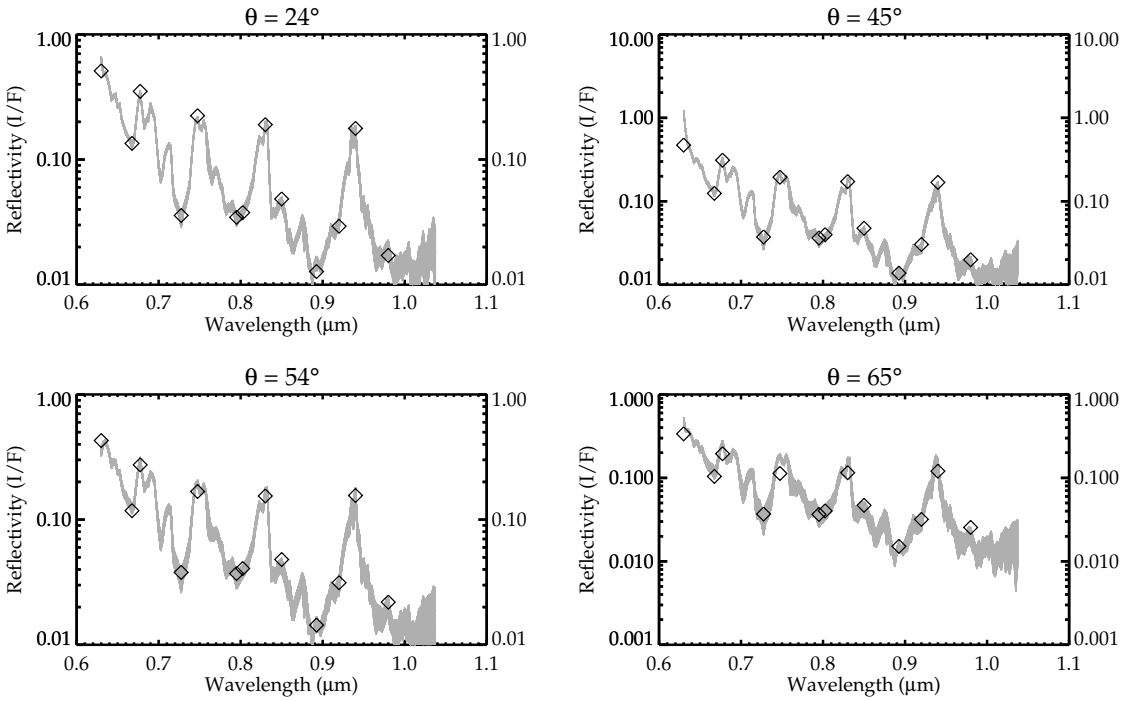

Figure 5.22: The model fit to data at 0° is shown at the four zenith angles retrieved, as indicated above each panel. Diamonds on the plots are the spectral points that were retrieved, while the grey spectrum is the observational data and total uncertainty (random noise, geometric error, and forward-modelling error). Goodness-of-fit for the model is $\chi^2/n_y = 1.76$.

altitude of $p = 0.07$ bar ($h = 48$ km) and a total opacity of $\tau = 0.05 \pm 0.02$ at 1.0 μm, making it much higher in altitude and much less opaque than its counterpart at 30° S.

Note that the imaginary refractive index of the group α UH, shown in figure 5.20, is nearly three orders of magnitude smaller (much less absorbing) than that found at 30° S (figure 5.12). Because of this, it might be assumed that the resulting Mie-calculated single-scattering albedo for group α would be much closer to 1.0 than the $\bar{\omega}_{\text{avg}} \simeq 0.5$ found at 30° S and shown in figure 5.13. Figure 5.21, however, reveals that this is not the case, and that the group α example has a UH $\bar{\omega}_{\text{avg}} \simeq 0.3$. The apparent contradiction is resolved, however, when we consult tables 5.1 and 5.2 and recall that the group α particle size is also an order of magnitude smaller than at 30° S, resulting in a much different relationship between imaginary refractive index and single-scattering albedo.

5.3.4 Bright Band at 30° N

The mirror image of the 30° S bright band is just visible in the northern hemisphere in the SWIFT images. As a result, the data is limited to high zenith angles ($\theta \geq 56°$), which limits the information content of the data. Despite this, determining whether the composition and structure mirror the southern midlatitude band is an interesting question, so results are included, as well as multiple caveats to their accuracy and trustworthiness, in this subsection.

With only high zenith angle data available, the same cloud and particle parameters as in the previous three subsections are retrieved at three zenith angles that were located close to those found in the quadrature scheme (see figure 5.23. Data was sampled to $\Delta\lambda = 0.0014$ μm, and the entire spectrum at this resolution was used in order to maximise the information content of the data.

Before examining results from the retrieval, it is important to remember that with large errors from the geometric error addition (see section 5.2.2, the results will prob-

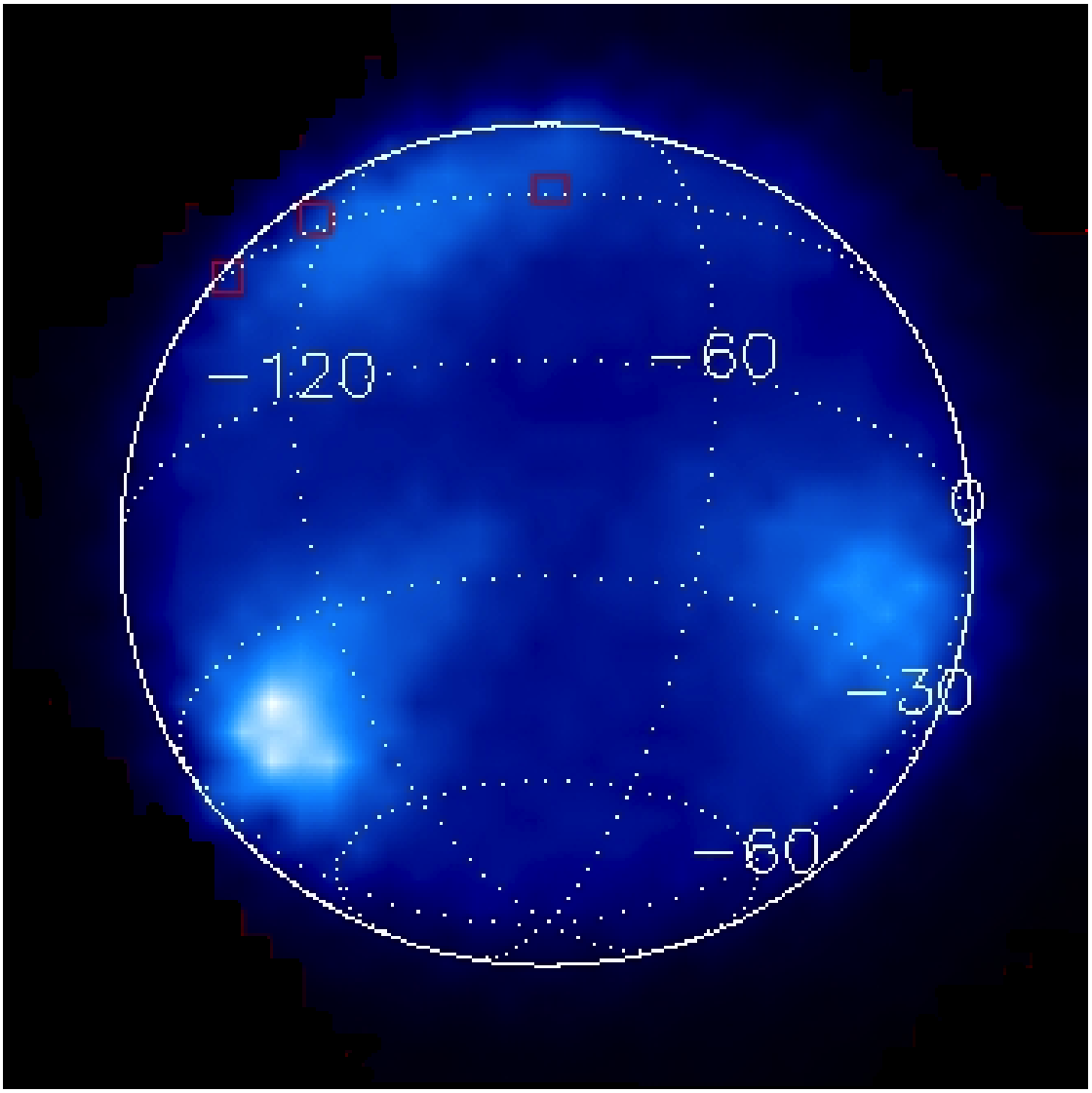

Figure 5.23: Image of Neptune recorded on 02 Jul 2012. Red boxes indicate which three pixels were selected for different viewing angles of the bright band at 30° N.

ably be more poorly restrained than results in the previous two latitude bands examined. It is also important to remember that when viewing only at high zenith angles, the atmosphere is always being viewed at a highly slanted path. This, in turn, means that stratospheric methane absorption will prevent light transmission to levels in the atmosphere that are as deep as were routinely seen in previous results. To demonstrate this effect, figure 5.4 shows transmission from space to various depths in the model Neptune atmosphere retrieved in section 5.3.1.

With these caveats in mind, we look first to the example results shown in table 5.3 and figures 5.24 – 5.27. No trends were evident that pointed to a particular preferred base height or fractional scale height in the UH, so the example displayed here is that retrieval that had the best fit to data, with a $\chi^2/n_y = 1.77$. It is important to remember that because two zenith angles associated with retrievals at this latitude are significantly above 65°, the low χ^2/n_y is a bit misleading. Because the zenith angles were high, the observational uncertainty was too forgiving at this latitude, resulting in χ^2/n_y values that were quite low.

First note the improvement factors for the TC of the retrieval in table 5.3. It appears, unsurprisingly given the sharp slant paths of all the observations, that the data at 30° N did not contain enough information to improve upon the *a priori* values of any TC parameter. The TC evidently lies too deep in the atmosphere to see, and so no useful results are obtained here. Consequently, the two usual figures displaying refractive indices, albedos, cross-sections, and phase function have been omitted for the TC.

In the UH, much better constraint is achieved on retrieved values. Results of this example retrieval, which assumed a UH fractional scale height of 2.2, indicate a total opacity of $tau = 0.11$ (18% uncertainty), a base altitude of $1.1 \leq p \leq 2.0$ bar or $h = -10 \pm 7$ km, and a particle size of 0.27 μm for the UH. When expanding to consider all the results, and not just this sample, all the retrievals set opacities in the range

Table 5.3: Retrieval results for the physical parameters of the Neptunian clouds at 30° N. 'τ' denotes total opacity of cloud, 'Base' denotes base altitude of cloud, 'FSH' denotes fractional scale height, 'a' is the mean radius of the standard gamma particle size distribution, and 'b' is the associated variance. The errors associated with these values are fractional in every case except base altitude, in which a traditional standard deviation is listed. The improvement factor for values with fractional errors, presented as a percentage, is equal to $\left(1-\frac{\varsigma_{\rm ret}/x_{\rm ret}}{\varsigma_{\rm apr}/x_{\rm apr}}\right)\times 100$ where 'ret' denotes retrieved values, 'apr' denotes *a priori* values, and $\ln\varsigma$ is the standard deviation of the value $\ln x$. The improvement factor for base altitude is simply $\left(1-\frac{\sigma_{\rm ret}}{\sigma_{\rm apr}}\right)\times 100$ where σ is the standard deviation.

Cloud Deck	Parameter	*A priori* Value	Error	Retrieved Value	Error	Improvement Factor (%)
TC	τ	1.0	1.0	0.06	0.06	0
	Base	-18 ± 10 km		-24 ± 10 km		0
	FSH			0.1	[fixed]	
	a	1.0μm	0.2μm	0.9 μm	0.2 μm	0
	b	0.050	0.005	0.050	0.005	0
UH	τ	0.1	0.1	0.11	0.02	80
	Base	44 ± 10 km		-10 ± 7 km		30
	FSH			2.2	[fixed]	
	a	0.1 μm	0.02 μm	0.27 μm	0.01 μm	80
	b	0.050	0.005	0.042	0.004	5

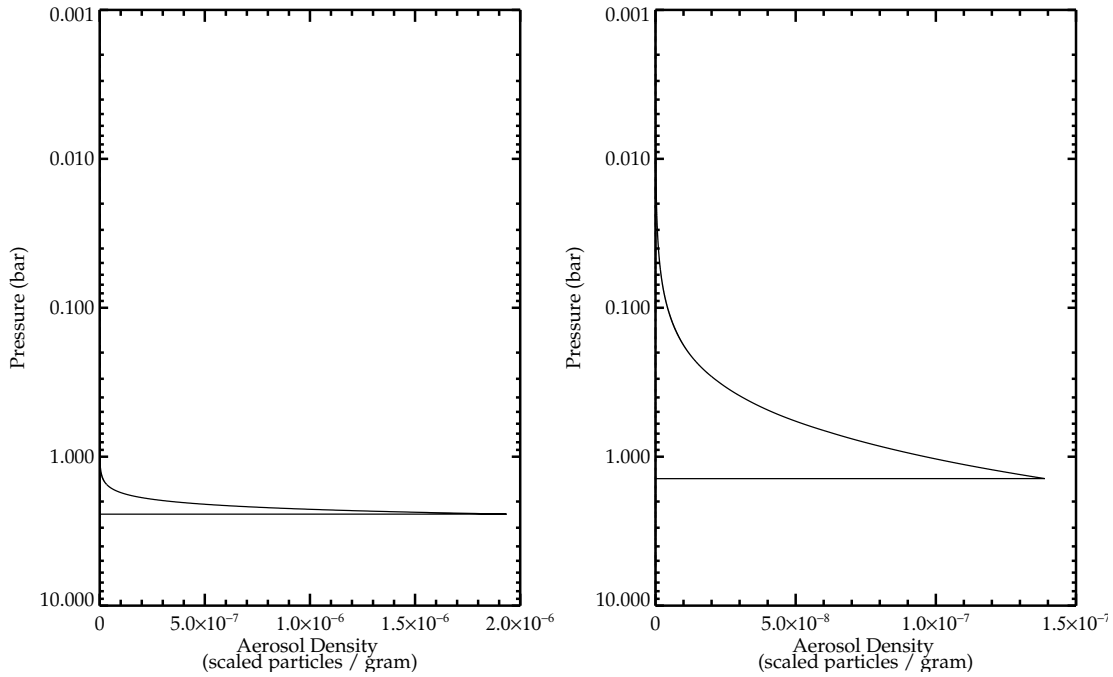

Figure 5.24: Retrieval results for the physical parameters of the Neptunian clouds at 30° N. The left panel shows the TC, which has a total opacity of $\tau = 0.6 \pm 0.6$ at 1.0 μm, and the right panel the UH, which has a total opacity of $\tau = 0.11 \pm 0.02$ at 1.0 μm. Due to using only high zenith angle data, it is doubtful that the results for the TC can be trusted, even with their large error values.

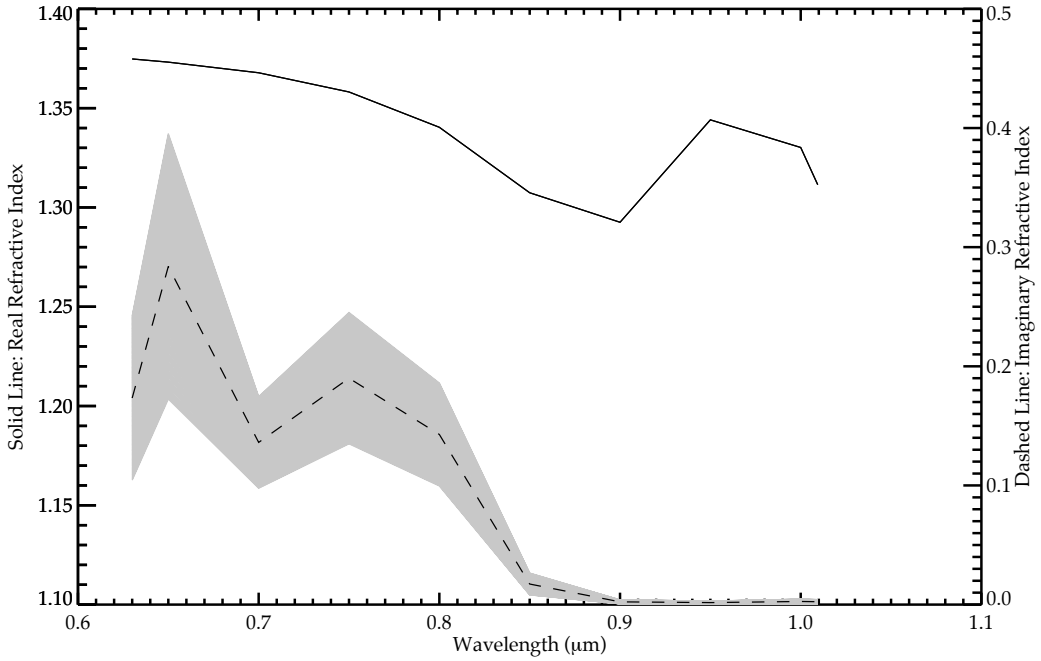

Figure 5.25: Retrieval results for the refractive index of the UH at the Neptunian bright band at 30° N. The dashed line (right axis) shows the retrieved imaginary part of the refractive index of aerosol particles in the UH, with error shown in grey. The solid line (left axis) shows the real part of the refractive index, calculated from the imaginary part with a Kramers-Kronig analysis using a reference value for the real refractive index at 1.0 μm of $n = 1.4$.

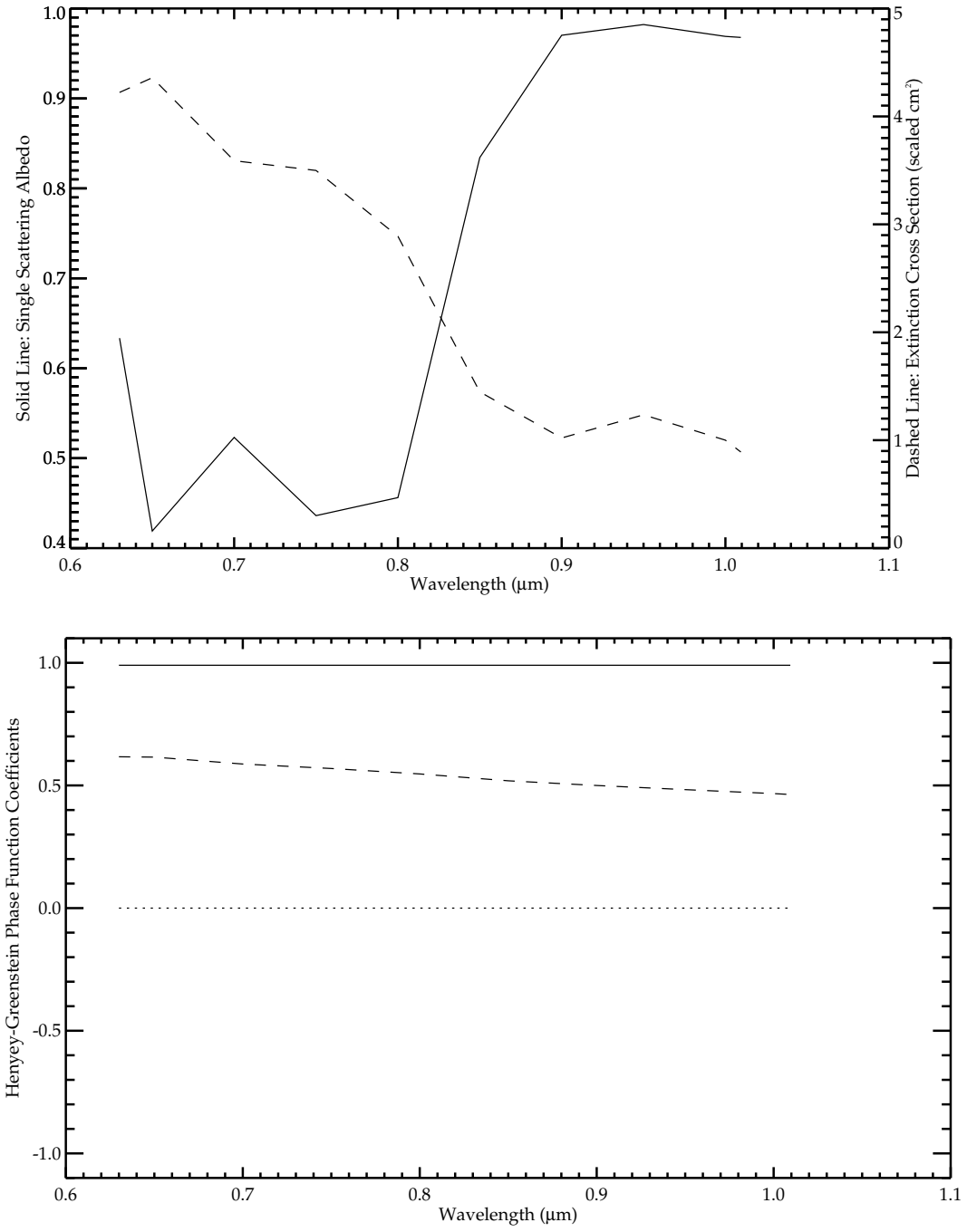

Figure 5.26: Self-consistently modelled aerosol cloud particle parameters for the UH in the Neptunian bright band at 30° N. Starting with the refractive indices shown in figure 5.25 and the retrieved particle size distribution, shown in table 5.3, the self-consistent single-scattering albedo and extinction cross-sections for particles in the UH are calculated. The results for single-scattering albedo (solid line, left axis) and extinction cross-section (dashed line, right axis) are shown in the upper panel. Note that the extinction cross-section has been normalised so that it equals 1.0 cm^2 at 1.0 μm. The lower panel shows the self-consistent Henyey-Greenstein parameters of the derived phase function. The solid line represents f, while g_1 and g_2 are the dashed line and dotted line, respectively. Notice that $g_2 \simeq 0$, which indicates that while the forward scattering peak (g_1) was constrained by the retrieval, the backscattering peak was not, and remained at the *a priori* value of 0.

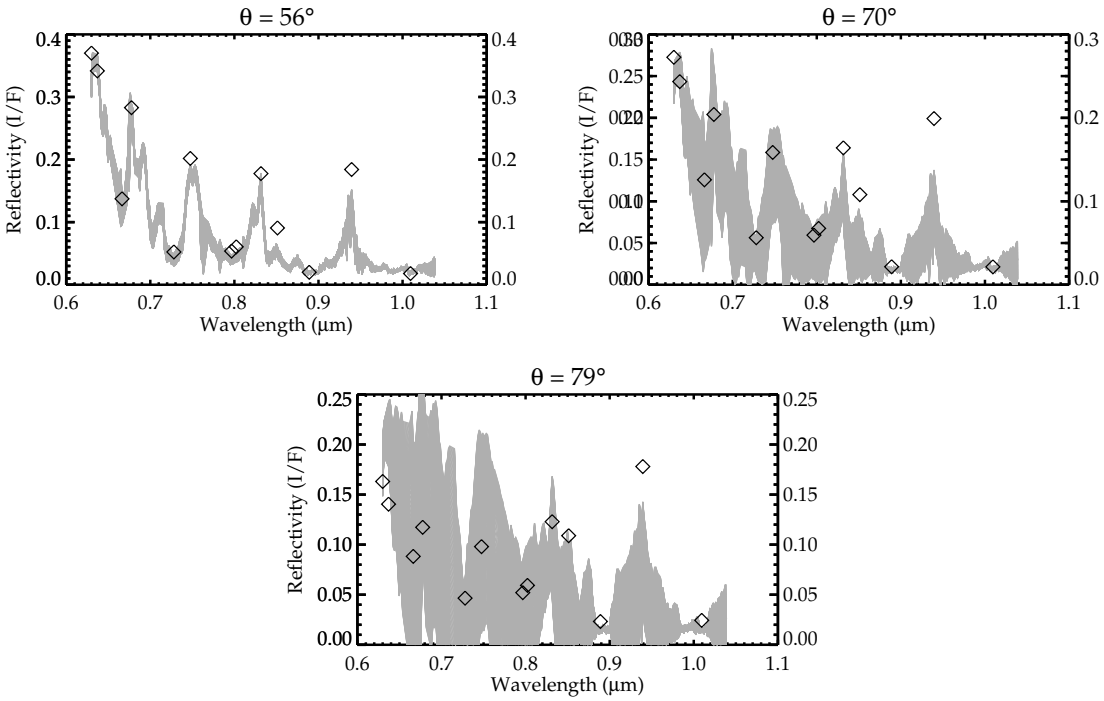

Figure 5.27: The model fit to data at 30° N is shown at the four zenith angles retrieved, as indicated above each panel. Diamonds on the plots are the spectral points that were retrieved, while the grey spectrum is the observational data and total uncertainty (random noise, geometric error, and forward-modelling error). Goodness-of-fit for the model is $\chi^2/n_y = 1.77$.

$0.05 \lesssim \tau \lesssim 0.10$, with the larger values in that range being selected more often. A much stronger trend was for UH particle size, which all fell in the range 0.25 μm $\lesssim r \lesssim$ 0.27 μm. This particle size is in agreement with trends from the 30° S retrieval results, in which retrieved UH radii fell into the range 0.25 μm $\lesssim r \lesssim$ 0.30 μm. In these early retrievals, neither this set at 30° N nor the set at 30° S showed a strong preference for a particular UH opacity. At this stage in the analysis, all that can be said regarding the opacity of the UH is that the most likely value is between 0.05, the lowest value from the 30° N retrievals, and 0.30, the highest opacity observed in the 30° S retrievals.

When comparing the reliable, UH portion of this example retrieval with the other specific examples in this chapter, which all represent some of the best-fitting models at their respective latitudes, it appears that fairly good agreement is found in the UH in both the midlatitudinal bright bands. As can be seen when comparing tables 5.1 and 5.3, the northern UH appears more vertically extended (fractional scale height = 2.2) than the southern (fractional scale height = 1.0), though admittedly one of these values was fixed while the other was retrieved. Despite their difference in vertical extent, the northern and southern UHs are both centred at the same level of the atmosphere, both residing primarily between the tropopause and the 1.0 bar level (figures 5.9 and 5.24). The UH layers' opacities in the examples, shown in tables 5.1 and 5.3, are $\tau_{\text{north}} = 0.11$ (18% uncertainty) and $\tau_{\text{south}} = 0.18$ (22% uncertainty). These values are nearly within error of one another, which is reasonable given that the midlatitudinal UH layers are likely similar, but not necessarily identical, in optical thickness. Unsurprisingly, the darker equatorial band, shown in table 5.2, has a UH much less optically thick ($\tau = 0.05$), though the examples here place it much higher (base pressure = 0.07 bar) than its midlatitudinal counterparts in tables 5.1 and 5.3. The 30° N UH fractional scale height of 1.0 is the same as the southern midlatitudinal UH (compare tables 5.1 and 5.3).

Looking specifically at the UH constituent particles, the northern and southern midlatitudes agree very well, which indicates that the same constituent particles, as might be expected, reside in both midlatitudinal UHs. The particle size, shown in tables 5.1 and 5.3, is $r = 0.27$ μm (4% uncertainty) in the northern UH and $r = 0.26$ μm (12% uncertainty) in the southern. One argument in favour of the equatorial group β retrievals is that their UH particle size is also roughly $r = 0.25$ μm, since it seems reasonable that the equatorial haze, though thinner, might be composed of similar particles. There is also good agreement between the retrieved imaginary refractive indices in the midlatitudes, shown in figures 5.12 and 5.25. They both have a maximum value of 0.3 at short wavelengths and then gradually decrease to nearly 0.0 as wavelength increases. The only difference is that the northern index peaks sharply at 0.65 μm and reaches its minimum longward of 0.9 μm, while in the southern UH the peak is broader and centred at 0.75 μm, becoming a conservative scatterer longward of 0.95 μm. The single-scattering albedos, derived from the imaginary refractive index, naturally have similar agreement to the imaginary refractive indices, as seen in the upper panels of figures 5.13 and 5.26. The extinction cross-sections in the same panels show good agreement between northern and southern UH layers, each starting at about 5 scaled cm^2 at short wavelengths and descending to the fixed value of 1.0 scaled cm^2 at 1.0 μm. The lower panels of the same figures show nearly identical phase functions in the northern and southern UHs, both with an indeterminate back-scattering peak.

That concludes the results to-date that have been analysed for Neptune data. The final chapter, Conclusions and Future Work which now summarise findings on both Uranus and Neptune, and lay out a proposed path for future work.

Chapter 6

Conclusions and Future Work

Science never solves a problem without creating ten more.

— George Bernard Shaw, Speech at the *Einstein Dinner*, 28 Oct 1930

In the first section of this chapter, 6.1, the major results from chapter 4: Uranus from IRTF SpeX Observations are summarised, followed by a review of chapter 5: Neptune from Palomar SWIFT Observations results in section 6.2. Section 6.3 then presents and discusses the most important results and their implications to our understanding of the Ice Giants. To conclude this thesis, section 6.4 reviews some shortcoming and omissions from the research for this thesis, and discusses ways that these issues can be overcome or improved in future study.

6.1 Uranus

2009 Uranus data acquired with the NASA IRTF were reduced using a series of custom-built procedures designed to work in tandem with the IDL SpeXtool package (Cushing et al., 2004; Vacca et al., 2003). This augmentation allowed latitudinal data from an extended source to be analysed rather than focusing on the bright centre-

of-disc point on the planet. The strength of the dataset, once reduced, was its wide spectral range, stretching from 0.8 to 1.8 μm, as well as the high spectral resolution ($R = 1200$) around the 825-nm collision-induced hydrogen quadupole absorption.

The wide spectral range, particularly that region of the spectrum extending below 1.0 μm, allowed for improved analysis of the scattering properties of the clouds and hazes of the upper atmosphere. This analysis was completed using NEMESIS, a multiple-scattering retrieval model developed by Irwin et al. (2008).

Two parameterised clouds were used in the atmospheric model to reduce the number of free variables, and found that the best fitting results ($\chi^2/n_y = 0.96$ when averaged across all latitudes) were obtained when modelling the tropospheric cloud (TC) deck and the upper haze (UH) with different cloud particles. The choice was made to model the optical properties of each cloud layer by calculating their wavelength-dependent scattering cross-sections assuming the particles were spherical Mie scatterers, and then relaxing this constraint and using a wavelength-invariant, single Henyey-Greenstein phase function and a wavelength-dependent single-scattering albedo. This proved the simplest model that achieved a good fit to data. Given the choice to model the phase function of both scattering particles with a Henyey-Greenstein function of unvarying asymmetry $g = 0.7$, these models were strongly dependent on single-scattering albedos of the particles. Best fits were obtained for TC particles with a single-scattering albedo of $\bar{\omega} = 1.0$ at the shortest SpeX wavelengths and $\bar{\omega} = 0.7$ at the highest wavelengths. The transition between these two values occurred smoothly between 1.0 and 1.4 μm. The UH particles, again given the assumption of unvarying Henyey-Greenstein phase functions, maintained high single-scattering albedos of 1.0 for all regions of the 0.8 – 1.8 μm spectrum, with the exception of a sharp drop to $\bar{\omega} = 0.6$ at 1.0 μm. The wings of this drop in albedo extended between 0.8 and 1.1 μm.

Given these single-scattering albedos, if was discovered that the model strongly

favoured hazes with bases lying at or below the 1.0-bar level.This haze was modelled with 0.10-μm particle radii. This haze and its derived properties model the dominant scattering above the TC, and likely represent the net scattering from optically-thin, vertically-extended hazes in the troposphere and stratosphere as well as the predicted methane condensation cloud around 1.0 bar. Model results strongly favoured TC deck particle radii of 1.35 μm, and in the simplistic case of latitudinally constant methane, a cloud-top that decreased in pressure from the equator to the midlatitudes.

The high spectral resolution in the I-Band (0.8 – 0.9 μm) allowed for a further look into the possibility of latitudinally varying methane abundance. This possibility was studied in two ways. The first variability analysis was done using a reflectivity technique developed first in Karkoschka and Tomasko (2009). In the second method, retrievals were performed that allowed methane to vary from an *a priori* profile by a multiplicative factor, adding this additional free parameter to the five cloud parameters that varied in the 0.8 – 1.8-μm scattering analysis already discussed. In both analysis techniques, raw I-Band data were analysed at their natural, unsmoothed resolution of 0.0002 μm. This resolution, ten times higher than that used for the previous 0.8 – 1.8 μm study, allowed us to better focus the results on the distinction between methane and aerosol opacity.

It was first confirmed that this model, using parameterised clouds rather than continuous ones, would behave like the models employed in Irwin et al. (2011a, 2012a) and adjust the pressure of the tropospheric cloud bases when different methane profiles were considered. Like the earlier study with continuous clouds, changes were observed of more than 1.0 bar to the cloud base pressure as the methane profiles changed. This amount of variation indicates that the latitudinal changes observed in the Uranian spectra can, theoretically, be accurately described through either changes in cloud base height or by variations in methane. After verify-

ing this behaviour, it was also confirmed that the reduced data range would retrieve the same cloud results, within error, as the previous, lower-spectral-resolution cloud retrievals over the full range of data.

The data, which covers Uranus from 50° S to 65° N latitude and between 0.8 and 0.9 μm, adds to the current literature on Uranian methane variability and provides a unique opportunity to study both hemispheres of the planet and distinguish between spectral changes from cloud opacity and methane abundance. Synthesising the results from both methods of analysis, it was found that the spectral changes observed are best explained not by adjustment to cloud-top height, but instead by a methane abundance that is enriched at the equator when compared to the mid-latitudes of both hemispheres. Due to the low spatial resolution of this data, which served to “dampen" the enrichment values that were obtained, it was only possible to identify a lower boundary for equatorial methane enrichment. The two studies together indicate a lower boundary for equatorial methane enrichment of 9%, easily permitting Karkoschka and Tomasko (2009)'s 50%, as expected. Though the error was large, it should also be noted that the methane retrieval study, when taken independently, produced a methane enrichment value of 36%, suggesting, as in Karkoschka and Tomasko (2009), that the actual enrichment levels are probably much higher. Also as predicted, methane retrievals ($\chi^2/n_y = 0.35$ when averaged across all latitudes) indicated that from 30° S to 45° N latitude the TC did not exhibit the changes in cloud-top pressure that were evident with cloud retrievals using a fixed methane profile, consistent with findings in Irwin et al. (2012a), though at slight odds with the results of Irwin et al. (2012b), where a gradual thinning and a decrease in cloud base pressure was evident when moving polewards from the equator. The discrepancy between Tice et al. (2013) and Irwin et al. (2012b) is presumably the same as between the two Irwin papers, namely, that new methane line data was applied in the later Irwin publication, along with line-by-line, rather than a correlated-κ, computation

in the model.

The likelihood that the degree of equatorial methane enrichment may have evolved since the Karkoschka and Tomasko (2009) study should also be noted. The earlier study observed Uranus five years prior to equinox, while ours occurred two years after (2002 and 2009, respectively). Further study, as Uranus moves further into the northern spring, will be necessary to support or refute the temporal variability issue.

The argument for an equatorial methane enrichment of at least 9% compared with both northern and southern midlatitudes is consistent with the most recently suggested Uranian circulation models, which all indicate the likelihood of deep, methane-rich air upwelling at low latitudes (Irwin et al., 2012a; Karkoschka and Tomasko, 2009; Sromovsky et al., 2011). This methane-rich air would provide the mechanism for the suggested enrichment at the equator. As the air moved into the troposphere and cooled, it would condense out its methane, and subsequently move to higher latitudes where it would cool and ultimately subside to the deep atmosphere once again.

Finally, the weighted average of the two methods of analysis undertaken suggest that the extent of maximum methane enrichment is quite broad, extending over 20° – 30° of the equatorial region of the planet with its centre at $4 \pm 2°$ S latitude. This position is nearly 10° north of the more narrow enrichment determined by Karkoschka and Tomasko (2009). While IRTF SpeX spatial resolution is poor, the position of the maximum is probably a real change due to variation of the latitudinal methane profile in the years surrounding the equinox, because it is difficult to discount it because of poor spatial resolution. It is less clear whether the SpeX data is sufficiently spatially resolved to provide evidence of a broadening of the methane enrichment.

This methane profile evolution indicates an atmospheric circulation that evolved during the years surrounding the equinox. This conclusion seems reasonable given

Uranus' 98° obliquity and consequently the extreme shift in solar forcing between 2002 and 2009. Additionally, this conclusion is not without precedent. Irwin et al. (2007, 2009, 2010, 2011a, 2012a) have documented clear equinoctial trends in which the peak of tropospheric cloud opacity shifted northward during the years from 2006 to 2010. The evidence here from the 0.8 – 0.9-μm region strengthens that conclusion, which was determined with data exclusively longer than 1.0 μm.

6.2 Neptune

Observation of Neptune were acquired with the Hale telescope's P3K adaptive optics system and the SWIFT spectrograph at the Palomar Observatory in 2012. Following the processing pipeline employed by Oxford Astrophysics (Houghton R., in progress), a further IDL-based processing pipeline was developed for this study. Once reduced, numerous images of the entire disc of Neptune, taken over the course of four consecutive nights in June and July, were recorded with a spectra range covering 0.6 – 1.0 μm. The strengths of this data are the high spatial resolution (better than 0.3" seeing), the high spectral resolution ($R_{0.650\ \mu m} = 3250$ linearly rising to $R_{1.0\ \mu m} = 4400$), the wide spectral range, and the number of observations in a short time (18 images over the 4 nights), allowing for tracking of discrete cloud features across the planet.

The wide spectral range shortward of 1.0 μm allowed good constraints on the size distribution and optical properties of small-radii scattering particles in the stratospheric hazes of Neptune. The images of the full planetary disc allowed simultaneous retrievals of latitude bands at multiple zenith angles to help further constrain results. These retrievals of physical cloud parameters and optical particle parameters utilised NEMESIS, including a newly-developed capability to retrieve imaginary refractive indices (Irwin et al., 2015). These imaginary refractive index spectra, along with a fixed real imaginary refractive index at one wavelength, were then used to self-consistently

built optical models that included real refractive indices, single-scattering albedos, scattering cross-sections, and complete phase functions.

Two unexpected inconveniences negatively impacted analysis of the data. First, it was discovered that simultaneous retrievals that included high zenith angles, even if data was drastically under-sampled, required more than a week of continuous processing. This rendered the initial plan of retrievals of 9 simultaneous zenith angles incompatible with the required deadline for submission of this thesis. Secondly, it was discovered that due to a variety of reasons, the most important of which was probably 'bleeding' of dark space into as many as 4 edge pixels of the planet, the highest zenith angles required a large amount of additional observational uncertainty. In the end, it was decided that zenith angles higher than 65° should be avoided, if possible. This procedure unfortunately reduced the ability to constrain the retrieved parameters as well as had been initially hoped.

After the issues in the above paragraph were dealt with, there was only time for a partial analysis of the data. To improve computational speed, retrievals of just four simultaneous zenith angles were chosen, with one near-nadir zenith and the three highest that fell below 65°. An exception to this was with the data for the 30° N cloud belt, which was near the edge of the Uranian disc. For this belt, only three zenith angles were used, two of which were above the 65° angle. In addition to limiting the number of zenith angles, computation speed was accelerated by under-sampling the data, choosing just 11 spectral locations which defined all relative minima and maxima, as well as a few other features, of the Neptunian spectrum.

Since the general structures (deep optically-thick cloud below various optically-thin hazes) of both ice giants is similar, it was decided to streamline the analysis by using the same parameterised two-cloud model arrived at in chapter 4, since that had worked well for reproducing Uranus spectra. Some changes were made, however, the most important of which was to incorporate the new refractive indices re-

trieval scheme. In the end, the tropospheric cloud (TC) was fixed at a fractional scale height of 0.1, since like with Uranus the model only seemed sensitive to the cloud-top, making fractional scale height and base altitude strongly correlated. The same two values seemed strongly correlated in the upper haze (UH) as well, at least with the artificially-limited number of zenith angles. As a result, a series of retrievals was made at a range of fixed UH fractional scale heights that seemed likely, and a second set where a range of plausible base altitudes was fixed. This allowed us to examine goodness-of-fit values to see if the models favoured a particular base altitude of fractional scale height in the UH. All retrievals left total opacity free in both clouds. Base altitude was always free in the TC, while either base altitude or fractional scale height (whichever wasn't fixed) was free in the UH. Both clouds were characterised by independent cloud particles, for which nine values of imaginary refractive index with wavelength were retrieved. Additionally, a standard-gamma size distribution described by a particle radius and variance was retrieved for each cloud.

The analysis described above was performed at three latitude bands which seemed to be characterised by relatively stable, circumplanetary clouds with bright reflectivity in the northern and southern midlatitudes (about 30° N, S) and a belt of darker albedo clouds at the equator. Favoured trends in fractional scale height and base altitude for the upper haze were discussed, though more definitive results would be possible given the time to reanalyse with more zenith angles. More finely spaced spectral sampling might also have improved results, though it did seem that retrieval results, when forward-modelled, fit the entire spectra about as well as the under-sampled spectra had.

Still, with these retrievals, goodness-of-fit values of $\chi^2/n_y = 3.46,\ 1.76,$ and 1.77 were achieved for the southern, equatorial, and northern latitude belts, respectively. Control runs of fully sampled, 8-zenith angle retrievals revealed that moderate gains of $\Delta(\chi^2/n_y) = -0.5$ were possible in fitting the southern latitude band, where strato-

spheric hazes were highly reflective, though no such improvement was apparent in the equatorial region, where high hazes were less important to the spectrum overall. The northern midlatitudes, where only high zenith angles were available for analysis, had very large observational uncertainty, so the χ^2/n_y value is misleading low. In the review of results that follows, all retrievals of TC values at this latitude will be ignored, because they were wholly inconsistent and unconstrained, indicating that at the high zenith angle slant paths through the atmosphere, information was simply not available in the northern midlatitudes about depths below the tropopause.

Results suggest that in all three latitude regions, a TC with a cloud-top at approximately 3.4 bar exists with a fairly thick, total opacity average of $\tau = 2.2 \pm 0.2$. The location cited here for the TC agree with findings from Irwin et al. (2010, 2011b, 2013), which placed the putative-H_2S layer at between 2 and 3 bar, a location slightly higher in altitude than those results from Baines et al. (1995a,b); Sromovsky et al. (2001a), which preferred a values of 3.13 and 3.8 bar, respectively. As for the total opacity, results in this study showed no significant difference between the opacity of the TC at 30° S and the TC at the equator. In contrast, Irwin et al. (2010, 2011b, 2013) found best agreement with data when his deep cloud was slightly more opaque at 1.6 μm in the dark equatorial region than at 30° S. This discrepancy could probably be due to Irwin's sensitivity to larger particles, since the haze presumably has a range of particle sizes, with larger particles influencing the spectrum at larger wavelengths more strongly, or it could simply reflect a change over time since the observations in question were two years apart.

Analysis here of 0.6 – 1.0 μm data suggests that cloud particles in the TC deck had real refractive indices between 1.3 and 1.4 at all wavelengths in that range. Particle radii were determined to be $r = 1.084 \pm 0.006$ assuming a standard-gamma size distribution of variance $v = 0.5$. This is just slightly larger than the particles assumed by Baines et al. (1995a,b); Irwin et al. (2010, 2011b, 2013); Karkoschka (2001);

Karkoschka and Tomasko (2011); Sromovsky et al. (2001a), who all used models with 1.0 μm particle radii. Like longer-wavelength studies from Irwin et al. (2010, 2011b, 2013), the particles in the TC in this study appeared to be strongly forward-scattering in the 0.6 – 1.0 μm range. The previous study used a single (forward only) Henyey-Greenstein phase function, citing a forward asymmetry parameter of $g_1 = 0.75$ longward of 1.0 μm. This study used a double Henyey-Greenstein phase function with an $f \geq 0.8$, indicating strong forward-scattering, with a higher slightly higher value for g_1, ranging between 0.80 and 0.85.

Though altitude, opacity, particle size, and particle scattering properties of the TC seemed consistent at all latitude regions examined, more analysis is required due to some marked differences in the imaginary refractive indices and the resulting single-scattering albedos. The particles in the southern midlatitude band had an imaginary refractive index nearly an order of magnitude larger than the particles in the equatorial band, though both regions had imaginary refractive index spectra that were largely flat except for an abrupt maximum at 0.95 μm. The single-scattering albedos determined by Baines and Hammel (1994) between 0.634 and 0.826 μm are markedly different than those retrieved here. Firstly, while those of Baines range from $0.775 \lesssim \bar{\omega} \lesssim 0.915$, while those retrieved here in the same wavelength range never drop below 0.950 in the southern midlatitudes and never below 0.965 at the equator. Both studies do see a relative minimum in albedo at 0.75 μm, though this minimum is dwarfed in this study by a much larger one at 0.95 μm, a wavelength not covered in Baines and Hammel (1994). Also relevant to this issue is Sromovsky et al. (2001a), who put an upper limit of 0.2 on single-scattering albedo at 1.27 μm. It seems unlikely that such a drastic change would occur between 1.27 μm and 1.0 μm where a value of nearly 1.0 is found. While this analysis is not yet complete, no explanation has yet been discovered for the discrepancies other than a possible change in time between the 1986 (Baines and Hammel, 1994), 1998 (Sromovsky et al., 2001a), and

2012 measurements, which seems very possible on the dynamically active Neptune.

In the UH, recall that studies at similar wavelengths noted in the Introduction find particles of $r \leq 0.2$ μm (Baines and Hammel, 1994; Gibbard et al., 2002; Karkoschka and Tomasko, 2011; Pryor et al., 1992). Results of this analysis indicate particle sizes slightly larger, with an average $r = 0.269 \pm 0.003$ μm in both midlatitudes.

This study has thus far been inconclusive to the UH particle size in the equatorial region. Most equatorial retrievals preferred a size similar to those seen in the midlatitudes, however the six best-fitting examples, including the control with all zenith angles retrieved, interestingly converged upon a particle size one order of magnitude smaller, with $r = 0.02$ μm. These small particles did have a 30% improvement factor over *a priori* parameters, comparable with a 40% improvement factor for UH particle size at 30° S but dwarfed by the 80% improvement factor at 30° N. Perhaps the most important consideration in this puzzle is, however, that the equatorial band is much darker than the midlatitudes, and the haze there is so thin (all equatorial retrievals in this study found $\tau < 0.1$), that the particle size may not be terribly relevant even if it is retrievable.

UH haze altitude is a topic on which a wide range of results have been published due to the rapid evolution and variety of planet-wide hazes. In the midlatitudes, preliminary results of this study favour extended UH hazes of fractional scale heights greater than 0.5, with base pressures at or just above 1.0 bar. In the equatorial region, results seem to suggest hazes that are higher in altitude and slightly less vertically extensive, with base pressures less than $p < 0.1$ bar. These results are well inside the range of stratospheric hazes in Baines and Hammel (1994); Irwin et al. (2010, 2011b, 2013); Karkoschka (2011); Karkoschka and Tomasko (2011); Pryor et al. (1992).

Results for refractive indices and single-scattering albedos for the UH were well within previously published ranges as well (Baines and Hammel, 1994; Irwin et al., 2010, 2011b, 2013; Karkoschka, 2011; Karkoschka and Tomasko, 2011; Pryor et al.,

1992). In the midlatitudes, most UH refractive indices here ranged from 1.22 – 1.46 (real) and 0.0 – 0.3 (imaginary). 0.3 is very large, and is quite surprising, demanding particular attention in future retrievals. It falls three times higher than the 0.099 upper limit at 0.89 μm suggested by Baines and Hammel (1994), which is the largest value among the studies that have determined refractive indices in comparable wavelengths. After providing this upper limit, however, Baines and Hammel (1994) did suggest a nominal value of 0.0. Pryor et al. (1992) found values approximately one order of magnitude smaller than 0.3. Finally, even tholins, the most highly absorbent material for which we are aware of laboratory data, have $n_i < 0.02$ in the 0.6 – 1.0 μm wavelength range being studied (Khare, 1984). Despite this surprising magnitude, the fact remains that numerous retrievals in this study did include peaks to 0.3 at wavelengths $\lambda \leq 0.8\,\mu$m. In accordance with the imaginary refractive indices, single-scattering albedos in the midlatitudinal UH ranged from 0.4 at the shortest wavelengths analysed to 1.0 at the longest. In the equatorial region, the thinness of the haze made the results difficult to trust.

Finally, phase functions in this study for the midlatitudinal UH seemed to have great difficulty constraining the back-scattering lobe, but consistently produced forward-scattering lobes of asymmetry $g_1 \simeq 0.5$.

Comparing Neptune results to other research is difficult due to the highly variable (spatially and temporally) atmosphere. While analysis here is unfortunately not yet completed, to this point results seem in general accordance with other published works. The major exception is the puzzlingly high value (0.3) of imaginary refractive indices in the midlatitudinal UH. Already discussed above, the topic will be revisited briefly in the final section of this thesis.

6.3 Key Results: Implications & Discussion

This section opens with a list of five results from this research that stand out as particularly noteworthy. Following this, a short discussion of each point suggests the implications of each result, including comparisons of the cloud model results with those cloud layers predicted in the ECCM of each planet (see section 1.2 and figures 1.4 and 1.5). The section concludes with discussion of some principle similarities and differences between the Ice Giants that were highlighted in this thesis.

1. **Uranian equatorial methane enrichment is better characterised** both spatially and temporally by this analysis.

2. In light of equatorial methane enrichment, **Uranian tropospheric cloud top pressures are shown to be nearly constant** from northern to southern midlatitudes.

3. **The Neptunian visible/IR spectrum is dominated by a single, extended tropospheric cloud** extending, with relatively unvarying properties, from the northern to the southern midlatitudes.

4. **Both Neptunian midlatitudes contain similar, thick stratospheric hazes**; the equatorial band, in contrast, appears to have a nearly transparent stratosphere.

5. **A sharp drop in reflectivity close to 1.0 μm** characterises both the Uranian stratospheric haze and the tropospheric Neptunian cloud.

The first two results in the list, both involving the relative enrichment of methane at the Uranian equator, provide an important extension to the work done in Karkoschka and Tomasko (2009). In that earlier research, 2002 observations indicated a strong equatorial methane enrichment relative to the southern midlatitudes. Due, however, to the orientation of the planet, which was still emerging from the

southern summer, it was impossible to determine if this latitudinal dependance was mirrored in the northern hemisphere, which was just coming into view.

The methane analysis presented in section 4.3 (Tice et al., 2013) extends this work in several important ways. First, a much improved view of the northern midlatitudes were available in the 2009 data analysed here, and it was shown that relative methane depletion in the northern midlatitudes was almost identical in magnitude to that in the southern midlatitudes.

Second, the peak of the equatorial enrichment was shown to have been drifting northward between the observations in 2002 and 2009. The 10° shift in the enrichment peak represents a significant shift in a fundamental characteristic of the planet, and adds to the body of work that provide concrete examples of large-scale changes in the planet's circulation surrounding the 2007 equinox. These results all show that the distinctive equatorial features of the planet are shifting northwards, following the correlative shift of direct sunlight. Irwin et al. (2007, 2009, 2010, 2011a, 2012a) records the northward journey of the tropospheric cloud deck's opacity peak, while this thesis (Tice et al., 2013) shows the same change to the methane enrichment peak.

Finally, the equatorial methane enrichment modifies the results of the retrieved cloud model so that the cloud-top in the troposphere remains at largely the same pressure throughout the latitude range observed here. This result is satisfying because of the documented correlation between methane abundance and the cloud-top pressure of the tropospheric cloud (Irwin et al., 2012a; Tice et al., 2013). Recall that the methane abundance retrievals in this research (section 4.3.3) agreed with methane abundances derived from the reflectivity analysis (section 4.3.2). Because this latter method, which relies on the strong hydrogen absorption at 825 nm, largely removes the correlation between the two parameters, greater confidence can be placed in the retrieved methane abundance. This added confidence, in turn, translates to greater confidence in the retrieved cloud-top pressure than was possible in

previous cloud results.

A fair degree of agreement can be seen when comparing the ECCM-predicted cloud layers to those clouds produced from the variable-methane retrievals that led to these first two results. Though the ECCM predicts that an H_2S layer would exist below the 3 bar-level, which is deeper than the tropospheric cloud retrieved here, it seems likely that this H_2S cloud is the one modelled as the Uranian TC. The precise methane profile is not known, and it is quite possible that a different methane profile, which preserved the same equatorial enrichment discovered in chapter 4, would serve to require a deeper modelled cloud. It is equally possible that the physics not included in the ECCM (most notably any vertical and horizontal mixing of air) would actually serve to vertically extend this cloud from its predicted base to a higher altitude, which would bring the ECCM cloud into closer agreement with the $\sim$ 1.0 bar retrieved tropospheric cloud-top.

The second modelled cloud layer, namely the Uranian UH, agrees more cleanly and obviously with the clouds predicted in the Uranian ECCM. Retrievals here showed a strong requirement that the UH have a base at least as deep as 1.0 bar, and fixing the base at this level produced a cloud with a large vertical extent. Looking at the ECCM for a cloud of this description, it is clear that the UH likely models the spectral effects produced by the CH_4 cloud.

The one striking discrepancy between the top two ECCM clouds and the two modelled clouds is that in the ECCM, the higher of the two clouds is significantly more optically-thick, where the opposite is true in model results. This problem can be easily explained, again, by considering the physics the ECCM lacks. Without considering mixing occurring between rising air parcels and surrounding air, the rate of formation of aerosol particles, and thus the size of these particles is likely inaccurate in the ECCM. If particle size is inaccurate, the cloud density and overall opacity could also, in turn, be unreliable.

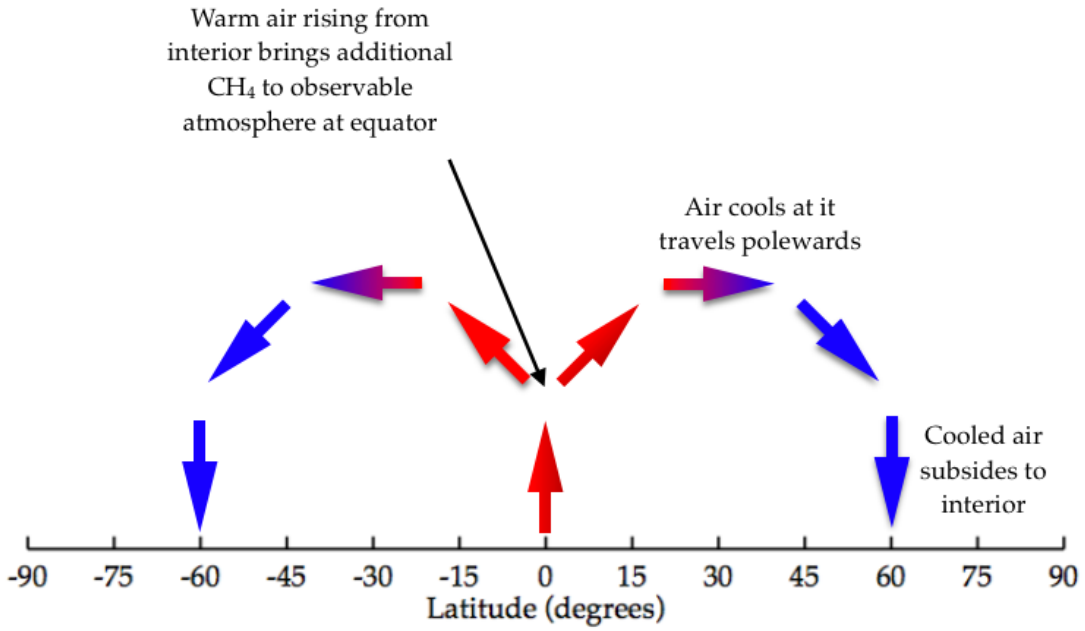

Figure 6.1: Uranian circulation pattern suggested by equatorial methane enrichment found in the upper atmosphere. Red represents relatively warmer air, blue represents relatively cooler air, black is for explanatory purposes only and has no physical significance.

These methane results, highlighted in the first two 'key results', are also important because they provide further evidence of probable planet-wide circulation patterns. The additional methane located at the equator must come from within the planet's interior. Its existence thus suggests that there is a consistent, large-scale upwelling in the equatorial region of the planet, which lifts deep, relatively-warmer, methane-rich air into the observable atmosphere (see figure 6.1). This air from the interior presumably drifts towards the midlatitudes before cooling and descending again to the interior. Not without precedent, a similar circulation pattern has been suggested in recent years by Irwin et al. (2012a), Karkoschka and Tomasko (2009), and Sromovsky et al. (2011).

The Neptunian tropospheric clouds, as summarised in result (3), seem to be latitudinally invariant, just like the tropospheric clouds retrieved on Uranus in the case

of variable methane case. Since the composition of the two Ice Giants is quite similar, this result provides a nice commonality between the tropospheric clouds of the two planets. Specifically on Neptune, where the self-consistent particle retrieval was employed, this tropospheric cloud seemed to have a cloud-top of 3.4 bar and a strongly constrained particle size of 1.08 μm regardless of the overall reflectivity of the latitude band. Since the cloud layers on Neptune presumably form, either directly or indirectly, from condensed material lifted from the interior of the planet, it is quite reasonable to conclude that such a thick cloud layer would be formed due to large-scale, planet wide processes which would produce a planet-wide cloud of relatively invariable properties.

Result (4) highlights the key difference observed between the midlatitudinal regions of Neptune and the equator, namely that the an optically-thick, vertically-extended haze is evident in the midlatitudes and is conspicuously absent (or at least is much thinner and less important to the reflected spectrum) from the equator. Though this Neptunian UH, where it exists, is an order of magnitude less optically-thick than its deeper neighbour, it still contributes strongly, unlike the Uranian UH, to the reflected spectrum of the planet, and seems to be the primary contributor to the clear banded structure that divides the central, dark equatorial region from the much brighter midlatitudes.

In the following comparison of results (3) and (4) to the Neptunian ECCM, and the subsequent consideration of implications about Neptunian circulation and dynamics, it must be remembered that the Neptune results are incomplete at this point. It follows that any conclusions formed that are based on the Neptune retrieval results are highly speculative in nature. Before accepting these conclusions, they require a great deal of additional scrutiny, accompanied by further refinement of the Neptune results themselves.

First, in comparing the two retrieved cloud layers to the Neptune ECCM, we see, as we did with Uranus, a fairly clear correspondence between the two model layers and the top two layers of the ECCM, but again the equivalence is by no means perfect. As before, the H_2S layer in the ECCM has a cloud-top slightly deeper than the retrieved cloud-top of 3.4 bar. Also like was found on Uranus, the vertical extent of the ECCM CH_4 layer does not perfectly mirror that of the retrieval, but does reflect the retrieved clouds' wide horizontal extent and approximate base and cloud-top heights. Finally, and also just as with the Uranus ECCM analysis, the relative opacities of the two retrieved clouds is reversed from that shown in the ECCM. As was detailed in the corresponding Uranus results, all these discrepancies can be readily explained by the simplistic physics in the ECCM, and the identification of model layers from the top two ECCM layers is highly probable.

When considering the implications of results (3) and (4) on Neptunian circulation, the key clue comes in the lack of the putative CH_4 cloud (UH) in the equator. If these ice clouds in the Ice Giant atmospheres form, as the ECCM predicts, from condensing species rising from the warmer interior of the planet, the strange absence of the UH in the equatorial belt might suggest that uplift from the planet's interior is reduced at the equator. Again, bearing in mind that the Neptunian results are not yet fully robust, this might suggest an atmospheric circulation which is characterised by convective uplift in the midlatitudes, equator-ward movement of air which cools, and in which UH particles 'rain' out of the top ice cloud, and finally subsistence in the equatorial region of the planet. See figure 6.2 for a schematic representation of this proposed circulation. Like the proposed Uranian circulation, this implication for Neptunian circulation is not without support from previous literature (Conrath et al., 1989, 1998; Irwin et al., 2011b), though contrasting circulation models have also been suggested (Karkoschka, 2011; Karkoschka and Tomasko, 2011).

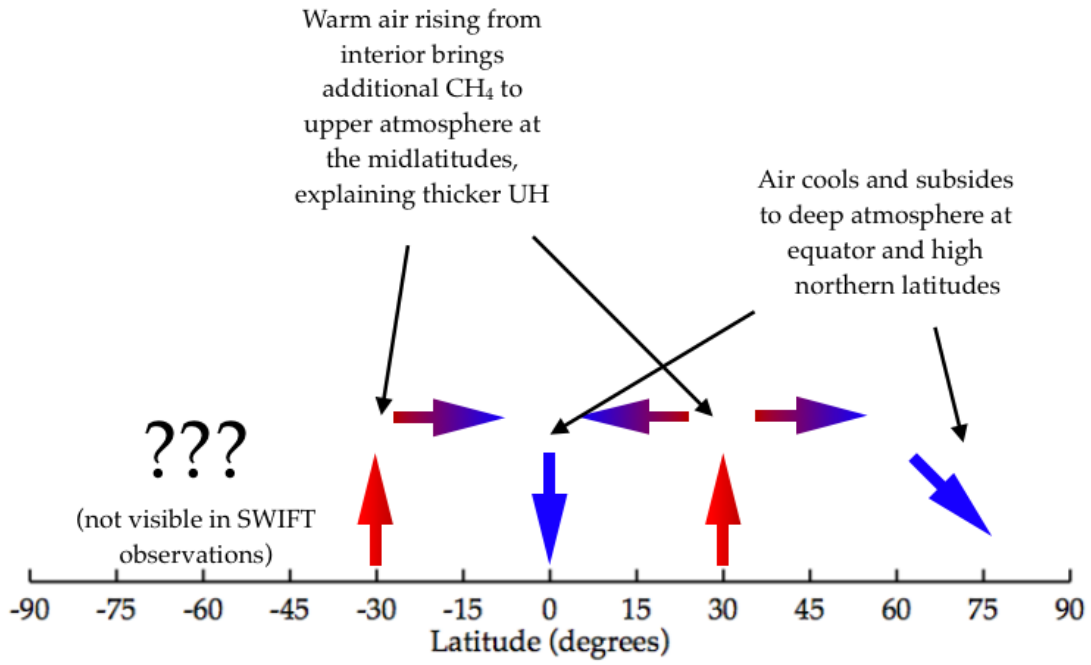

Figure 6.2: Neptunian circulation pattern suggested by stratospheric haze characteristics of the the three latitude regions analysed. Red represents relatively warmer air, blue represents relatively cooler air, black is for explanatory purposes only and has no physical significance.

Result (5) is important because it might provide concrete clues, rather than merely implicit ones based on the ECCM, as to the identity of the Uranian UH and Neptunian TC. It is generally believed, as mentioned in chapters 1, 4, and 5, that the real refractive index of the particles in the Ice Giant condensation clouds is between 1.3 and 1.4, but the absorptive qualities of these cloud particles, as modelled with imaginary refractive index or single-scattering albedo, is much less clear. The large and abrupt reflectivity feature found near 1.0 μm in each of these two cloud layers will provide an important means of identifying the constituents of these layers through comparison to laboratory reflectance data. Unfortunately, there exist few laboratory results that cover candidate species in the correct spectral range. Where laboratory results do exist, they are generally insufficiently spectrally resolved to include the narrow features seen in chapters 4 and 5. The best laboratory data available are shown in figure 6.3, which makes it clear that any identification of these species at this time is not possible. Finally, it is also important to remember that the features observed in the two clouds are not quite at the same spectral location (the reflectivity feature in the Uranian UH peaks at 1.0 μm, while the Neptunian TC feature is at 0.95 μm) so they do not necessarily represent the same species.

These five key results highlight the unique properties of the Ice Giants, which as discussed in chapter 1, are in some ways quite similar to each other, while in other ways so unique. It has been shown that both planets' visible/IR spectrums are dominated by methane absorption and the spectral results of two cloud layers, modelled here as an optically-thick, vertically-thin cloud in the upper troposphere that serves as the effective 'bottom' of the visible atmosphere, and a vertically-extended haze that while thinner, still plays an important role in reflecting the sunlight to create the spectra of the two planets. It is likely, based on theoretical predictions, that the lower of these two layers is H_2S ice, while the upper is a haze composed of CH_4 ice.

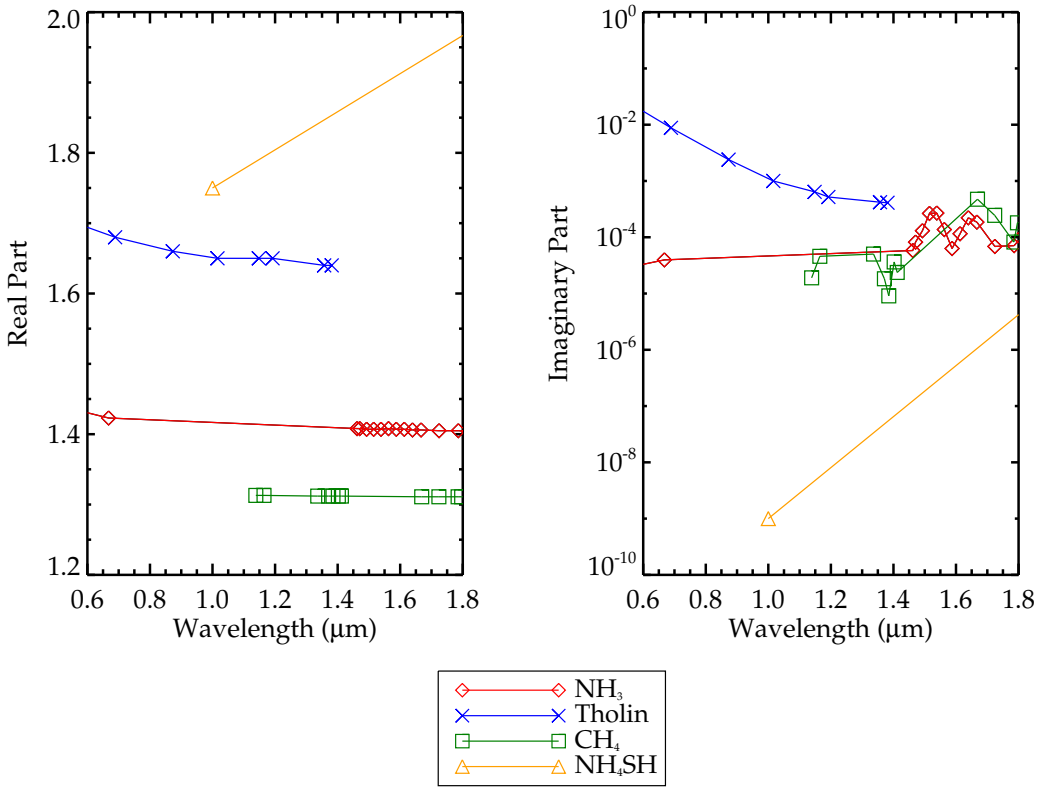

Figure 6.3: Laboratory data showing refractive indices (real on the left and imaginary on the right) of four possible candidate particles for Ice Giant cloud condensation layer constituents. Symbols shown in the plots represent the constituents identified in the legend at the bottom, with no data obtained for other possible candidate particles. Colour is included to aid in distinguishing the curves, but has no inherent meaning beyond this. As can be easily seen in the figure, none of the data is sufficient to identify the ~ 1.0 μm features, which should show up as a positive spike in the imaginary refractive index, either due to lack of data or lack of data resolution.

The particles in the lower haze are strongly forward-scattering on both planets, and of similar size on both planets, with results indicating a strong preference for radii of 1.3 μm on Uranus and retrieved radii of 1.084 ± 0.006 μm on Neptune. The upper haze, too, exhibits similar properties on both planets, thought the Neptunian haze is significantly more optically-thick. Despite this difference, both haze layers extend from pressures at or just above 1.0 bar well into the troposphere. The UH has particles about an order of magnitude smaller than the TC on both planets, with 0.10 μm-radii producing good fits on Uranus and $r_{UH} = 0.269 \pm 0.003$ μm on Neptune. Both cloud layers on both planets seem to be consistent with scattering particles of a 1.3 or 1.4 refractive index.

Analysis in this thesis indicates that these similarities, which are likely due to both planets possessing similar size, temperature, and composition, then give way to an equally long list of differences. Perhaps due to the great difference in planetary obliquity (see table 1.1), the vastly different amounts of latent heat, or some other elusive cause, this thesis provides an equally compelling case for each planet's distinct and unique character.

As already mentioned, the Uranian UH is much less optically-thick than the Neptunian UH, and while it has been shown to be necessary for high levels of model agreement with observations, its impact on the spectrum is nowhere near as great as that of the Neptunian haze. But of course the Neptunian haze, unlike the Uranian one which covers the entire latitudinal range of our data, blankets only the midlatitudes, with almost no haze effects on the spectrum at the Neptunian equator. When investigating the lower cloud on both planets, we find that while the Uranian cloud-top seems to be at about 1.0 bar, the Neptunian cloud is significantly deeper, with a cloud-top pressure of closer to 3.4 bar. Perhaps the most dramatic contrast between the two planets comes not from the cloud analysis directly, but from the circulation that the analysis seems to imply. The atmospheric circulation seems to be very differ-

ent, with convective cells moving upwards at the equator on Uranus, but downward at the equator on Neptune.

Arguably the two most similar planets among the eight in the solar system, Uranus and Neptune nevertheless represent two very different puzzles for scientific inquiry.

6.4 Future Work

As has already been touched upon, one of the biggest failings of the Uranus research found in chapter 4 and Tice et al. (2013) is the lack of a self-consistent, wavelength-dependent scheme for classifying the aerosols in the atmosphere. Thankfully, the task of remedying this is already underway (Irwin et al., 2015).

Moving forward from that upcoming paper, following the evolution of methane profiles as Uranus settles firmly into the long northern hemisphere day/summer will be important. Based on the southern day/summer which *Voyager 2* imaged nearly 30 years ago, it is highly likely that the planet will settle once again into a quiescent state. Current evidence indicates that the equator is highly enriched in methane abundance, and that the peak of this enrichment has been moving northward over the past several years. It is unclear at this time whether the level of enrichment might have been evolving as well. Perhaps the biggest question the focus on methane enrichment begs at this time is what will happen to this characteristic once the planet returns to a dynamically stable state in the northern summer. Will the equatorial methane enrichment remain, or slowly fade away? There is the suggestion, mentioned previously in section 6.1, that the enrichment might be due to a circulation cell in which warm methane upwells at the equator, moves towards the poles, and finally subsides from the troposphere back into the deep atmosphere. If the mechanism driving this circulation has been the rapidly changing solar forcing, then it is

reasonable to believe that the nature of this methane enrichment will change dramatically in the coming years. Clearly to answer these questions will require more observational data as Uranus continues its march toward the long northern summer. As the SWIFT data analysed here has shown, observations that cover a range of zenith angles with the high spatial resolution provided by adaptive optics would be a boon to analysis, and greatly assist in characterising not only the latitudinal methane profile, but also help probe to different atmospheric pressure levels and thereby provide increased constraint on the vertical profiles as well.

Much remains to be done with the Neptune data that was discussed in this thesis. Preliminary results about the cloud structure at the midlatitudes and equatorial belts are promising, but more work is needed to clear up a few contradictions and tighten final uncertainties in the retrieval. With additional time, hopefully much of this can be accomplished by retrieving with more zenith angles, more finely sampled spectra, or both. Another possibile method to improve the current results would be to develop a more refined method of choosing spectral points to sample. With a more rigorous method of choosing spectral sample points, it could be ensured that maximum information content were being retrieved with the minimum number of spectral locations, thus obtaining more constrained results with less computational expense. While implementing any of these improvements, particular care must be given to studying the imaginary refractive index of the particles in the midlatitudinal UH. These values represent the most suspect results of these early retrievals, so careful examination to make sure these aren't being produced in error will be important.

Other models should also be tested, however, as it is not clear that two parameterised clouds is the best means of reproducing the spectra. Models have been employed in the past that have two, three, four, or even five separate cloud layers. Also, some models have achieved good results by trading the vertically compact lower cloud (the TC here) for a more vertically-extended haze. These other past models

should be tested to see if improvements in the model fit quality can be achieved in this way, and to see what further implications the various models have for the planet's constituents. It might also be interesting to test the dark equatorial belt with a 1 cloud retrieval, since any haze that exists at the latitude seems to have an almost negligible effect on the spectrum.

Once the best model is chosen and results on the "background" of clouds and hazes in the equator and midlatitudes are in final form, the SWIFT data and the small amount of SpeX data on Neptune both have obvious applications. The resulting model from SWIFT should be applied to the SpeX Neptune data. The spatial resolution of that data will limit analysis to a "background" at the equator and another at the southern midlatitudes. But because SpeX covers a spectral range from 0.8 – 1.8 μm, it will be very informative to see if a self-consistent model can be applied that not only provides good observation reproduction at the SWIFT range of 0.6 – 1.0 μm, but then continues on to provide good results to wavelengths as long as 1.8 μm.

Two other studies with the SWIFT data itself will be very interesting once the current "background" is achieved. First, a study of latitudinal methane variation will be useful, to see if there is any latitudinal variation like that seen on Uranus (Irwin et al., 2012b; Karkoschka and Tomasko, 2009; Tice et al., 2013), and proposed but not verified in some papers on Neptune (Irwin et al., 2011b, 2013; Orton et al., 2007a; Karkoschka, 2011). The data is of a sufficiently high information content that a variable methane abundance should be retrievable, especially if certain cloud properties, such as the particle sizes and refractive indices, are fixed. With the current view of the planet, a variable methane profiles should be achievable for latitudes between 30° N and the south pole, even if the pixels nearest the limb are not useable.

Finally, a study of the many discrete cloud features visible on the planet would be an important next step. The available data would provide means of tracking cloud features as they rotate around the planet, viewing them, like was done with the lati-

tudinal bands, from several different zenith angles to probe different levels of the atmosphere and tightly constrain their cloud properties. Seeing whether these clouds have similar particles to those found in the stable cloud bands, or different particles, would be an important tool in further describing the dynamics and photochemistry of the planet.

In addition to further work that can be done on this current dataset, their is great need for future datasets to be acquired. Open questions remain. Does the TC, which seems to be pervasive and invariant in most latitude regions of the planet continue as far as the poles? Is there a UH like that found in the midlatitudes at the poles, or perhaps a different type of UH, or perhaps no haze at all? As with the future datasets already suggested for Uranus, a series of observational datasets of Neptune would help, as the planet continues its seasonal cycle, to answer these questions about the poles.

George Bernard Shaw was clearly correct in this instance: science has answered a few questions and asked ten more about the ice giants. With these data, future observations, and hopefully future satellite missions to the ice giants, the two most distant inhabitants of our solar system promise to provide more fascinating discoveries for generations of scientists to come.

Bibliography

Andrews, D. G. (2000). *An Introduction to Atmospheric Physics*. Cambridge University Press, Cambridge UK.

Atreya, S., Egeler, P., and Baines, K. (2006). Water-ammonia ionic ocean on Uranus and Neptune? *Geophys. Res. Abs.*, 8: 05179.

Baines, K. H. and Bergstralh, J. T. (1986). The structure of the Uranian atmosphere: Constraints from the geometric albedo spectrum and H_2 and CH_4 line profiles. *Icarus*, 65: 406 – 441.

Baines, K. H. and Hammel, H. (1994). Clouds, hazes, and stratospheric methane abundance in Neptune. *Icarus*, 109: 20 – 39.

Baines, K. H., Hammel, H. B., Rages, K. A., Romani, P. N., and Samuelson, R. E. (1995a). Clouds and hazes in the atmosphere of Neptune. In Cruikshank, D. P., editor, *Neptune and Triton*, pages 489 – 546. University of Arizona Press, Tucson.

Baines, K. H., Mickelson, M. E., Larson, L. E., and Ferguson, D. W. (1995b). The abundances of methane and ortho-para hydrogen on Uranus and Neptune: Implications of new laboratory 4-0 H_2 quadrupole line parameters. *Icarus*, 144: 328 – 340.

Bézard, B. and Romani, P. (1991). Hydrocarbons in Neptune's stratosphere from Voyager infrared observations. *J. Geophys. Res. Planets*, 96: 18,961 – 18,975.

Bézard, B., Romani, P. N., Feuchtgruber, H., and Encrenaz, T. (1999). Detection of the methyl radical on Neptune. *Astrophys. J.*, 515: 868 – 872.

Bishop, J., Atreya, S. K., Romani, P. N., Orton, G. S., Sandel, B. R., and Yelle, R. V. (1995). The middle and upper atmosphere of Neptune. In Cruikshank, D. P., editor, *Neptune and Triton*, pages 427 – 488. University of Arizona Press, Tucson.

Borysow, A. (1991). Modeling of collision-induced infrared absorption spectra of H_2-H_2 pairs in the fundamental band at temperatures from 20 to 300 K. *Icarus*, 92(2): 273 – 279.

Borysow, A. (1992). New model of collision-induced infrared absorption spectra of H_2-He pairs in the 2 – 2.5 μm range at temperatures from 20 to 300 K: An update. *Icarus*, 96: 169 – 175.

Borysow, A., Borysow, J., and Fu, Y. (2000). Semi-empirical model of collision-induced absorption spectra of H_2-H_2 complexes in the second overtone band of hydrogen at temperatures from 50 to 500 K. *Icarus*, 145: 601 – 608.

Boyd, R. W. (1978). The wavelength dependence of seeing. *J. Opt. Soc. Am.*, 68: 877 – 883.

Brunetto, R., Caniglia, G., Baratta, G. A., and Palumbo, M. E. (2008). Integrated near-infrared band strengths of solid CH_4 and its mixtures with N_2. *Astrophys. J.*, 686: 1,480 – 1,485.

Burgdorf, M., Orton, G. S., Davis, G. R., Sidher, S. D., Feuchtgruber, H., Griffin, M. J., and Swinyard, B. M. (2003). Neptune's far-infrared spectrum from the ISO long-wavelength and short-wavelength spectrometers. *Icarus*, 164: 244 – 253.

Conrath, B., Flasar, F. M., Hanel, R., Kunde, V., Maguire, W., Pearl, J., Pirraglia, J., Sameulson, R., Gierasch, P., Weir, A., Bézard, B., Gautier, D., Curuikshank, D., Horn,

L., Springer, R., and Shaffer, W. (1989). Infrared observations of the Neptunian System. *Science*, 246: 1,454 - 1,459.

Conrath, B. J., Gautier, D., Owen, T. C., and Samuelson, R. E. (1993). Constraints on N_2 in Neptune's atmosphere from Voyager measurements. *Icarus*, 101: 168 – 172.

Conrath, B. J., Gierasch, P. J., and Ustinov, E. A. (1998). Thermal structure and para hydrogen fraction on the outer planets from Voyager IRIS measurements. *Icarus*, 135: 501 – 517.

Courtin, R., Gautier, D., and Stobel, D. (1996). The CO abundance on Neptune from HST observations. *Icarus*, 123: 37 – 55.

Cushing, M. C., Vacca, W. D., and Rayner, J. T. (2004). Spextool: A spectral extraction package for SpeX, a 0.8 – 5.5 micron cross-dispersed spectrograph. *Publ. Astron. Soc. Pac.*, 116: 362 – 376.

de Bergh, C., Lutz, B. L., Owen, T., Brault, J., and Chauville, J. (1986). Monodeuterated methane in the outer solar system. II: Its detection on Uranus at 1.6 microns. *Astrophys. J.*, 311: 501 – 510.

de Bergh, C., Lutz, B. L., Owen, T., and Maillard, J. P. (1990). Monodeuterated methane in the outer solar system: IV: Its detection and abundance on Neptune. *Astrophys. J.*, 355: 661 – 666.

de Pater, I., Fletcher, L. N., Luszcz-Cook, S. H., DeBoer, D., Butler, B., Hammel, H. B., Sitko, M. L., Orton, G. S., and Marcus, P. S. (2014). Neptune's global circulation deduced from multi-wavelength observations. *Icarus*, 237: 211 – 238.

Encrenaz, T., Serabyn, E., and Weisstein, E. W. (1996). Millimeter spectroscopy of Uranus and Neptune: Constraints on CO and PH_3 tropospheric abundances. *Icarus*, 124: 616 – 624.

Encrenaz, T., Feuchtgruber, H., Atreya, S. K., Bézard, B., Lellouch, E., Bishop, J., Edgington, S., de Graauw, T., Griffin, M., and Kessler, M. F. (1996). ISO observations of Uranus: the stratospheric distribution of C_2H_2 and the eddy diffusion coefficients. *Astron. Astrophys.*, 333: L42 – L46.

Encrenaz, T. (2004). Neutral atmospheres of the giant planets: an overview of composition measurements. *Space Sci. Rev.*, 116: 99 – 119.

Encrenaz, T., Lellouch, E., Drossart, P., Feuchtgruber, H., Orton, G. S., and Atreya, S. K. (2004). First detection of CO in Uranus. *Astron. Astrophys.*, 413: L5 – L9.

Feuchtgruber, H., Lellouch, E., de Graauw, T., Bézard, B., Encrenaz, T., and Griffin, M. (1997). External supply of oxygen to the atmospheres of the Giant Planets. *Nature*, 389: 159.

Feuchtgruber, H., Lellouch, E., Bézard, B., Encrenaz, T., de Graauw, T., and Davis, G. R. (1999). Detection of HD in the atmospheres of Uranus and Neptune: a new determination of the D/H ratio. *Astron. Astrophys.*, 341: L17 – L21.

Feuchtgruber, H., Lellouch, E., Orton, G. S., de Graauw, T., Vandenbussche, B., Swinyard, B., Moreno, R., Jarchow, C., Billebaud, F., Cavalié, T., Sidher, S., and Hartogh, P. (2013). The D/H ratio in the atmospheres of Uranus and Neptune from Herschel-PACS observations. *Astron. Astrophys.*, 551: A126.

Fletcher, L. N., Drossart, P., Burgdorf, M., Orton, G. S., and Encrenaz, T. (2010). Neptune's atmospheric composition from AKARI infrared spectroscopy. *Astron. Astrophys.*, 514: A17.

Fletcher, L. N., de Pater, I., Orton, G., Hammel, H., Sitko, M. L., and Irwin, P. G. J. (2014). Neptune at summer solstice: Zonal mean temperatures from ground-based observations, 2003 – 2007. *Icarus*, 231: 146 – 167.

Fouchet, T., Lellouch, E., and Feuchtgruber, H. (2003). The hydrogen ortho-to-para ratio in the stratospheres of the giant planets. *Icarus*, 161: 127 – 143.

Fried, D. L. (1966). Optical resolution through a randomly inhomogeneous medium for very long and very short exposures. *J. Opt. Soc. Am.*, 56: 1,372 – 1,379.

Gibbard, S. G., Roe, H., de Pater, I., Macintosh, B., Gavel, D., Max, C. E., Baines, K. H., and Ghez, A. (2002). High-resolution infrared imaging of Neptune from the Keck Telescope. *Icarus*, 156: 1 – 15.

Gibbard, S. G., de Pater, I., Roe, H. G., Martin, S., Macintosh, B. A., and Max, C. E. (2003). The altitude of Neptune cloud features from high-spatial-resolution near-infrared spectra. *Icarus*, 166: 359 – 374.

Goody, R. M. and Yung, Y. L. (1989). *Atmospheric Radiation: Theoretical Basis*. Oxford University Press, 2nd edition.

Greathouse, T. K., Richter, M., Lacy, J., Moses, J., Orton, G. S., Encrenaz, T., Hammel, H. B., and Jaffe, D. (2011). A spatially resolved high spectral resolution study of Neptune's stratospheres. *Icarus*, 214: 606 – 621.

Guilloteau, S., Dutrey, A., Marten, A., and Gautier, D. (1993). Co in the troposphere of Neptune: Detection of the J = 1 - 0 line in absorption. *Astron. Astrophys.*, 279: 661 – 667.

Hammel, H. B., de Pater, I., Gibbard, S., Lockwood, G. W., and Rages, K. (2005). Uranus in 2003: Zonal winds, banded structure, and discrete features. *Icarus*, 175: 534 – 545.

Hammel, H. B., Lynch, D. K., Russel, R. W., Sitko, M. L., Berstein, L. S., and Hewagama, T. (2006). Mid-infrared ethane emission on Neptune and Uranus. *Astrophys. J.*, 644: 1,326 – 1,333.

Hammel, H. B., Sitko, M. L., Lynch, D. K., Orton, G. S., Russel, R. W., Geballe, T. R., and de Pater, I. (2007). Distribution of ethane and methane emission on Neptune. *Astron. J.*, 134: 637 – 641.

Hammel, H. B. and Lockwood, G. W. (2007). Long-term atmospheric variability on Uranus and Neptune. *Icarus*, 186: 291 – 301.

Hansen, J. E. and Travis, L. D. (1974). Light-scattering in planetary atmospheres. *Space Sci. Rev.*, 16: 527 – 610.

Herbert, F. and Sandel, B. R. (1999). Ultraviolet observations of Uranus and Neptune. *Planet. Space Sci.*, 47: 1,119 – 1,139.

Hesman, B. E., Davis, G. R., Matthews, H. E., and Orton, G. S. (2007). The abundance profile of CO in Neptune's atmosphere. *Icarus*, 186: 342 – 353.

Houghton, J. (2002). *The Physics of Atmospheres*. Cambridge University Press, 3rd edition.

Irwin, P. G. J., Calcutt, S. B., Taylor, F. W., and Weir, A. L. (1996). Calculated κ distribution coefficients for hydrogen- and self-broadened methane in the range 2000 – 9500 cm^{-1} from exponential sum fitting to band-modelled spectra. *J. Geophys. Res.*, 101: 26,137 – 26,154.

Irwin, P. G. J., Sromovsky, L. A., Strong, E. K., Sihra, K., Teanby, N. A., Bowles, N., Calcutt, S. B., and Remedios, J. J. (2006). Improved near-infrared methane band models and κ-distribution parameters from 2000 to 9500 cm^{-1} and implications for interpretation of outer planet spectra. *Icarus*, 181: 309 – 319.

Irwin, P. G. J., Teanby, N. A., and Davis, G. R. (2007). Latitudinal variations in Uranus' vertical cloud structure from UKIRT UIST observations. *Astrophys. J.*, 665: L71 – L74.

Irwin, P. G. J., Teanby, N. A., de Kok, R., Fletcher, L. N., Howett, C. J. A., Tsang, C. C. C., Wilson, C. F., Calcutt, S. B., Nixon, C. A., and Parrish, P. D. (2008). The NEMESIS planetary atmosphere radiative transfer and retrieval tool. *J. Quant. Spectrosc. Ra.*, 109: 1,136 – 1,150.

Irwin, P. G. J. (2009). *Giant Planets of our Solar System: Atmospheres, Composition, and Structure*. Praxis Publishing Ltd, Chichester, UK, 2nd edition.

Irwin, P. G. J., Teanby, N. A., and Davis, G. R. (2009). Vertical cloud structure of Uranus from UKIRT/UIST observations and changes seen during Uranus' northern spring equinox from 2006 to 2008. *Icarus*, 203: 287 – 302.

Irwin, P. G. J., Teanby, N. A., Davis, G. R., Fletcher, L. N., Orton, G. S., Tice, D. S., Hurley, J., and Calcutt, S. B. (2010). Revised vertical cloud structure of Uranus from UKIRT/UIST observations and changes seen during Uranus' Northern Spring Equinox from 2006 to 2008: Application of new methane absorption data and comparison with Neptune. *Icarus*, 208: 913 – 926.

Irwin, P. G. J., Teanby, N. A., Davis, G. R., Fletcher, L. N., Orton, G. S., Tice, D., and Kyffin, A. (2011a). Uranus' cloud structure and seasonal variability from Gemini-North and UKIRT observations. *Icarus*, 212: 339 – 350.

Irwin, P. G. J., Teanby, N. A., Davis, G. R., Fletcher, L. N., Orton, G. S., Tice, D., Hurley, J., and Calcutt, S. B. (2011b). Multispectral imaging observations of Neputne's cloud structure with Gemini-North. *Icarus*, 216: 141 – 158.

Irwin, P. G. J., Teanby, N. A., Davis, G. R., Fletcher, L. N., Orton, G. S., Calcutt, S. B., Tice, D. S., and Hurley, J. (2012a). Further seasonal changes in Uranus' cloud structure observed by Gemini-North and UKIRT. *Icarus*, 218: 47 – 55.

Irwin, P. G. J., de Bergh, C., Courtin, R., Bézard, B., Teanby, N. A., Davis, G. R., Fletcher, L. N., Orton, G. S., Calcutt, S. B., Tice, D., and Hurley, J. (2012b). The application

of new methane line absorption data to Gemini-N/NIFS and KPNO/FTS observations of Uranus' near-infrared spectrum. *Icarus*, 220: 369 – 382.

Irwin, P. G. J., Lellouch, E., de Bergh, C., Courtin, R., Bézard, B., Fletcher, L. N., Orton, G. S., Teanby, N. A., Calcutt, S. B., Tice, D. S., Hurley, J., and Davis, G. R. (2013). Line-by-line analysis of Neptune's Near-IR spectrum observed with Gemini/NIFS and VLT/CRIRES. *Icarus*, 227: 37 – 48.

Irwin, P. G. J., Tice, D. S., Fletcher, L. N., Barstow, J. K., Teanby, N. A., Orton, G. S., and Davis, G. R. (2015). Reanalysis of Uranus' cloud scattering properties from IRTF/SpeX observations using a self-consistent scattering cloud retrieval scheme. *Icarus*, 250: 462 – 476.

Karkoschka, E. (1998). Clouds of high contrast on Uranus. *Science*, 280: 570.

Karkoschka, E. (2001). Uranus' apparent seasonal variability in 25 HST filters. *Icarus*, 151: 84 – 92.

Karkoschka, E. and Tomasko, M. (2009). The haze and methane distributions on Uranus from HST-STIS spectroscopy. *Icarus*, 202: 287 – 309.

Karkoschka, E. and Tomasko, M. (2010). Methane absorption coefficients for the Jovian planets from laboratory, Huygens, and HST data. *Icarus*, 205: 674 – 694.

Karkoschka, E. and Tomasko, M. G. (2011). The haze and methane distributions on Neptune from HST-STIS spectroscopy. *Icarus*, 211: 780 – 797.

Karkoschka, E. (2011). Neptune's cloud and haze variations 1994–2008 from 500 HST-WFPC2 images. *Icarus*, 215: 759 – 773.

Khare, B. N., Sagan, C., Thompson, W. R., Arakawa, E. T., Suits, F., Callcott, T. A., Williams, M. W., Shrader, S., Ogino, H., Willingham, T. O. and Nagy, B. (1984). The organic aerosols of Titan. *Adv. Space Res.*, 4: 59 – 68.

Lacis, A. A. and Oinas, V. (1991). A description of the correlated kappa-distribution method for modeling nongray gaseous absorption, thermal emission, and multiple-scattering in vertically inhomogeneous atmospheres. *J. Geophys. Res. Atmos.*, 96: 9,027 – 9,063.

Lellouch, E., Romani, P., and Rosenqvist, J. (1994). The vertical distribution and origin of HCN in Neptune's atmosphere. *Icarus*, 108: 112 – 136.

Lellouch, E., Hartogh, P., Feuchtgruber, H., Vandenbussche, B., de Graauw, T., Moreno, R., Jarchow, C., Cavalié, T., Orton, G., Banaszkiewicz, M., Blecka, M. I., Bockel'ee-Morvan, D., Crovisier, J., Encrenaz, T., Fulton, T., Küppers, M., Lara, L. M., Lis, D. C., Medvedev, A. S., Rengel, M., Sagawa, H., Swinyard, B., Szutowicz, S., Bensch, F., Bergin, E., Billebaud, F., Biver, N., Blake, G. A., Blommaert, J. A. D. L., Cernicharo, J., Courtin, R., Davis, G. R., Decin, L., Encrenaz, P., Gonzalez, A., Jehin, E., Kidger, M., Naylor, D., Portvankina, G., Schneider, R., Sidher, S., Thomas, N., de Val-Borro, M., Verdugo, E., Waelkens, C., Walker, H., Aarts, H., Comito, C., Kawamura, J. H., Maestrini, A., Peacocke, T., Teipen, R., Tils, T., and Wildeman, K. (2010). First results of Herschel-PACS observations of Neptune. *Astron. Astrophys.*, 518: L152.

Lindal, G. F. (1992). The atmosphere of Neptune: an analysis of radio occultation data acquired with Voyager 2. *Astron. J.*, 103: 967 – 982.

Lodders, K. and Fegley, Jr., B. (1994). The origin of cargon monoxide in Neptune's atmosphere. *Icarus*, 112: 368 – 375.

Luszcz-Cook, S. H., de Pater, I., Ádámkovics, M., and Hammel, H. B. (2010). Seeing double at Neptune's south pole. *Icarus*, 208: 938 – 944.

Marten, A., Gautier, D., Owen, T., Sanders, D. B., Matthews, H. E., Atreya, S. K., Tilanus, R. P. J., and Deane, J. R. (1993). First observations of CO and HCN on Nep-

tune and Uranus at millimetre wavelengths and their implications for atmospheric chemistry. *Astrophys. J.*, 406: 285 – 297.

Marten, A., Matthews, H. E., Owen, T., Moreno, R., Hidayat, T., and Biraud, Y. (2005). Improved constraints on Neptune's atmosphere from submillimetre-wavelength observations. *Astron. Astrophys.*, 429: 1,097 – 1,105.

Martonchik, J. V., Orton, G. S., and Appleby, J. F. (1984). Optical properties of NH_3 ice from the far infrared to the near ultraviolet. *Appl. Optics*, 23: 541 – 547.

Martonchik, J. V. and Orton, G. S. (1994). Optical constants of liquid and solid methane. *Appl. Optics*, 33: 8,306 – 8,307.

Max, C. E., Macintosh, B. A., Gibbard, S. G., Gavel, D. T., Roe, H. G., de Pater, I., Ghez, A. M., Acton, D. S., Lai, O., Stomski, P., and Wizinowich, P. L. (2003). Cloud structures on Neptune observed with Keck Telescope adaptive optics. *Astron. J.*, 125: 364 – 375.

Meadows, V. S., Orton, G., Line, M., Liang, M., Yung, Y. L., Cleve, J. V., and Burgdorf, M. J. (2008). First Spitzer observations of Neptune: Detection of new hydrocarbons. *Icarus*, 197: 585 – 589.

Moses, J. I., Fouchet, T., Bézard, B., Gladstone, G. R., Lellouch, E., Feuchtgruber, H. (2005). Photochemistry and diffusion in Jupiter's stratosphere: constraints from ISO observations and comparisons with other giant planets. *J. Geophys. Res.*, 110: 8,001.

Naylor, D. A., Davis, G. R., Griffin, M. J., Clark, T. A., Gautier, D., and Marten, A. (1994). Broad-band spectroscopic detection of the CO $J = 3-2$ tropospheric absorption in the atmosphere of Neptune. *Astron. Astrophys.*, 291: L51 – L53.

Norwood, J. W. and Chanover, N. J. (2009). Spatial and short-term temporal variations in Uranus' near-infrared spectrum. *Icarus*, 203: 331 – 335.

Orton, G. S., Baines, K. H., Bergstralh, J. T., Brown, R. H., Caldwell, J., and Tokunaga, A. T. (1987a). Infrared radiometry of Uranus and Neptune at 21 and 32 μm. *Icarus*, 69: 230 – 238.

Orton, G. S., Aitken, D. K., Smith, C., Roche, P. F., Caldwell, J., and Snyder, R. (1987b). The spectra of Uranus and Neptune at 8 – 14 and 17 – 23 μm. *Icarus*, 70: 1 – 12.

Orton, G. S., Baines, K. H., Caldwell, J., Romani, P., Tokunaga, A. T. and West, R.A. (1990). Calibration of the 7- to 14-μm brightness spectra of Uranus and Neptune. *Icarus*, 85: 257 – 265.

Orton, G. S., Encrenaz, T., Leyrat, C., Puetter, R., and Friedson, A. J. (2007). Evidence for methane escape and strong seasonal and dynamical perturbations of Neptune's atmospheric temperatures. *Astron. Astrophys.*, 473: L5 – L8.

Orton, G., Hofstadter, H., Leyrat, C., and Encrenaz, T. (2007a). Spatially resolved thermal imaging and spectroscopy of Uranus and Neptune. *Workshop on Planetary Atmospheres*.

Podolak, M. and Helled, R. (2012). What do we really know about Uranus and Neptune? *Astrophys J Lett*, 759: L32: 7pp.

Pollack, J. B., Rages, K., Pope, S. K., Tomasko, M. G., Romani, P. N., and Atreya, S. K. (1987). Nature of the stratospheric haze on Uranus: Evidence for condensed hydrocarbons. *J. Geophys. Res. Space Phys.*, 92: 15,037 – 15,065.

Pryor, W. R., West, R. A., Simmons, K. E., and Delistsky, M. (1992). High-phase-angle observations of Neptune at 2650 and 7500 Å: Haze structure and particle properties. *Icarus*, 99: 302 – 317.

Rages, K., Pollack, J. B., Tomasko, M. G., and Doose, L. R. (1991). Properties of scatterers in the troposphere and lower stratosphere of uranus based on Voyager imaging data. *Icarus*, 89: 359 – 376.

Rages, K. A., Hammel, H. B., and Friedson, A. J. (2004). Evidence for temporal change at Uranus' south pole. *Icarus*, 172: 548 – 554.

Rayner, J. T., Tooney, D. W., Onaka, P. M., Denault, A. J., Stahlberger, W. E., Vacca, W. D., Cushing, M. C., and Wang, S. (2003). SpeX: A medium-resolution 0.8 – 5.5 micron spectrograph and imager for the NASA Infrared Telescope Facility. *Publ. Astron. Soc. Pac.*, 115: 362 – 382.

Rodgers, C. D. (2000). *Inverse Methods for Atmospheric Sounding: Theory and Practice*. World Scientific, Singapore.

Rosenqvist, J., Lellouch, E., Romani, P. N., Paubert, G., and Encrenaz, T. (1992). Millimeter-wave observations of Saturn, Uranus, and Neptune: CO and HCN on Neptune. *Astrophys. J.*, 392: L99 – L102.

Satorre, M. A., Domingo, M., Millán, C., Luna, R., Vilaplana, R., and Santonja, C. (2008). Density of CH_4, N_2 and CO_2 ices at different temperatures of deposition. *Planet. Space Sci.*, 56: 1,748 – 1,752.

Selby, M. J., Wade, R., and Magro, C. S. (1979). Speckle interferometry in the near-infrared. *Mon*, 187: 553 – 566.

Sheik-Bahae, M. (2005). Nonlinear optics basics: Kramers-Krönig relations in nonlinear optics. In Guenther, R. D., editor, *Encyclopedia of Modern Optics*. Academic Press, Amsterdam.

Signorell, R. and Jetzki, M. (2007). Phase behavior of methane haze. *Phys. Rev. Lett.*, 98: 013,401.

Sromovsky, L. A. (1991). Latitudinal and longitudinal oscillations of cloud features on Neptune. *Science*, 254(5032): 684 – 686.

Sromovsky, L. A., Limaye, S. S., and Fry, P. M. (1993). Dynamics of Neptune's major cloud features. *Icarus*, 105: 110 – 141.

Sromovsky, L. A., Limaye, S. S., and Fry, P. M. (1995). Clouds and circulation on Neptune: implications of 1991 HST observations. *Icarus*, 118: 25 – 38.

Sromovsky, L. A., Fry, P. M., Dowling, T. E., Baines, K. H., and Limaye, S. S. (2001a). Coordinated 1996 HST and IRTF imaging of Neptune and Triton: III. Neptune's atmospheric circulation and cloud structures. *Icarus*, 149: 459 – 488.

Sromovsky, L. A., Fry, P. M., Dowling, T. E., Baines, K. H., and Limaye, S. S. (2001b). Neptune's atmospheric circulation and cloud morphology: Changes revealed by 1998 HST imaging. *Icarus*, 150: 244 – 260.

Sromovsky, L. A., Fry, P. M., and Baines, K. H. (2002). The unusual dynamics of northern dark spots on Neptune. *Icarus*, 156: 16 – 36.

Sromovsky, L. A., Fry, P. M., Limaye, S. S., and Baines, K. H. (2003). The nature of Neptune's increasing brightness: Evidence for a seasonal response. *Icarus*, 163: 256 – 261.

Sromovsky, L. A. and Fry, P. M. (2005). Dynamics of cloud features on Uranus. *Icarus*, 179: 459 – 484.

Sromovsky, L. A. and Fry, P. M. (2007). Spatially resolved cloud structure on Uranus: Implications of near-IR adaptive optics imaging. *Icarus*, 192: 527 – 557.

Sromovsky, L. A., Fry, P. M., Hammel, H. B., de Pater, I., Rages, K. A., and Showalter, M. R. (2007). Dynamics, evolution, and structure of Uranus' brightest cloud features. *Icarus*, 192: 558 – 575.

Sromovsky, L. A. and Fry, P. M. (2008). The methane abundance and structure of Uranus' cloud bands inferred from spatially resolved 2006 Keck grism spectra. *Icarus*, 193: 252 – 266.

Sromovsky, L. A., Fry, P. M., Hammel, H. B., Ahue, W. M., de Pater, I., Rages, K. A., Showalter, M. R., and van Dam, M. A. (2009). Uranus at equinox: Cloud morphology and dynamics. *Icarus*, 203: 265 – 286.

Sromovsky, L. A., Fry, P. M., and Kim, J. H. (2011). Methane on Uranus: The case for a compact CH_4 cloud layer at low latitudes and a severe CH_4 depletion at high-latitudes based on re-analysis of voyager occultation measurements and STIS spectroscopy. *Icarus*, 215: 292 – 312.

Tecza, M., Thatte, N., Clarke, F., Goodsall, T., and Symeonidis, M. (2006). Swift: An adaptive optics assisted I/z band integral feild spectrograph. *New Astron. Rev.*, 49: 647 – 654.

Thatte, N., Tecza, M., Clarke, F., Goodsall, T., Lynn, J., Freeman, D., and Davies, R. L. (2006). The Oxford SWIFT integral field spectrograph. *P. Soc. Photo-Opt. Inst.*, 6269: L2693 - L2693.

Tice, D. S., Irwin, P. G. J., Fletcher, L. N., Teanby, N. A., Hurley, J., Orton, G. S., and Davis, G. R. (2013). Uranus' cloud particle properties and latitudinal methane variation from IRTF SpeX observations. *Icarus*, 223: 684 – 698.

Vacca, W. D., Cushing, M. C., and Rayner, J. T. (2003). A method of correcting near-infrared spectra for telluric absorption. *Publ. Astron. Soc. Pac.*, 115: 389 – 409.

Wynne, C. G. (1999). Optical imaging in very large telescopes. *Mon. Not. R. Astron. Soc.*, 302: 830 – 832.

Yelle, R.V., McConnel, J. C., Strobel, D. R., and Doose, L. R. (1989). The far ultraviolet reflection spectrum of Uranus: results from the Voyager. *Icarus*, 77: 439 – 456.

Zheng, C. G. and Borysow, A. (1995). Modeling of collision-induced infrared-absorption spectra of H_2 pairs in the first overtone band at temperatures from 20 to 500 K. *Icarus*, 113: 84 – 90.